

REPORT DOCUMENTATION PAGE				Form Approved OMB NO. 0704-0188	
<p>The public reporting burden for this collection of information is estimated to average 1 hour per response, including the time for reviewing instructions, searching existing data sources, gathering and maintaining the data needed, and completing and reviewing the collection of information. Send comments regarding this burden estimate or any other aspect of this collection of information, including suggestions for reducing this burden, to Washington Headquarters Services, Directorate for Information Operations and Reports, 1215 Jefferson Davis Highway, Suite 1204, Arlington VA, 22202-4302. Respondents should be aware that notwithstanding any other provision of law, no person shall be subject to any penalty for failing to comply with a collection of information if it does not display a currently valid OMB control number.</p> <p>PLEASE DO NOT RETURN YOUR FORM TO THE ABOVE ADDRESS.</p>					
1. REPORT DATE (DD-MM-YYYY) 08-12-2011		2. REPORT TYPE Final Report		3. DATES COVERED (From - To) 1-Jun-2005 - 1-Oct-2011	
4. TITLE AND SUBTITLE Investigation of an Electromagnetic Induction Sensor				5a. CONTRACT NUMBER W911NF-05-1-0257	
				5b. GRANT NUMBER	
				5c. PROGRAM ELEMENT NUMBER 643619	
6. AUTHORS Waymond R. Scott, Jr.				5d. PROJECT NUMBER	
				5e. TASK NUMBER	
				5f. WORK UNIT NUMBER	
7. PERFORMING ORGANIZATION NAMES AND ADDRESSES Georgia Tech Applied Research Corporation Office of Sponsored Programs 505 Tenth St., NW Atlanta, GA 30332 -0001				8. PERFORMING ORGANIZATION REPORT NUMBER	
9. SPONSORING/MONITORING AGENCY NAME(S) AND ADDRESS(ES) U.S. Army Research Office P.O. Box 12211 Research Triangle Park, NC 27709-2211				10. SPONSOR/MONITOR'S ACRONYM(S) ARO	
				11. SPONSOR/MONITOR'S REPORT NUMBER(S) 48742-EV.20	
12. DISTRIBUTION AVAILABILITY STATEMENT Approved for Public Release; Distribution Unlimited					
13. SUPPLEMENTARY NOTES The views, opinions and/or findings contained in this report are those of the author(s) and should not be construed as an official Department of the Army position, policy or decision, unless so designated by other documentation.					
14. ABSTRACT In recent years, advanced EMI sensors that use a broad range of frequencies long with advanced signal processing have been shown to be capable of discrimination between buried land mines and many types of buried metal clutter. For these EMI sensors to be effective, they must be able to accurately, repeatably, and quickly measure the response of a buried target. This is difficult because the sensor must operate with bandwidths greater than 100 to 1 while accurately measuring signals that are more than 80dB smaller than the direct coupling between the coils. To					
15. SUBJECT TERMS Landmine Detection, EMI, Electromagnetic Induction, Metal Detector					
16. SECURITY CLASSIFICATION OF:			17. LIMITATION OF ABSTRACT UU	15. NUMBER OF PAGES	19a. NAME OF RESPONSIBLE PERSON Waymond Scott
a. REPORT UU	b. ABSTRACT UU	c. THIS PAGE UU			19b. TELEPHONE NUMBER 404-894-3048

Report Title

Investigation of an Electromagnetic Induction Sensor

ABSTRACT

In recent years, advanced EMI sensors that use a broad range of frequencies long with advanced signal processing have been shown to be capable of discrimination between buried land mines and many types of buried metal clutter. For these EMI sensors to be effective, they must be able to accurately, repeatably, and quickly measure the response of a buried target. This is difficult because the sensor must operate with bandwidths greater than 100 to 1 while accurately measuring signals that are more than 80dB smaller than the direct coupling between the coils. To accomplish this, the EMI sensor must be very cleverly designed to account for the coupling and for the secondary effects such as the resonances in the coils. In this work, we are investigating a new methods of constructing and extracting information from such EMI sensors. The ultimate goal of this research is the development of an EMI measurement system that can accurately measure the broad-band response of a buried target for both very strong and weak targets.

Enter List of papers submitted or published that acknowledge ARO support from the start of the project to the date of this printing. List the papers, including journal references, in the following categories:

(a) Papers published in peer-reviewed journals (N/A for none)

<u>Received</u>	<u>Paper</u>
2011/12/01 1: 8	James H. McClellan, Waymond R. Scott, Mu-Hsin Wei. Estimation of the Discrete Spectrum of Relaxations for Electromagnetic Induction Responses Using ℓ_1 -Regularized Least Squares for $0 \leq p \leq 1$, IEEE GEOSCIENCE AND REMOTE SENSING LETTERS, (03 2011): 0. doi: 10.1109/LGRS.2010.2060391
2011/12/01 1: 7	Mu-Hsin Wei, W.R. Scott, J.H. McClellan. Robust Estimation of the Discrete Spectrum of Relaxations for Electromagnetic Induction Responses, IEEE Transactions on Geoscience and Remote Sensing, (03 2010): 0. doi: 10.1109/TGRS.2009.2029981

TOTAL: 2

Number of Papers published in peer-reviewed journals:

(b) Papers published in non-peer-reviewed journals (N/A for none)

<u>Received</u>	<u>Paper</u>
-----------------	--------------

TOTAL:

Number of Papers published in non peer-reviewed journals:

(c) Presentations

1. Waymond R. Scott, Jr. and Michael Malluck, "Electromagnetic Induction Sensor that Uses a Bucking Transformer," 2006 Annual International Symposium on Aerospace/Defense Sensing, Simulation, and Controls, Vol. 6217, Orlando, FL, April 2006.
2. Waymond R. Scott, Jr., "Electromagnetic Induction Sensor that Uses a Bucking Transformer," presented at the 9th Annual Army Landmine/UXO Basic Research Technical Review Meeting, Springfield, VA, Feb. 22-23, 2006.
3. Waymond R. Scott, Jr., "Broadband Electromagnetic Induction Sensor," 2007 Annual International Symposium on Aerospace/Defense Sensing, Simulation, and Controls, Orlando, FL, April 2007.
4. Waymond R. Scott, Jr., "Broadband Electromagnetic Induction Sensor for Detecting Buried Landmines," presented at the 10th Annual Army Landmine/UXO Basic Research Technical Review Meeting, Springfield, VA, Jan. 31-Feb. 1, 2007.
5. Waymond R. Scott, Jr., "Broadband Electromagnetic Induction Sensor for Detecting Buried Landmines," presented at the 11th Annual Army Landmine/UXO Basic Research Technical Review Meeting, Springfield, VA, Jan. 29-30, 2008.
6. W. Scott, G. Larson, M.-H. Wei, & J. McClellan, "Representation of Electromagnetic Induction Signatures by a Discrete Spectrum of Relaxations," Joint ARO-ERDC Review Meeting of ARO Terrestrial Science Program Basic Research, 28-29 July 2009
7. Waymond R. Scott, Jr., "Broadband Target Response of an Electromagnetic Induction Sensor," 12th Annual Landmine & Buried Explosive Object Detection Research Review Meeting, 28-29 January 2009
8. Waymond R. Scott, Jr., "Modeling the measured EM induction response of targets as a sum of dipole terms each with a discrete relaxation frequency," 13th Annual Landmine Detection & Buried Explosive Object Research Review Meeting, Catholic University of America, Washington DC, January 27-28, 2010
9. Waymond R. Scott, Jr., "Measured and Modeling EM Responses," AMDS AWG meeting, Georgia Institute of Technology, Atlanta, Georgia, January 21, 2010
10. Waymond R. Scott, Jr., "Investigation of Broadband Electromagnetic Induction Sensors for Detecting Buried Targets," 14th Annual Landmine Detection & Buried Explosive Object Research Review Meeting, Catholic University of America, Washington DC, February 2-3, 2011

Number of Presentations: 10.00

Non Peer-Reviewed Conference Proceeding publications (other than abstracts):

<u>Received</u>	<u>Paper</u>
-----------------	--------------

TOTAL:

Number of Non Peer-Reviewed Conference Proceeding publications (other than abstracts):

Peer-Reviewed Conference Proceeding publications (other than abstracts):

<u>Received</u>	<u>Paper</u>
2011/12/01 1: 19	Waymond R. Scott. Broadband electromagnetic induction sensor for detecting buried landmines, 2007 IEEE International Geoscience and Remote Sensing Symposium. 2007/07/23 00:00:00, Barcelona, Spain. : ,
2011/12/01 1: 18	Waymond R. Scott. Broadband Array of Electromagnetic Induction Sensors for Detecting Buried Landmines, IGARSS 2008 - 2008 IEEE International Geoscience and Remote Sensing Symposium. 2008/07/07 00:00:00, Boston, MA, USA. : ,
2011/12/01 1: 17	Mu-Hsin Wei, James H. McClellan, Waymond R. Scott. Application of Lp-regularized least squares for $0 \leq p \leq 1$ in estimating discrete spectrum models from sparse frequency measurements, 2010 IEEE International Conference on Acoustics, Speech and Signal Processing. 2010/03/14 00:00:00, Dallas, TX, USA. : ,
2011/12/01 1: 16	Waymond R. Scott, Jr., Gregg D. Larson. Automated, non-metallic measurement facility for testing and development of electromagnetic induction sensors for landmine detection, Detection and Sensing of Mines, Explosive Objects, and Obscured Targets XIV. , Orlando, FL, USA. : ,
2011/12/01 1: 15	Ali C. Gurbuz, Waymond R. Scott, Jr., James H. McClellan. Location estimation using a broadband electromagnetic induction array, Detection and Sensing of Mines, Explosive Objects, and Obscured Targets XIV. , Orlando, FL, USA. : ,
2011/12/01 1: 14	Waymond R. Scott, Mu-Hsin Wei, James H. McClellan. Estimation and application of discrete spectrum of relaxations for electromagnetic induction responses, 2009 IEEE International Geoscience and Remote Sensing Symposium. 2009/07/12 00:00:00, Cape Town, South Africa. : ,
2011/12/01 1: 13	Mu-Hsin Wei, Waymond R. Scott, Jr., James H. McClellan, Gregg D. Larson. Application of \square Lp-regularized Least Squares For $0 \leq p \leq 1$ in Estimating Discrete Spectrum of Relaxations For Electromagnetic Induction Responses, Detection and Sensing of Mines, Explosive Objects, and Obscured Targets XV. , Orlando, Florida, USA. : ,
2011/12/01 1: 12	Waymond R. Scott, Jr., Gregg D. Larson. Measured dipole expansion of discrete relaxations to represent the electromagnetic induction response of buried metal targets, Detection and Sensing of Mines, Explosive Objects, and Obscured Targets XV. , Orlando, Florida, USA. : ,
2011/12/01 1: 11	Waymond R. Scott, Gregg D. Lars. Modeling the measured em induction response of targets as a sum of dipole terms each with a discrete relaxation frequency, IGARSS 2010 - 2010 IEEE International Geoscience and Remote Sensing Symposium. 2010/07/25 00:00:00, Honolulu, HI, USA. : ,
2011/12/01 1: 10	James H. McClellan, Mu-Hsin Wei, Waymond R. Scott. Landmine detection using the discrete spectrum of relaxation frequencies, IGARSS 2011 - 2011 IEEE International Geoscience and Remote Sensing Symposium. 2011/07/24 00:00:00, Vancouver, BC, Canada. : ,
2011/12/01 1: 9	Waymond R. Scott. Calibration technique for broadband electromagnetic induction sensors, IGARSS 2011 - 2011 IEEE International Geoscience and Remote Sensing Symposium. 2011/07/24 00:00:00, Vancouver, BC, Canada. : ,

TOTAL: 11

Number of Peer-Reviewed Conference Proceeding publications (other than abstracts):

(d) Manuscripts

<u>Received</u>	<u>Paper</u>
2011/02/25 1: 6	M. Wei, W. Scott Jr, J. McClellan. Robust estimation of the discrete spectrum of relaxations for electromagnetic induction responses, (02 2011)
2011/02/25 1: 5	M. Wei, J. McClellan, W. Scott Jr. APPLICATION OF ℓ_p -REGULARIZED LEAST SQUARES FOR $0 \leq p \leq 1$ IN ESTIMATING DISCRETE SPECTRUM MODELS FROM SPARSE FREQUENCY MEASUREMENTS, (02 2011)
2011/02/25 1: 4	W. Scott, G. Larson. Measured dipole expansion of discrete relaxations to represent the electromagnetic induction response of buried metal targets, (02 2011)
2011/02/25 1: 3	M. Wei, W. Scott Jr, J. McClellan. Application of L_p -regularized least squares for $0 \leq p \leq 1$ in estimating discrete spectrum of relaxations for electromagnetic induction responses, (02 2011)
2011/02/25 1: 2	M. Wei, J. McClellan, W. Scott Jr. Estimation of the discrete spectrum of relaxations for electromagnetic induction responses using L_p -regularized least squares for $0 \leq p \leq 1$," IEEE , (02 2011)
2011/02/25 1: 1	W. Scott Jr, G. Larson. MODELING THE MEASURED EM INDUCTION RESPONSE OF TARGETS AS A SUM OF DIPOLE TERMS EACH WITH A DISCRETE RELAXATION FREQUENCY, (02 2011)

TOTAL: 6

Number of Manuscripts:

Books

Received Paper

TOTAL:

Patents Submitted

Patents Awarded

Awards

Waymond R. Scott, Jr. was elected to Fellow of the IEEE for his contributions to the detection of buried objects using GPR.

Graduate Students

<u>NAME</u>	<u>PERCENT SUPPORTED</u>	Discipline
Ann Czwartkowskyj	0.00	
Ricardo Lopez	0.00	
Mu-Hsin Wei	0.00	
Ali Cafer Gurbuz	0.00	
Kyle Krueger	0.00	
Mario Malave	0.00	
Daniel Guyon	0.00	
Jonathan Gabbay	0.00	
FTE Equivalent:	0.00	
Total Number:	8	

Names of Post Doctorates

<u>NAME</u>	<u>PERCENT SUPPORTED</u>
Ali Gurbuz	0.00
FTE Equivalent:	0.00
Total Number:	1

Names of Faculty Supported

<u>NAME</u>	<u>PERCENT SUPPORTED</u>	National Academy Member
Waymond Scott	0.00	
James McClellan	0.00	
FTE Equivalent:	0.00	
Total Number:	2	

Names of Under Graduate students supported

<u>NAME</u>	<u>PERCENT SUPPORTED</u>
FTE Equivalent:	
Total Number:	

Student Metrics

This section only applies to graduating undergraduates supported by this agreement in this reporting period

The number of undergraduates funded by this agreement who graduated during this period:	0.00
The number of undergraduates funded by this agreement who graduated during this period with a degree in science, mathematics, engineering, or technology fields:.....	0.00
The number of undergraduates funded by your agreement who graduated during this period and will continue to pursue a graduate or Ph.D. degree in science, mathematics, engineering, or technology fields:.....	0.00
Number of graduating undergraduates who achieved a 3.5 GPA to 4.0 (4.0 max scale):.....	0.00
Number of graduating undergraduates funded by a DoD funded Center of Excellence grant for Education, Research and Engineering:.....	0.00
The number of undergraduates funded by your agreement who graduated during this period and intend to work for the Department of Defense	0.00
The number of undergraduates funded by your agreement who graduated during this period and will receive scholarships or fellowships for further studies in science, mathematics, engineering or technology fields:	0.00

Names of Personnel receiving masters degrees

<u>NAME</u>	
Ann Czwartkowskyj	
Daniel Guyon	
Mu-Hsin Wei	
Mario Malave	
Total Number:	4

Names of personnel receiving PHDs

<u>NAME</u>
Total Number:

Names of other research staff

<u>NAME</u>	<u>PERCENT_SUPPORTED</u>
Gregg Larson	0.00
Michael Malluck	0.00
Daniel Guyon	0.00
FTE Equivalent:	0.00
Total Number:	3

Sub Contractors (DD882)

Inventions (DD882)

Scientific Progress

See Attachment

Technology Transfer

Scientific Summary for the Final Report

of the project

Investigation of an Electromagnetic Induction Sensor

by

Waymond R. Scott, Jr.

Georgia Institute of Technology
School of Electrical and Computer Engineering
Atlanta, GA 30332-0250

December 2011

The work performed this project is summarized by the attached papers.

Refereed Journal Papers

1. Wei, M.-H., Scott, W. R., Jr., and McClellan, J. H. "Robust Estimation of the Discrete Spectrum of Relaxations for Electromagnetic Induction Responses," *IEEE Trans. Geoscience and Remote Sensing*, vol. 48, no. 3, pp. 1169–1179, Mar. 2010.
Doi:10.1109/TGRS.2009.2029981
2. Wei, M.-H., McClellan, J. H., and Scott, W. R., Jr., "Estimation of the Discrete Spectrum of Relaxations For Electromagnetic Induction Responses Using p-Regularized Least Squares for $0 \leq p \leq 1$," *IEEE Trans. Geoscience and Remote Sensing Letters*, Vol. 48, No 3, pp 233-237, 2011. Doi: 10.1109/LGRS.2010.2060391

Refereed Presentations with Proceedings

1. Scott, W.R., Jr., "Broadband Electromagnetic Induction Sensor for Detecting Buried Landmines," *2007 IEEE International Geoscience and Remote Sensing Symposium*, Barcelona, Spain, pp. 22-25, July 23 – 27, 2007. Doi: 10.1109/IGARSS.2007.4422720
2. Scott, W.R., Jr., "Broadband Array of Electromagnetic Induction Sensors for Detecting Buried Landmines," *2008 IEEE International Geoscience and Remote Sensing Symposium*, Boston, Massachusetts, pp. 375 -378, July 6 - 11, 2008. Doi: 10.1109/IGARSS.2008.4779006
3. Larson, G.D. and Scott, W.R., Jr., "Automated, non-metallic measurement facility for testing and development of electromagnetic induction sensors for landmine detection," *Proceedings of the SPIE: 2007 Annual International Symposium on Aerospace/Defense*, Orlando, FL, Vol. 7303, April 2009. doi:10.1117/12.819855
4. Gurbuz, A.C., Scott, W.R., Jr., McClellan, J.H., "Location Estimation Using a Broadband Electromagnetic Induction Array," *Proceedings of the SPIE: 2007 Annual International*

Symposium on Aerospace/Defense, Orlando, FL, Vol. 7303, April 2009. Doi: 10.1117/12.819837

5. Wei, M.-H., Scott, W.R., Jr., and McClellan, J.H., "Estimation and Application of Discrete Spectrum of Relaxations For Electromagnetic Induction Responses," *2009 IEEE International Geoscience and Remote Sensing Symposium*, pp. 105 – 108, Cape Town, South Africa, July 12 - 17, 2009. Doi: 10.1109/IGARSS.2009.5418012
6. Wei, M.-H., McClellan, J.H., and Scott, W.R., Jr., "Application of Lp-Regularized Least Squares For $0 \leq p \leq 1$ in Estimating Discrete Spectrum Models from Sparse Frequency Measurements," *2010 IEEE International Conference on Acoustics, Speech, and Signal Processing (ICASSP)*, pp. 4010 – 4014, March 15 - 19, 2010, Dallas, Texas. Doi: 10.1109/ICASSP.2010.5495769
7. Mu-Hsin Wei, Waymond R. Scott, Jr., James H. McClellan and Gregg D. Larson, "Application of ℓ_p -regularized least squares for $0 \leq p \leq 1$ in estimating discrete spectrum of relaxations for electromagnetic induction responses", *Proc. SPIE 7664*, 76640F (2010). doi: 10.1117/12.852397
8. Waymond R. Scott, Jr. and Gregg D. Larson, "Measured dipole expansion of discrete relaxations to represent the electromagnetic induction response of buried metal targets", *Proc. SPIE 7664*, 76640E (2010). doi: 10.1117/12.852669
9. Scott, W.R., Jr. and Larson, G.D., "Modeling the Measured EM Induction Response of Targets as a Sum of Dipole Terms Each with a Discrete Relaxation Frequency," *2010 IEEE International Geoscience and Remote Sensing Symposium*, pp. 4188 – 4191, Honolulu, Hawaii, July 25-30, 2010. Doi: 10.1109/IGARSS.2010.5652315
10. Wei, M.-H., Scott, W.R., Jr., and McClellan, J.H., "Landmine detection using the discrete spectrum of relaxation frequencies," *2011 IEEE International Geoscience and Remote Sensing Symposium*, pp. 834 – 837, Vancouver, Canada, July 24 - 29, 2011. Doi: 10.1109/IGARSS.2011.6049260
11. Scott, W.R., Jr, "Calibration technique for broadband electromagnetic induction sensors," *2011 IEEE International Geoscience and Remote Sensing Symposium*, pp. 59 – 62, Vancouver, Canada, July 24 - 29, 2011. Doi: 10.1109/IGARSS.2011.6048897

MS Thesis

1. Mu-Hsin Wei, "Estimation of the discrete spectrum of relaxations for electromagnetic induction responses"

Robust Estimation of the Discrete Spectrum of Relaxations for Electromagnetic Induction Responses

Mu-Hsin Wei, *Student Member, IEEE*, Waymond R. Scott, Jr., *Fellow, IEEE*, and James H. McClellan, *Fellow, IEEE*

Abstract—The electromagnetic induction response of a target can be accurately modeled by a sum of real exponentials. However, it is difficult to obtain the model parameters from measurements when the number of exponentials in the sum is unknown or the terms are strongly correlated. Traditionally, the time constants and residues are estimated by nonlinear iterative search. In this paper, a constrained linear method of estimating the parameters is formulated by enumerating the relaxation parameter space and imposing a nonnegative constraint on the parameters. The resulting algorithm does not depend on a good initial guess to converge to a solution. By using tests on synthetic data and laboratory measurement of known targets, the proposed method is shown to provide accurate and stable estimates of the model parameters.

Index Terms—Discrete spectrum of relaxation frequencies (DSRFs), electromagnetic induction (EMI), magnetic polarizabilities, sum of exponentials.

I. INTRODUCTION

ELECTROMAGNETIC induction (EMI) sensors work by illuminating a target of interest with a time-varying magnetic field and then detecting the scattered magnetic field which is generated by the eddy currents induced on the target. Recent research has shown that advanced EMI sensors, which measure the scattered field at a broad range of frequencies or measurement times, are capable of discriminating between certain types of targets [1]–[3]. Target discrimination is realizable because the measurements are strongly related to the target's physical size, shape, orientation, and composition. In a broadband system, it is possible that measurements at a small number of frequencies are sufficient to represent a target. Several researchers have demonstrated subsurface target discrimination based on the EMI response [4], [5].

Several different approaches have been developed to analyze the EMI response of targets. Miller *et al.* [6] proposed a three-parameter model for targets of compact shapes and a four-parameter model as its extension. The measured frequency response can be approximated by fitting the parameters of these models, and then, identification is performed based on the fitted parameters. Many others have worked out the theoretical model for the response of canonical targets [7], [8]. These

models, however, do not appropriately describe objects with more general shapes.

Interestingly, the dielectric response of materials has similar characteristics to the EMI frequency response. Thus, models and methods developed for dielectric materials can be applied to the EMI response. One advantage of doing so is that many of the dielectric models and methods have been well studied over the past 50 years and that much is known about the behavior and properties of the models. For example, the parametric model proposed by Miller *et al.* can be rewritten in the form of the Cole–Cole dielectric relaxation model [9]. Other parametric models well known in polymer science, such as the Havriliak–Negami and Cole–Davidson models, could also be used in modeling the EMI response of targets with more complex shapes [10], [11].

A. DRT

One analysis tool used in polymer science to characterize materials is expressing the dielectric response in terms of a distribution of relaxation times (DRT) [12]. The DRT can reveal characteristics of materials that are not obvious in the raw measurements. Because the DRT representation makes less assumptions about the structure of the response, it offers a model that is more general than the parametric models. The normalized DRT $G(\tau)$ is defined as

$$H(\omega) = g_0 + g_\Delta \int_0^\infty \frac{G(\tau)}{1 + j\omega\tau} d\tau \quad (1)$$

where $H(\omega)$ is the frequency response, τ is the relaxation time, and g_0 and g_Δ are constants. The DRT $G(\tau)$ is normalized to have unity area.

The DRT of some parametric models can be derived analytically. For example, the Cole–Cole model (hence, Miller's model) [13] is

$$H_{CC}(\omega) = g_0 + \frac{g_\Delta}{1 + (j\omega\tau_0)^\alpha} \quad (2)$$

$$G_{CC}(\tau) = \frac{1}{2\pi\tau} \frac{\sin(\alpha\pi)}{\cosh(\alpha \log(\tau/\tau_0)) + \cos(\alpha\pi)} \quad (3)$$

where τ_0 and α are model parameters. Here, $G_{CC}(\tau)$ is restricted to be symmetric with respect to τ_0 in $\log\text{-}\tau$ space because of the assumed structure of H_{CC} . In describing a target response with a parametric model, details and features may be lost in the fitting process. For example, not all targets have symmetric DRTs. Using Cole–Cole to model such targets would result in a loss of information. Describing a target directly in terms of its DRT can be more accurate.

Manuscript received December 2, 2008; revised May 29, 2009. First published October 6, 2009; current version published February 24, 2010. This work was supported in part by the U.S. Army Night Vision and Electronic Sensors Directorate, Science and Technology Division, Countermine Branch, and in part by the U.S. Army Research Office under Contract W911NF-05-1-0257.

The authors are with the School of Electrical and Computer Engineering, Georgia Institute of Technology, Atlanta, GA 30332-0250 USA (e-mail: gth879w@mail.gatech.edu; waymond.scott@ece.gatech.edu; jim.mcclellan@ece.gatech.edu).

Digital Object Identifier 10.1109/TGRS.2009.2029981

B. DSRF

In the study of EMI, several researchers have provided a theoretical basis for representing the EMI response of a metallic object as a discrete sum of damped real exponentials [14], [15]. In terms of the DRT, an EMI response can be represented by (1) with a *discrete* DRT. In addition, we have found that it is more intuitive and convenient to write (1) in terms of *relaxation frequencies* rather than relaxation times. By using the notation of relaxation frequency, we can rewrite (1) in discrete form as

$$H(\omega) = c_0 + \sum_{k=1}^K \frac{c_k}{1 + j\omega/\zeta_k} \quad (4)$$

where c_0 is the shift, K is the model order, c_k is the real spectral amplitudes, and $\zeta_k = 1/\tau_k$ are the relaxation frequencies. The shape of the EMI frequency response of a target can be precisely represented by the set $S = \{(\zeta_k, c_k) : k = 1, \dots, K\}$ which we will call the discrete spectrum of relaxation frequencies (DSRFs). Each pair (ζ_k, c_k) is one relaxation. The parameter c_0 is not considered to be part of the DSRF because it is just a shift of the frequency response. The response at zero frequency $H(0) = \sum_{k=0}^K c_k$ is due to the dc magnetization of the target. The term DSRF and spectrum will be used interchangeably throughout this paper.

The frequency response $H(\omega)$ is proportional to the projection of the magnetic polarizability tensor of the target being measured by the EMI sensor. The magnetic polarizability, hence the DSRF, of several canonical targets can be calculated analytically, and these formulas show how the DSRF is related to the target's physical properties such as conductivity, permeability, shape, size, and orientation [16]–[18].

The DSRF representation has several useful properties. Not only is the DSRF an alternative to representing a target response but also it is directly related to the physical properties of a target. In addition, the relaxation frequencies of a target are invariant to its relative orientation and position to the sensor. Only the spectral amplitudes change with orientation and position, and this makes the DSRF a valuable feature for target discrimination. Baum has coined the term “magnetic singularity identification” when using the relaxations (singularities) for identifying targets.

C. Difficulties

While modeling the EMI response in terms of a distribution is of great value in examining target characteristics, estimating the DRT, both continuous and discrete, from the frequency response is not straightforward. Many methods have been developed in many fields of science for solving such problems. In the case of a continuous DRT, one solves a Fredholm integral equation of the first kind. Methods such as Tikhonov regularization [19], a nonparametric Bayesian approach [20], and a Monte Carlo method [21] could be useful. In the discrete case, the problem is to find the parameters of a sum of exponentials. Techniques such as iterative nonlinear least squares (LSQ) fitting, the matrix pencil method, and modified Prony's methods have been used in the past [22], [23]. Often, these methods do not perform well when three or more relaxations are present.

The goodness of fit strongly depends on a good guess of the model order and is also very sensitive to the initial guess for the model parameters. More discussion on the performance of these methods can be found in [5] and [24].

In practice, a good initial guess is hard to determine, and it is difficult, if not impossible, to have prior knowledge on the model order. For these reasons, most existing estimation methods are prone to not converging in the fitting process. Even if the fitting method converges well with a small residual, there is the concern that the estimated relaxations could be very different from the actual ones. It is possible that the estimate is merely a good numerical fit, but has no physical significance [24].

One robust spectrum estimation method is the MATLAB function `invfreqs` which implements the algorithm proposed by Levy [25]. `invfreqs` is robust in the sense that it can accurately estimate the spectrum of three or more relaxations, and its convergence is not sensitive to the initial guess. The major downside of this method is that it can return complex spectral amplitudes or negative relaxation frequencies that have no physical meaning.

In this paper, we propose a method of estimating the DSRF that requires no prior knowledge of the model order and always returns real model parameters. The proposed method assumes a nonnegative DSRF. While it has not been proven that the DSRF is nonnegative for all targets, the proposed method works well in practice. Even with the constraint, the proposed method can represent a much larger class of responses than the parametric models such as the Cole–Cole and Havriliak–Negami models. For well-known canonical targets, as presented in this paper, the estimated DSRF is an approximate, if not an exact, representation of the actual physical DSRF.

II. ESTIMATION METHOD

When the target response is measured at N distinct frequencies, (4) can be written in a matrix form

$$\begin{bmatrix} H(\omega_1) \\ H(\omega_2) \\ \vdots \\ H(\omega_N) \end{bmatrix} = \begin{bmatrix} 1 & \frac{1}{1+j\omega_1/\zeta_1} & \frac{1}{1+j\omega_1/\zeta_2} & \cdots & \frac{1}{1+j\omega_1/\zeta_K} \\ 1 & \frac{1}{1+j\omega_2/\zeta_1} & \frac{1}{1+j\omega_2/\zeta_2} & \cdots & \frac{1}{1+j\omega_2/\zeta_K} \\ \vdots & \vdots & \vdots & \ddots & \vdots \\ 1 & \frac{1}{1+j\omega_N/\zeta_1} & \frac{1}{1+j\omega_N/\zeta_2} & \cdots & \frac{1}{1+j\omega_N/\zeta_K} \end{bmatrix} \begin{bmatrix} c_0 \\ c_1 \\ c_2 \\ \vdots \\ c_K \end{bmatrix} \quad (5)$$

$$\mathbf{h} = \mathbf{Z}\mathbf{c}$$

where $\omega_{\min} = \omega_1 < \omega_2 < \cdots < \omega_N = \omega_{\max}$, \mathbf{h} is the observation vector, \mathbf{c} is the spectral amplitude vector augmented by the shift c_0 , and \mathbf{Z} is a matrix containing information about the relaxation frequencies ζ 's. The dimension of the matrix \mathbf{Z} is dependent on the number of relaxations present in the spectrum (i.e., the model order). In the case of a simple thin wire circular loop, there is only one relaxation, so \mathbf{Z} has two columns; the first column is always one to account for c_0 .

A. Method Formulation

To estimate the DSRF (i.e., ζ_k and c_k) from a given observation \mathbf{h} , the usual approach is to minimize the norm of the error, $\|\mathbf{h} - \mathbf{Z}\mathbf{c}\|$, but this leads to a *nonlinear* optimization problem.

Instead, we follow the strategy of basis pursuit to reformulate (5) as a linear problem with an overcomplete dictionary [26] and then use nonnegative LSQ to select the best basis, i.e., the best ζ . The overcomplete dictionary is actually a matrix \tilde{Z} that has the same form as Z in (5), but with many more columns. To generate the columns, we enumerate a large set of possible relaxation frequencies in $\log\text{-}\zeta$ space and create one column for each enumerated ζ . The enumeration is done by discretizing a range of relaxation frequencies into M sample points $\tilde{\zeta}_m$ that are uniformly distributed in the $\log\text{-}\zeta$ space. The range of relaxation frequencies is chosen such that $\tilde{\zeta}_{\min} \approx \omega_{\min}$ and $\tilde{\zeta}_{\max} \approx \omega_{\max}$. The number M should be chosen large enough to ensure that some $\tilde{\zeta}_m$'s are in close proximity to the actual relaxation frequencies ζ_k 's. From our simulations, a good choice of M gives roughly 25 sample points per decade. More discussion on the choice of M can be found in Appendix B.

Since the matrix \tilde{Z} has many more columns than the expected number of relaxations, we define the unknown as an $(M+1)$ -element weighted selector vector \tilde{c} and rewrite the problem as

$$\mathbf{h} = \tilde{Z}\tilde{c} + \text{error} \quad (6)$$

where we expect the solution for \tilde{c} to have many zero elements. The vector \tilde{c} contains the shift estimator \tilde{c}_0 followed by the spectral amplitude estimators \tilde{c}_m 's. Ideally, when the error between \mathbf{h} and $\tilde{Z}\tilde{c}$ is minimized, only those \tilde{c}_m 's with corresponding $\tilde{\zeta}_m$'s that are near a true ζ_k will be nonzero, and they will take on the correct spectral amplitudes c_k 's. It follows that a DSRF can then be deduced from the nonzero estimated \tilde{c}_m 's and their corresponding $\tilde{\zeta}_m$'s.

The challenge in obtaining the correct \tilde{c} is that M is much greater than N , so the system in (6) is underdetermined, and there is not a unique \tilde{c} to minimize the error. Any vector in the null space of \tilde{Z} can be added to \tilde{c} without changing the error. There are many ways to select an LSQ solution. The Moore–Penrose pseudoinverse picks the LSQ solution that has the smallest ℓ_2 norm. One can also compute an LSQ solution with the fewest nonzero components. However, neither of these LSQ solutions produces the correct spectrum. Details about existing techniques and the difficulties of solving such a system can be found in [24], [27], and [28].

In the EMI application, we have found that imposing a nonnegative constraint on \tilde{c} effectively eliminates a large portion of the null space of \tilde{Z} and that the remaining solution space contains reasonable answers. We suggest that the nonnegative constraint can be used where applicable. Mathematically, the DSRF can be found by optimizing

$$\begin{aligned} & \arg \min_{\tilde{c}} \|\tilde{Z}'\tilde{c} - \mathbf{h}'\| \quad \text{subject to } \tilde{c} \geq 0 \\ & \text{where } \tilde{Z}' = \begin{bmatrix} \Re(\tilde{Z}) \\ \Im(\tilde{Z}) \end{bmatrix} \quad \text{and} \quad \mathbf{h}' = \begin{bmatrix} \Re(\mathbf{h}) \\ \Im(\mathbf{h}) \end{bmatrix}. \end{aligned} \quad (7)$$

Separating the real and imaginary parts makes the whole system real. The first element in \tilde{c} , i.e., \tilde{c}_0 , can be guaranteed nonnegative by adding a sufficiently large value to the frequency response \mathbf{h} .

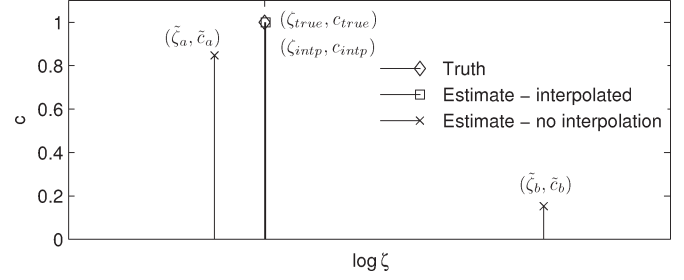


Fig. 1. Splitting of an expected relaxation followed by interpolation. The sample points $\tilde{\zeta}_m$'s do not coincide with ζ_{true} , so ζ_{true} is split into the two nearest sample points: $\tilde{\zeta}_a$ and $\tilde{\zeta}_b$. The estimation accuracy is increased by interpolating in $\tilde{\zeta}$ using \tilde{c}_a and \tilde{c}_b .

B. Implementation

The proposed estimation method can be easily implemented through the function `lsqnonneg` in MATLAB which uses the algorithm found in [29]. An alternative to `lsqnonneg` is the CVX package which implements convex optimization under MATLAB [30]. Both optimizers provide satisfactory results. However, CVX is a larger and more sophisticated program but is slightly slower than `lsqnonneg` which was written exactly to solve LSQ problems with a nonnegative constraint. Nevertheless, CVX would be of great interest if more constraints are to be added.

When using either `lsqnonneg` or CVX, we found that normalizing the input data \mathbf{h} to have an ℓ_2 norm of unity increases the accuracy of estimation. Therefore, all data will be scaled to an ℓ_2 norm of unity before optimization and scaled back to the original norm after optimization because the original norm may contain useful information for target identification.

C. Interpolation

We observed that, in the estimated DSRF, an expected relaxation $(\zeta_{\text{true}}, c_{\text{true}})$ often gets split into two peaks located at the two sample points adjacent to ζ_{true} , as shown in Fig. 1. We also observed that the two estimated spectral amplitudes add up to the true spectral amplitude c_{true} and that ζ_{true} is closer to $\tilde{\zeta}$ with larger \tilde{c} . This phenomenon can be understood: The splitting of relaxation happens when the sample points $\tilde{\zeta}_m$'s do not coincide with ζ_{true} , and c_{true} gets distributed among the two sample points that are the closest to ζ_{true} .

We can increase the accuracy of the estimation by taking advantage of this well-behaved and consistently recurring phenomenon. We can reverse the splitting processes. A true relaxation frequency could be restored by interpolating between two adjacent $\tilde{\zeta}_m$'s with nonzero \tilde{c}_m according to their spectral amplitudes. The interpolated spectral amplitude is simply the sum of the two adjacent spectral amplitudes. Mathematically

$$c_{\text{intp}} = \tilde{c}_a + \tilde{c}_b \quad (8)$$

$$\log(\zeta_{\text{intp}}) = \log(\tilde{\zeta}_a) + \frac{\tilde{c}_b}{\tilde{c}_a + \tilde{c}_b} \log(\tilde{\zeta}_b / \tilde{\zeta}_a). \quad (9)$$

The quantities are shown in Fig. 1. The sample points $\tilde{\zeta}_m$'s are placed close enough that a simple linear interpolation in $\log\text{-}\zeta$ space gives satisfactory results. The interpolation is applied only on two adjacent nonzero relaxations.

After the interpolation is performed, any \tilde{c}_m with a value of zero is eliminated along with its corresponding $\tilde{\zeta}_m$. We denote the resulting relaxation frequencies as $\hat{\zeta}_l$, with spectral amplitudes \hat{c}_l , or, in vector notation, as $\hat{\zeta}$ and \hat{c} , both with length L . It is convenient and desirable to interpret the estimation results by looking at $\hat{\zeta}$ and \hat{c} . Every entry in $\hat{\zeta}$ is an estimate of one relaxation frequency of the target with its corresponding estimated spectral amplitude in \hat{c} . The estimated DSRF $\hat{S} = \{(\hat{\zeta}_l, \hat{c}_l) : l = 1, \dots, L\}$ is then compactly stored in $\hat{\zeta}$ and \hat{c} . In addition, the vector length L is an estimate of the model order K . Note that \tilde{c}_0 is not part of the DSRF, and therefore not interpolated, and is not in the vector \hat{c} .

D. Summary

To estimate the unknown DSRF $S = \{(\zeta_k, c_k)\}$ from a given set of observations \mathbf{h} over N frequencies, we first decide on a relaxation frequency range $[\tilde{\zeta}_{\min}, \tilde{\zeta}_{\max}]$ and the number of points M to be sampled in this range. Then, we generate the sample points $\tilde{\zeta}_m$'s, construct a dictionary matrix $\tilde{\mathbf{Z}}$, perform the optimization described in (7), and finally obtain the estimated DSRF $\hat{S} = \{(\hat{\zeta}_l, \hat{c}_l)\}$ by interpolating the solution $\tilde{\mathbf{c}}$ returned by the optimizer.

In the following three sections, we present the estimation results from synthetic, laboratory, and field data. All estimations are performed with $M = 100$ and optimized with `lsqnonneg`. In assessing the signal strength, the signal-to-noise ratio (SNR) is used. The signal power is computed by $\sum_{i=1}^N |H(\omega_i)|^2 / N$. The noise power in synthesized data is equal to the variance of the noise. In laboratory and field data, the background signal can be measured and is treated as noise when calculating the SNR. All presented spectra are normalized such that $\sum_{i=1}^N c_i = 1$ (c_0 is separate). Normalization removes the influence of the signal amplitude which changes for many reasons.

III. SYNTHETIC DATA

In this section, the proposed estimation method is tested against synthetic data to show its functionality, robustness, and stability. The synthesized data are sampled at 21 frequencies approximately logarithmically distributed over the range of 300 Hz–90 kHz. The range of ζ for estimation is chosen such that $\log(\tilde{\zeta}_{\min})$ and $\log(\tilde{\zeta}_{\max})$ are 2.4470 and 6.6223, respectively. This corresponds to a frequency range of 45 Hz–670 kHz, which is larger than the measured frequency range. With $M = 100$, the spacing between two sample points is 0.0422 decades. The number of samples and the frequencies are chosen to be the same as an existing hardware system, but the proposed method can also perform under different settings.

1) *Notation:* ζ and c are the true/theoretical relaxation frequencies and spectral amplitudes; $\hat{\zeta}$ and \hat{c} are the estimates.

A. Dissimilarity Measure Between Two DSRF

Before we can evaluate the goodness of estimation, some kind of measure is needed to assess the dissimilarity between the estimated DSRF and the truth. It is difficult, however, to compare two sparse spectra when the number of relaxations is different, which happens frequently. When the number of

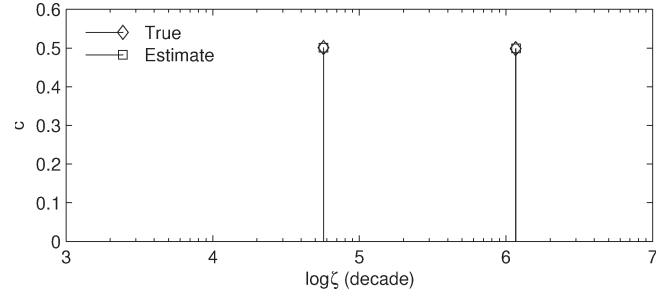


Fig. 2. Estimation of a simulated two coplanar coaxial circular loop target, for which $\log \zeta_k$ and c_k are (4.7552, 6.0651) and (0.5013, 0.4987), respectively. The estimates for $\log \hat{\zeta}_l$ and \hat{c}_l are (4.7557, 6.0672) and (0.5010, 0.4990), respectively.

relaxations is the same ($K = L$), a possible measure of the dissimilarity between two spectra is

$$D(\hat{S}, S) = \frac{1}{I} \sum_{i=1}^I |\log \hat{\zeta}_i - \log \zeta_i| \quad \forall i \quad \hat{\zeta}_i \leq \hat{\zeta}_{i+1} \quad \text{and} \quad \zeta_i \leq \zeta_{i+1} \quad (10)$$

where $I = K = L$. In (10), only the relaxation frequencies ζ_k 's are considered, and spectral amplitudes c_k 's are ignored. This approximation is reasonable and convenient when two spectra are visually similar. We refer to this dissimilarity measure as the deviation. It has the units of decades.

Another measure that is more comprehensive is the Earth Mover's Distance (EMD) [31], [32]. The EMD consistently quantifies the dissimilarity between two spectra, even when $K \neq L$. Intuitively, the EMD measures how much work it takes to morph one spectrum into the other. Specifically, one spectrum represents piles of earth with volume \hat{c}_l located at the associated $\hat{\zeta}_l$. The other spectrum represents holes in the ground with capacity c_k located at ζ_k . The distance between a pile of earth and a hole is naturally defined to be the difference between $\hat{\zeta}_l$ and ζ_k in log space, and the work to move some earth into a hole would be the amount of earth moved times the distance traveled. Then, the EMD is proportional to the least amount of work needed to move as much earth into the holes. For the DSRF, the EMD is measured in decades because it is almost always examined in $\log\text{-}\zeta$ space. See Appendix A for details about the EMD.

B. Two Coplanar Coaxial Loops

We simulate the frequency response for a structure with two coplanar coaxial circular loops of copper wire. A theoretical EMI response and the DSRF of this target are provided in Appendix C. The circumferences of the two loops are chosen to be 200 and 150 mm, respectively. The larger loop has a wire radius of 0.0635 mm (#36 AWG¹), and the smaller one has a wire radius of 0.3215 mm (#22 AWG). The EMI response is simulated at a 70-dB SNR with additive white Gaussian noise (AWGN). The estimated spectrum is shown in Fig. 2 along with the true spectrum. The estimated spectrum is almost identical to the truth. The deviation from the true spectrum is

¹ American wire gauge.

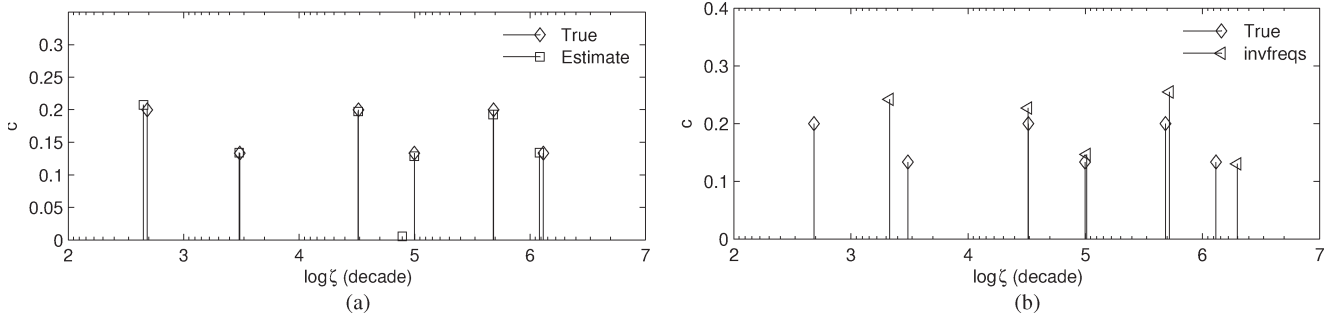


Fig. 3. Estimation of a six-relaxation DSRF. See Table I for numerical data. (a) Estimates by the proposed method. (b) Estimates by *invfreqs* with nonphysical parameters removed.

TABLE I
ESTIMATION OF A SIX-RELAXATION DSRF

Truth	c_k	0.2000	0.1333	0.2000	0.1333	0.2000	0.1333			
	$\log \zeta_k$	2.6842	3.4855	4.5135	4.9985	5.6839	6.1162			
Proposed method	\hat{c}_l	0.2076	0.1343	0.1973	0.1286	0.1928	0.1341	0.0052		
	$\log \hat{\zeta}_l$	2.6515	3.4803	4.5109	4.9981	5.6801	6.0809	4.8931		
invfreqs	\hat{c}_l^\dagger		0.2418	0.2269	0.1465	0.2546	0.1301	$-0.3902 \cdot 10^{-4}$	$-0.3902 \cdot 10^{-4}$	0.1334
	$\log \hat{\zeta}_l^\dagger$		3.3303	4.5111	5.0126	5.7188	6.2983	$-0.0012 + 0.0042i$	$-0.0012 - 0.0042i$	-0.0127

\dagger Negative or complex values are not logged

0.0013 decades, which is very small compared to the detectable ζ range, about 4 decades. The computation took 0.11 s on a 2.66-GHz CPU with 960-MB RAM.

C. Six-Relaxation DSRF

While existing sum-of-exponential estimation methods can also successfully estimate a two-relaxation case, when the number of relaxations is three or more, these methods start to encounter problems such as returning complex model parameters or not converging [24]. We test our method on a six-relaxation DSRF. The target response is synthesized at 70-dB SNR with AWGN

$$H(\omega) = 1 + \sum_{k=1}^6 \frac{c_k}{1 + j\omega/\zeta_k} + \text{noise}. \quad (11)$$

The relaxation frequencies are chosen such that two ζ_k 's coincide with a sample point, one ζ_k is half way between two $\log\text{-}\zeta$ sample points, and the rest are randomly in between sample points. The relaxation frequencies are chosen this way to demonstrate the functionality of the proposed method when the sample points do not coincide with the true relaxation frequencies.

The synthesized and estimated DSRFs are shown in Fig. 3(a) and Table I. All six relaxation frequencies are correctly recovered. The estimated model parameters are real, and the deviation from truth is small. The EMD between the estimate and truth is 0.0365 decades. There is a seventh relaxation in the estimate introduced by the noise, but its spectral amplitude is small.

Now, we estimate the DSRF of the same data using *invfreqs*. The *a priori* model order is chosen to be 8 which is slightly higher than the actual but is reasonable because, in practice, it is difficult to know the actual model order. The estimated model parameters are recorded in Table I. There are two estimated ζ 's that are complex and one negative. We can

try to obtain a physically possible DSRF by throwing away these complex or negative relaxation frequencies. The resulting estimated DSRF is shown in Fig. 3(b). Three relaxations are correctly recovered, but the two left most expected relaxations are not. The EMD between the estimate and truth is 0.3323 decades, much higher than the EMD of the proposed method.

Although a physically possible DSRF can be obtained by throwing away the nonphysical estimates, the resulting spectrum can be quite different from the truth. Using the actual model order or its neighboring numbers as the *a priori* model order does not preclude complex model parameters either. Nevertheless, when the true model order is low and the SNR is high, satisfactory estimates can be obtained from *invfreqs* by throwing out nonphysical parameters.

Returning complex or nonphysical estimates is a problem that plagues many methods, and there is not a proper way to deal with the complex estimates. The best way is perhaps to restrict the model parameters to be real and physical when setting up the problem, and this is the approach taken in the proposed method.

D. SNR

To see how the proposed method performs in noise, a Monte Carlo simulation versus SNR is run on a target with a four-relaxation DSRF. Goodness of estimation is measured by the EMD between the estimate and truth. The simulation result, shown in Fig. 4, shows the robustness of the estimation method at different SNRs.

As expected, the EMD between the estimate and the truth increases as the SNR decreases. This suggests that the proposed method is functional in a range of SNR where the EMD is below some threshold. This threshold, however, depends on the application of the estimated spectrum. For example, in the case of classification, a more robust classifier may tolerate worse estimations and therefore allow lower SNR.

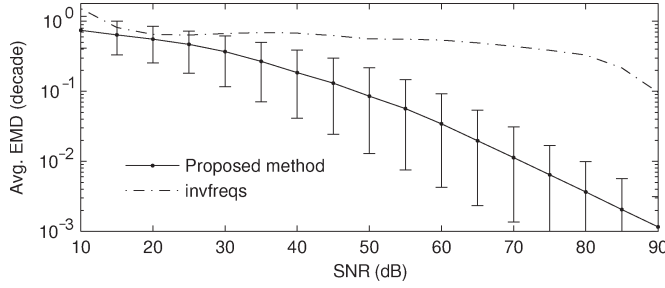


Fig. 4. Monte Carlo simulation on goodness of estimation versus SNR performed on a four-relaxation DSRF. Sample size is 10 000 at each SNR. Error bars indicate the range of EMD between the 10th and 90th percentiles.

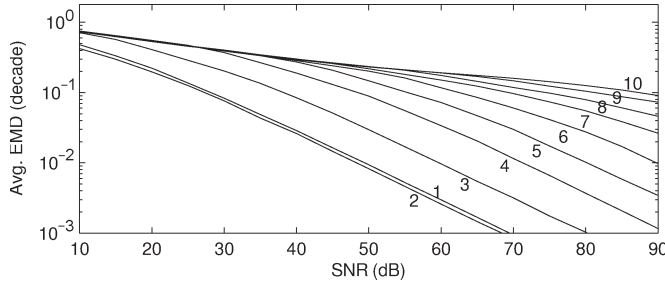


Fig. 5. Monte Carlo simulation on goodness of estimation versus SNR for different DSRFs with model order ranging from 1 to 10. Sample size is 10 000.

The same noise simulation was also performed on *invfreqs* using the actual model order as the *a priori* model order. Non-physical parameters are removed from the estimate. As shown in Fig. 4, *invfreqs* barely functions except at around 90-dB SNR where its average EMD drops to 0.1 decades. In comparison, the proposed method has an average EMD 100 times smaller than that of *invfreqs* at 90-dB SNR and has low EMD for a wide range of SNR.

In reality, the depth and size of the target are two dominant factors of SNR. The SNR increases with the size of the target and decreases with the buried depth. In our laboratory measurements, a typical SNR for loop targets in this work is 70 dB when the target is placed 10 cm below the EMI sensor.

Fig. 5 shows the same Monte Carlo simulation performed on DSRFs with different model orders using the proposed method. It is seen that a higher model order DSRF requires a higher SNR to achieve a given goodness of fit (EMD). Although the curves are different for each model order, all curves have the same behavior, i.e., the goodness of estimation is positively correlated to the SNR. The consistent trend of these curves suggests that the proposed method is stable and functional over a wide range of SNR.

IV. LABORATORY DATA

In this section, we are concerned with the physical meaning of the estimated DSRF. We will show that the estimated spectrum agrees with the theoretical and physical DSRFs derived from the electromagnetic theory, and the estimate is not just another good fit to the data, which can be a problem for other estimation methods [24]. The data are measured with a wideband EMI sensor operating at 21 frequencies approximately logarithmically distributed over the range of 300 Hz–90 kHz [33].

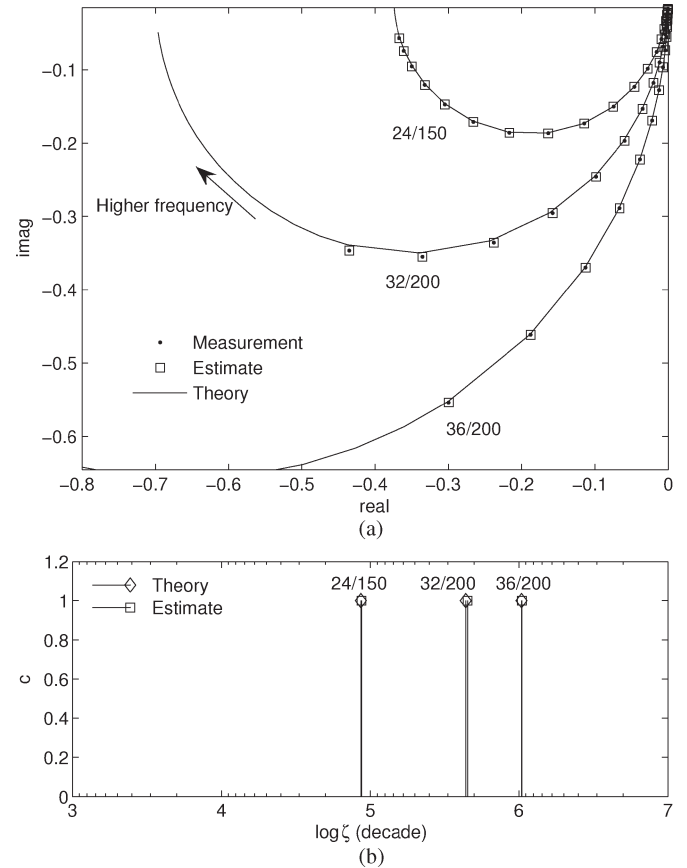


Fig. 6. (a) Frequency response of three independently measured single loops on an Argand diagram. Responses are normalized such that $\|\mathbf{h}\|_2 = 1$. Measurements are labeled in the form of AWG/circumference (in millimeters). (b) Theoretical and estimated DSRFs. Theoretical $\log \zeta_k$, from left to right, are 4.9364, 5.6416, and 6.0167. Estimated $\log \hat{\zeta}_k$, from left to right, are 4.9411, 5.6534, and 6.0195. All relaxations have an amplitude of unity.

The frequency response of targets will be presented on Argand diagrams. Specifically, complex frequency response functions are plotted on a complex plane with the imaginary part as the vertical axis, the real part as the horizontal axis, and frequency as the parameter.

A. Single Loop

We first examine the simplest case—a single thin-wire circular loop. The theoretical EMI frequency response and DSRF can be found in [16]. This target contains only one relaxation located at $\zeta = R/L$, where L is the inductance and R is the resistance of the loop. These quantities can be computed according to (19) and (20) in Appendix C.

Fig. 6(a) shows three independently measured EMI responses for circular copper loops of circumferences 150, 200, and 200 mm and AWG Nos. 24, 32, and 36, respectively. The theoretical and estimated DSRFs are shown together in Fig. 6(b). The estimates are seen to agree with the theory. The deviations from the theory are 0.0047, 0.0117, and 0.0028 decades for the loops with AWG Nos. 24, 32, and 36, respectively. All deviations are relatively small in the observable relaxation frequency range, so we conclude that the estimated DSRF is an accurate representation of the physical DSRF.

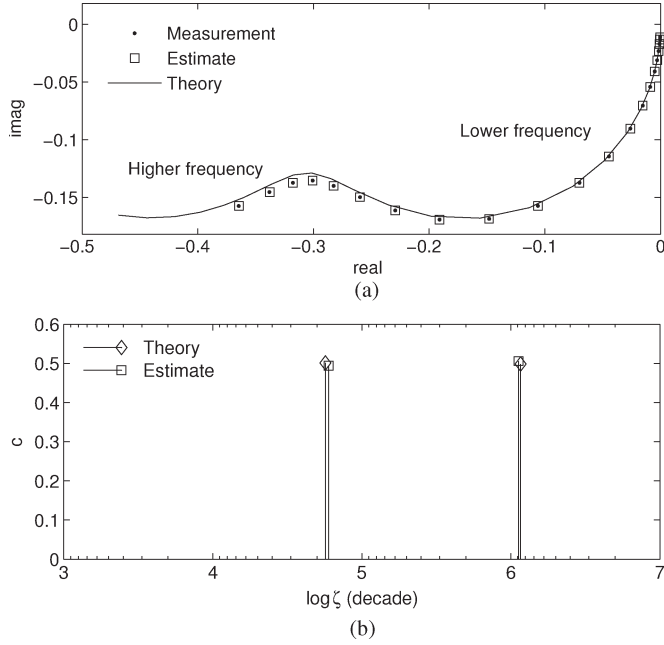


Fig. 7. (a) Laboratory-measured frequency response of two coplanar coaxial circular loops on an Argand diagram. Theory deviates from the measurement at higher frequencies. Responses are normalized such that $\|\mathbf{h}\|_2 = 1$. (b) Theoretical and estimated DSRFs. $\log \zeta_k$ and c_k are (4.7552, 6.0651) and (0.5013, 0.4987), respectively. The estimate $\log \hat{\zeta}_l$ and \hat{c}_l are (4.7768, 6.0514) and (0.4941, 0.5059), respectively.

B. Two Coplanar Coaxial Circular Loops

To test the method on a more complicated spectrum, we revisit the case of a target with two coplanar coaxial circular loops considered earlier. A physical target was built according to the same specifications described in Section III-B. The EMI response of this target was measured in the laboratory and is shown in Fig. 7(a). The SNR is about 70 dB. The estimated and theoretical DSRFs are shown in Fig. 7(b).

The estimated DSRF deviates from the theory slightly with a deviation of 0.0177 decades. We believe that this is mostly due to the thin-wire approximation used in the theory. In the theory, the wire radius is assumed to be much smaller than the loop radius. The inner loop (#22 AWG) has a loop radius to wire radius ratio of about of 47 which is not very high, meaning that the wire cannot be modeled as infinitely thin. In addition, thicker wires have a secondary relaxation due to the off-wire-axial current flow which is not accounted for in the theory. At any rate, the deviation is small, and the estimated spectrum is very close to the theory. We can thus conclude that this estimated DSRF is an accurate representation of the true DSRF of the physical target.

C. Nonmagnetic Sphere

The spectrum of a metallic sphere is difficult to estimate because it contains an infinite sequence of relaxations, and the spacing between successive relaxation frequencies decreases as the relaxation frequency decreases [17]. The decrease in spacing makes the relaxations in the region of these closely spaced ζ 's indistinguishable from one another. It is therefore

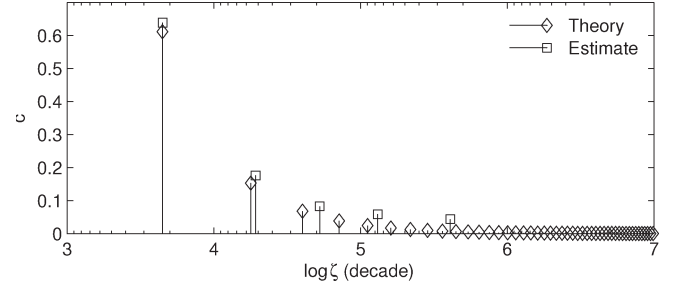


Fig. 8. DSRF estimation of a laboratory-measured sphere. The theoretical DSRF has an infinite sequence of relaxation frequencies.

understood that it is impossible to perfectly recover the spectrum of a sphere. Here, the proposed method is tested against the EMI response of an aluminum sphere measured in the lab. The sphere has a radius of 0.9525 cm. The theoretical and estimated DSRFs are shown in Fig. 8. The EMD between the truth and estimate is 0.1088 decades.

In the estimated DSRF, the first two relaxations are correctly recovered, but the remaining theoretical relaxations are accounted for by the other three estimated ones. We observed that closely spaced theoretical relaxations in one region are combined into one estimated relaxation, and the theoretical spectral amplitudes in that region roughly add up to the estimated spectral amplitude. For example, the right most estimated relaxation has an amplitude of 0.0438, and it accounts for the infinitely many theoretical relaxations to its right, which have an amplitude sum of 0.0521. The estimated DSRF, even though it cannot recover exactly the theoretical DSRF, is seen to approximate the theory. In this case of a sphere, the estimated DSRF is an approximation to the physical DSRF, and it is not just a good fit, but a fit that can be related to the physical properties of the target.

V. FIELD DATA

As a final demonstration of the proposed method, we estimate the DSRF of three types of landmines (Fig. 9). The EMI measurement system uses a dipole transmit coil and a quadrupole receive coil along with a down-track filter that is important to make the nonnegative constraint applicable for this system [33]. For each type of landmine, measurements were collected from several mines buried at different depths and locations, and the DSRF of each sample was estimated and then plotted together with others of the same type. The spectral amplitudes are represented by the color intensity.

Fig. 9(a) shows the DSRF of seven Type-A mines: low metal content, nonmagnetic, and moderate EMI response antipersonnel mines. The SNR ranges from about 45 to 60 dB. All seven Type-A mines exhibit consistency in the relaxation frequencies and the spectral amplitudes. The average EMD between pairs of mines is 0.0594 decades.

Fig. 9(b) shows the DSRF of eight Type-B mines: medium-metal content, magnetic, and strong EMI response antipersonnel mines. The SNR ranges from about 55 to 70 dB. The spectra are consistent; both ζ and \hat{c} exhibit the same behavior in all eight samples. Mine #7 differs from the others somewhat

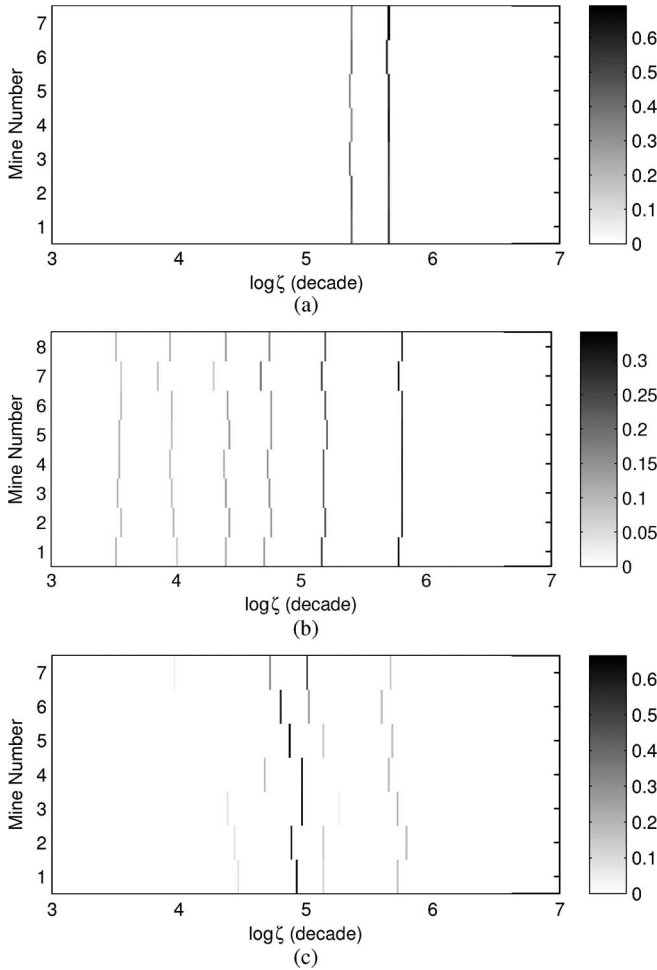


Fig. 9. Estimated DSRF of real landmines. The spectral amplitude is represented by the intensity: The darker the color, larger the amplitude. (a) Seven Type-A mine. (b) Eight Type-B mines. (c) Seven Type-C mines.

in $\hat{\zeta}$, but the number of relaxations and the trend of spectral amplitudes are the same as that of the other seven Type-B mines. The average EMD between pairs of mines is 0.1536 decades.

Fig. 9(c) shows the DSRF of seven Type-C mines: low metal content, magnetic, and weak EMI response antipersonnel mines. The SNR ranges from about 20 to 35 dB. The spectra are less consistent compared to that of Type-A and Type-B mines, but notice that the prominent relaxations are all located around $\log \zeta = 5$ decades. Since the response is weak, the noise could move the relaxations around as observed in Fig. 9(c). The average EMD between mine pairs is 0.1490 decades, which is slightly lower than the average EMD in Fig. 9(b). This is because the two prominent relaxations in Fig. 9(b) are farther away from each other.

The estimated $H(0)$ is normalized and shown in Fig. 10 for the three types of mines. The normalized $H(0)$ reflects the magnetic properties of the mines. Type-A mines are nonmagnetic and therefore have a normalized $H(0)$ close to zero. The other two types of mines have a normalized $H(0)$ well above zero which reflects the magnetic content of the mines. Variations in the estimated $H(0)$ are consistent with the variations in the DSRF.

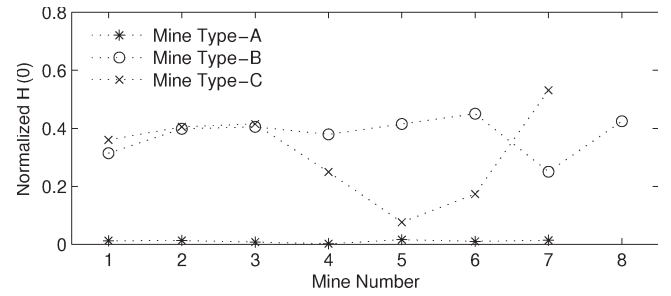


Fig. 10. Normalized estimated $H(0)$ for landmines in Fig. 9. $H(0)$ is normalized by $\sum_{l=1}^L \hat{c}_l$.

The variation of the estimated DSRF and $H(0)$ could be caused by several factors such as manufacturing variations, corrosion, the magnetic properties of the soil, or measurement errors. Manufacturing variations in the shape of the metal parts and their electrical and magnetic properties can cause variations in the DSRF. Corrosion can change the properties of the metal parts which will change its response. We believe that mine #7 in Fig. 9(b) has a metal part slightly different from the other seven instances. The lower normalized $H(0)$ suggests a different magnetic property, and the slightly different DSRF reaffirms this small variation in the metal.

The response due to the magnetic properties of the soil can also influence the DSRF since the response of the soil is superimposed on the response of the target and it is not possible to completely separate the two. For the mines shown Fig. 9(c), we believe that the variation in the estimated $H(0)$ is primarily due to the magnetic properties of the soil. Since the magnetic shift observed in the response of the soil is on the same order of magnitude as the response of these mines, the soil can have a strong influence on the mine responses. On the other hand, mines shown in Fig. 9(b) have much stronger EMI responses, and influence from the soil is therefore insignificant.

In general, landmine of one type has consistent estimated DSRFs. These stable and recurring DSRFs could be a valuable feature to be exploited in target discrimination. The estimated $H(0)$ can also be used as a feature when it is not overwhelmed by the noise or ground response.

VI. CONCLUSION

The proposed method has been tested with a wide variety of data, targets, and noise levels and has been found to give stable, accurate, and quick estimates of the DSRF of a target. When the DSRF cannot be exactly recovered, the estimate is an approximation to the actual. In all cases, the estimated DSRF is directly related to the physical properties of the target, and the same DSRF is robustly estimated in different instances of the same target.

In the future, more work can be put into investigating the applicability of the proposed method, even in other fields of science. In addition, the useful properties that the estimated DSRF possesses suggest that the proposed method would be a promising way to generate features for object identification. More work can be put into designing classifiers based on the estimated DSRF to provide more robust and reliable detectors.

APPENDIX A

EMD

Given two distributions $\hat{S} = \{(\hat{\zeta}_i, \hat{c}_i) : i = 1, \dots, L\}$ and $S = \{(\zeta_j, c_j) : j = 1, \dots, K\}$, the EMD between the two distributions can be computed by solving the optimization problem [32]

Define
$$d_{ij} = |\log \hat{\zeta}_i - \log \zeta_j| \quad (12)$$

$$EMD(\hat{S}, S) = \min_{f_{ij}} \frac{\sum_{i=1}^L \sum_{j=1}^K f_{ij} d_{ij}}{\sum_{i=1}^L \sum_{j=1}^K f_{ij}} \quad (13)$$

subject to

$$\sum_{j=1}^K f_{ij} \leq \hat{c}_i, \quad i = 1, \dots, L \quad (14)$$

$$\sum_{i=1}^L f_{ij} \leq c_j, \quad j = 1, \dots, K \quad (15)$$

$$\sum_{i=1}^L \sum_{j=1}^K f_{ij} = \min \left(\sum_{i=1}^L \hat{c}_i, \sum_{j=1}^K c_j \right) \quad (16)$$

$$f_{ij} \geq 0, \quad i = 1, \dots, L; j = 1, \dots, K \quad (17)$$

where f_{ij} is an intermediate variable used during the optimization. Adapting the illustration in Section III-A, \hat{S} is the pile of earth and S denotes the holes. Equation (14) guarantees no overdraw from each pile of earth, (15) guarantees no over fill at each hole, (16) sets the problem to fill up the holes with as much earth as possible, and (17) allows only moving earth into holes and not the reverse.

In our application, spectra should be normalized by having the sum of all spectral amplitudes be unity ($\sum c_i = 1$). In this case, the aforementioned optimization problem is simplified to having the denominator in (13) be one and the right-hand side of (16) be unity. The EMD also becomes symmetric.

APPENDIX B

DENSITY OF DISCRETIZATION OF THE RELAXATION FREQUENCY SPACE

The number M in (5) decides the number of sample points placed in a relaxation frequency range. Equivalently, M controls the density of discretization of the ζ space. The denser the discretization, the more likely the sampled ζ is close to the true ζ . In the extreme case, if an infinite number of sample points fill up the relaxation frequency range, there must be one sampled ζ that coincides with the true ζ . Of course, computationally, it would be impossible to estimate a DSRF with an infinite number of sample points. Even if the number of samples is kept finite, with a fixed number of observations N , the null space of \hat{Z} gets larger and larger as M increases, and the number of possible bad estimates increases. It is therefore desirable to have M just large enough, so that the estimate is likely correct while the computational cost remains low.

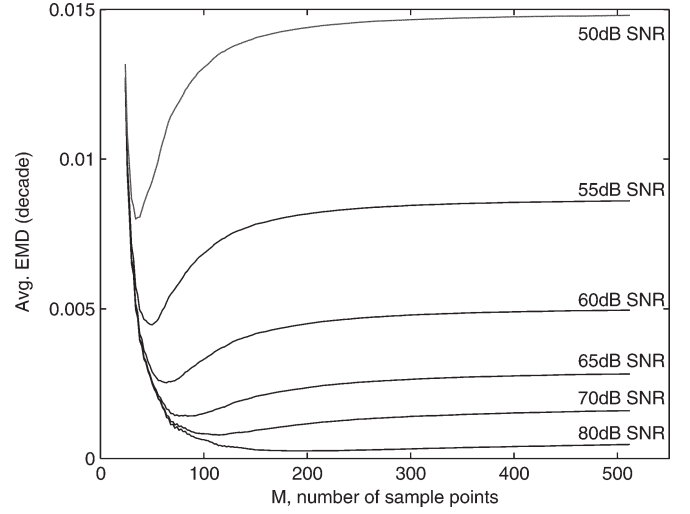


Fig. 11. Monte Carlo simulation on density of discretization of ζ space. Each point on the curve is the average EMD over 10 000 samples.

A Monte Carlo simulation on the density of discretization of ζ space is performed over a range of M with different noise levels. The simulation result is shown in Fig. 11, where a higher EMD value means worse estimates. The figure suggests that M should be greater than 60 to avoid bad estimation due to not enough sample points, while M should be no greater than 200 because adding more sample points does not improve the goodness of fit. We see that within the range $60 < M < 200$, at lower SNRs (50–60 dB), better estimation is obtained with $M \approx 70$. While at higher SNRs (65–80 dB), better estimation is obtained with $M \approx 120$. In other words, at lower SNR, lower discretization density gives more robust performance, which agrees with the intuition that larger dictionaries are more sensitive to perturbation of noise. On the other hand, when the SNR is high, higher discretization density delivers more accurate estimates. To accommodate a wide range of SNR, we compromise to have $M \approx 100$, and since the relaxation frequency range is about 4 decades, there are about 25 sample points per decade.

Although the Monte Carlo simulation is performed on a two-relaxation target, the result should well represent the behavior of the estimation process in general. This is true as observed in simulations of different DSRFs. We can therefore infer that, in general, a good choice of M is around 25 sample points per decade. As shown in the figure, the goodness of fit is not sensitive to the chosen M given it is large enough, so there is some freedom in choosing M .

APPENDIX C

CIRCUIT MODEL FOR TWO COPLANAR COAXIAL CIRCULAR LOOPS

This section derives a theoretical approximation to the magnetic polarizability of two coplanar coaxial circular loops in the low-frequency realm. A larger loop of radius r_1 with wire radius a_1 is placed around a smaller loop of radius r_2 with wire radius a_2 . The wires have electric conductivity σ and relative permeability μ_r . Two loops are on the same plane and share the

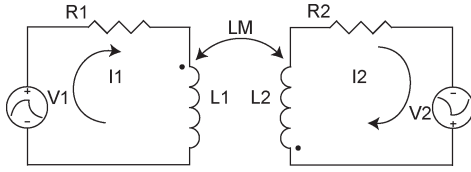


Fig. 12. Circuit model for two coplanar coaxial circular loops.

same center. The wire radius is assumed to be much smaller than the loop radius, i.e., $a \ll r$. This configuration of two coplanar coaxial circular loops can be modeled as a simple two coupled LR circuits shown in Fig. 12.

The voltage $V(s)$ induced by the incident magnetic field on the loop is related to the incident magnetic excitation H^{inc} in Laplace domain through

$$V(s) = -s\mu_0 H^{\text{inc}} A \quad (18)$$

where A is the loop area and μ_0 is the permeability of free space. Assume that the incident magnetic field is normal to the plane containing the loops. In low frequency, the resistance R of the loop is

$$R = \frac{2r}{a^2 \sigma} \quad (19)$$

and the inductance L is [34]

$$L = r\mu_0 \left[\left(1 + \frac{a^2}{8r^2}\right) \ln\left(\frac{8r}{a}\right) + \frac{a^2}{24r^2} - 2 + \frac{\mu_r}{4} \right]. \quad (20)$$

The mutual inductance L_M between the two loops is [35]

$$L_M = \frac{2\mu\sqrt{r_1 r_2}}{k} \left[\left(1 - \frac{1}{2}k^2\right) K(k) - E(k) \right] \quad (21)$$

where

$$k^2 = \frac{4r_1 r_2}{(r_1 + r_2)^2} \quad (22)$$

and K and E are the complete elliptic integrals.

In Laplace domain, the system equation for the circuit is [16]

$$\begin{bmatrix} V_1 \\ V_2 \end{bmatrix} = \begin{bmatrix} R_1 + sL_1 & sL_M \\ sL_M & R_2 + sL_2 \end{bmatrix} \begin{bmatrix} I_1 \\ I_2 \end{bmatrix}. \quad (23)$$

Solve for the currents

$$\begin{bmatrix} I_1 \\ I_2 \end{bmatrix} = \frac{-s\mu_0 H^{\text{inc}}}{(R_1 + sL_1)(R_2 + sL_2) - (sL_M)^2} \cdot \begin{bmatrix} R_2 + sL_2 & -sL_M \\ -sL_M & R_1 + sL_1 \end{bmatrix} \begin{bmatrix} A_1 \\ A_2 \end{bmatrix}. \quad (24)$$

The magnetic polarizability \mathcal{M} is then

$$\mathcal{M}(s) = \frac{A_1 I_1 + A_2 I_2}{H^{\text{inc}}} \quad (25)$$

$$= \frac{-s\mu_0 [A_1^2(R_2 + sL_2) + A_2^2(R_1 + sL_1) - 2sA_1 A_2 L_M]}{(R_1 + sL_1)(R_2 + sL_2) - (sL_M)^2}. \quad (26)$$

Perform partial fraction expansion

$$\mathcal{M}(s) = -s \left(\frac{Q_1}{s - s_1} + \frac{Q_2}{s - s_2} \right) \quad (27)$$

$$= -(Q_1 + Q_2) + \frac{Q_1}{1 - s/s_1} + \frac{Q_2}{1 - s/s_2} \quad (28)$$

where s_1 and s_2 are the roots of the denominator in (26) [18]

$$s_{1,2} = \frac{-(R_1 L_2 + R_2 L_1) \pm \sqrt{(R_1 L_2 - R_2 L_1)^2 + 4R_1 R_2 L_M^2}}{2(L_1 L_2 - L_M^2)}. \quad (29)$$

Variables Q_1 and Q_2 are simply

$$Q_1 = \frac{\mu_0 [A_1^2(R_2 + s_1 L_2) + A_2^2(R_1 + s_1 L_1) - 2s_1 A_1 A_2 L_M]}{s_1 - s_2} \quad (30)$$

$$Q_2 = \frac{\mu_0 [A_1^2(R_2 + s_2 L_2) + A_2^2(R_1 + s_2 L_1) - 2s_2 A_1 A_2 L_M]}{s_2 - s_1}. \quad (31)$$

By using (29)–(31), the DSRF of two coplanar coaxial circular loops can be computed. The relaxation frequency $\zeta_k = -s_k$ with corresponding spectral amplitude Q_k .

ACKNOWLEDGMENT

The authors would like to thank Dr. A. C. Gurbuz for the insightful comments and for suggesting the applicability of CVX and ℓ_1 minimization.

REFERENCES

- [1] D. A. Keiswetter, I. J. Won, J. Miller, T. Bell, E. Cespedes, and K. O'Neill, "Discriminating capabilities of multifrequency EMI data," in *Proc. IGARSS*, Honolulu, HI, Jul. 2000, vol. 4, pp. 1415–1417.
- [2] P. Gao, L. Collins, P. M. Garber, N. Geng, and L. Carin, "Classification of landmine-like metal targets using wideband electromagnetic induction," *IEEE Trans. Geosci. Remote Sens.*, vol. 38, no. 3, pp. 1352–1361, May 2000.
- [3] E. B. Fails, P. A. Torriano, W. R. Scott, Jr., and L. M. Collins, "Performance of a four parameter model for modeling landmine signatures in frequency domain wideband electromagnetic induction detection systems," *Proc. SPIE*, vol. 6553, p. 655 30D, Apr. 2007.
- [4] L. Collins, P. Gao, and L. Carin, "An improved Bayesian decision theoretic approach for land minedetection," *IEEE Trans. Geosci. Remote Sens.*, vol. 37, no. 2, pp. 811–819, Mar. 1999.
- [5] L. S. Riggs, J. E. Mooney, and D. E. Lawrence, "Identification of metallic mine-like objects using low frequency magnetic fields," *IEEE Trans. Geosci. Remote Sens.*, vol. 39, no. 1, pp. 56–66, Jan. 2001.
- [6] J. T. Miller, T. H. Bell, J. Soukup, and D. Keiswetter, "Simple phenomenological models for wideband frequency-domain electromagnetic induction," *IEEE Trans. Geosci. Remote Sens.*, vol. 39, no. 6, pp. 1294–1298, Jun. 2001.
- [7] F. S. Grant and G. F. West, *Interpretation Theory in Applied Geophysics*. New York: McGraw-Hill, 1965, ch. 17.
- [8] S. H. Ward, "Electromagnetic theory for geophysical applications," in *Mining Geophysics*, vol. 2, D. A. Hansen, W. E. Heinrichs, Jr., R. C. Holmer, R. E. MacDougall, G. R. Rogers, J. S. Sumner, and S. H. Ward, Eds. Tulsa, OK: Soc. Explor. Geophys., 1967, ch. 2, pp. 10–196.
- [9] K. S. Cole and R. H. Cole, "Dispersion and absorption in dielectrics. I. alternating current characteristics," *J. Chem. Phys.*, vol. 9, no. 4, pp. 341–351, Apr. 1941.
- [10] D. W. Davidson and R. H. Cole, "Dielectric relaxation in glycerol, propylene glycol, and n-propanol," *J. Chem. Phys.*, vol. 19, no. 12, pp. 1484–1490, Dec. 1951.

- [11] S. Havriliak and S. Negami, "A complex plane representation of dielectric and mechanical relaxation processes in some polymers," *Polymer*, vol. 8, no. 4, pp. 161–210, 1967.
- [12] J. Honerkamp and J. Weese, "A nonlinear regularization method for the calculation of relaxation spectra," *Rheol. Acta*, vol. 32, no. 1, pp. 65–73, Jan. 1993.
- [13] E. Barsoukov and J. R. Macdonald, *Impedance Spectroscopy*. Hoboken, NJ: Wiley-Interscience, 2005, ch. 2, p. 37.
- [14] A. A. Kaufman and P. A. Eaton, *The Theory of Inductive Prospecting*. Amsterdam, The Netherlands: Elsevier, 2001, ch. 3.
- [15] C. E. Baum, "On the singularity expansion method for the solution of electromagnetic interaction problems," Air Force Weapons Lab., Albuquerque, NM, Dec. 1971.
- [16] G. D. Sower, "Eddy current responses of canonical metallic targets theory and measurements," EG&G MSI, Albuquerque, NM, May 1997.
- [17] C. E. Baum, "Low-frequency near-field magnetic scattering from highly, but not perfectly, conducting bodies," in *Detection and Identification of Visually Obscured Targets*, C. E. Baum, Ed. Philadelphia, PA: Taylor & Francis, 1999, ch. 6, pp. 163–218.
- [18] N. Geng, C. E. Baum, and L. Carin, "On the low-frequency natural response of conducting and permeable targets," *IEEE Trans. Geosci. Remote Sens.*, vol. 37, no. 1, pp. 347–359, Jan. 1999.
- [19] A. N. Tikhonov, "Solution of incorrectly formulated problems and the regularization method," *Soviet Math. Dokl.*, vol. 4, pp. 1035–1038, Oct. 1963.
- [20] R. L. Wolpert, K. Ickstadt, and M. B. Hansen, "A nonparametric Bayesian approach to inverse problems," in *Bayesian Statistics 7*, J. M. Bernardo, A. P. Dawid, J. O. Berger, M. West, D. Heckerman, M. J. Bayarri, and A. F. M. Smith, Eds. Oxford, U.K.: Clarendon, 2003, pp. 403–418.
- [21] E. Tuncer and S. M. Gubanski, "On dielectric data analysis. Using the Monte Carlo method to obtain relaxation frequency distribution and comparing non-linear spectral function fits," *IEEE Trans. Dielectr. Elect. Insul.*, vol. 8, no. 3, pp. 310–320, Jun. 2001.
- [22] T. K. Sarkar and O. Pereira, "Using the matrix pencil method to estimate the parameters of a sum of complex exponentials," *IEEE Antennas Propag. Mag.*, vol. 37, no. 1, pp. 48–55, Feb. 1995.
- [23] M. R. Osborne and G. K. Smyth, "A modified Prony algorithm for exponential function fitting," *SIAM J. Sci. Comput.*, vol. 16, no. 1, pp. 119–138, Jan. 1995.
- [24] Y. Das and J. E. McFee, "Limitations in identifying objects from their time-domain electromagnetic induction response," *Proc. SPIE*, vol. 4742, pp. 776–788, Apr. 2002.
- [25] E. C. Levy, "Complex-curve fitting," *IRE Trans. Autom. Control*, vol. 4, no. 1, pp. 37–43, May 1959.
- [26] S. S. Chen, D. L. Donoho, and M. A. Saunders, "Atomic decomposition by basis pursuit," *SIAM Rev.*, vol. 43, no. 1, pp. 129–159, Aug. 2001.
- [27] P. C. Hansen, *Rank-Deficient and Discrete Ill-Posed Problems: Numerical Aspects of Linear Inversion*. Philadelphia, PA: Soc. Ind. Math., 1998.
- [28] K. Holmström and J. Petersson, "A review of the parameter estimation problem of fitting positive exponential sums to empirical data," *Appl. Math. Comput.*, vol. 126, no. 1, pp. 31–61, Feb. 2002.
- [29] C. L. Lawson and R. J. Hanson, *Solving Least Squares Problems*. Englewood Cliffs, NJ: Prentice-Hall, 1974, ch. 23.
- [30] M. Grant, S. Boyd, and Y. Ye, CVX: Matlab Software for Disciplined Convex Programming, Jul. 2008. [Online]. Available: <http://www.stanford.edu/~boyd/cvx/>
- [31] Y. Rubner, C. Tomasi, and L. J. Guibas, "A metric for distributions with applications to image databases," in *Proc. ICCV*, Bombay, India, Jan. 1998, pp. 59–66.
- [32] B. Fisher, The Earth Mover's Distance, Oct. 2008. [Online]. Available: http://homepages.inf.ed.ac.uk/rbf/CVonline/LOCAL_COPIES/RUBNER/emd.htm
- [33] W. R. Scott, Jr., "Broadband array of electromagnetic induction sensors for detecting buried landmines," in *Proc. IGARSS*, Boston, MA, Jul. 2008, pp. II-375–II-378.
- [34] W. R. Smythe, S. Silver, J. R. Whinnery, and D. J. Angelakos, "Electricity and magnetism," in *American Institute of Physics Handbook*, D. E. Gray, Ed. New York: McGraw-Hill, 1963, ch. 5, p. 29.
- [35] W. R. Smythe, *Static and Dynamic Electricity*. New York: McGraw-Hill, 1968, ch. 8, p. 335.

Mu-Hsin Wei (S'09), received the B.S. degree in electrical and computer engineering from Georgia Institute of Technology, Atlanta, in 2007. He is currently working toward the Ph.D. degree with the School of Electrical and Computer Engineering, Georgia Institute of Technology.



Waymond R. Scott, Jr. (S'81–M'82–SM'03–F'08) received the B.E.E., M.S.E.E., and Ph.D. degrees from the Georgia Institute of Technology, Atlanta, in 1980, 1982, and 1985, respectively.

In 1986, he joined the School of Electrical and Computer Engineering, Georgia Institute of Technology, as an Assistant Professor, where he is currently a Professor. His research involves the interaction of electromagnetic and acoustic waves with materials. This research spans a broad range of topics, including the measurement of the properties of materials, experimental and numerical modeling, and systems for the detection of buried objects. His research is currently concentrated on investigating techniques for detecting objects buried in the earth. This work has many practical applications, for example, the detection of underground utilities, buried hazardous waste, buried structures, unexploded ordnance, and buried land mines.



James H. McClellan (S'69–M'74–SM'79–F'85) received the B.S. degree in electrical engineering from Louisiana State University, Baton Rouge, in 1969 and the M.S. and Ph.D. degrees from Rice University, Houston, TX, in 1972 and 1973, respectively.

Since 1987, he has been a Professor with the School of Electrical and Computer Engineering, Georgia Institute of Technology, where he is currently the John and Marilu McCarty Chair. He is the coauthor of *Number Theory in Digital Signal Processing*, *Computer Exercises for Signal Processing*, *DSP First: A Multimedia Approach*, and *Signal Processing First*, which received the McGraw-Hill Jacob Millman Award for an outstanding innovative textbook in 2003.

Prof. McClellan was a corecipient of the IEEE Jack S. Kilby Signal Processing Medal in 2004.

Estimation of the Discrete Spectrum of Relaxations for Electromagnetic Induction Responses Using ℓ_p -Regularized Least Squares for $0 \leq p \leq 1$

Mu-Hsin Wei, *Student Member, IEEE*, James H. McClellan, *Fellow, IEEE*, and Waymond R. Scott, Jr., *Fellow, IEEE*

Abstract—The electromagnetic induction response of a target can be accurately modeled by a sum of real exponentials. However, in practice, it is difficult to obtain the model parameters from measurements. We previously proposed a constrained linear method that can robustly estimate the model parameters when they are nonnegative. In this letter, we present a modified ℓ_p -regularized least squares algorithm, for $0 \leq p \leq 1$, that eliminates the nonnegative constraint. An empirical method for choosing the regularization parameter is also studied. Using tests on synthetic data and laboratory measurements, the proposed method is shown to provide robust estimates of the model parameters in practice.

Index Terms—Electromagnetic induction (EMI), discrete spectrum of relaxation frequencies (DSRF), ℓ_1 minimization, sum of exponentials.

I. INTRODUCTION

RECENT research has shown that broadband electromagnetic induction (EMI) sensors are capable of discriminating between certain types of targets [1], [2]. The EMI frequency response $H(\omega)$ of a metallic target can be expressed as [3]

$$H(\omega) = c_0 + \sum_{k=1}^K \frac{c_k}{1 + j\omega/\zeta_k} \quad (1)$$

where c_0 is the shift, K is the model order, c_k denotes the real spectral amplitudes, and ζ_k denotes the relaxation frequencies. The parameter set $S = \{(\zeta_k, c_k) : k = 1, \dots, K\}$ is called the discrete spectrum of relaxation frequencies (DSRF) or simply the spectrum; each pair (ζ_k, c_k) is one relaxation.

It is advantageous to model the EMI signal with (1) because the relaxation frequencies are invariant to target orientation, and this is valuable in target detection. However, it is difficult in practice to obtain the model parameters in (1) from a small number of measurements. For most existing estimation methods, a good guess of the model order K is required for the fitting

process to converge. Prior knowledge of K , however, is usually unavailable. The highly correlated summands in (1) and the nonlinear relation between $H(\omega)$ and ζ_k also make estimation difficult. Most existing methods often give suboptimal solutions that are far from the truth or return complex parameters that sometimes lack physical meaning [4].

In [5], we proposed a constraint linear method that can robustly estimate the DSRFs without prior knowledge of the model order. The method however presumes nonnegative spectra for the targets, which are valid for most targets using our system [6]; however, some targets can have a spectrum with positive and negative relaxations. In this letter, we propose an estimation method using ℓ_p -regularized least squares ($0 \leq p \leq 1$) that removes the nonnegative constraint. Since we ultimately want to solve for the ℓ_0 -regularized problem, more accurate estimates may be obtained using $p < 1$ than $p = 1$ when approximating, as argued in [7]. As with the previously proposed constrained optimization method, the ℓ_p method always returns real model parameters and is stable under noise. While the proposed method is presented here in a frequency-domain application, the method can also be extended to time-domain applications in a straightforward manner.

II. ESTIMATION METHOD

We formulate the DSRF estimation problem as a set of linear equations, as described in [5, Sec. II]. When the target response is measured at N distinct frequencies ($\omega_{\min} = \omega_1 < \omega_2 < \dots < \omega_N = \omega_{\max}$), the problem can be written in a matrix form

$$\begin{bmatrix} H(\omega_1) \\ H(\omega_2) \\ \vdots \\ H(\omega_N) \end{bmatrix} = \underbrace{\begin{bmatrix} 1 & \frac{1}{1+j\omega_1/\tilde{\zeta}_1} & \frac{1}{1+j\omega_1/\tilde{\zeta}_2} & \cdots & \frac{1}{1+j\omega_1/\tilde{\zeta}_M} \\ 1 & \frac{1}{1+j\omega_2/\tilde{\zeta}_1} & \frac{1}{1+j\omega_2/\tilde{\zeta}_2} & \cdots & \frac{1}{1+j\omega_2/\tilde{\zeta}_M} \\ \vdots & \vdots & \vdots & \ddots & \vdots \\ 1 & \frac{1}{1+j\omega_N/\tilde{\zeta}_1} & \frac{1}{1+j\omega_N/\tilde{\zeta}_2} & \cdots & \frac{1}{1+j\omega_N/\tilde{\zeta}_M} \end{bmatrix}}_{\tilde{\mathbf{Z}}} \begin{bmatrix} \tilde{c}_0 \\ \tilde{c}_1 \\ \tilde{c}_2 \\ \vdots \\ \tilde{c}_M \end{bmatrix} + \text{error} \quad (2)$$

$$\tilde{\mathbf{h}} = \tilde{\mathbf{Z}}\tilde{\mathbf{c}} + \text{error}$$

where $\tilde{\zeta}_m$ denotes the *sampled* relaxation frequencies, \tilde{c}_m denotes the corresponding spectral amplitude estimates, $\tilde{\mathbf{h}}$ is

Manuscript received December 21, 2009; revised May 19, 2010; accepted June 29, 2010. Date of publication September 7, 2010; date of current version February 25, 2011. This work was supported in part by the U.S. Army REDCOM CERDEC Night Vision and Electronic Sensors Directorate, Science and Technology Division, Countermine Branch, and in part by the U.S. Army Research Office under Contract W911NF-05-1-0257.

The authors are with the School of Electrical and Computer Engineering, Georgia Institute of Technology, Atlanta, GA 30332-0250 USA (e-mail: m.wei@gatech.edu).

Color versions of one or more of the figures in this paper are available online at <http://ieeexplore.ieee.org>.

Digital Object Identifier 10.1109/LGRS.2010.2060391

the observation vector, and $\tilde{\mathbf{Z}}$ is the overcomplete dictionary. The sampled $\tilde{\zeta}_m$ is generated by enumerating a large set of M possible relaxation frequencies uniformly distributed in the $\log\text{-}\zeta$ space ($M \gg K$). $\tilde{\mathbf{c}}$ is the weighted selector vector containing the shift estimator \tilde{c}_0 followed by the spectral amplitude estimators. We expect the solution for $\tilde{\mathbf{c}}$ to have many zero elements because $M \gg K$, i.e., $\tilde{\mathbf{c}}$ will be sparse.

We then utilize the ℓ_p -regularized least squares technique, for $0 \leq p \leq 1$, because it promotes sparse solutions [8]

$$\arg \min_{\tilde{\mathbf{c}}} \|\tilde{\mathbf{Z}}' \tilde{\mathbf{c}} - \tilde{\mathbf{h}}'\|_2^2 + \lambda \|\tilde{\mathbf{c}}\|_p^p, \quad 0 \leq p \leq 1$$

$$\text{where } \tilde{\mathbf{Z}}' = \begin{bmatrix} \Re(\tilde{\mathbf{Z}}) \\ \Im(\tilde{\mathbf{Z}}) \end{bmatrix} \quad \text{and} \quad \tilde{\mathbf{h}}' = \begin{bmatrix} \Re(\tilde{\mathbf{h}}) \\ \Im(\tilde{\mathbf{h}}) \end{bmatrix} \quad (3)$$

where λ is the regularization parameter. Separating the real and imaginary parts in $\tilde{\mathbf{Z}}$ makes the whole system real. Ideally, in the optimal $\tilde{\mathbf{c}}$, only those \tilde{c}_m with corresponding $\tilde{\zeta}_m$ that is near a true ζ_k will be nonzero, and they will take on the correct spectral amplitudes c_k . It follows that a DSRF can then be deduced from the nonzero estimated \tilde{c}_m and its corresponding $\tilde{\zeta}_m$.

The ℓ_p -regularized least squares solution for $p < 1$ can be approximated by the iteratively reweighted ℓ_1 algorithm proposed by Candès *et al.* [8]. The weights are updated as suggested in [9]. We also adopt the ϵ -regularization technique used in the same paper. In summary, (3) is approximated by the following (see also [10]):

Algorithm 1: Approximated ℓ_p -regularized least squares

Input $\tilde{\mathbf{Z}}', \mathbf{h}', p, \lambda, \tilde{\mathbf{c}}^0$

```

1:  $\tilde{\mathbf{c}}^n \leftarrow \tilde{\mathbf{c}}^0$ 
2: for  $k \leftarrow 0$  to  $-8 \text{ step } -1$  do
3:    $\epsilon \leftarrow 10^k$ 
4:   repeat
5:      $\tilde{\mathbf{c}}^{n-1} \leftarrow \tilde{\mathbf{c}}^n$ 
6:      $w_i^n \leftarrow (|\tilde{c}_i^{n-1}| + \epsilon)^{p-1}$ 
7:      $\tilde{\mathbf{c}}^n \leftarrow \arg \min \|\tilde{\mathbf{Z}}' \tilde{\mathbf{c}} - \mathbf{h}'\|_2^2 + \lambda \sum_{i=1}^{M+1} w_i^n |\tilde{c}_i|$ 
8:   until  $\|\tilde{\mathbf{c}}^n - \tilde{\mathbf{c}}^{n-1}\|_2 < \sqrt{\epsilon}/100$ 
9: return  $\tilde{\mathbf{c}}^n$ 

```

The ℓ_1 minimization problem in step 7 is solved by `l1_ls`, which is a MATLAB optimizer proposed by Kim *et al.* [11]. We have also found that normalizing the input data \mathbf{h} , as well as the columns of $\tilde{\mathbf{Z}}'$, to have unit ℓ_2 norm increases the accuracy of estimation. While it is often suggested to initialize $\tilde{\mathbf{c}}^0$ using the least squares solution [9], we observe that setting entries of $\tilde{\mathbf{c}}^0$ to all ones also seems to be effective and converges faster. The nonzero entries of $\tilde{\mathbf{c}}$ selected by (3), along with the corresponding $\tilde{\zeta}_m$, are the relaxations needed in the estimated DSRF, $\hat{S} = \{(\hat{\zeta}_l, \hat{c}_l) : l = 1, \dots, L\}$.

III. ESTIMATION RESULTS

The proposed estimation method is tested against synthetic and laboratory data to show its functionality, accuracy, and stability. The hardware system used is a wideband EMI sensor operating at 21 frequencies that are approximately logarithmically distributed over the range 300 Hz–90 kHz (2.5 decades) [6]. The synthetic data are generated in accordance with the hardware specification. The range of ζ for estimation is chosen such that $\log(\tilde{\zeta}_{\min})$ and $\log(\tilde{\zeta}_{\max})$ are 2.45 and 6.62, respectively, i.e., 4.17 decades. All estimations are performed with $M = 100$, and all presented spectra are normalized such that $\sum |c_i| = 1$. Spectral amplitudes less than 10^{-5} are not displayed. All frequency responses are normalized such that $\|\mathbf{h}\|_2 = 1$. Unless specified, $p = 0.5$ is chosen as a representative case. The regularization parameter λ is chosen based on the method described in Section IV. The results presented in this section may achieve higher accuracy with a more sophisticated λ selection rule. Here, we demonstrate the usability of the proposed algorithm with a simple λ selection rule. See Section IV for more discussion on the choice of λ .

Notation: ζ and c are the true/theoretical relaxation frequencies and spectral amplitudes; $\hat{\zeta}$ and \hat{c} are the estimates.

A. Dissimilarity Measure Between Two DSRFs

In order to evaluate the performance between the estimated DSRF and the true spectrum, we need to define a measure of dissimilarity that is appropriate for sparse spectra with multiple peaks. We use the Earth Mover's Distance (EMD) [12] which quantifies the “amount of work” to morph one spectrum into another. Strictly speaking, the EMD is only defined for positive spectra, but we can account for negative spectral amplitudes by defining the distance function between two relaxations (ζ_i, c_i) and $(\hat{\zeta}_j, \hat{c}_j)$ to be

$$d_{ij} = \begin{cases} |\log \zeta_i - \log \hat{\zeta}_j|, & c_i \hat{c}_j \geq 0 \\ 1 + |\log \zeta_i - \log \hat{\zeta}_j|, & c_i \hat{c}_j < 0 \end{cases}$$

which penalizes relaxations with different signs. Spectra are made nonnegative and normalized prior to the EMD computation. Finally, notice that the EMD is measured in decades because it is examined in the $\log\text{-}\zeta$ space.

The EMD compares two spectra as a whole; thus, the effect of very small amplitude relaxations is tiny in the EMD, and neglecting these small components amounts to assuming that they are near the noise level of the measured frequency response.

B. Synthetic Six-Relaxation DSRF

We test our method (using $p = 0.5$) on a six-relaxation DSRF synthesized at 70-dB signal-to-noise ratio (SNR) with additive white Gaussian noise (Fig. 1). This is a case that cannot be handled by traditional nonlinear parameter optimization [4] or the nonnegative linear method [5]. All six relaxation frequencies are recovered by using Algorithm 1. The estimation is nearly perfect, because the estimated model parameters are real, and the deviation from truth is small. The EMD between the estimated and the true DSRF is 0.01 decade. There is one extra

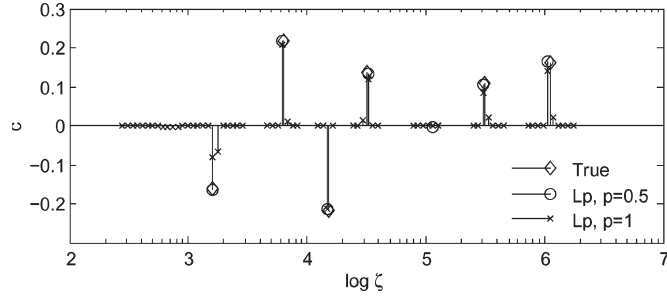


Fig. 1. Estimation of a synthetic six-relaxation DSRF.

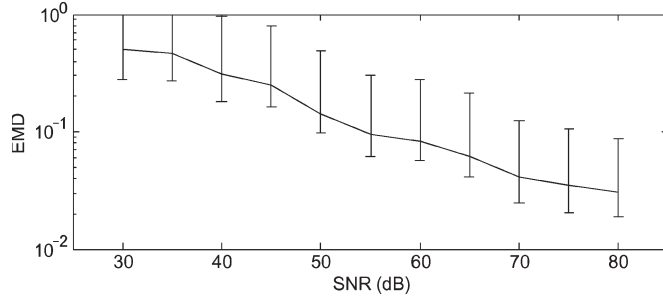


Fig. 2. Monte Carlo simulation on goodness of estimation versus SNR performed on a four-relaxation DSRF. The sample size is 100 per SNR.

relaxation near $\log \zeta = 5$ in the estimated spectrum of Fig. 1, but it has very small amplitude and can be safely neglected.

This spectrum is also estimated with $p = 1$ using `l1_ls`. In this case, many extra relaxations are introduced by the fitting process (Fig. 1); the EMD is 0.03. Real targets are not likely to have a spectrum with many small relaxations around a strong relaxation. In fact, Baum argues that physical relaxation frequencies are discrete [3]. However, the small relaxations introduced by $p = 1$ seem to give a continuous spectrum of relaxation frequencies. In this sense, $p < 1$ gives a sparser solution that more accurately resembles a physical spectrum, even though this may not always be reflected in the EMD measure.

C. SNR

To see how the proposed method performs in noise, a Monte Carlo simulation versus SNR is performed. The true spectrum is from a target with a four-relaxation DSRF including negative relaxations. The simulation result, shown in Fig. 2, shows the robustness of the estimation method at different SNRs. The EMD between the estimate and the truth increases as the SNR decreases. This suggests that the proposed method is usable in a range of SNR, where the EMD is below some threshold. This threshold, however, depends on the application of the estimated spectrum. For example, if the DSRF produces features for classification, a more robust classifier may tolerate worse estimations and, therefore, allow lower SNR. For our purpose, spectra with an EMD below 0.1 are considered visually similar; those with an EMD above 0.2 exhibit visual differences, but may still resemble each other. In our laboratory measurements, a typical SNR for loop targets is 70 dB.

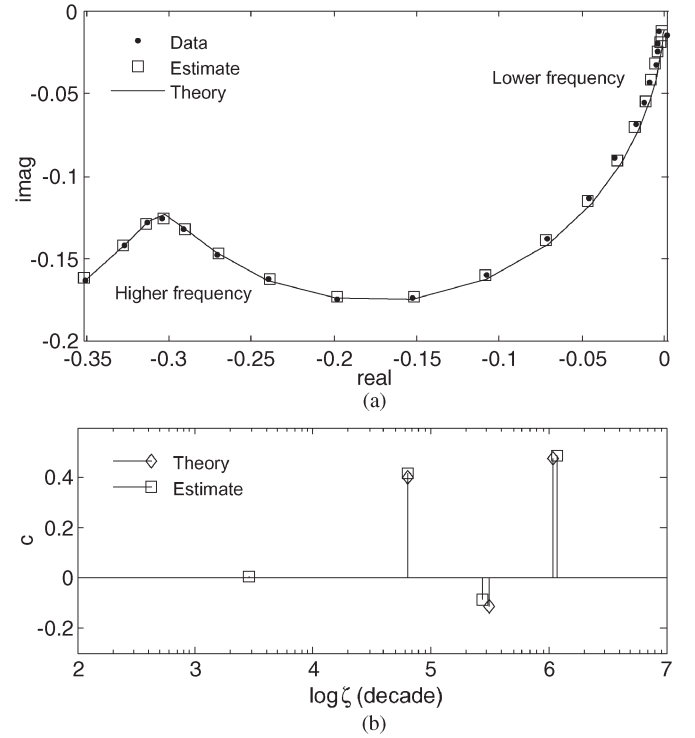


Fig. 3. (a) Frequency response of three mutually orthogonal copper loops. (b) Theoretical and estimated DSRFs of the response in (a).

D. Laboratory Data

We verify the functionality of the estimation method on laboratory data, where we know the theoretical DSRF [13]. We examine a target that consists of three mutually orthogonal copper loops. The loop diameters and thickness are 3/20, 4/30, and 5/36, respectively, in cm/AWG.¹ We pick a specific orientation and position relative to the EMI sensor that best shows the bipolar relaxation amplitudes in a spectrum. The target frequency response of this configuration is shown in Fig. 3(a) (the SNR is 38 dB) and its estimated DSRF in Fig. 3(b). Theoretical data are also displayed. We see that the estimate and theory agree well, and the EMD between the theoretical and estimated DSRFs is 0.10 decades.

Next, we examine the changes in the DSRF as the target moves relative to the EMI sensor. The same target configured at a fixed orientation is displaced at different positions along a horizontal axis, which we will call x . The vertical distance between the target and sensor is 6 cm. The EMI sensor is located at $x = 0$. Samples of the measured target responses are shown in Fig. 4(a); their corresponding spectra are in Fig. 4(b). Theoretical results are also shown. Overall, the theory and measurement agree. The disagreement at $x = -0.5$ may be because of approximations in the model and/or inaccuracies in the positions measured in the experiment.

As expected from the theory, while the frequency response changes dramatically as the target moves along the x axis, the corresponding change in the spectral domain only occurs in the spectral amplitudes. The three dominant relaxation frequencies remain unchanged. The proposed method successfully

¹ American wire gauge.

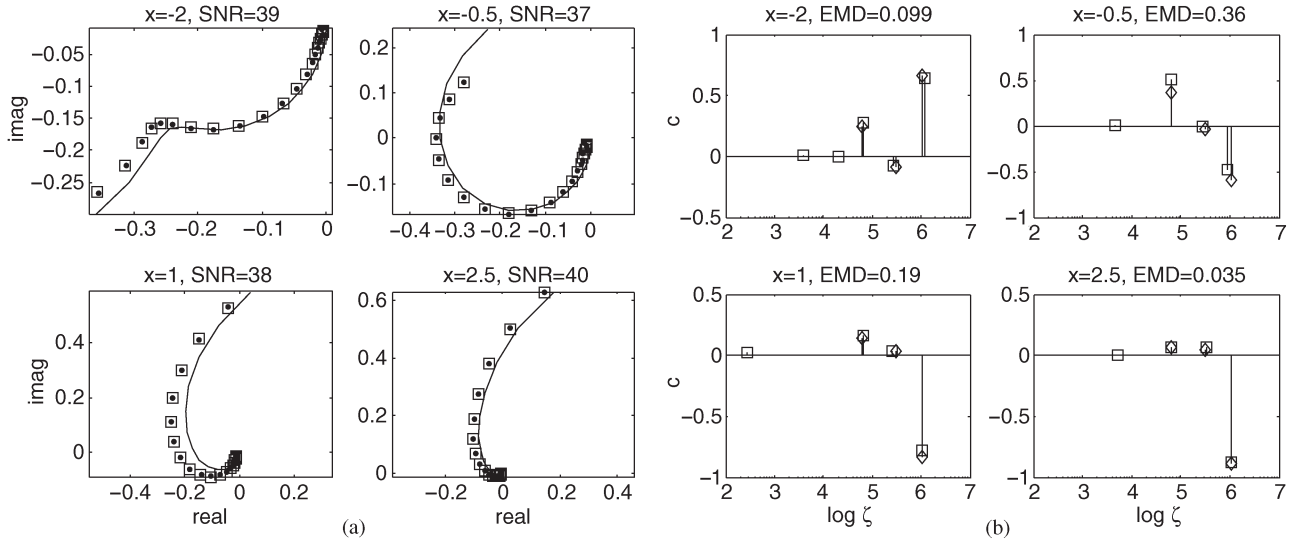


Fig. 4. Plots share the same annotation as Fig. 3. (a) Frequency responses of the three mutually orthogonal copper loops at different locations. (b) Theoretical and estimated DSRFs of the corresponding responses in (a). The SNR is measured in decibels, the x positions in centimeters, and the EMD in decades.

estimates the spectra that agree with this phenomenon. All three relaxation frequencies are consistently estimated. The extra relaxations all have small amplitudes that can be safely ignored. This invariant property of the relaxation frequencies makes the DSRF valuable, particularly for target discrimination.

IV. CHOOSING λ

In this section, we first examine the behavior of the proposed method in relation to the regularization parameter λ , and then, we propose a simple λ selection rule exploiting the observed properties of λ . All discussions and figures presented here assume $p = 0.5$ unless otherwise specified.

To understand how the goodness of fit changes with λ and SNR, we conduct a cross-validation-like simulation. First, we build a collection of synthetic spectra with different model orders and a variety of distributions of relaxations. For each spectrum at a fixed SNR, the spectrum is estimated 100 times for each λ within a range, and the average goodness of fit, measured by the EMD between the available truth and the estimate, is recorded. This is done for a range of SNRs. The simulation result for a four-relaxation spectrum, as an example, is shown in Fig. 5. We see that not only the EMD surface is well behaved (i.e., smooth) with respect to the SNR and λ but also, more importantly, the surface itself is convex shaped. Thus, at each SNR, the minimum EMD is achievable by a unique λ . The wide valley of the surface also shows that the goodness of fit is not very sensitive near the optimal λ that gives the minimum EMD per SNR.

Simulations of spectra for other model orders and distributions also exhibit the same property (Fig. 6). Moreover, the valleys of the EMD surface all occur in nearly the same SNR- λ region. In other words, the λ that produces the minimum EMD at a given SNR is quasi-independent of the model order. Fig. 7 shows the averaged EMD of different model orders in Fig. 6. The resulting surface still exhibits the properties described earlier. This allows us to pick a near-optimal λ based solely on the SNR.

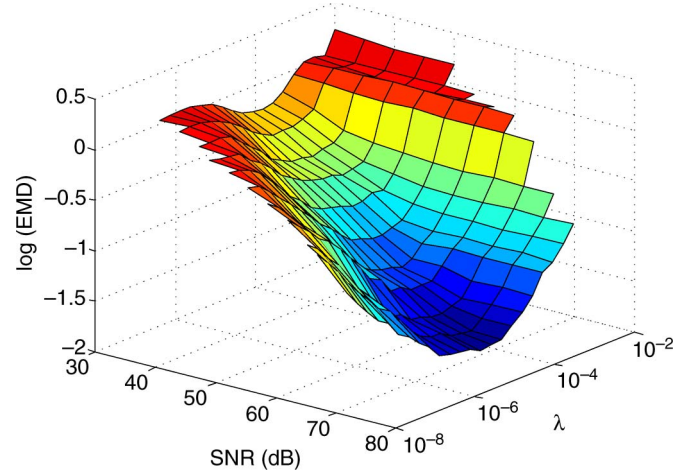


Fig. 5. Monte Carlo simulation of the goodness of estimation (EMD) of a four-relaxation spectrum at different SNRs and λ 's.

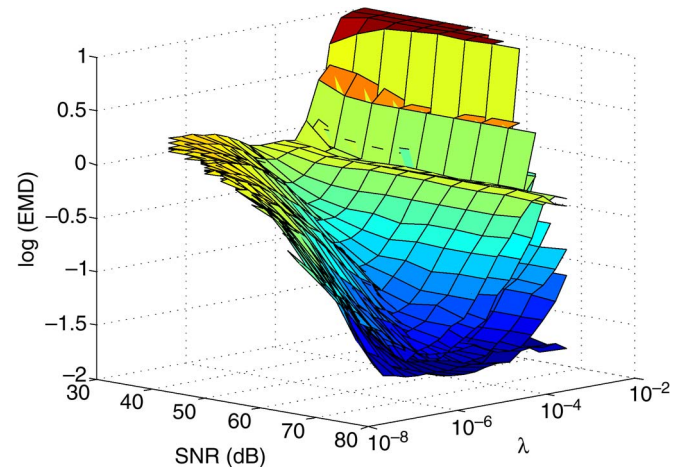


Fig. 6. Same simulation as in Fig. 5 but for spectra of different model orders (one to six). Each spectrum constitutes one surface in the figure. All surfaces have their minimum in the same SNR- λ region.

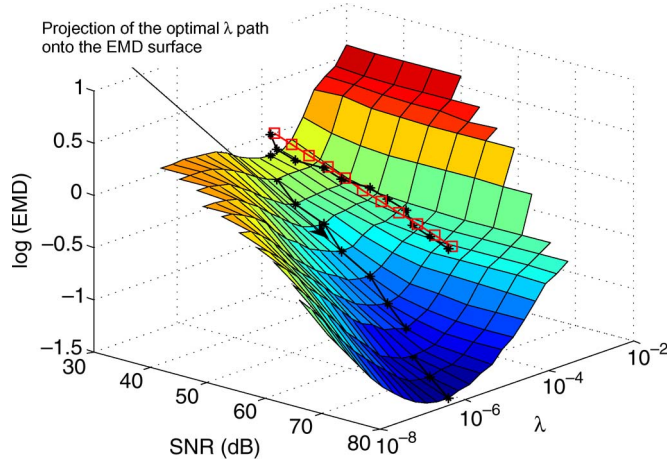


Fig. 7. Average of EMD surfaces in Fig. 6. The curve with asterisk markers traces out the optimal λ 's. The line with square markers is the approximated optimal λ curve used to select λ in practical estimation.

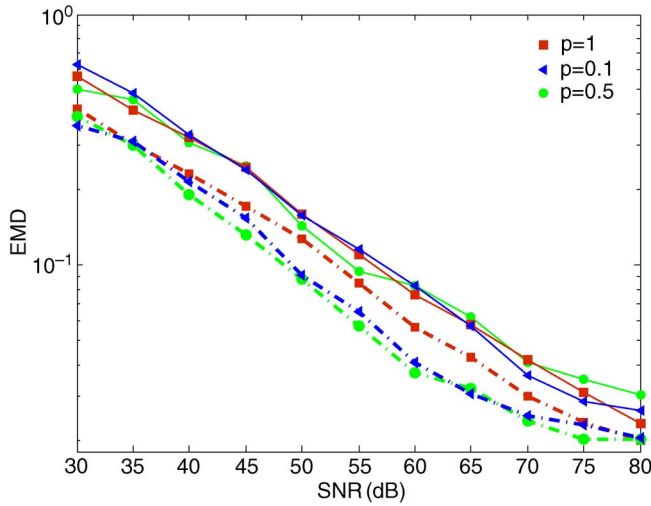


Fig. 8. Goodness of fit using the linear log- λ selection rule for several p 's. The true spectrum is the same as in Fig. 5. The dashed-dotted curves denote the optimal λ , and the solid lines denote the linear log- λ selection rule.

From the data in Fig. 7, we can find the optimal λ at each SNR, which is also plotted in the same figure. Using the wide-valley property, we can achieve the near-minimum EMD by choosing λ 's that are near the optimal λ in the valley. Here, we approximate the optimal λ with a semilog function of SNR. This is done by fitting the optimal log- λ curve with a linear function. Weights may be added to promote certain SNRs that are more important. For our problem setup, the λ is chosen by (also shown in Fig. 7)

$$\log \lambda = -0.05 \cdot \text{SNR} - 2.2. \quad (4)$$

In practice, this log- λ selection rule that is linear in SNR allows the regularization parameter to be determined with negligible computation time. When processing the laboratory data, we use (4) along with an estimate of the SNR to determine λ for use in Algorithm 1. The same empirical method can be repeated

for other p 's, and the result is also a linear relationship between $\log \lambda$ and SNR.

Fig. 8 shows the goodness of estimation of a four-relaxation target using the linear log- λ selection rule and the optimal λ which uses the true spectrum that is not available in practice. We see a slight increase in the EMD when the linear log- λ selection rule is used, which is reasonable and expected. The increase is acceptable, and hence, the linear log- λ selection rule is an appropriate λ selector.

Also shown in Fig. 8 are the performances of other p values. It is shown that $p < 1$ gives more accurate results than $p = 1$ when the optimal λ is used, but this advantage is significantly diminished when the linear log- λ selection rule is used. While this lessens the advantages of using $p < 1$, we emphasize that $p = 1$ tends to give estimates with many relaxation frequencies while $p < 1$ gives sparser spectra which are more physically accurate (see Section III-B). It is possible that both the accuracy and sparsity advantages for $p < 1$ could be obtained with a better λ selection rule. Lastly, since the performance of a certain p value is dependent on the λ selection rule used, different optimum p values would be determined if the λ selection rule is changed.

REFERENCES

- [1] P. Gao, L. Collins, P. M. Garber, N. Geng, and L. Carin, "Classification of landmine-like metal targets using wideband electromagnetic induction," *IEEE Trans. Geosci. Remote Sens.*, vol. 38, no. 3, pp. 1352–1361, May 2000.
- [2] E. B. Fails, P. A. Torrione, W. R. Scott, Jr., and L. M. Collins, "Performance of a four parameter model for modeling landmine signatures in frequency domain wideband electromagnetic induction detection systems," in *Proc. SPIE*, Orlando, FL, Apr. 2007, vol. 6553, p. 655 30D.
- [3] C. E. Baum, "On the singularity expansion method for the solution of electromagnetic interaction problems," Air Force Weapons Lab., Kirtland AFB, NM, Interaction Notes 88, 1971.
- [4] Y. Das and J. E. McFee, "Limitations in identifying objects from their time-domain electromagnetic induction response," in *Proc. SPIE*, Orlando, FL, Apr. 2002, vol. 4742, pp. 776–788.
- [5] M. Wei, W. R. Scott, Jr., and J. H. McClellan, "Robust estimation of the discrete spectrum of relaxations for electromagnetic induction responses," *IEEE Trans. Geosci. Remote Sens.*, vol. 48, no. 3, pp. 1169–1179, Mar. 2010.
- [6] W. R. Scott, Jr., "Broadband array of electromagnetic induction sensors for detecting buried landmines," in *Proc. IGARSS*, Boston, MA, Jul. 2008, pp. II-375–II-378.
- [7] R. Chartrand, "Exact reconstruction of sparse signals via nonconvex minimization," *IEEE Signal Process. Lett.*, vol. 14, no. 10, pp. 707–710, Oct. 2007.
- [8] J. Candès, M. B. Wakin, and S. P. Boyd, "Enhancing sparsity by reweighted ℓ_1 minimization," *J. Fourier Anal. Appl.*, vol. 14, no. 5, pp. 877–905, Dec. 2008.
- [9] R. Chartrand and W. Yin, "Iteratively reweighted algorithms for compressive sensing," in *ICASSP*, Las Vegas, NV, Mar. 2008, pp. 3869–3872.
- [10] M. A. T. Figueiredo and R. D. Nowak, "A bound optimization approach to wavelet-based image deconvolution," in *Proc. ICIP*, Genoa, Italy, 2005, vol. 2, pp. 782–785.
- [11] S. J. Kim, K. Koh, M. Lustig, and S. Boyd, "An efficient method for compressed sensing," in *Proc. ICIP*, San Antonio, TX, 2007, vol. 3, pp. 117–120.
- [12] Y. Rubner, C. Tomasi, and L. J. Guibas, "A metric for distributions with applications to image databases," in *Proc. ICCV*, Bombay, India, Jan. 1998, pp. 59–66.
- [13] G. D. Larson and W. R. Scott, Jr., "Automated, non-metallic measurement facility for testing and development of electromagnetic induction sensors for landmine detection," in *Proc. SPIE*, Orlando, FL, Apr. 2009, vol. 7303, p. 730 30X.

Broadband Electromagnetic Induction Sensor for Detecting Buried Landmines

Waymond R. Scott, Jr.

School of Electrical and Computer Engineering
Georgia Institute of Technology
Atlanta, Georgia 30332-0250
waymond.scott@ece.gatech.edu

Abstract— A broadband electromagnetic induction (EMI) sensor is developed to help discriminate between buried land mines and metal clutter. The detector uses simple dipole transmit and receive coils along with a secondary bucking transformer to mostly cancel the coupling between the coils. The technique allows the cancellation that can be obtained using a quadrupole receive coil while maintaining the depth sensitivity and simple detection zone of a dipole coil. Experimental results are presented for several targets.

Keywords; *Electromagnetic Induction, EMI, Mine, Landmine, Metal Detector.*

I. INTRODUCTION

For many years, extensive effort has been expended developing techniques for efficiently locating buried landmines. For a mine detection technique to be successful there must be sufficient contrast between the properties of the mine and the earth. There also must be sufficient contrast between the properties of the mine and common types of clutter such as rocks, roots, cans, etc. so that the mine can be distinguished from the clutter. The latter condition is the most problematic for most mine detection techniques. For example, simple electromagnetic induction (EMI) sensors are capable of detecting most mines; however, they will also detect every buried metal object such as bottle tops, nails, shrapnel, bullets, etc. This results in an unacceptable false alarm rate. This is even more problematic for low-metal anti-personnel mines as they are extremely difficult to distinguish from clutter using a simple EMI sensor. In recent years, advanced EMI sensors that use a broad range of frequencies or a broad range of measurement times along with advanced signal processing have been shown to be capable of discrimination between buried land mines and many types of buried metal clutter [1-4]. For these advanced EMI sensors to be effective, they must be able to accurately, repeatably, and quickly measure the response of a buried target. This is difficult because the sensor must operate with bandwidths greater than 100 to 1 while accurately measuring signals that are more than 100 dB smaller than the direct coupling between the coils on the EMI sensor. In order to accomplish this, the EMI sensor must be very

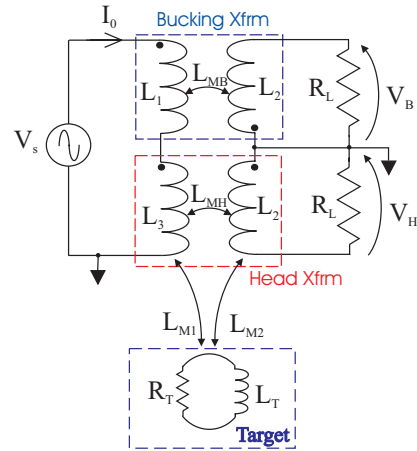


Figure 1. Basic configuration of the technique.

cleverly designed to account for the coupling and for the secondary effects such as resonances in the coils.

In most EMI sensors, the coupling between the coils is handled by one of two methods. In time-domain sensors, the coupling between the coils can be mostly removed by time gating if the coils are properly designed. In frequency-domain sensors, the coupling is mostly removed by using a quadrupole receive coil which minimizes the mutual inductance between the coils. The quadrupole receive coils have the disadvantage of being less sensitive to deeply buried targets and having a complicated detection zone when compared to a dipole receive coil.

A technique is presented for canceling the coupling between the induction coils while maintaining the depth sensitivity and simple detection zone of a dipole coil. Here, simple dipole transmit and receive coils are used along with a secondary bucking transformer to cancel the coupling between the coils. A prototype system using this technique is presented that operates over the frequency range 300 Hz to 90 kHz. Sample measurements made with the system are shown.

This work is supported in part by the U.S. Army Research Office under contract number W911NF-05-1-0257.

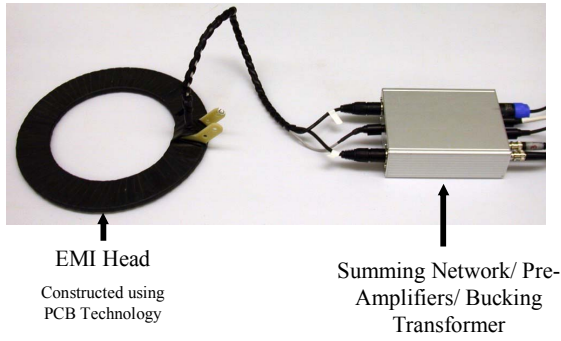


Figure 2. Prototype EMI System

II. SYSTEM

Figure 1 shows a basic diagram of the system where simple dipole transmit and receive coils are used along with a secondary transformer to cancel the direct coupling between the coils. Here, the exciting current I_o passes through the primary coils of both the bucking and head transformers and induces a voltage in the secondary transformers. The voltage induced in the secondary windings of the head transformer depends on its mutual inductance as well as the coupling through the target:

$$V_H = j\omega L_{MH} I_o - \frac{\omega^2 L_{M1} L_{M2}}{R_T + j\omega L_T} I_o.$$

The first term in the equation above is due to the direct coupling between the coils of the head transformer, and it is generally much larger than the second term which is due to the target. The voltage induced in the secondary windings of the bucking transformer depends only on its mutual inductance:

$$V_B = -j\omega L_{MB} I_o.$$

The response of the target is obtained from the relation

$$R = \frac{V_H + V_B}{V_B} = \frac{j\omega L_{M1} L_{M2}}{L_{MB} (R_T + j\omega L_T)}$$

if we make $L_{MH} = L_{MB}$. This is the ideal response (scaled by L_{MB} , L_{M1} , and L_{M2}) that we want to obtain with the direct coupling term eliminated. It is difficult to exactly match the mutual inductances, so a simple voltage divider is used to compensate for the difference. The transformers are not ideal and will have significant parasitic effects such as the distributed capacitance between the windings. The parasitic elements can significantly reduce the effectiveness of the cancellation at the higher frequencies. Additional elements were added to the circuit to mostly match the parasitics effects for the two transformers. With these additional elements the resulting cancellation was greater than 60 dB across the entire frequency range. To further enhance the cancellation, the response of the sensor in air is subtracted from the subsequent measurements. After the subtraction the effective cancellation is approximately 120 dB over the entire bandwidth of the sensor.

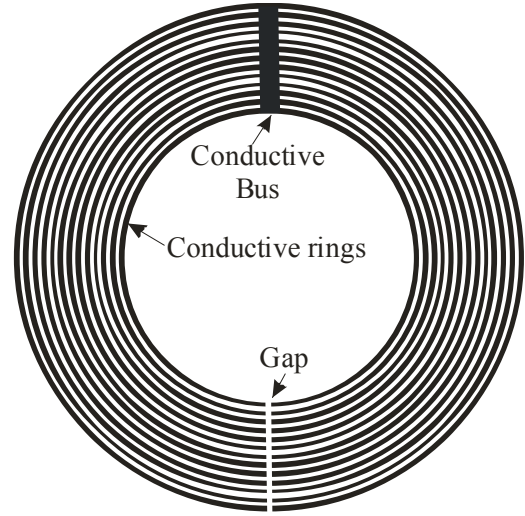


Figure 3. Diagram of the shield for the EMI head.

The prototype system consists of a head constructed using PCB technology that has a transmit coil with a diameter of approximately 25 cm and a receive coil with a diameter of approximately 21 cm, as shown in Figure 2. This is an improved version of the system presented previously [6]. The improvements include improved shielding of the EMI head and a much smaller bucking transformer made using a ferrite core.

The coupling between the transmit and receive coils is not purely inductive as in the model, figure 1. Part of the coupling is due to the capacitance between the transmit and receive coils. The capacitive coupling can be comparable to or larger than the inductive coupling with the target. The capacitive coupling can vary significantly as an unshielded EMI head is moved in close proximity to the soil and can mask/corrupt the inductive responses of the desired targets. The effect is most problematic at the higher frequencies. Ideally, the shield will completely eliminate the variations in the capacitive coupling due to the presence of the soil or other objects that are in close proximity to the head while not affecting the inductive coupling to the target. The shield developed for this work is shown in figure 3. The shield is made using PCB technology and consists of closely spaced conducting rings with a gap so the rings will not form closed loops. The narrow width of the rings and the gap in the rings greatly reduce the eddy currents induced on the shield. The eddy currents are undesirable because they corrupt the desired inductive response. This shield has performed much better than the conductive Mylar shield used in the previous work.

The data for the prototype system was taken at 21 frequencies that were approximately logarithmically spaced from 330 HZ to 90.03 KHz. The frequencies deviated from logarithmic spacing to minimize interference from power line harmonics. A multi-sine excitation signal was generated using the 21 frequencies and used to excite the EMI sensor. The response due to this multi-sine excitation was recorded in 0.1 s increments. These time records were transformed into the frequency domain and used to construct the response of the sensor.

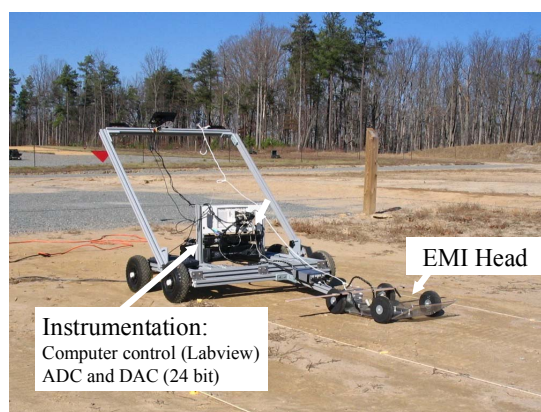


Figure 4. Cart based EMI data collection system.

III. EXPERIMENTAL RESULTS

The prototype system was used to collect data at a test facility. The test facility consisted of a number of lanes divided into 1.5 by 1.5 m squares. A target was buried at the center of most of the squares. The data was collected in a lane based manner in which the sensor was pushed down the lane and the response was recorded in 0.1 s time increments along with the spatial location in the grid. The response at the beginning of the grid is subtracted from the subsequent responses to partially remove the ground response.

The response for three of the target types is shown in figure 5 in two types of graphs. For the graphs in the left column, the response at the center of the grid square is graphed on Argand diagrams where the imaginary part of the response is graphed as a function of the real part with frequency as a parameter. The curves are shifted along the real axis so that they are centered; this further removes part of the ground response which is mostly a shift in the real part of the response. The response of a simple target with a single relaxation will form a perfect semicircle on this type of graph. The fidelity of the data is generally apparent on this type of graph so it is a good way to show the measured data. The shape of the curve is dependent on the shape of the buried object and can be used to discriminate different targets from each other. These graphs are very similar to the Cole-Cole graphs commonly used to show the complex permittivity of materials with dipolar type relaxations.

The responses from eight different grid locations that contain TS-50 landmines with burial depths from 0 cm to 5 cm are plotted in figure 5a. The eight curves are almost perfect scaled replicas of each other which demonstrates the consistency and the fidelity of the EMI sensor. The curves form a portion of a semicircle indicating that this landmine has a single simple relaxation. Only part of the semicircle is evident because of the limited frequency range of the measurement. The variation in the size of the curves is due to the differences in burial depth. The responses from six different grid locations that contain MAI-75 landmines with burial depths from 0 cm to 5 cm are plotted in figure 5b. The shapes of the six curves are very similar to each other, again showing the consistency and the fidelity of the EMI sensor.

The shapes of these curves are more complex than a semicircle indicating that this landmine has multiple relaxations. The responses from three different grid squares which contain a buried 30 cm by 30 cm patio stone are shown in figure 5c. One would not expect to see a response from the patio stone, but it is clearly evident. The response may be due to the stone having a different conductivity [8] and/or permeability than the surrounding soil. Using the frequency dependent response of the targets, it is possible to discriminate between landmines and many types of clutter [9].

The graphs on the right column of figure 5 are the response as a function of distance along the centerline of the grid. The magnitude of the response is plotted for all 21 frequencies on these graphs. The response for these three graphs is peaked near the center of the grid and reaches a noise floor away from the center of the grid. The noise floor is seen to be approximately 120 dB below V_B . The peak response for the TS-50 mine is about 80 dB below V_B , for the MAI-75 mine is about 90 dB below V_B , and for the patio stone is about 110 dB below V_B .

IV. ACKNOWLEDGEMENT

The author would like to thank Dr. Gregg D. Larson for constructing the data collection system and helping with the field measurements.

REFERENCES

- [1] P. Gao, L. Collins, P.M. Garber, N. Geng, and L. Carin, "Classification of Landmine-Like Metal Targets Using Wideband Electromagnetic Induction," *IEEE Transactions on Geoscience and Remote Sensing*, Vol. 38, No. 3, May 2000.
- [2] L. Collins, P. Gao, and L. Carin, "An Improved Bayesian Decision Theoretic Approach for Land Mine Detection," *IEEE Transactions on Geoscience and Remote Sensing*, Vol. 37, No. 2, March 1999.
- [3] G. D. Sower and S. P. Cave, "Detection and identification of mines from natural magnetic and electromagnetic resonances," in *Proc. SPIE*, Orlando, FL, 1995.
- [4] C. E. Baum, "Low Frequency Near-Field Magnetic Scattering from Highly, but Not Perfectly Conducting Bodies," *Phillips Laboratory, Interaction Note 499*, Nov. 1993.
- [5] G.T. Mallick, Jr. W.J. Carr, Jr., and R.C. Miller, "Multiple Frequency Magnetic Field Technique for Differentiating between Classes of Metal Objects," U.S. Patent 3,686,564, Aug. 22, 1972.
- [6] Scott, W.R., Jr. and Malluck, M., "New cancellation technique for electromagnetic induction sensors," *Proceedings of the SPIE: 2005 Annual International Symposium on Aerospace/Defense Sensing, Simulation, and Controls*, Vol. 5794, Orlando, FL, April 2005.
- [7] L.S. Riggs, L.T. Lowe, J.E. Mooney, T. Barnett, R. Ess, and F. Paca, "Simulants (decoys) for Low-Metallic Content Mines: Theory and Experimental Results," in *Proc. SPIE*, Vol. 3710, Orlando, FL, 1999.
- [8] T. Yu and L. Carin, "Analysis of the electromagnetic inductive response of a void in a conducting-soil background," *IEEE Transactions on Geoscience and Remote Sensing*, Vol. 38, No. 3, May 2000.
- [9] E.B. Fails, P.A. Torrone, W. R. Scott, Jr, and L.M. Collins, "Performance of a four parameter model for modeling landmine signatures in frequency domain wideband electromagnetic induction detection systems," *Proceedings of the SPIE: 2007 Annual International Symposium on Aerospace/Defense Sensing, Simulation, and Controls*, Vol. 6553, Orlando, FL, May 2007.

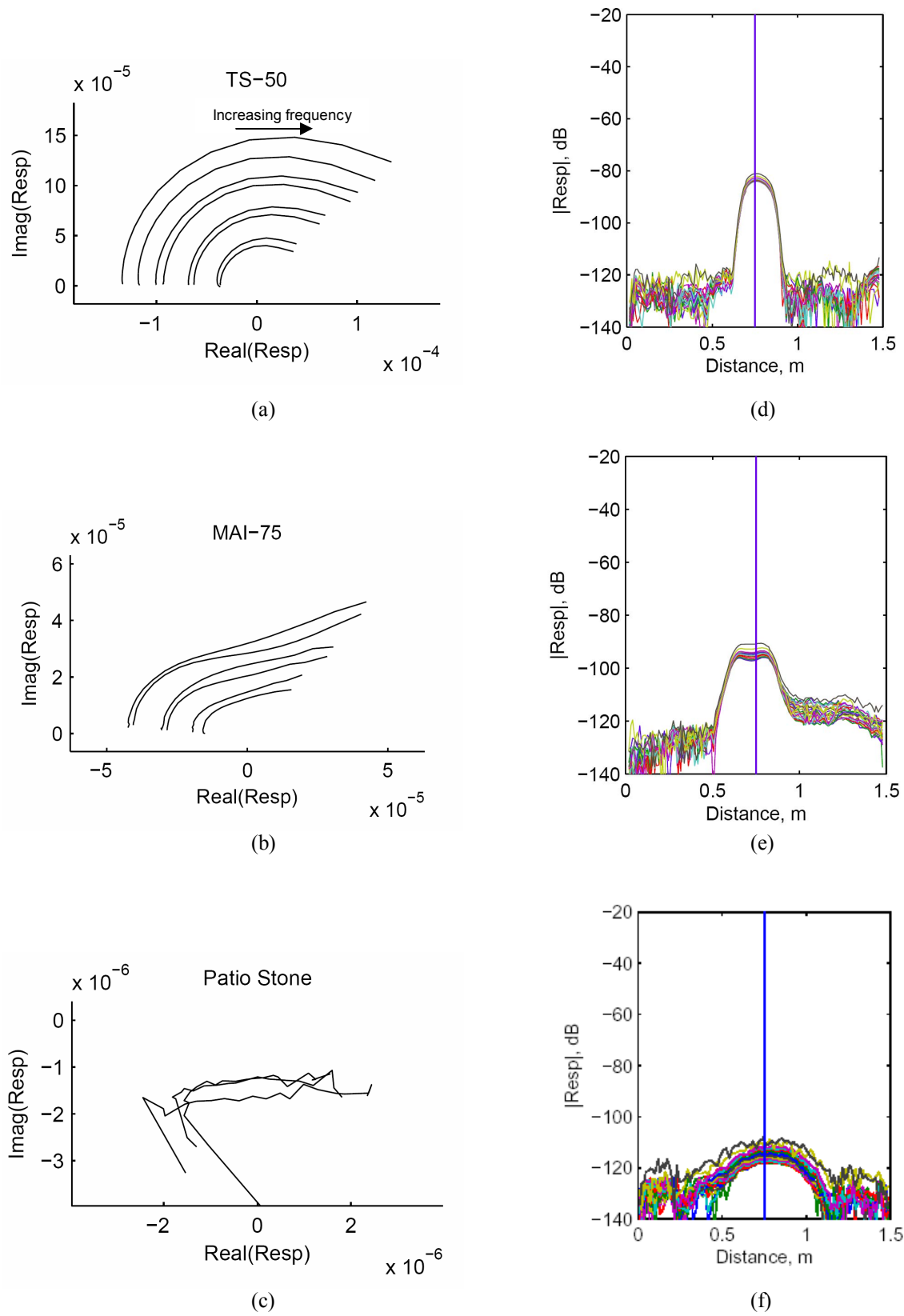


Figure 5. Respose plotted on an Argand diagram over the center of a) TS-50 anti-personnel landmines buried 0 to 5 cm deep, b) MAI-75 anti-personnel landmines buried 0 to 5 cm deep, and c) patio stones buried 2.5 to 11 cm deep. Magnitude of the respose at the 21 measurment frequencies plotted as a function of downtract distance for d) a TS-50 landmine buried 5 cm deep, e) a MAI-75 landmine buried 5 cm deep, and patio stone buried 7.5 cm deep.

Broadband Array of Electromagnetic Induction Sensors for Detecting Buried Landmines

Waymond R. Scott, Jr.

School of Electrical and Computer Engineering
Georgia Institute of Technology
Atlanta, Georgia 30332-0250
waymond.scott@ece.gatech.edu

Abstract— A broadband electromagnetic induction (EMI) sensor is developed to help discriminate between buried landmines and metal clutter. The detector uses a single dipole transmit coil and an array of three quadrapole receive coils. The sensor operates in the frequency domain and collects data at 21 logarithmically spaced frequencies from 300 Hz to 90 kHz. Experimental results are presented for several targets.

Keywords; *Electromagnetic Induction, EMI, Mine, Landmine, Metal Detector.*

I. INTRODUCTION

For many years, extensive effort has been expended developing techniques for efficiently locating buried landmines. For a mine detection technique to be successful, there must be sufficient contrast between the properties of the mine and the earth. There also must be sufficient contrast between the properties of the mine and common types of clutter such as rocks, roots, cans, etc. so that the mine can be distinguished from the clutter. The latter condition is the most problematic for most mine detection techniques. For example, simple electromagnetic induction (EMI) sensors are capable of detecting most mines; however, they will also detect every buried metal object such as bottle tops, nails, shrapnel, bullets, etc. This results in an unacceptable false alarm rate. This is even more problematic for low-metal anti-personnel mines as they are extremely difficult to distinguish from clutter using a simple EMI sensor. In recent years, advanced EMI sensors that use a broad range of frequencies or a broad range of measurement times along with advanced signal processing have been shown to be capable of discrimination between buried land mines and many types of buried metal clutter [1-4]. For these advanced EMI sensors to be effective, they must be able to accurately, repeatably, and quickly measure the response of a buried target with a bandwidth greater than 100 to 1 while accurately measuring extremely weak signals.

The sensor developed for this work uses a single dipole transmit coil and an array of three quadrapole receive coils constructed using PCB technology, as in figure 1. A prototype system using this array is presented that operates over the frequency range 300 Hz to 90 kHz, a 300 to 1 bandwidth. This system evolved from an earlier system with a dipole receive

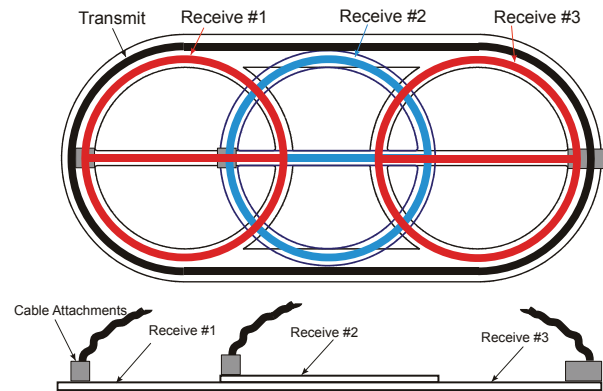


Figure 1. Diagram of the quadrapole array.

coil [5]. Sample measurements made with the system are shown.

II. SYSTEM

Figure 2 shows a basic diagram of the system with a dipole transmit and a quadrapole receive coil that are used along with a secondary reference transformer. Here, the exciting current I_0 passes through the primary coils of both the reference and head transformers and induces a voltage in the secondary of the transformers. The voltage induced in the secondary windings of the head transformer depends on its direct coupling as well

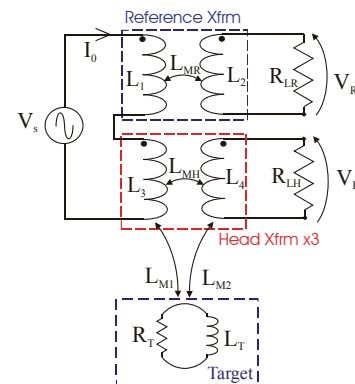


Figure 2. Schematic diagram of the system.

This work is supported in part by the U.S. Army Research Office under contract number W911NF-05-1-0257.

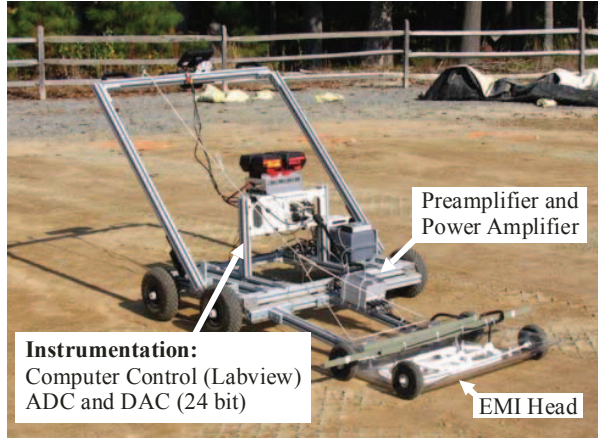


Figure 3. Cart-based EMI data collection system.

as the coupling through the target:

$$V_H = D(\omega) - \frac{\omega^2 L_{M1} L_{M2}}{R_T + j\omega L_T} I_0.$$

Here $D(\omega)$ represents the direct coupling between the coils of the head transformer and is due to both the inductive and capacitive coupling between the coils. The inductive and capacitive coupling between the transmit and receive coils is very small because of the manner in which the coils are wound. The voltage induced in the secondary coils of the reference transformer depends only on its mutual inductance:

$$V_R = -j\omega L_{MR} I_0.$$

The response of the target is obtained from the relation

$$R = \frac{V_H - D(\omega)}{V_R} = \frac{j\omega L_{M1} L_{M2}}{L_{MR}(R_T + j\omega L_T)}$$

where $D(\omega)/V_R$ is obtained by measuring a response without a target present.

The coupling between the coils of the EMI head and the target is not purely inductive as in the model, figure 2. Part of the coupling is due to the capacitance between coils and the target. The capacitive coupling can be comparable to or larger than the inductive coupling with the target. The capacitive coupling can vary significantly as an unshielded EMI head is moved in close proximity to the soil and can mask/corrupt the inductive responses of the desired targets. The effect is most problematic at the higher frequencies. Thus, a shield is needed to lessen the capacitive interactions. Ideally, the shield will completely eliminate the variations in the capacitive coupling due to the presence of the soil or other objects that are in close proximity to the head while not affecting the inductive coupling to the target. The shield developed for this work is similar to that developed earlier [5]. The shield is made using PCB technology and consists of closely spaced conducting rings with a gap so the rings will not form closed loops. The narrow width of the rings and the gap in the rings greatly reduce the eddy currents induced on the shield.

The data for the prototype system was taken at 21 frequencies that were approximately logarithmically spaced from 330 HZ to 90.03 KHz. The frequencies deviated from logarithmic spacing to minimize interference from power line harmonics. A multi-sine excitation signal was generated using the 21 frequencies and used to excite the EMI sensor. The response due to this multi-sine excitation was recorded in 0.1 s increments. These time records were transformed into the frequency domain and used to construct the response of the sensor.

III. EXPERIMENTAL RESULTS

The prototype system was used to collect data at a test facility. The test facility consisted of a number of lanes divided into 1.5 by 1.5 m squares. A target was buried at the center of most of the squares. The data was collected in a lane based manner in which the sensor was pushed down the lane and the response was recorded in 0.1 s time increments along with the down-track location in the grid.

The measured data are filtered in the down-track direction by convolving the measured data with the zero-mean template shown in figure 4a. The magnitude of the response for all 21

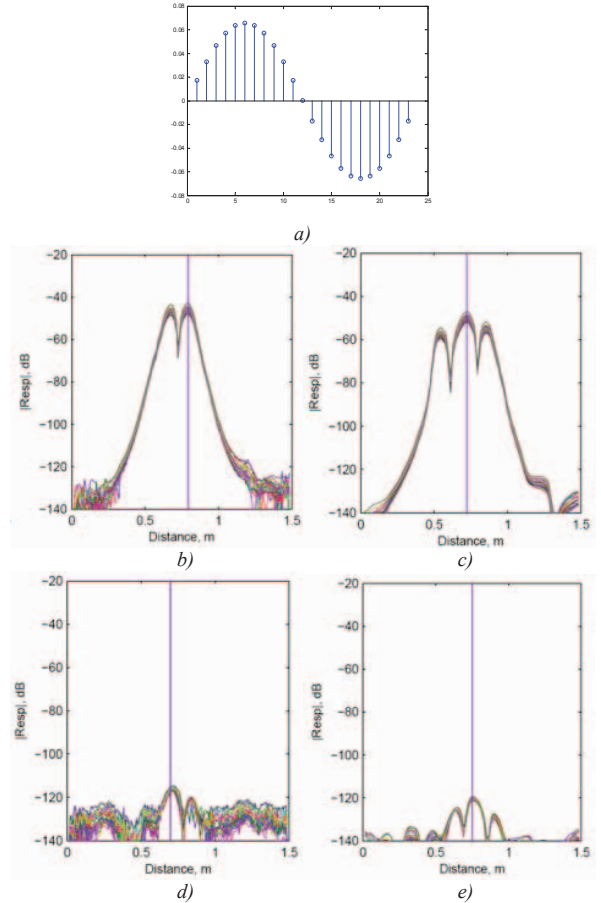


Figure 4. a) Down-track filter template. Down-track response for b) unfiltered and c) filtered PMD mine 0 cm deep. Down-track response for d) unfiltered and e) filtered M14 mine 5 cm

frequencies is shown in figure 4 as a function of down-track distance for a PMN and an M-14 landmine before and after filtering. The unfiltered response for both mines is weak directly above the mine and has a peak on either side of the mine due to the quadrapole receive coil. The filter has four beneficial effects. First, it mostly removes the ground response by differencing closely located portions of the ground. Second, it mostly removes the drift in the system by differencing measurements made only a short time apart. Third, it averages the data over several locations which will improve the signal to noise ratio. Fourth, the filtered data has a maximum directly over the target, while the unfiltered data has a minimum directly over the target. The filtered response of the M14 mine is much better defined than that of the unfiltered response. The noise floor is approximately -135 dB for the filtered response, which is about 10 dB better than for the unfiltered response. Note that the peak response for the M-14 mine is very weak, about -120 dB, while the response for the PMN mine is much stronger.

The response from multiple occurrences of four landmines is shown in figure 5 for all three receive channels when the landmine is approximately below the center receive head. The responses are graphed on Argand diagrams where the imaginary part of the response is graphed as a function of the real part with frequency as a parameter. The curves are shifted along the real axis so that they are centered; this further removes part of the ground response which is mostly a shift in the real part of the response. The fidelity of the data is generally apparent on this type of graph which makes it a good way to show the measured data. These graphs are very similar to the Cole-Cole graphs commonly used to show the complex permittivity of materials with dipolar type relaxations.

The shapes of the curves on the Argand diagrams are indicative of the type and distribution of metal in a target. The response of a simple target with a single relaxation will form a perfect semicircle on this type of graph. The response of each of the mines has a characteristic shape. The M-14 has a shape that is almost a semicircle indicating that its response is mostly due to a single relaxation. The other mines have more complex shapes indicating that their response is due to multiple relaxations. Note that the shapes of the curves for each mine are consistent in that they are scaled replicas of each other. The scaling of the response is due to the burial depth of the mine. The response is weaker of the deeper mines. Because these shapes of the different targets are quite different, it is possible to discriminate between some landmines and many types of clutter [6].

The response from the center channel is stronger than the side channels for all of the mines, as expected. The response is strongest in the channel closet to the mine. The response in the side channels is apparent on these graphs for a few of the mines when they are slightly off center. Note that the shape of the response in the side channels is almost the same as in the center channel. The response of the stronger mines would be readily apparent in a graph like figure 4 due to the higher dynamic range of the graph.

The responses at the center of the blank grid locations are graphed on Argand diagram in figure 6. Ideally these

responses will be zero; however, they are clearly nonzero and have a defined structure. The responses mostly take the shape of a line parallel to the real axis with a length proportional to their imaginary part. The real part is approximately proportional to $\ln(f)$. This response is believed to be due to the magnetic response of the soil which is not completely removed by the down-track filter since the magnetic properties of the soil vary with position. This response is very similar to that due to a magnetic material with a uniform logarithmic distribution of relaxation times [7-9].

IV. ACKNOWLEDGEMENT

The author would like to thank Dr. Gregg D. Larson for constructing the data collection system and helping with the field measurements.

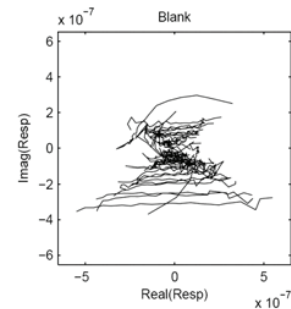


Figure 6. Response plotted on an Argand diagram over the center of empty grid locations.

REFERENCES

- [1] P. Gao, L. Collins, P.M. Garber, N. Geng, and L. Carin, "Classification of Landmine-Like Metal Targets Using Wideband Electromagnetic Induction," *IEEE Transactions on Geoscience and Remote Sensing*, Vol. 38, No. 3, May 2000.
- [2] L. Collins, P. Gao, and L. Carin, "An Improved Bayesian Decision Theoretic Approach for Land Mine Detection," *IEEE Transactions on Geoscience and Remote Sensing*, Vol. 37, No. 2, March 1999.
- [3] G. D. Sower and S. P. Cave, "Detection and identification of mines from natural magnetic and electromagnetic resonances," in *Proc. SPIE*, Orlando, FL, 1995.
- [4] C. E. Baum, "Low Frequency Near-Field Magnetic Scattering from Highly, but Not Perfectly Conducting Bodies," *Phillips Laboratory, Interaction Note* 499, Nov. 1993.
- [5] Scott, W.R., Jr., "Broadband electromagnetic induction sensor for detecting buried landmines," *Proceedings of the 2007 IEEE Geoscience and Remote Sensing Symposium*, Barcelona, Spain, July 2007.
- [6] E.B. Fails, P.A. Torrione, W. R. Scott, Jr, and L.M. Collins, "Performance of a four parameter model for modeling landmine signatures in frequency domain wideband electromagnetic induction detection systems," *Proceedings of the SPIE: 2007 Annual International Symposium on Aerospace/Defense Sensing, Simulation, and Controls*, Vol. 6553, Orlando, FL, May 2007.
- [7] S. Chikazumi, *Physics of Magnetism*, Wiley, New York, 1964.
- [8] Y. Das, "Effects of magnetic soil on metal detectors: preliminary experimental results," *Proc. SPIE* 6553, 655306 (2007)
- [9] Gordon F. West and Richard C. Bailey, "An instrument for measuring complex magnetic susceptibility of soils," *Proc. SPIE* 5794, 124 (2005)

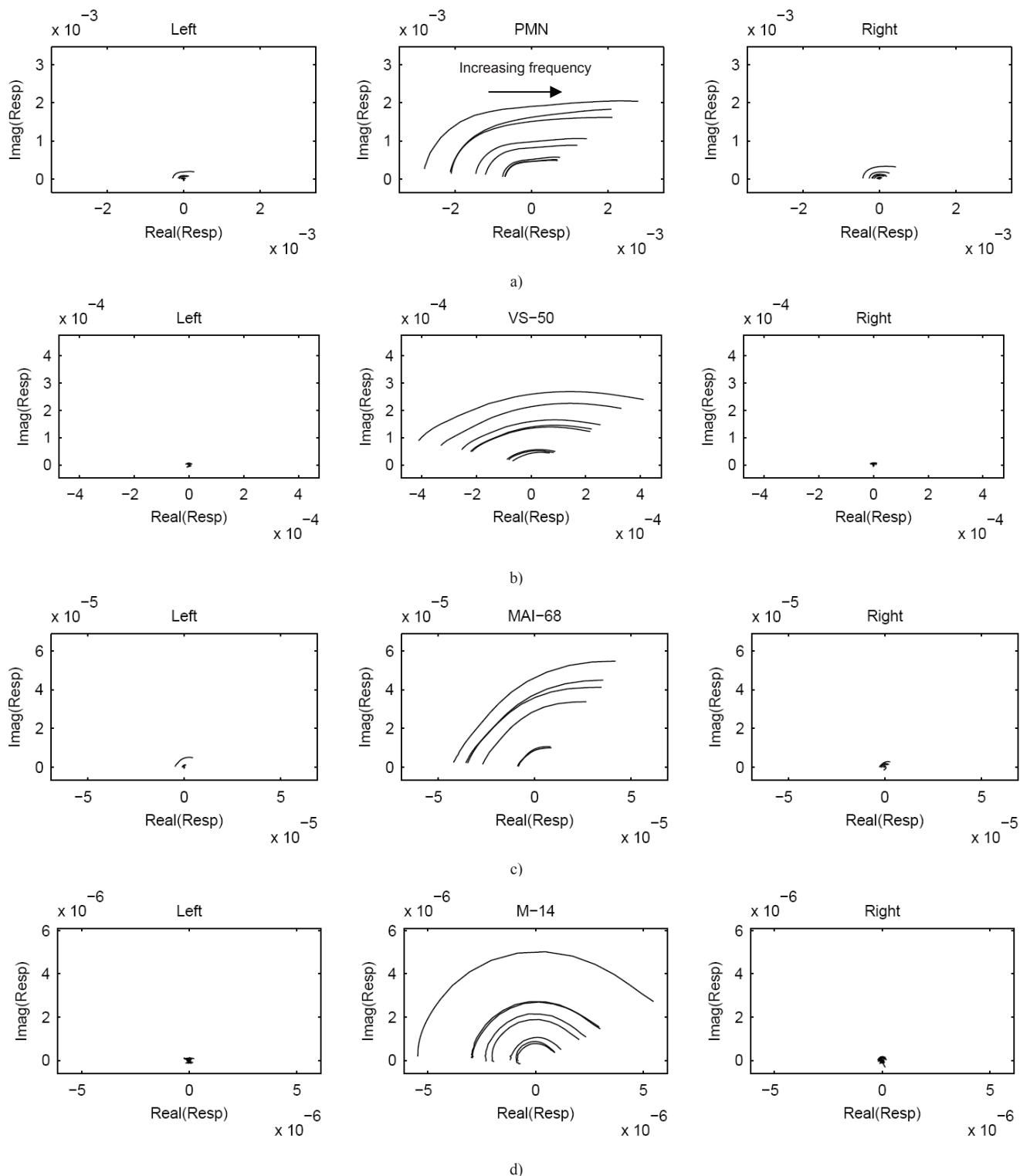


Figure 5. Response of four mines plotted on an Argand diagram for the left, center, and right receive coils when a mine is below the center of the array: a) PMN, b) VS-50, c) MAI-68, and d) M-14 anti-personnel landmines. There are 6 to 8 occurrences of each mine which are buried between 0 and 5 cm deep.

ESTIMATION AND APPLICATION OF DISCRETE SPECTRUM OF RELAXATIONS FOR ELECTROMAGNETIC INDUCTION RESPONSES

Mu-Hsin Wei, Waymond R. Scott, Jr., and James H. McClellan

Georgia Institute of Technology
School of Electrical and Computer Engineering
777 Atlantic Drive NW, Atlanta, GA 30332-0250

ABSTRACT

The EMI response of a target can be accurately modeled by a sum of real exponentials. However, it is difficult to obtain the model parameters from measurements when the number of exponentials in the sum is unknown. In this paper, a constrained linear method for estimating the parameters is formulated by enumerating the relaxation parameter space and imposing a nonnegative constraint on the parameters. Using tests on synthetic data and laboratory measurement of known targets the proposed method is shown to provide accurate and stable estimates of the model parameters. The estimated parameters are then used to cluster different targets types for classification.

Index Terms— Electromagnetic induction (EMI), discrete spectrum of relaxation frequencies (DSRF), sum of exponentials, magnetic polarizabilities, detection.

1. INTRODUCTION

Recent research has shown that broadband electromagnetic induction (EMI) sensors together with advanced signal processing is capable of discriminating between certain types of buried targets [1]. The EMI response of a metallic target can be accurately modeled by a sum of real exponentials [2]. In the frequency domain, an EMI target response $H(\omega)$, which is proportional to a projection of the magnetic polarizability tensor of the target, can be expressed as:

$$H(\omega) = c_0 + \sum_{k=1}^K \frac{c_k}{1 + j\omega/\zeta_k} \quad (1)$$

where c_0 is the shift, K the model order, c_k the real spectral amplitudes, and ζ_k the relaxation frequencies. The frequency response can be characterized by the set $S = \{(\zeta_k, c_k) : k = 1 \dots K\}$ which we will call the Discrete Spectrum of Relaxation Frequencies (DSRF). Each pair (ζ_k, c_k) is one relaxation. The response at zero frequency $H(0) = \sum_{k=0}^K c_k$ is due to the DC magnetization of the target. The term DSRF and spectrum will be used interchangeably.

It is difficult in practice to obtain the model parameters in (1) from measurements. For most existing estimation methods, a good guess of the model order K is required for the fitting process to converge. Prior knowledge of K , however, is usually impossible to obtain. The highly correlated summands in (1) and the nonlinear relation between c_k and ζ_k also make estimation difficult. Most existing methods often suffer from (a) sub-optimal solutions that are far from the truth and (b) complex parameters that do not have physical meaning [3].

In this paper, we present a constrained DSRF estimation method that requires no prior knowledge of K and always returns real parameters. We demonstrate its robustness with results on synthetic, laboratory, and field data. We also propose using the DSRF in target discrimination by showing how to cluster DSRFs of eleven types of targets.

2. A CONSTRAINED ESTIMATION METHOD

When the target response is measured at N distinct frequencies, (1) can be written in matrix form:

$$\begin{bmatrix} H(\omega_1) \\ H(\omega_2) \\ \vdots \\ H(\omega_N) \end{bmatrix} = \underbrace{\begin{bmatrix} 1 & \frac{1}{1+j\omega_1/\zeta_1} & \frac{1}{1+j\omega_1/\zeta_2} & \cdots & \frac{1}{1+j\omega_1/\zeta_K} \\ 1 & \frac{1}{1+j\omega_2/\zeta_1} & \frac{1}{1+j\omega_2/\zeta_2} & \cdots & \frac{1}{1+j\omega_2/\zeta_K} \\ \vdots & \vdots & \vdots & \ddots & \vdots \\ 1 & \frac{1}{1+j\omega_N/\zeta_1} & \frac{1}{1+j\omega_N/\zeta_2} & \cdots & \frac{1}{1+j\omega_N/\zeta_K} \end{bmatrix}}_{\mathbf{Z}} \begin{bmatrix} c_0 \\ c_1 \\ c_2 \\ \vdots \\ c_K \end{bmatrix} \quad (2)$$

$$\mathbf{h} = \mathbf{Z}\mathbf{c}$$

where $\omega_{min} = \omega_1 < \omega_2 < \cdots < \omega_N = \omega_{max}$, \mathbf{h} is the observation vector, \mathbf{c} the spectral amplitude vector augmented by the shift c_0 , and \mathbf{Z} a matrix containing information about the relaxation frequencies ζ .

To estimate the DSRF (i.e., ζ_k and c_k) from a given observation \mathbf{h} , the usual approach is to minimize the norm of the error, but this leads to a *nonlinear* optimization problem. Instead, we follow the strategy of basis pursuit to linearize the problem with an overcomplete dictionary. The overcomplete dictionary is a matrix $\tilde{\mathbf{Z}}$ that has the same form as \mathbf{Z} in (2),

but with many more columns. To generate the columns, we enumerate a large set of M ($M \gg K$) possible relaxation frequencies uniformly distributed in the $\log\text{-}\zeta$ space, and create one column for each enumerated ζ [4].

Since the matrix $\tilde{\mathbf{Z}}$ has $(M+1)$ columns, we redefine the unknown as an $(M+1)$ -element *weighted selector vector* $\tilde{\mathbf{c}}$ and rewrite the problem as:

$$\mathbf{h} = \tilde{\mathbf{Z}}\tilde{\mathbf{c}} + \text{error} \quad (3)$$

where we expect the solution for $\tilde{\mathbf{c}}$ to have many zero elements because $M \gg K$. The vector $\tilde{\mathbf{c}}$ contains the shift estimator \tilde{c}_0 followed by the spectral amplitude estimators \tilde{c}_m . Ideally, when the error between \mathbf{h} and $\tilde{\mathbf{Z}}\tilde{\mathbf{c}}$ is minimized, only those \tilde{c}_m with corresponding $\tilde{\zeta}_m$ that are near a true ζ_k will be nonzero, and they will take on the correct spectral amplitudes c_k . It follows that a DSRF can then be deduced from the nonzero estimated \tilde{c}_m and their corresponding $\tilde{\zeta}_m$.

Since M is also much greater than N , the system in (3) is underdetermined and there is not an unique $\tilde{\mathbf{c}}$ to minimize the error. Any vector in the null space of $\tilde{\mathbf{Z}}$ can be added to $\tilde{\mathbf{c}}$ without changing the error. In the EMI application, we have found that imposing a nonnegative constraint on $\tilde{\mathbf{c}}$ effectively eliminates a large portion of the null space of $\tilde{\mathbf{Z}}$ and the remaining solution space contains reasonable answers. Although the assumption of nonnegative spectral amplitudes cannot be rigorously justified at present, it works well in practice, and can be used where applicable. Mathematically, the DSRF can be found by optimizing:

$$\arg \min_{\tilde{\mathbf{c}}} \|\tilde{\mathbf{Z}}'\tilde{\mathbf{c}} - \mathbf{h}'\| \quad \text{subject to } \tilde{\mathbf{c}} \geq 0 \quad (4)$$

$$\text{where } \tilde{\mathbf{Z}}' = \begin{bmatrix} \Re(\tilde{\mathbf{Z}}) \\ \Im(\tilde{\mathbf{Z}}) \end{bmatrix} \text{ and } \mathbf{h}' = \begin{bmatrix} \Re(\mathbf{h}) \\ \Im(\mathbf{h}) \end{bmatrix}$$

which can be easily implemented using `lsqnonneg` or `CVX` in MATLAB. Separating the real and imaginary parts makes the whole system real. The first element in $\tilde{\mathbf{c}}$, \tilde{c}_0 , can be made nonnegative by adding a sufficiently large value to \mathbf{h} . We have also found that normalizing the input data \mathbf{h} to have an ℓ_2 norm of unity increases the accuracy of estimation.

We have observed that in the estimated DSRF, an expected relaxation (ζ_{true}, c_{true}) often gets split into two peaks located at the two sample points adjacent to ζ_{true} . Furthermore, the two estimated spectral amplitudes add up to the true spectral amplitude c_{true} , and ζ_{true} is closer to the $\tilde{\zeta}$ with larger \tilde{c} . We can reverse this splitting processes through interpolation of adjacent relaxations [4].

After the interpolation is performed, any \tilde{c}_m with a value of zero is eliminated along with its corresponding $\tilde{\zeta}_m$. We denote the resulting relaxation frequencies as $\hat{\zeta}_l$, with spectral amplitudes, \hat{c}_l , or in vector notation, $\hat{\zeta}$ and $\hat{\mathbf{c}}$, both with length L . The estimated DSRF $\hat{S} = \{(\hat{\zeta}_l, \hat{c}_l) : l = 1 \dots L\}$ is then compactly stored in $\hat{\zeta}$ and $\hat{\mathbf{c}}$. In addition, the vector length L is an estimate of the model order K .

Table 1. Estimation of a six-relaxation DSRF

c_k	0.18	0.12	0.18	0.24	0.18	0.12	
$\log \zeta_k$	3.10	3.52	4.30	5.04	5.62	6.20	
\hat{c}_l	0.17	0.12	0.17	0.24	0.18	0.11	0.01
$\log \hat{\zeta}_l$	3.09	3.51	4.29	5.05	5.64	6.25	4.52

3. ESTIMATION RESULTS

In this section, the proposed estimation method is tested against synthetic, laboratory, and field data to show its functionality, accuracy, and stability. The hardware system used is a wideband EMI sensor operating at 21 frequencies approximately logarithmically distributed over the range 300 Hz–90 kHz. The measured data is post processed by a down-track filter that is important to make the nonnegative constraint applicable for this system [5]. The synthetic data is generated in accordance with the hardware specification. The range of ζ for estimation is chosen such that $\log(\tilde{\zeta}_{min})$ and $\log(\tilde{\zeta}_{max})$ are 2.45 and 6.62, respectively. All estimations are performed with $M = 100$, and all presented spectra are normalized such that $\sum_{i=1} c_i = 1$.

Notation: ζ and c are the true/theoretical relaxation frequencies and spectral amplitudes; $\hat{\zeta}$ and $\hat{\mathbf{c}}$ are the estimates.

3.1. Dissimilarity Measure Between Two DSRF

Before we can evaluate the goodness of estimation, some kind of measure is needed to assess the dissimilarity between the estimated DSRF and the truth. The Earth Mover's Distance (EMD) [6] is a measure that can consistently quantify the dissimilarity between two spectra even when they have different numbers of relaxations. Intuitively, the EMD measures how much work it takes to morph one spectrum into the other. In the case of the DSRF, spectra are normalized prior to computing the EMD. Finally, the EMD is measured in decades because it is almost always examined in $\log\text{-}\zeta$ space.

3.2. Synthetic Six-relaxation DSRF

We test our method on a six-relaxation DSRF synthesized at 70 dB SNR with AWGN (Table 1). This is a case that cannot be handled by traditional nonlinear parameter optimization which tends to get complex-valued estimates [3]. All six relaxation frequencies are correctly recovered by solving (4). The estimated model parameters are real, and the deviation from truth is small. The EMD between the estimated and the true DSRF is 0.02 decades. There is a seventh relaxation in the estimate introduced by the noise, but its spectral amplitude is small. Thus the proposed method returns a satisfactory result even when the model order is high and unknown.

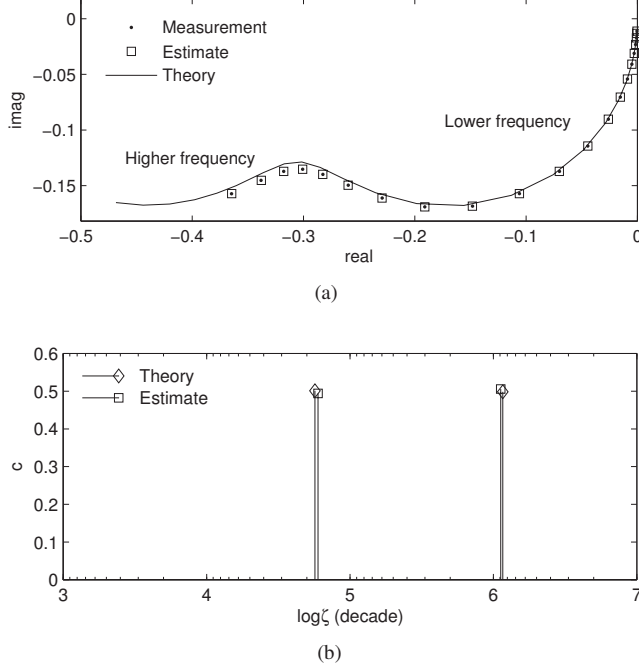


Fig. 1. (a) Laboratory measured frequency response of two coplanar coaxial circular loops. Responses are normalized such that $\|\mathbf{h}\|_2 = 1$. (b) Theoretical and estimated DSRF. $\log \zeta_k$ and c_k are (4.76 6.07) and (0.50 0.50), respectively. $\log \hat{\zeta}_l$ and \hat{c}_l are (4.78 6.05) and (0.49 0.51), respectively.

3.3. Two Coplanar Coaxial Circular Loops

For laboratory data, a target with two coplanar coaxial circular loops of copper wire was constructed. The circumferences of the two loops were chosen to be 200 mm and 150 mm. The larger loop has a wire radius of 0.06 mm, and the smaller one of 0.32 mm. A theoretical EMI response and the DSRF of this target can be found in [4]. The EMI response of this target was measured in the laboratory and is shown in Fig. 1(a), and the estimated and theoretical DSRF are displayed in Fig. 1(b). The estimated DSRF deviates from the theory slightly with an EMD of 0.03 decades. We believe this is mostly due to the thin-wire approximation used in the theory. We can safely conclude that this estimated DSRF is an accurate representation of the physical DSRF of the target.

3.4. Field Data

As a final demonstration of the proposed method, we estimate the DSRF of two types of landmines (Fig. 2), which are buried at different depths and locations. The DSRF of each sample was estimated and then plotted together with others of the same type. The average EMD between all pairs of the seven mines presented in Fig. 2(a) is 0.06 decades, and 0.07 decades for the eight mines in Fig. 2(b). In both types of mines, we

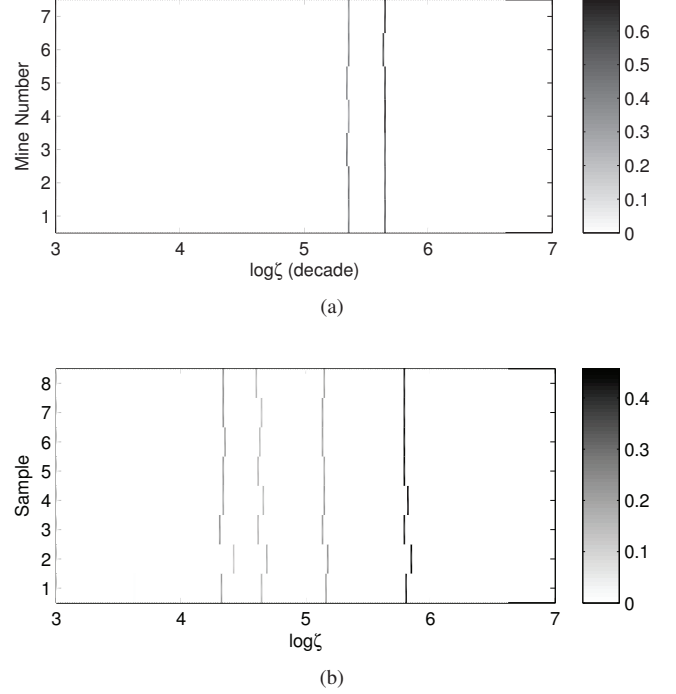


Fig. 2. Estimated DSRF of real landmines. The spectral amplitude is represented by the intensity: darker the color, larger the amplitude. (a) Low-metal content, moderate EMI response antipersonnel mines. (b) Low-metal content, strong EMI response antipersonnel mines.

observe stability and consistency in the estimated DSRF. The small variation in the estimated DSRF could be caused by several issues such as manufacturing variations, corrosion, the magnetic properties of the soil, or measurement errors. Indeed, not all landmines have similar estimated DSRFs, but, as we see in the next section, a landmine usually has an estimated DSRF similar to others of the same type.

4. APPLICATION

In this section, we explore the possibility of using the DSRF in target discrimination. We choose one hundred independently measured field samples from eleven types of landmines and various metal clutter objects [5]. We then compute the EMD between all pairs of DSRFs in order to generate the dissimilarity map shown in Fig. 3. The diagonal is zero because that is the EMD between a DSRF and itself which is zero.

We clearly see that mines of the same type are, in EMD units, close to each other, meaning mines of the same type are similar. Mines of type I do not have small EMD among its sample pairs. The reason is unclear, but we speculate that this target has negative components in its spectrum and thus the estimated DSRF is inaccurate. Mines and clutter, on the other hand, are far from each other, with few exceptions. Clutter

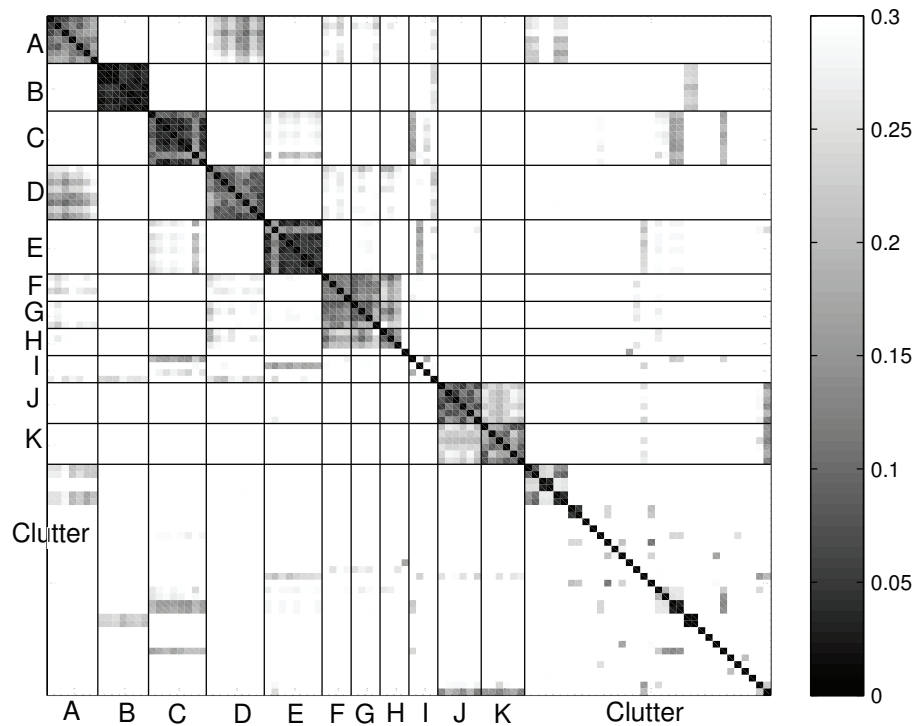


Fig. 3. The EMD between samples from eleven types of mines (A to K) and metal clutter. Darker colors denote smaller distances which indicate that two samples are more similar.

that is similar to mines may cause false alarms, but notice that the EMD from clutter to any type of mine is mostly smaller than the EMD within that mine type. The plot simply shows the clustering of mines and suggests the applicability of the DSRF for target discrimination.

5. CONCLUSIONS

We have examined the performance of the proposed DSRF method and shown its potential for target discrimination. The proposed method gives accurate and stable estimates of the DSRF with a variety of data. Future work will be directed at developing new algorithms that permit us to drop the non-negative constraint, as well as designing more sophisticated classifiers based on the estimated DSRF to provide more robust and reliable detectors.

6. ACKNOWLEDGMENT

This work is supported in part by the US Army Night Vision and Electronic Sensors Directorate, Science and Technology Division, Countermine Branch and in part by the U. S. Army Research Office under Contract Number W911NF-05-1-0257.

7. REFERENCES

- [1] P. Gao, L. Collins, P. M. Garber, N. Geng, and L. Carin, "Classification of landmine-like metal targets using wide-band electromagnetic induction," *IEEE Trans. Geosci. Remote Sens.*, vol. 38, no. 3, pp. 1352–1361, May 2000.
- [2] C. E. Baum, "On the singularity expansion method for the solution of electromagnetic interaction problems," Interaction Notes 88, Air Force Weapons Laboratory, 1971.
- [3] Y. Das and J. E. McFee, "Limitations in identifying objects from their time-domain electromagnetic induction response," in *Proc. SPIE*, Orlando, FL, Apr. 2002, vol. 4742, pp. 776–788.
- [4] M. Wei, W. R. Scott, Jr., and J. H. McClellan, "Robust estimation of the discrete spectrum of relaxations for electromagnetic induction responses," *IEEE Trans. Geosci. Remote Sens.*, accepted for publication.
- [5] W. R. Scott, Jr., "Broadband array of electromagnetic induction sensors for detecting buried landmines," in *Proc. IGARSS*, Boston, MA, July 2008.
- [6] Y. Rubner, C. Tomasi, and L. J. Guibas, "A metric for distributions with applications to image databases," in *Proc. ICCV*, Bombay, India, Jan. 1998, pp. 59–66.

LOCATION ESTIMATION USING A BROADBAND ELECTROMAGNETIC INDUCTION ARRAY

Ali C. Gurbuz^a, Waymond R. Scott, Jr.^b, James H. McClellan^b

^aDepartment of Electric and Electronics Engineering,
TOBB University of Economics and Technology, Ankara, Turkey 06560

^bSchool of Electrical and Computer Engineering,
Georgia Institute of Technology, Atlanta, GA, USA 30332-0250

ABSTRACT

A broadband quadrupole electromagnetic induction (EMI) array with one transmitter and three receiver coils is built for detecting buried metallic targets. In this paper, it is shown that the locations of multiple metallic targets including their depth and cross-range position can be estimated accurately with the EMI array using an orthogonal matching pursuit (OMP) approach. Conventional OMP approaches use measurement dictionaries generated for each possible target space point which results in huge dictionaries for the 3D location problem. This paper exploits the inherent shifting properties of the scanning system to reduce the size of the dictionary used in OMP and to lower the computation cost for possibly a real-time EMI location estimation system. The method is tested on both simulated and experimental data collected over metal spheres at different depths and accurate location estimates were obtained. This method allows EMI to be used as a pre-screener and results in valuable location estimates that could be used by a multi-modal GPR or other sensor for enhanced operation.

Keywords: Electromagnetic Induction Sensor, Depth Estimation, Orthogonal Matching Pursuit, Location Estimation

1. INTRODUCTION

Electromagnetic Induction (EMI) is a very popular method used to detect the presence of metallic content in subsurface targets. EMI sensors work by affecting a region of interest with a time varying magnetic field and detecting the induced magnetic field generated by the eddy currents on the metallic target [1]. Much research has been performed on using EMI to detect buried targets such as landmines, UXO, etc.; however, much less work has been performed on making accurate estimates for the location of the target. The depth and cross-range location of the target is of particular interest here, because the down-track location of the targets are fairly apparent in the raw data from the sensor. Difficulties arise in making the location estimates, because of the nature of the EMI response. First, the EMI response doesn't measure a quantity like time delay in a radar which is directly proportional to distance. Second, the relationship between the strength and object distance is nonlinear and depends heavily on the objects size and metal content. A deep high-metal target could generate a stronger field strength than a shallow low-metal target. In [2], a polynomial curve is fitted to vertical gradient data and a classification scheme as "shallow" or "deep" is followed rather than a depth estimate. The results are rough and show a depth resolution of ± 8 inches which is not sufficient for most applications such as landmine detection. In [3], it is observed that the more distant signals have relatively stronger low frequency components and shallow targets provide stronger high frequency signals. However, no method to estimate the depth was presented.

In this paper, we propose a new method for location estimation of metallic targets in both depth and cross range using EMI data. Our technique uses the relative strength of the measured response at the receive coils of the EMI array along with the shape of the down-track response from the receive coils to make a location estimate. To use this information, the target space is discretized to generate a list of possible target positions and a model EMI response is generated for each target position to form an overcomplete dictionary of responses. Many methods have been developed to extract an optimal representation of received signal in terms of the given

For further information please contact authors: Ali C. Gurbuz: acgurbuz@etu.edu.tr, W. R. Scott, Jr.: waymond.scott@ece.gatech.edu, J. H. McClellan: jim.mcclellan@ece.gatech.edu

dictionary elements and this kind of search is generally called Basis Pursuit [4]. We use a type of basis pursuit algorithm, called orthogonal matching pursuit (OMP) [5], to extract the location information. Conventional OMP approaches use measurement dictionaries generated for each possible target space point which results in huge dictionary sizes for 3D location estimates. This paper exploits the inherent shifting property of the scanning system to reduce the size of the dictionary used in OMP and thereby reduces the computation cost which is necessary for a real-time EMI location estimation system.

Section 2 describes the EMI model data calculation, the dictionary generation process and the location estimation algorithm. In Section 3 experimental results with performance analysis are provided. Conclusions and future work are discussed in Section 4.

2. THEORY

2.1. EMI Model Data

In the EMI model, a transmitter generates a magnetic field, represented with a vector \mathbf{h}_T , at the target position as shown in Fig. 1. Here \mathbf{h}_T is a 3×1 vector containing the x , y and z components of the magnetic field generated by the transmitter coil, and \mathbf{h}_R is the receiver magnetic field vector at the target position when the receiver coil is used as a transmitter. These fields are calculated using the Bio-Savart law by dividing the coils into short line segments. The target is treated as a point target that can be modeled by the magnetic polarizability tensor, \mathbf{M} . It can be shown by using reciprocity that the received voltage due to the target is

$$V_{Rec} = \frac{j\omega\mu}{I_R} \mathbf{h}_R^T \mathbf{M} \mathbf{h}_T \quad (1)$$

Here \mathbf{M} can be viewed as a 3×3 symmetric matrix that represents the magnetic polarizability tensor of the target. For a metallic sphere, the tensor is diagonal $\mathbf{M} = M_0 \mathbf{I}$. The response measured by the EMI detector is

$$R = \frac{V_{Rec}}{V_{Ref}} = \frac{\mu}{L_{Ref} I_T I_R} \mathbf{h}_R^T \mathbf{M} \mathbf{h}_T \quad (2)$$

where the response is referenced to the voltage

$$V_{Ref} = j\omega L_{Ref} I_T. \quad (3)$$

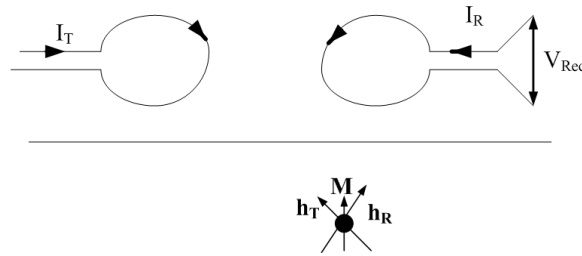


Figure 1. EMI scenario. \mathbf{h}_T is the magnetic field vector generated by transmitter. \mathbf{M} is the magnetic polarizability of the target. \mathbf{h}_R is the magnetic field vector if the receiver was used as the transmitter. V_{Rec} is the voltage measured at the receiver.

This EMI sensor measures the response at 21 logarithmically spaced frequencies from 330 Hz to 90.03 kHz for all the receive coils and records them every 0.1 s [6]. However, this work will only use the peak value of the imaginary part of the response because the method is based on relative amplitudes

Assume the quadrapole EMI array shown in Fig. 2 is scanned in the y direction to search the subsurface for targets. The response (2) for the three receivers is graphed in Fig. 3 as a function of the scan position with depth as a parameter for a target at $(x, y) = (0.17, 0)$ m buried at depths from 2 to 30 cm in 1 cm increments.

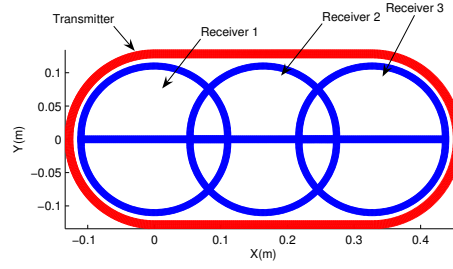


Figure 2. Quadrapole Array used for target localization.

The shape of the response as a function of scan position change noticeably as the target depth increases, and the relative amplitudes for the response of the receivers also change as a function of the target depth. The changes are more pronounced for shallow targets; less pronounced for deeper ones. Our proposed method collects all of these models into a dictionary of EMI responses for each possible target space point.

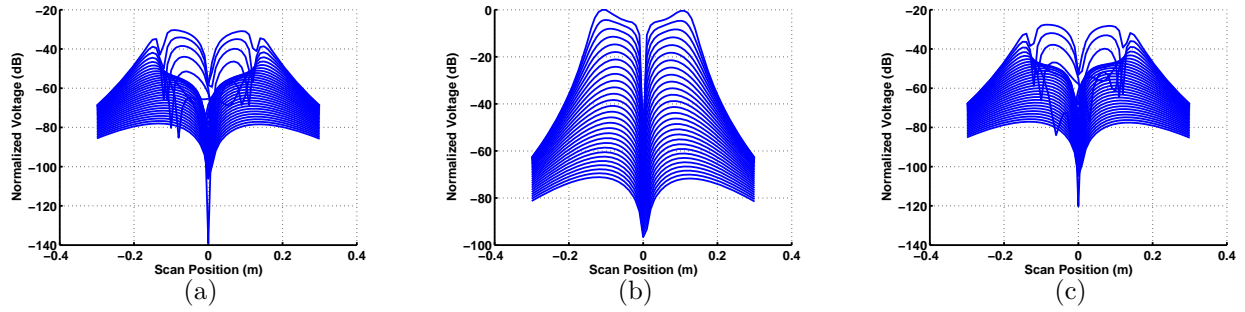


Figure 3. Normalized response for targets from 2 cm to 30 cm deep using the quadrapole array for (a) Receiver 1, (b) Receiver 2, (c) Receiver 3.

The other important location estimation parameter is the cross range, i.e., the x position of the target. The response is graphed as a function of scan position with the cross range as a parameter in Fig. 4. The target is at $y = 0$ and $z = -6$ cm with a cross range that varies from $x = 0$ to 34 cm with 2 cm increments as the array is scanned from $y = -30$ to $y = 30$ cm with 1 cm increments. The information of relative amplitude between the receivers as well as the shape of the response plays a very important role in estimating the cross range of the targets accurately.

2.2. Creating Dictionary of EMI Responses

To create a dictionary, Ψ , of EMI responses the target space π_T which lies in the product space $[x_i, x_f] \times [y_i, y_f] \times [z_i, z_f]$ must be discretized to create a finite set of possible target space points. Here (x_i, y_i, z_i) and (x_f, y_f, z_f) denote the initial and final positions of the target space along each axis. Hence, for any target position and at any scan location the received voltage can be calculated by (2) by setting $\alpha = 1$ and $\mathbf{M} = \mathbf{I}$ (assuming spherical targets). The dimensions of the dictionary Ψ will be $L \times N$ where L is the number of scan points in the scan direction. While working with such a matrix is manageable with scanning for a 2D slice of target space, for 3D target localization the number of target space points increases drastically depending on the resolution required, making it unrealistic to work with the dictionary Ψ . For example, localizing targets in an $1 \times 1 \times 1$ m³ area with 1 cm resolution would require a dictionary size of $L \times 10^6$. However, with a regular scanning pattern we can exploit a shift-invariance property of the scanning to decrease the size of the dictionary.

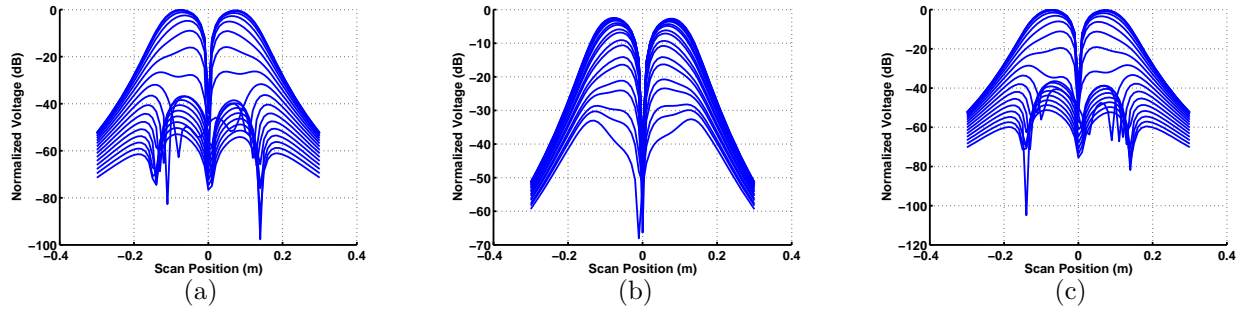


Figure 4. Normalized voltage values recorded at the receiver coils for targets at $y = 0$, $z = -6$ cm but varying in cross range with $x = 0$ to $x = 34$ cm using the quadrapole array for (a) Receiver 1, (b) Receiver 2, (c) Receiver 3.

Figure 5 shows a three-receiver, one-transmitter quadrapole array scanning along the y direction. As the array scans targets having shifted y locations but the same cross-range (x) and depth (z) values, the resulting responses in the receiver coils are shifted versions of each other. Hence it is sufficient to create a dictionary for the $y = 0$ cross range slice, and then use it to locate targets in 3D.

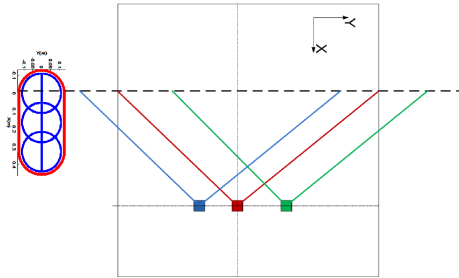


Figure 5. Quadrupole array scanning on y direction. Targets having the same x and z values create responses that are shifted versions of each other

So only the target space slice $[x_i, x_f] \times [z_i, z_f]$ is used to create the dictionary Ψ . Discretization generates a finite set of target points $\mathcal{B} = \{\pi_1, \pi_2, \dots, \pi_N\}$, where N determines the resolution and each π_j is a 3D vector $[x_j, 0, z_j]$. Creating the dictionary requires the calculation of all received voltage values for each π_j in the target space. The j^{th} column of the dictionary is the voltage levels v_j at the EMI receiver when only the target at π_j is present. If an array of receivers is used then the j^{th} column of the dictionary is generated by stacking the voltages $v_{j,i}$ $i = 1, 2, \dots, R_N$ as $v_j = [v_{j,1}; v_{j,2}; \dots; v_{j,R_N}]$, where R_N is the number of receivers in the EMI array. Finally, each column is normalized to have norm one to weight each target space point equally. After normalization each receiver dictionary Ψ_i can be separated. Using an EMI array of receivers and creating the dictionary by stacking up their voltage recordings before normalization allows us to use the relative amplitudes between the receivers for better cross range resolution.

2.3. Location Estimation with Orthogonal Matching Pursuit

We assume that the observed signals at the receivers are linear combinations of the responses from each target alone, thus the inter-target interaction is negligible. In this case, the following procedure is used to locate the targets:

1. Observe \mathbf{d}_i , $i = 1, 2, \dots, R_N$ voltage values at each receiver i ; so $\mathbf{d} = [\mathbf{d}_1; \dots; \mathbf{d}_{R_N}]$. Initialize row and column index sets: $\Lambda_{0,r} = \emptyset$ and $\Lambda_{0,c} = \emptyset$, the residual $\mathbf{r}_0 = \mathbf{d}$ and the loop index to $t = 1$.
2. Generate projection matrixes $\mathbf{P}_i = \mathbf{r}_i * \Psi_i$ where the operator $*$ means columnwise convolution. Sum individual projection matrixes $\mathbf{P} = \sum \mathbf{P}_i$

3. Determine the row and column indexes $\lambda_{t,r}$ and $\lambda_{t,c}$ for which \mathbf{P} is maximized.
4. Update the index sets $\Lambda_{t,r} \leftarrow \Lambda_{t-1,r} \cup \lambda_{t,r}$ and $\Lambda_{t,c} \leftarrow \Lambda_{t-1,c} \cup \lambda_{t,c}$
5. Find the weights \mathbf{c} of the least-squares problem $\min \|\mathbf{d} - \sum_{k=1}^t \mathbf{c}(\lambda_{k,c}) \Psi_{\lambda_{k,c}}\|_2$
6. Compute the new residual using the least-squares weights \mathbf{c} : $\mathbf{r}_t = \mathbf{d} - \sum_{k=1}^t \mathbf{c}(\lambda_{k,c}) \Psi_{\lambda_{k,c}}$
7. Increment the loop counter: $t \leftarrow t + 1$
8. If the stopping criteria has not been met, return to Step 2.

One can halt the procedure when the norm of the residual \mathbf{r}_t declines below a specified threshold which could be selected based on the noise energy in the received data. The target location information is stored in the row and column index sets $\Lambda_{t,r}$ and $\Lambda_{t,c}$. The row index set $\Lambda_{t,r}$ shows the shift in the scan direction from the $y = 0$ slice. The cross range information is stored in $\Lambda_{t,c}$. The cross range and depth of the targets are $\pi_{\Lambda_{t,c}}$.

3. RESULTS

To demonstrate the steps of the algorithm, consider a 2D simulation that uses a simple head with only one receiver, as in Fig. 7(a). The simple head scans with $x = 0$ cm from $y = -30$ cm to $y = 30$ cm with 1 cm increments. Assume there are two metal spheres at $(0, -19, -3.5)$ cm and at $(0, 11, 6.5)$ cm as shown in Fig. 6(a). As the simple head scans the region the recorded voltage values with a signal to noise ratio (SNR) of 20 dB is shown in Fig. 6(b).*

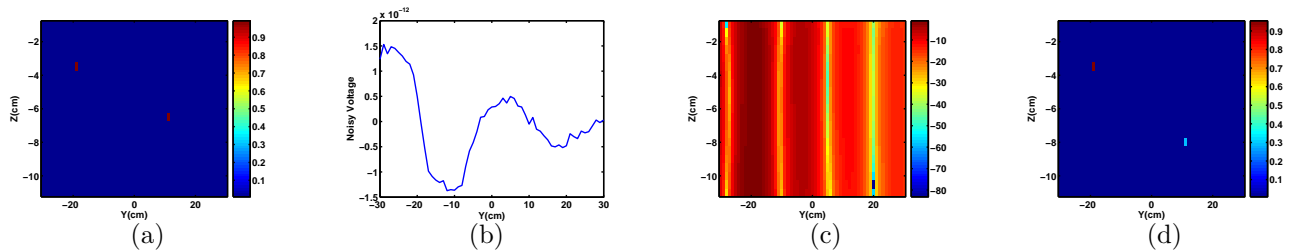


Figure 6. (a) Target space containing two targets. (b) Noisy voltage measurements (c) Projection of the measurements to each column of response dictionary (d) OMP result.

The EMI response dictionary is created with a resolution of 1 cm in y and 0.5 cm in z . One possible solution is to directly check the projection values of the received voltage measurements to each column of the EMI response matrix. Figure 6(c) shows the image containing these projection values in dB scale. It can be observed that it is directly very hard to extract the locations and the number of targets from direct projections. However, the OMP selects two targets at $(0, -19, -3.5)$ cm and $(0, 11, 8)$ cm. Although the depth information for the second target is 1.5 cm off, the locations and number of targets could be extracted with an acceptable error margin. The following results also indicate that using multiple receivers increases the accuracy of cross-range estimation.

3.1. Laboratory Depth Estimation with Quadrapole Head

To test the proposed algorithm with experimental data the quadrapole sensor in Fig. 7(a) is built. The simple quadrapole sensor is placed with its center at $x = y = z = 0$ and a metal sphere of diameter 0.5" is scanned along the track shown in Fig. 7(b) from 2 to 35 cm above the sensor level. The air response of the target-free environment is also measured and subtracted from the measurements with the target to reduce the effect of any background, e.g., moving devices and the laboratory room. The proposed algorithm is applied to air response subtracted raw data. The estimated depth values for the quadrapole sensor are shown in Fig. 7(c).

It can be observed that using the quadrapole sensor allows estimation of most depths very accurately. It is important to note here that the target is a metal sphere which matches with the model we used in dictionary generation. Also the noise level in the laboratory data is minimal once the air and lab responses are subtracted.

*Here the two targets are assumed to be far enough apart so that the interaction between them is negligible.

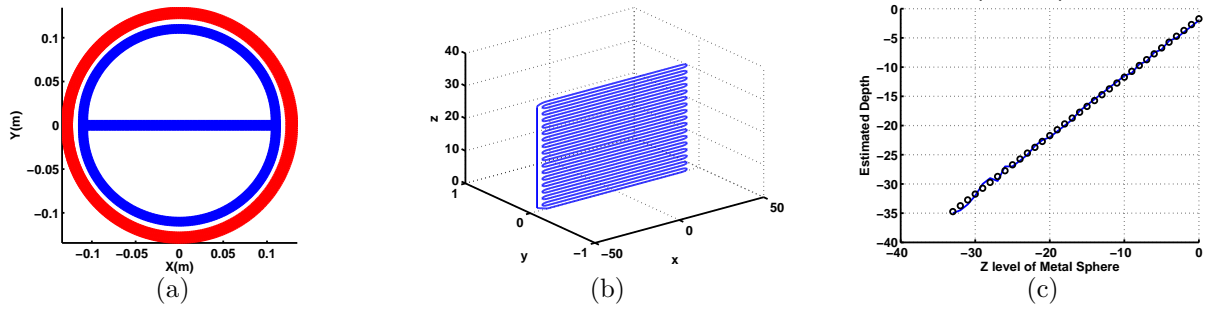


Figure 7. (a) Single Quadrapole Sensor, (b) Metal Sphere Track, (c) Depth estimates using quadrapole data.

3.2. Noise Performance

To analyze performance versus additive noise, the algorithm is applied to data created with targets at different depths from 0 to 20 cm and with varying noise levels from 10 to 50 dB. For each noise level and target depth, zero-mean gaussian noise is added to the data model for the given depth. Then the depth of the target is estimated for 100 independent trials with the proposed method. Figure 8 shows the variance from the true target position for the quadrapole sensor at each SNR level and target depth. It can be observed that even for

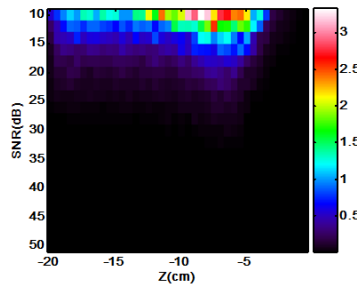


Figure 8. Variance of the depth estimates for varying levels of SNR and for targets at different depths using a single quadrapole sensor.

the case of 10 dB SNR the standard deviation of the depth estimate for the quadrapole sensor is around ± 2 cm. As the SNR increases the estimates get better as expected.

3.3. 3D Experimental Lab Results with the Quadrapole Array

A quadrapole array with three receivers and one transmitter coil, as shown in Fig. 2, is built for enhanced 3D target localization. The quadrapole array is held fixed at $x = y = z = 0$ and targets like a metal loop and an anti-personnel land mine are scanned to collect the EMI measurements.

In the first experiment, the target is a loop of 22 AWG wire with a diameter of 31.8 cm oriented so that the axis of the loop is z directed. The target is positioned at three different cross range values $x = (0.02, 0.17, 0.32)$ m. For each cross range, the target is moved in down range from $y = -50$ to $y = 50$ cm with 0.5 cm increments and from $z = -8$ cm to $z = -20$ cm with 1 cm increments from the level of the array. A dictionary using a z oriented loop target model is generated. Figure 9 shows the true and estimated depth, cross range and down-range values for the target. The location of the target is estimated relatively accurately for most of the cases even when the target is not directly under the center receiver.

Next a more interesting target, a low-metal anti-personnel mine, is tested. In this case, different cross ranges with $x = (0.07, 0.17, 0.27)$ were measured. The target was moved from $z = -7.5$ cm to $z = -28.5$ cm in 1 cm increments, and from $y = -50$ to $y = 50$ cm in 0.5 cm increments. A dictionary of responses including targets at $z = 1, 2, \dots, 30$ cm, and cross ranges from $x = -18$ to $x = 50$ cm with 2 cm increments is generated. Hence,

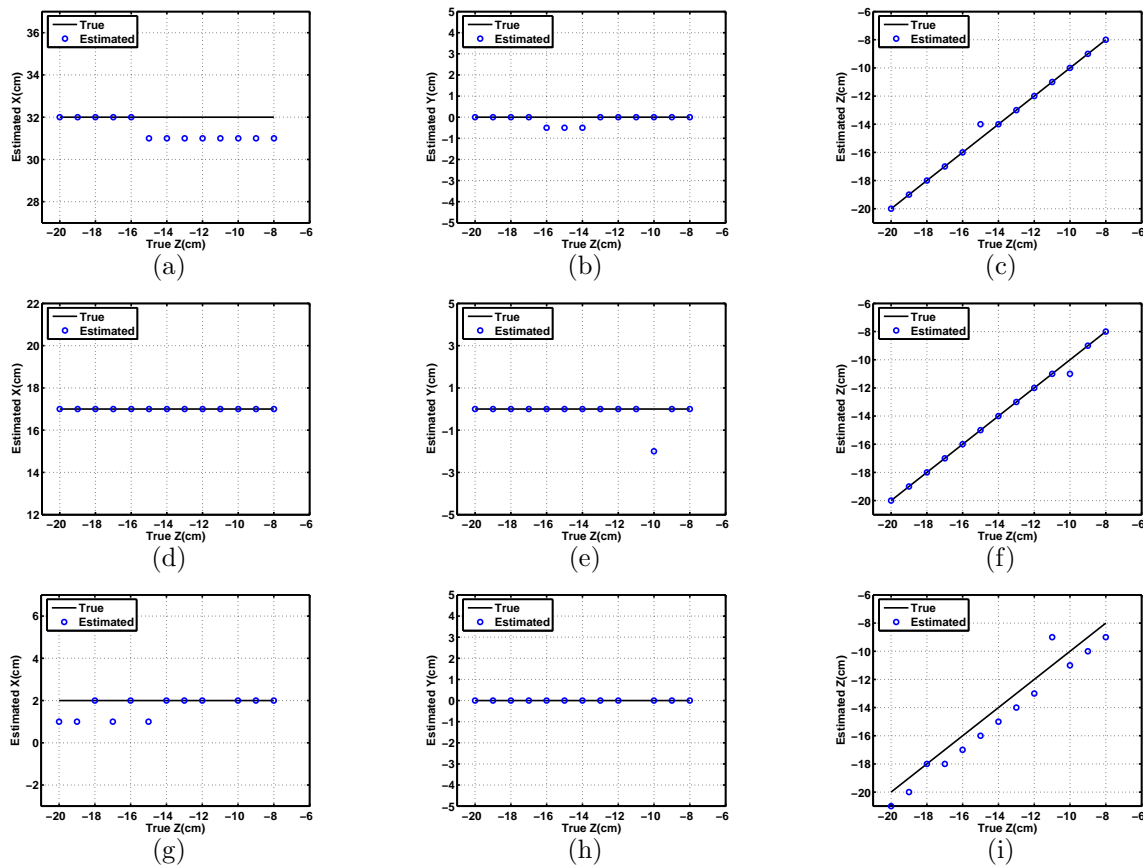


Figure 9. Location estimates for the coil target at (a,b,c) cross range $x = 7$ cm, (d,e,f) cross range $x = 17$ cm, (g,h,i) cross range $x = 27$ cm.

the exact target depths and cross ranges are not in the dictionary. A loop target model oriented in z direction is used for dictionary generation as in the loop target case. Note that the target polarization tensor is not known, and may be different than the loop target model used in dictionary generation. Despite these facts the location estimates obtained for varying cross ranges shown in Fig. 10 indicate ± 2 cm accuracy until the target depth is 17 cm. For depths below 17 cm, the estimation performance degrades. The cross-range estimation is also successful for depths less than 20 cm. In most of the cases, the down-track location estimate is very accurate.

3.4. 3D Field Data Results with the Quadrapole Array

The proposed algorithm is tested with the data collected with the quadrapole array shown in Fig. 2 at a field site over several buried targets. Each target is buried at different grids, and each grid is scanned with the array. The grid size is approximately $1.5 \text{ m} \times 1.5 \text{ m}$. The array is held approximately 1" above the ground level. Figure 11 shows the collected measurements from the three receivers taken by scanning a grid containing a low-metal anti-personnel mine buried approximately 2" depth from the ground level.

The target is close to the center of the grid and the quadrapole array is scanned across the grid. Hence, the voltage level in receiver 2 (center receiver) is much higher compared to the level in receivers 1 and 3. When the proposed algorithm is applied to measured data as in Fig. 11, the location of the target is estimated as $(x, y, z) = (0, 0.01, -0.08) \text{ m}$ which is very close to the expected location of the target $(x, y, z) = (0, 0, -0.08) \text{ m}$. Here the origin of the coordinate system is on the surface of the soil at the center of the grid; x is the cross-range coordinate, y is the down-range coordinate and z is the vertical coordinate. The location estimates for five additional occurrences of the same type of AP mine are shown in Table 1.

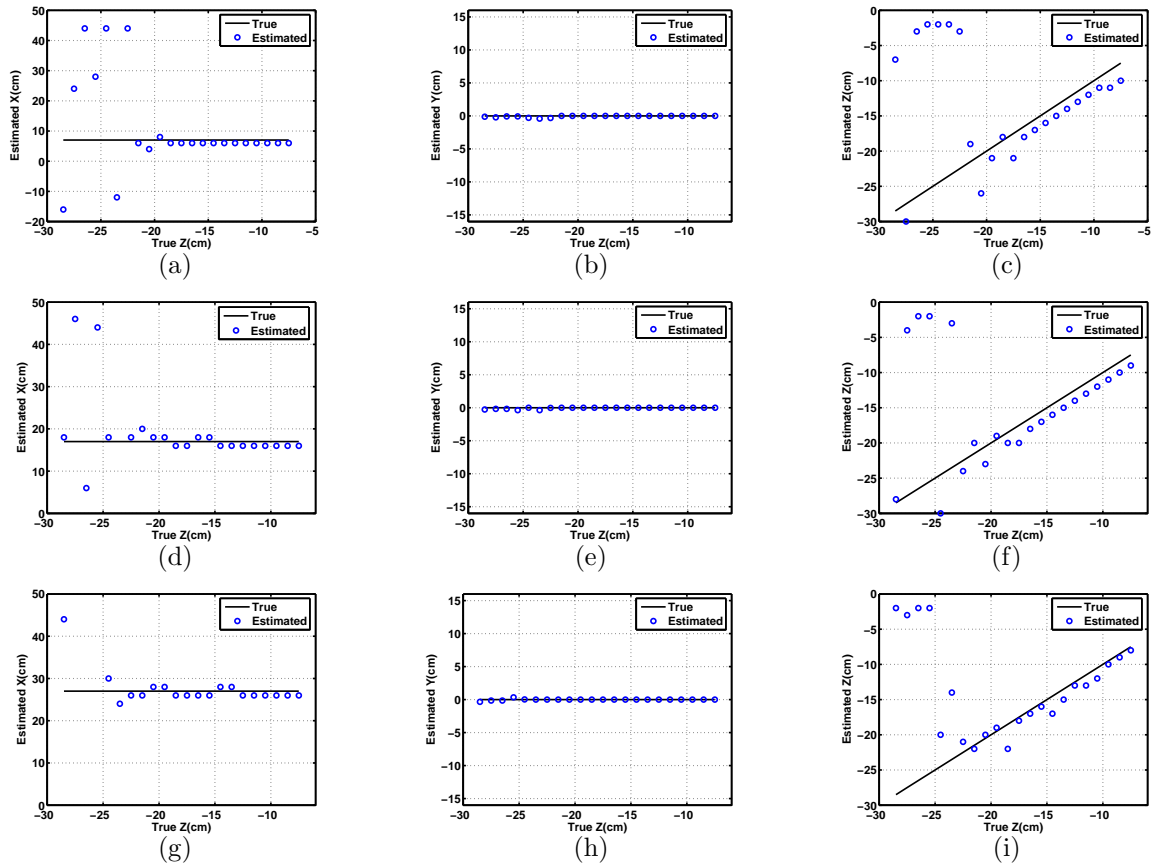


Figure 10. Location estimates for the anti-personnel mine at (a,b,c) cross range $x = 7$ cm, (d,e,f) cross range $x = 17$ cm, (g,h,i) cross range $x = 27$ cm.

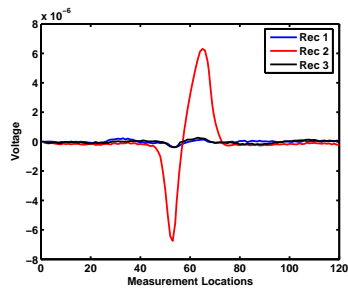


Figure 11. Imaginary part of the 11th frequency component for all three receivers.

Table 1. Field Data Location Estimates

Grid No	Expected Location $(x, y, z)(\text{m})$	Estimated Location $(x, y, z)(\text{m})$
1	(0, 0, -0.05)	(-0.01, 0.01, -0.06)
2	(0, 0, -0.05)	(-0.03, -0.01, -0.07)
3	(0, 0, -0.05)	(-0.02, 0.00, -0.05)
4	(0, 0, -0.08)	(0.05, 0.03, -0.11)
5	(0, 0, -0.08)	(-0.01, 0.02, -0.09)
6	(0, 0, -0.08)	(0.00, 0.01, -0.08)

It can be observed that in the field measurements the target locations and depths could be estimated to within approximately $\pm 3\text{cm}$. It is important to note that the approximate depth information is from the top of the AP mine, not from the metallic part. Also there might be small changes due to the burial process, or from targets being buried so long that their locations might change slightly. Nevertheless, the proposed method provides promising depth estimates in the tested field data.

4. CONCLUSIONS AND FUTURE WORK

A location estimation algorithm based on OMP using EMI data is proposed. Our initial tests on simulated, laboratory and field data indicate that target depth information can be extracted from EMI data with small errors. However, in a few cases the error can be significantly greater when the target is a poor match for the target model used in the dictionary. We are working to generalize the technique so that it is applicable to a wider range of targets.

5. ACKNOWLEDGMENTS

This work is supported in part by the US Army Night Vision and Electronic Sensors Directorate, Science and Technology Division, Countermine Branch and in part by the US Army Research Office under Contract Number W911NF-05-1-0257, and in part by an ARO-MURI grant: “Multi-Modal Inverse Scattering for Detection and Classification of General Concealed Targets,” under contract number DAAD19-02-1-0252.

REFERENCES

1. C. E. Baum, *Detection And Identification Of Visually Obscured Targets*, CRC, 1998.
2. Jay Marble and Ian McMichael and Denis Reidy, “Estimating object depth using a vertical gradient metal detector,” in *Proc. of SPIE*, **6953**, 2008.
3. James Traveyan, “Target depth estimation for a metal detector in the frequency domain,” in *IEE Conf. on Detection of abandoned land mines*, pp. 218–221, 1998.
4. S. S. Chen, D. L. Donoho, and M. A. Saunders, “Atomic decomposition by basis pursuit,” *SIAM J. Sci. Comput.* **20**, pp. 33–61, 1999.
5. J. Tropp and A. Gilbert, “Signal recovery from random measurements via orthogonal matching pursuit,” *IEEE Trans. Information Theory* **53**(12), pp. 4655–4666, Dec. 2007.
6. W. R. Scott, Jr., “Broadband array of electromagnetic induction sensors for detecting buried landmines,” in *IEEE International Geoscience and Remote Sensing Symposium*, pp. II-375–378, 7-11 July 2008.

Automated, non-metallic measurement facility for testing and development of electromagnetic induction sensors for landmine detection

Gregg D. Larson^{*} and Waymond R. Scott, Jr.[†]

^{*}Woodruff School of Mech. Eng., Georgia Institute of Technology, Atlanta, GA, USA 30332-0405

[†]School of Elec. and Comp. Eng., Georgia Institute of Technology, Atlanta, GA, USA 30332-0250

ABSTRACT

For development of electromagnetic induction (EMI) sensors for landmine detection, a testing facility has been established for automated measurements of typical targets with both individual sensors and arrays of sensors. A six-degree of freedom positioner has been built with five automated axes (three translational stages and two rotational stages) and one manual axis for target characterizations with no metal within the measurement volume. Translational stages utilize commercially-available linear positioner hardware. Rotational stages have been customized using non-metallic components to position the targets within the measurement volume. EMI sensors are held fixed in one location while the positioner orients the targets and moves them along a prescribed path through the region surrounding the sensor. The automated movement is computer-controlled and data are acquired continuously. Data are presented from three-dimensional scans of targets at various orientations. Typical targets include shell casings, wire loops, ball bearings, and landmines.

Keywords: Electromagnetic induction, EMI, landmine, detection, sensor, testing

1. INTRODUCTION

To detect the presence of landmines buried in soil, an electromagnetic induction (EMI) sensor has been developed and tested at multiple field locations¹⁻². Figure 1(a) shows a single broadband EMI sensor while Figure 1(b) shows a broadband array of EMI sensors, both at field locations. Both sensors were scanned close to the soil surface to detect buried targets. Details of the EMI sensor and its field testing can be found in the literature.

Sample data from field measurements of four anti-personnel landmines at various depths are shown in the Argand diagrams in Figure 2. The imaginary part of the response is graphed as a function of the real part with frequency as a parameter on the Argand diagrams. Each figure shows one type of target with responses plotted for different burial depths. The characteristic responses from the buried targets shown in Figure 2 are a function of the metal content and structure of the individual targets. Note that the shape of the response is consistent for each target and is insensitive to the burial depth. This shape information can be used to help discriminate between landmines and clutter³⁻⁷. However, little is known about how landmines and complex clutter objects behave when they are tilted at odd angles which could cause missed detections. To aid in the development of the EMI sensors and associated detection algorithms, a testing facility has been built to characterize the response of typical targets and clutter objects with respect to location and orientation. The data from these measurements will be used to study the response of the targets as a function of location and orientation. This type of measurement would be very difficult to perform in the field due to the difficulty of accurately placing and rotating the target. It is envisioned that the results of this work can be utilized to reduce false alarm rates and increase the probability of detection for EMI sensors through improvements in both the hardware and the processing algorithms used to detect and discriminate buried targets.

In the following sections, the testing facility will be described and experimental measurements will be shown along with theoretical results for representative targets including a single wire loop, three mutually orthogonal wire loops, and a 9 mm shell casing.

^{*} E-mail: gregg.larson@mc.gatech.edu, Tel: 404-894-6026

[†] E-mail: waymond.scott@ece.gatech.edu, Tel: 404-894-3048



Fig. 1. Field measurement systems using (a) a single broadband EMI sensor and (b) an array of three broadband EMI sensors.

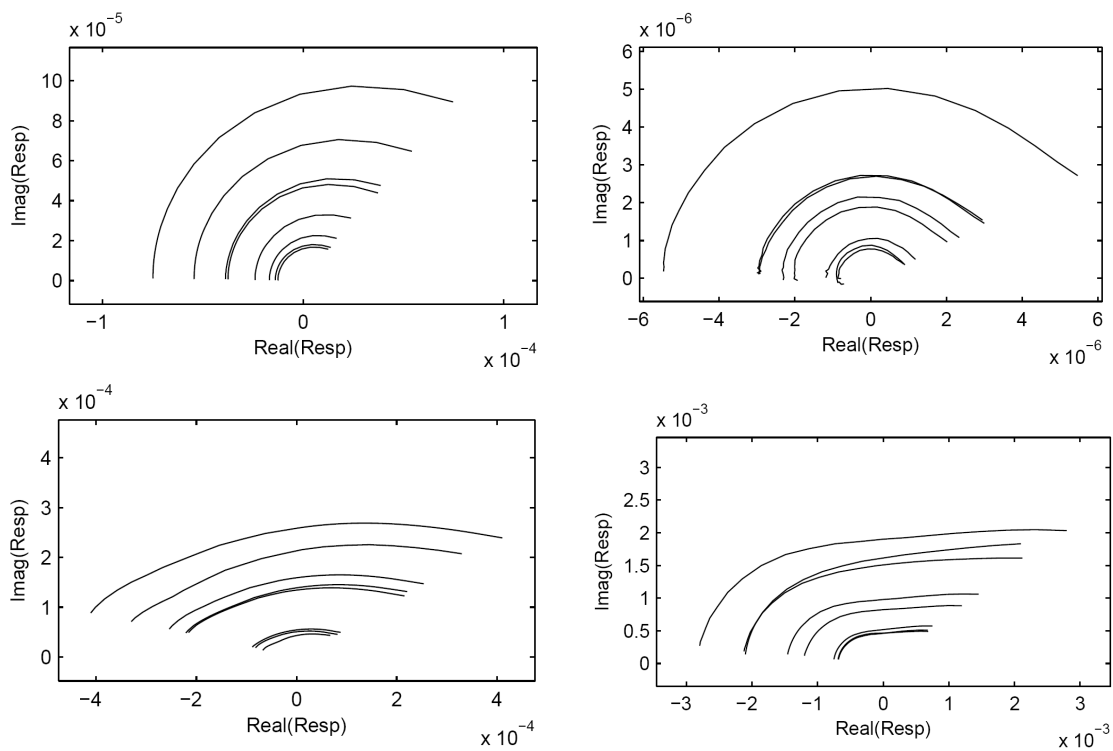


Fig. 2. Sample field data from four types of anti-personnel landmines presented in Argand diagrams. Each curve in figures (a) through (d) represents the response of a single target as a function of interrogation frequency. The response of multiple targets are shown in (a) through (d) with the amplitude differences between curves indicating targets with different burial depths.

2. EXPERIMENTAL FACILITY FOR CALIBRATION MEASUREMENTS

To measure the characteristic response of EMI sensors of several representative targets, a laboratory positioner was developed with three automated translational stages (x , y , and z), two automated rotational stages (yaw and pitch), and one manually-adjusted rotational stage (roll, not labeled) as indicated in Figure 3. A single EMI sensor is shown in Figure 3(b) with a single wire loop as the target while an array of three EMI sensors is shown in Figure 3(c) with a target that consists of three mutually orthogonal loops of different gauge wire. This system has been used to measure the response of targets in a three-dimensional region as a function of angular orientation. Other typical targets include shell casings, ball bearings, coplanar wire coils, and landmines.

The translational stages were built using commercially-available hardware including stepper motors, gear reducers, belts, and aluminum structural beams. The positioner can translate each target throughout a 2 m by 1 m by 0.5 m volume. The first automated rotational stage utilizes a Velmex rotary positioner (Model # B4818TS) with a stepper motor to control the yaw angle throughout a 360° range of motion. The second automated rotational stage was custom-built using fiberglass structural beams, polycarbonate connectors, fiberglass shafts, acetal/nylon/glass nonmetallic bearings, nylon miter gears, fiberglass-reinforced nylon sprockets, Delrin chains, and nylon bolts. A stepper motor controls the pitch angle throughout a 360° range of motion. The second rotational stage holds each target 70 cm from the nearest metal on the moving support beam. This second rotational stage is reconfigurable as the fiberglass structural beams can be replaced by different length beams to adjust to different size targets; this would also necessitate appropriate adjustments to the chains and fiberglass shafts.

The EMI sensor or array of EMI sensors is positioned in the middle of the measurement region, sufficiently distant from the floor (and its structural steel) and the aluminum beams of the positioner frame to minimize the measured response from the surrounding metal structures. Additionally, the response from the surrounding metal structures is subtracted from the measurements of the individual targets as a part of the EMI sensor's processing algorithms. While the EMI sensor is held fixed, the positioner orients the target in yaw and pitch and then translates it along a prescribed path computed by the data acquisition and motion control system. The path is continuous in the x direction with a discrete set of values for y and z . The path is repeated for each set of yaw and pitch angles.

The EMI sensor and the array of EMI sensors includes a surrounding coil that transmits an excitation signal. A multi-sine signal, composed of 21 distinct frequencies logarithmically spaced from 300 Hz to 90 kHz, is transmitted cyclically. The multi-sine signal has been optimized in regards to phase angle and amplitude as well as to minimize interference with power line harmonics. This cyclic transmission allows for continuous data acquisition in the time domain at 204 kSamples/second from each sensor with processing while the target is in motion. The time-domain data are transformed into the frequency domain using a fast Fourier transform. This operation is performed in real time and only the 21 complex-valued samples in the frequency domain for each measurement point are saved. This provides a substantial benefit in that the saved data can be reduced from 20,400 single-valued samples in the time domain to 21 complex-valued samples.

Continuously sampled data are acquired, processed, and saved at 0.1 second intervals while the target is in motion along the prescribed path. With the target moving at 4 cm/second in the x -direction, data are acquired every 0.4 cm along the x -axis. The data are then interpolated to 0.5 cm intervals for an evenly-spaced grid in the post-processing. As data are acquired at distinct y and z values, interpolation is not required in those dimensions.

A typical measurement for the EMI sensor array scans a target continuously from -51 cm to 51 cm in the x -direction and discretely at y -values from -30 cm to 30 cm in 10 cm increments and z -values from 0 cm to 22 cm in 1 cm increments for three yaw angles (0, 45, and 90 degrees) and five pitch angles (0, 22.5, 45, 67.5, and 90 degrees) over a 19 hour time period. Processing of the acquired data results in 30,581,145 complex data points. This is so much data that it is difficult to inspect it.

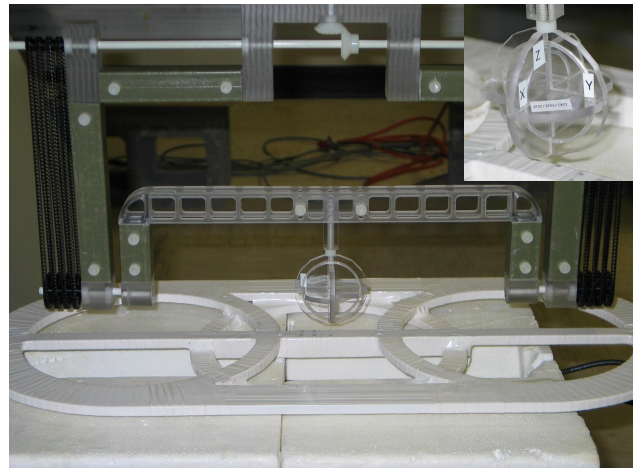
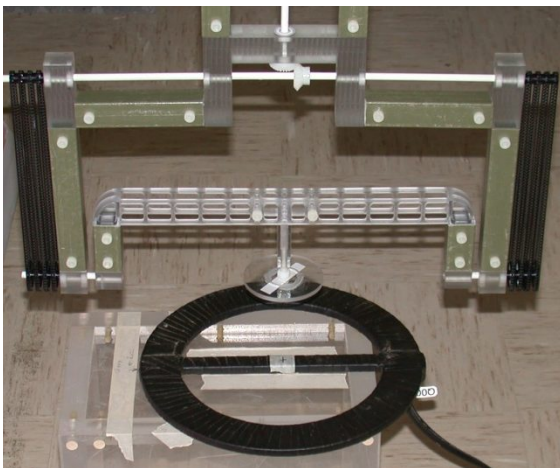
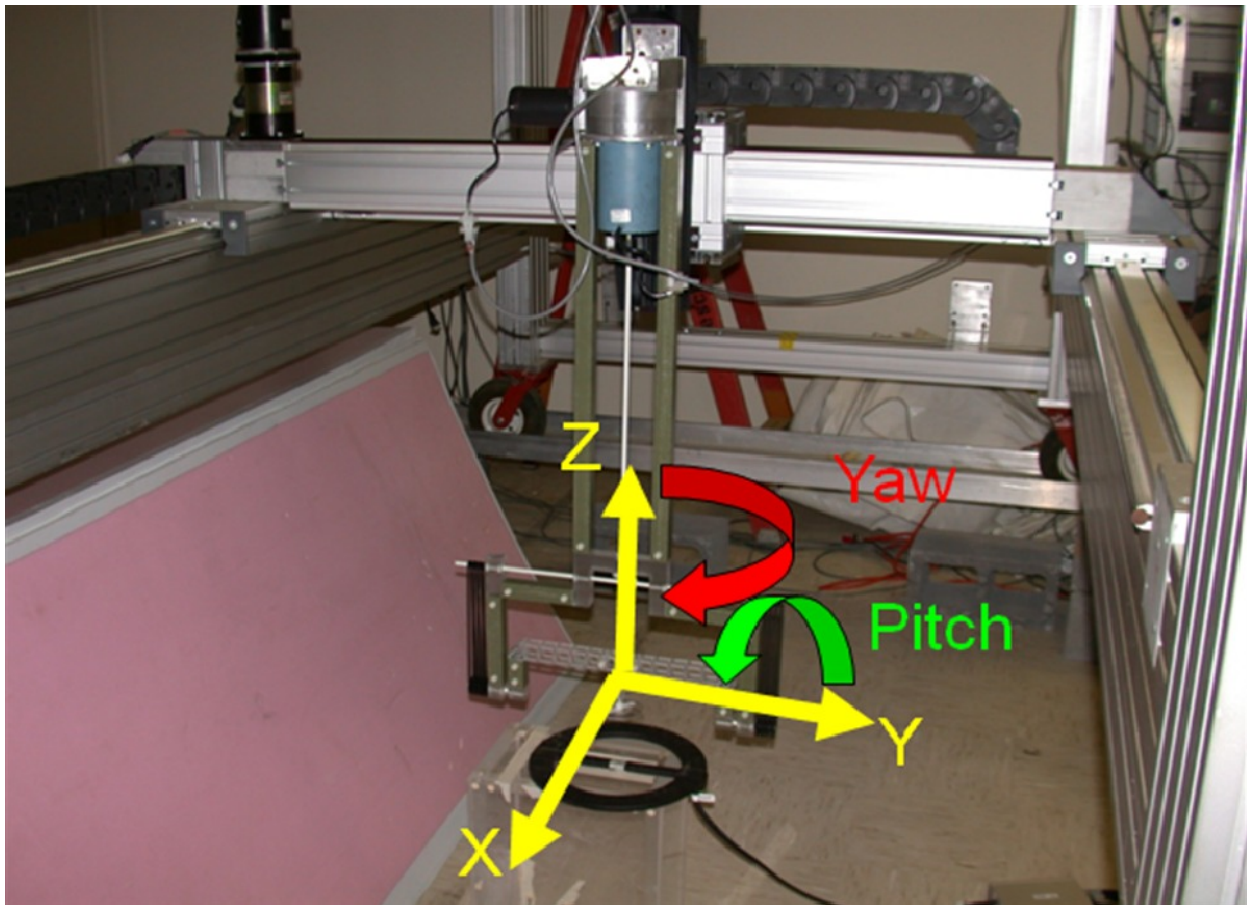


Fig. 3. Experimental measurement facility for EMI target characterization: (a) Automated translational (x , y , and z) and rotational (yaw about z and pitch about y) axes labeled, manual rotational (roll about x) axis not labeled; (b) Single wire loop target shown above single EMI sensor; and (c) Three mutually-orthogonal wire loops target (in inset photograph) shown above EMI sensor array (three EMI sensors).

3. EXPERIMENTAL AND NUMERICAL MEASUREMENTS

Measurements have been conducted of several typical EMI targets including landmines, shell casings, ball bearings, single wire coils, multiple coplanar wire coils, and three mutually orthogonal wire coils. Some targets are included due to practical interests in detection of the targets in the field while some are included for research and development of the EMI sensor hardware. All of the targets are of interest for detection and processing algorithm development efforts. Data from three targets (a single wire loop, a composite target with three mutually orthogonal wire loops, and a 9 mm shell casing) will be presented in this section; the wire loop targets are useful for demonstrating the EMI system performance capabilities while the shell casing has inherent practical interest and a comparatively simple response.

The measured data are filtered in the down-track direction by convolving the measured data with the zero-mean template shown in Figure 4. The filter is used to make the data from the measurement system directly comparable to that of the field systems in which the filter has three beneficial effects. First, it mostly removes the ground response by differencing closely located portions of the ground. Second, it mostly removes the drift in the system by differencing measurements made only a short time apart. Third, it averages the data over several locations which will improve the signal to noise ratio.

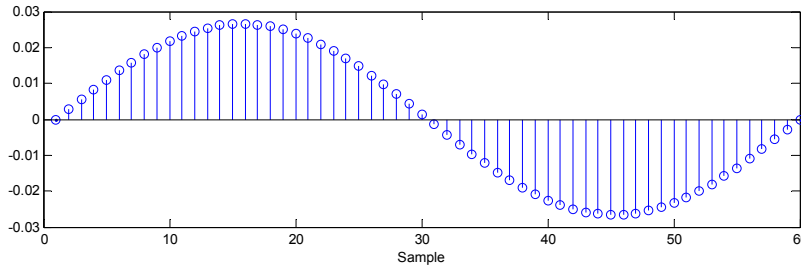


Fig. 4. Filter template.

The first target is a simple loop of 22 AWG copper wire formed into a loop with a circumference of 10 cm which has a theoretical relaxation frequency of 10.0 kHz. The loop is oriented so that its axis is z directed when the yaw and pitch angles are zero as shown on Figure 3b. The magnetic polarizability tensor of the loop is:

$$\mathbf{M}(\omega) = -\frac{\mu_0 A^2}{L} \left(\frac{j\omega/\zeta}{1 + j\omega/\zeta} \right) \begin{bmatrix} 0 & 0 & 0 \\ 0 & 0 & 0 \\ 0 & 0 & 1 \end{bmatrix} \quad (1)$$

where $\zeta = 2\pi f_r$ is the relaxation frequency, A is the area of the loop and, L is the self inductance of the loop. The measured response for the single loop is presented in Figures 5, 6, and 7. In Figure 5a, the magnitude of imaginary part of the response is presented in pseudo-color graphs as a function of x and z at $y=0$ and $f=5,190$ Hz for five pitch angles and three yaw angles. For $pitch = 0^\circ$, the graphs are as expected; the strongest response is at $x = 0$, the response is symmetric about $x = 0$, and the response gets weaker as z increases. For $pitch = 22.5^\circ, 45^\circ$, and 67.5° , the response is no longer symmetric about $x = 0$. For $pitch = 90^\circ$, the response is again symmetric about $x = 0$, but the maximum response is not at $x = 0$, and the response is almost zero when $yaw = 90^\circ$. In Figure 5b, the response computed from a theoretical model is shown which models the loop as in infinitesimal magnetic dipole with the magnetic polarizability tensor on equation 1. The theoretical results are very similar to the measured results.

In Figure 6, Argand diagrams of the response are presented from the experimental measurements and the theoretical model of the single-loop target at $x=0, y=0, z=4.5$ cm for three yaw and five pitch angles. The shape of the response is the same for all the rotation angles while the amplitude of the response changes with rotation angle. This is predicted theoretically since the loop only has a single relaxation.

In Figure 7, the discrete spectrum of relaxation frequencies⁸ of the response from experimental measurements and theoretical model of the single-loop target at $x=0$, $y=0$, $z=4.5\text{cm}$ for three yaw and five pitch angles. Here the data is fit to a relaxation (exponential) model, and the amplitude of each of the relaxation frequencies is plotted as a function of relaxation frequency. This analysis correctly identifies the 10 kHz relaxation frequency at all of the rotation angles except at $\text{pitch} = \text{yaw} = 90^\circ$ where the response is zero. The analysis also shows additional relaxations of very-low amplitude from the experimental data which may be due to secondary relaxations or noise.

The second target consists of three loops of copper wire that are at right angles to each other and is seen on Figure 3c. The magnetic polarizability tensor of the loops is:

$$\mathbf{M}(\omega) = -\frac{\mu_o A_x^2}{L_x} \left(\frac{j\omega / \zeta_x}{1 + j\omega / \zeta_x} \right) \begin{bmatrix} 1 & 0 & 0 \\ 0 & 0 & 0 \\ 0 & 0 & 0 \end{bmatrix} - \frac{\mu_o A_y^2}{L_y} \left(\frac{j\omega / \zeta_y}{1 + j\omega / \zeta_y} \right) \begin{bmatrix} 0 & 0 & 0 \\ 0 & 1 & 0 \\ 0 & 0 & 0 \end{bmatrix} - \frac{\mu_o A_z^2}{L_z} \left(\frac{j\omega / \zeta_z}{1 + j\omega / \zeta_z} \right) \begin{bmatrix} 0 & 0 & 0 \\ 0 & 0 & 0 \\ 0 & 0 & 1 \end{bmatrix} \quad (2)$$

where $\zeta_k = 2\pi f_{rk}$ are the relaxation frequencies, A_k are the areas of the loops and, L_k are the self inductances of the loops with $k = x, y, z$. The parameters for the loops are presented in Table I.

Table I. Parameters for the three-loop target.

Orientation	Diameter (cm)	Wire Gauge (AWG)	Relaxation Freq. (kHz)
x	5	36	10.1
y	4	30	50.2
z	3	22	172

The measured and theoretical responses for the three-loop target are presented in Figures 8, 9, and 10. In Figure 8, the magnitude of imaginary part of the response is presented in pseudo-color graphs as a function of x and z at $y=0$ and $f=5,190\text{ Hz}$ for five pitch angles and three yaw angles. For $\text{pitch} = 0^\circ$ and 90° , the response should be symmetric about $x = 0$; however, the experimental results are slightly asymmetric for $\text{pitch} = 90^\circ$ which is probability due to the target being slightly out of alignment. Otherwise, the experimental and theoretical results are very similar. In Figure 9, Argand diagrams of the response are presented from the experimental measurements and the theoretical model. The shape and amplitude of the response now changes as a function of the rotation angles. This is predicted theoretically since the loop has a different relaxation frequency along each axis. This will make it more challenging to use the shape information for identification of such a complex target. In Figure 10, the discrete spectrum of relaxation frequencies of the response from experimental measurements and theoretical model of the three-loop target. This analysis correctly identifies the three relaxation frequencies of the target. Note the relative amplitude of the relaxations change as a function of the rotation angles. This representation of the data may be helpful for the discrimination of complex targets with unknown orientation.

The third target is a 9 mm shell casing, and its measurements are shown in Figures 11, 12, and 13. It is difficult to see that the response of this target varies with rotation angle from the graphs in Figures 11 and 12, however, the difference is apparent in the graphs in Figure 13. The discrete spectrum of relaxation frequencies for this target consist of three relaxations that have amplitudes that vary with the rotation angles as seen in Figure 13. The magnetic polarizability tensor for this target is unknown but these measurements contain sufficient data to construct it. We plan on deriving the magnetic polarizability tensor in future work.

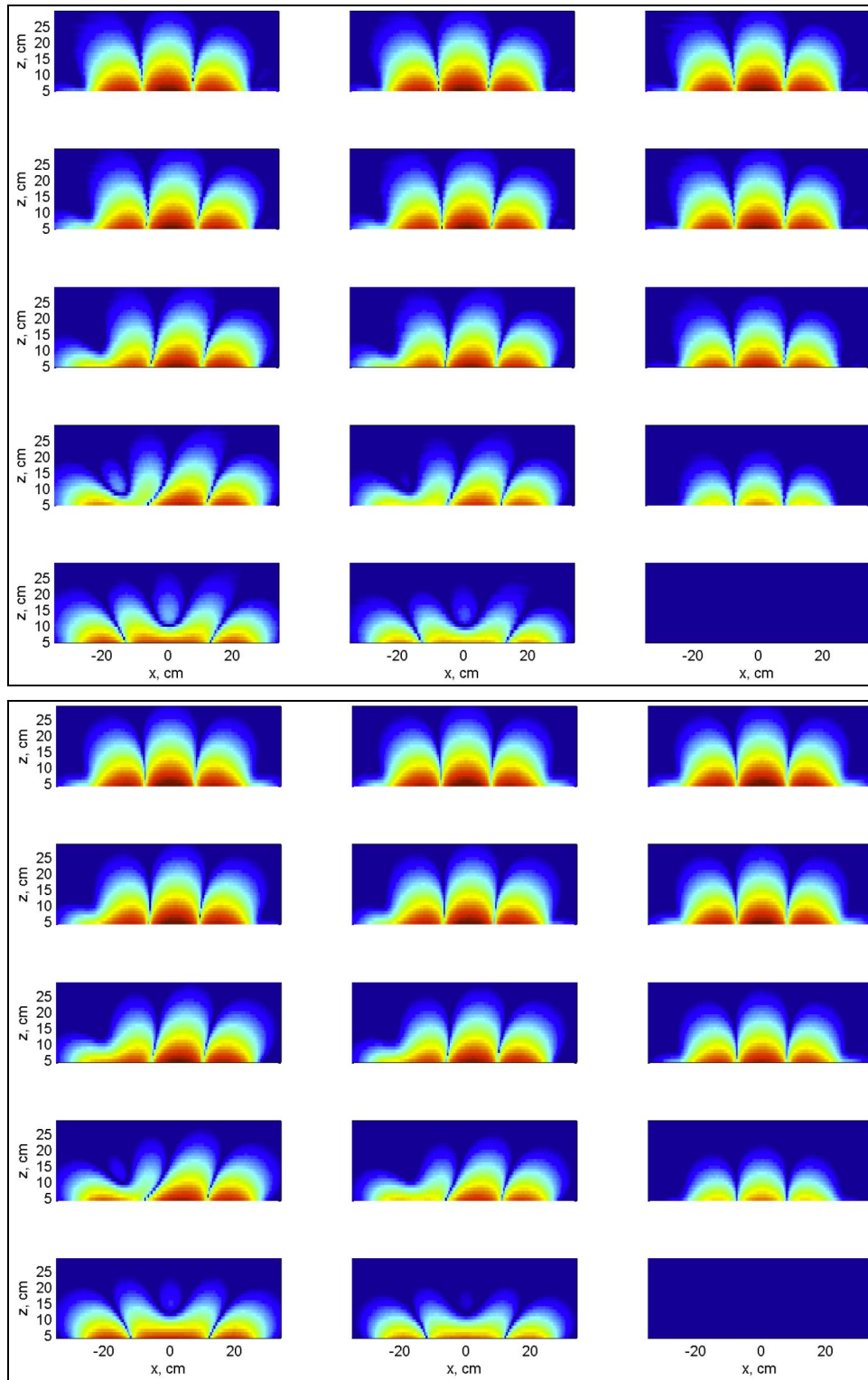


Fig. 5. Pseudo-color graphs of the magnitude of imaginary part of the response for the single-loop target from (a) experimental measurements and (b) theoretical modeling as a function of x and z at $y=0$ and $f=5,190$ Hz. The graphs are on a 60 dB scale using the Matlab jet color map. Pitch angles range from 0° to 90° in 22.5° increments from top to bottom. Yaw angles range from 0° to 90° in 45° increments from left to right in the figure.(color image in electronic version of manuscript)

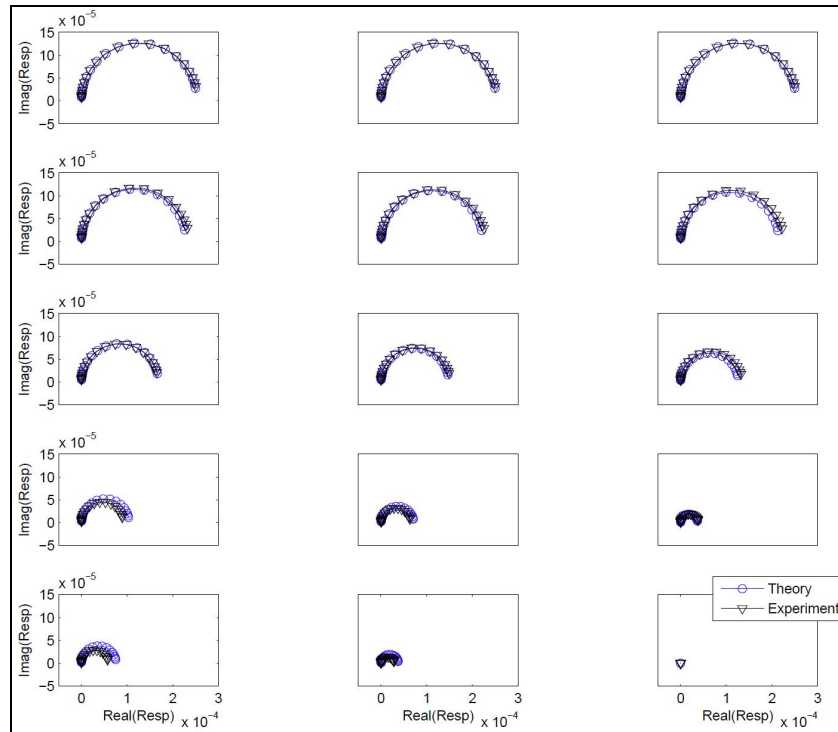


Fig. 6. Argand diagrams of the response from experimental measurements and theoretical modeling of the single-loop target at $x=0$, $y=0$, $z=4.5\text{cm}$ for three yaw and five pitch angles. Pitch angles range from 0° to 90° in 22.5° increments from top to bottom. Yaw angles range from 0° to 90° in 45° increments from left to right in the figure.

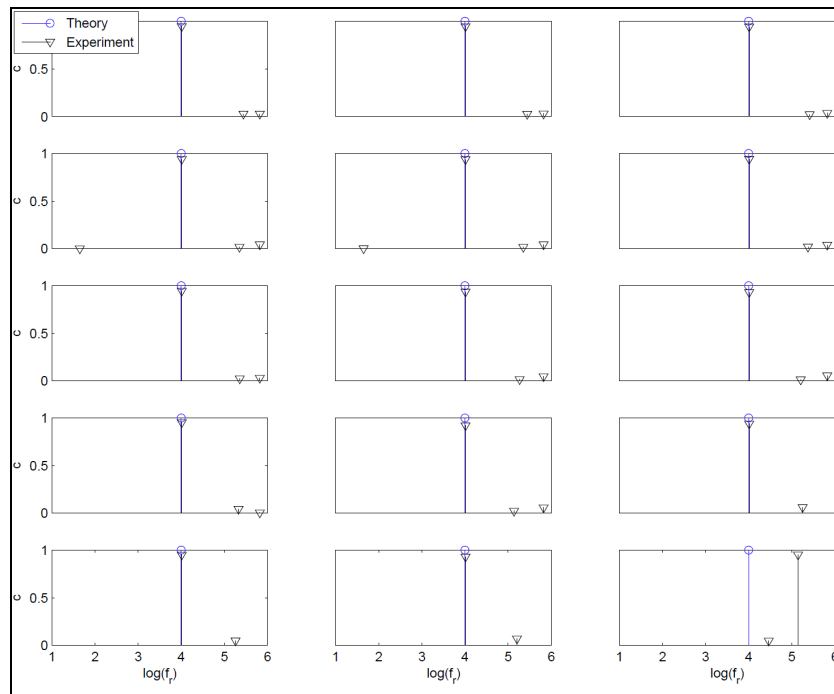


Fig. 7. Graphs of the discrete spectrum of relaxation frequencies of the response from experimental measurements and theoretical modeling of the single-loop target at $x=0$, $y=0$, $z=4.5\text{cm}$ for three yaw and five pitch angles. Pitch angles range from 0° to 90° in 22.5° increments from top to bottom. Yaw angles range from 0° to 90° in 45° increments from left to right in the figure.

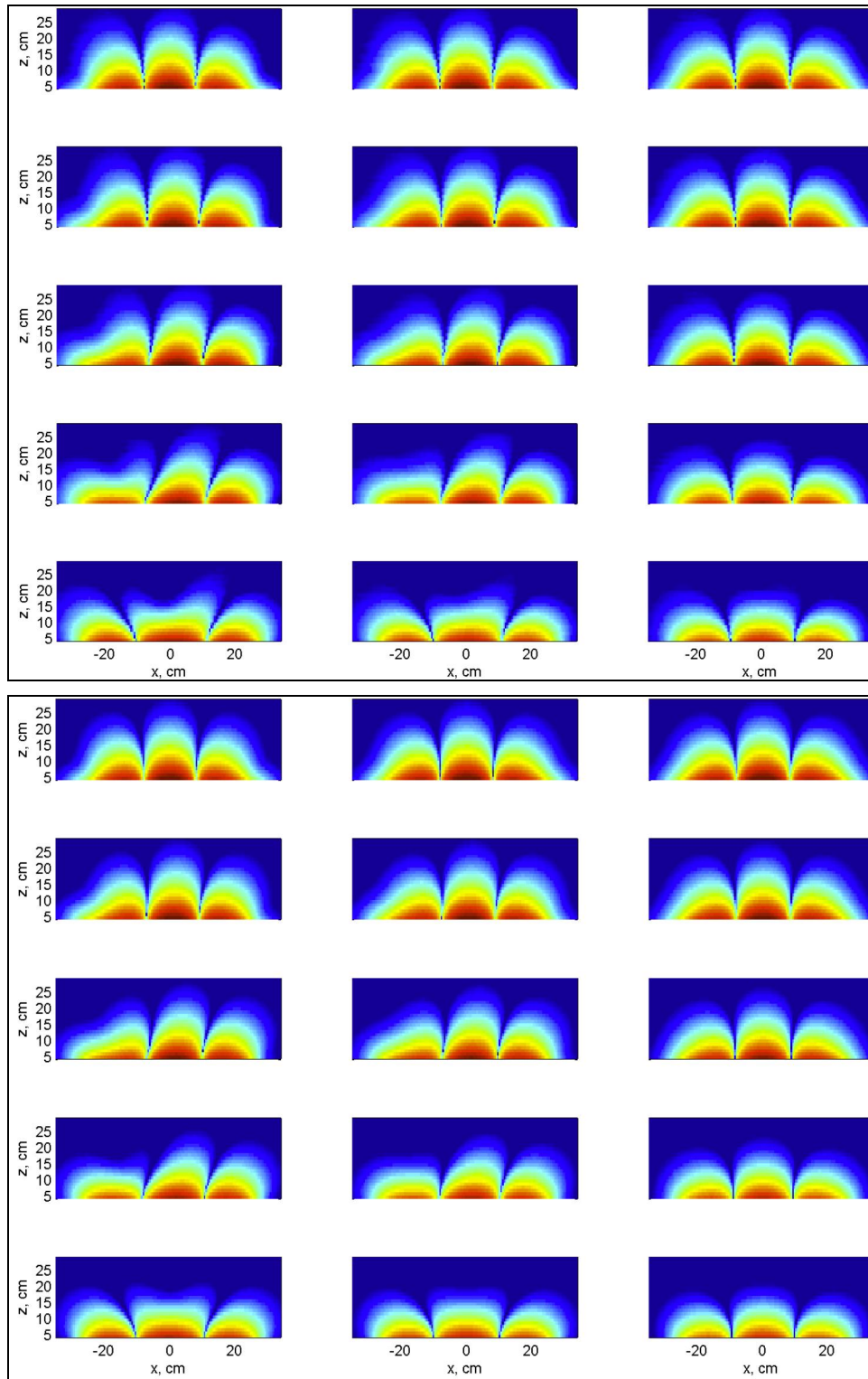


Fig. 8. Pseudo-color graphs of the magnitude of imaginary part of the response from (a) experimental measurements and (b) theoretical modeling for the three-loop target as a function of x and z at $y=0$ and $f=5,190$ Hz. The graphs are on a 60 dB scale using the Matlab jet color map. Pitch angles range from 0° to 90° in 22.5° increments from top to bottom. Yaw angles range from 0° to 90° in 45° increments from left to right in the figure. (color image in electronic version of manuscript)

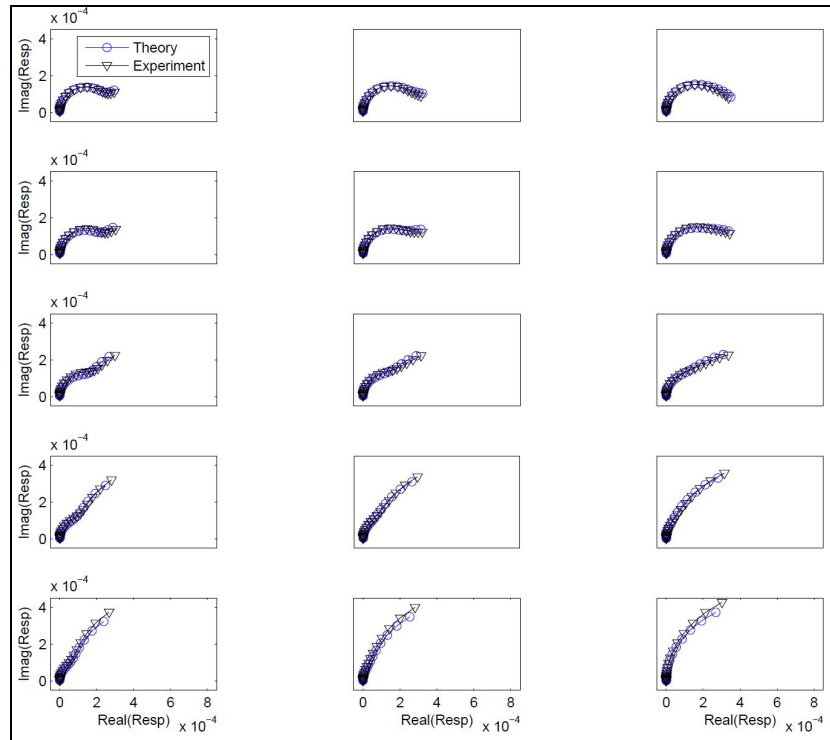


Fig. 9. Argand diagrams of the response from experimental measurements and theoretical modeling of the three-loop target at $x=0$, $y=0$, $z=4\text{cm}$ for three yaw and five pitch angles. Pitch angles range from 0° to 90° in 22.5° increments from top to bottom. Yaw angles range from 0° to 90° in 45° increments from left to right in the figure.

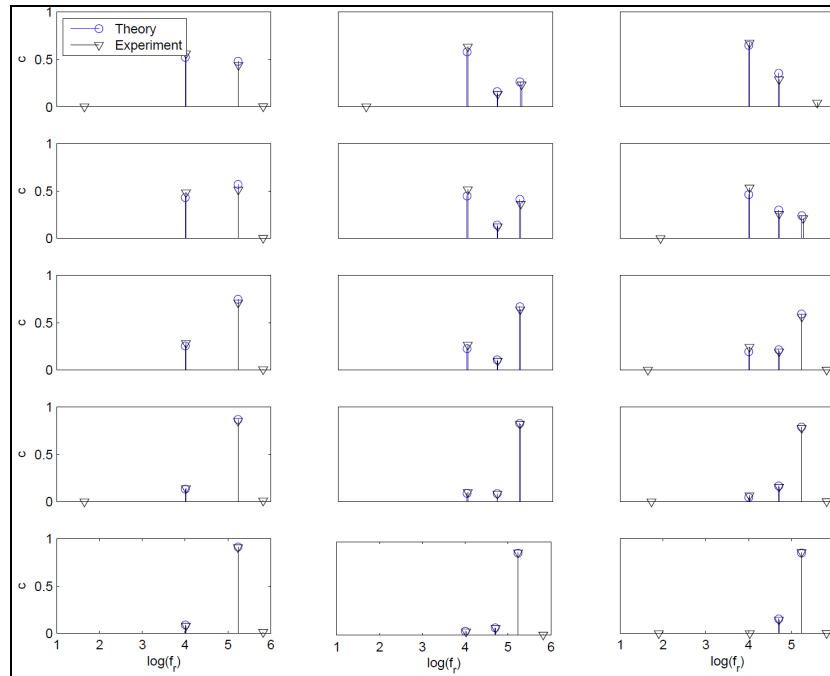


Fig. 10. Graphs of the discrete spectrum of relaxation frequencies of the response from experimental measurements and theoretical modeling of the three-loop target at $x=0$, $y=0$, $z=4\text{cm}$ for three yaw and five pitch angles. Pitch angles range from 0° to 90° in 22.5° increments from top to bottom. Yaw angles range from 0° to 90° in 45° increments from left to right in the figure.

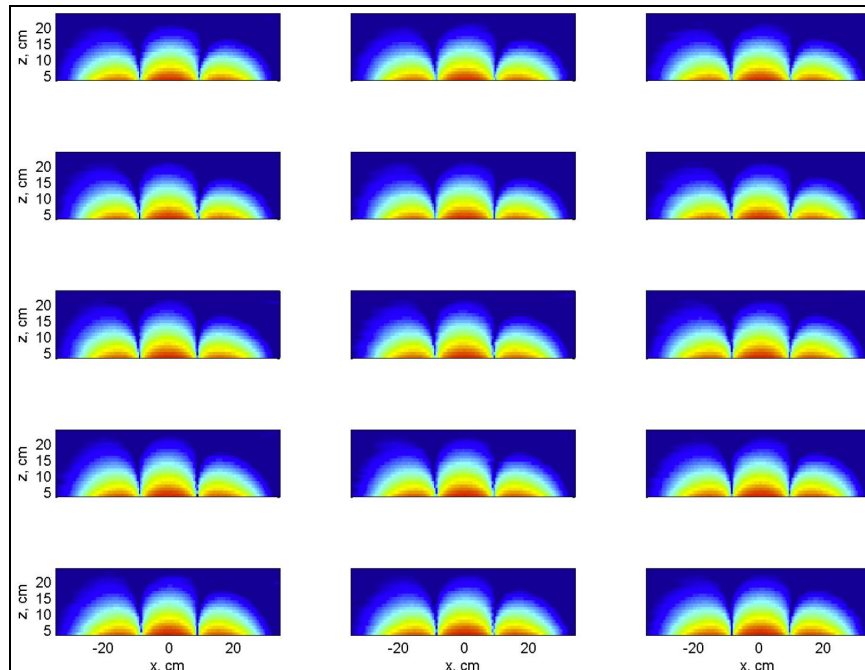


Fig. 11. Pseudo-color graphs of the magnitude of imaginary part of the response from experimental measurements of a 9 mm shell casing as a function of x and z at $y=0$ and $f=5,190$ Hz. The graphs are on a 60 dB scale using the Matlab jet color map. Pitch angles range from 0° to 90° in 22.5° increments from top to bottom. Yaw angles range from 0° to 90° in 45° increments from left to right in the figure. (color image in electronic version of manuscript)

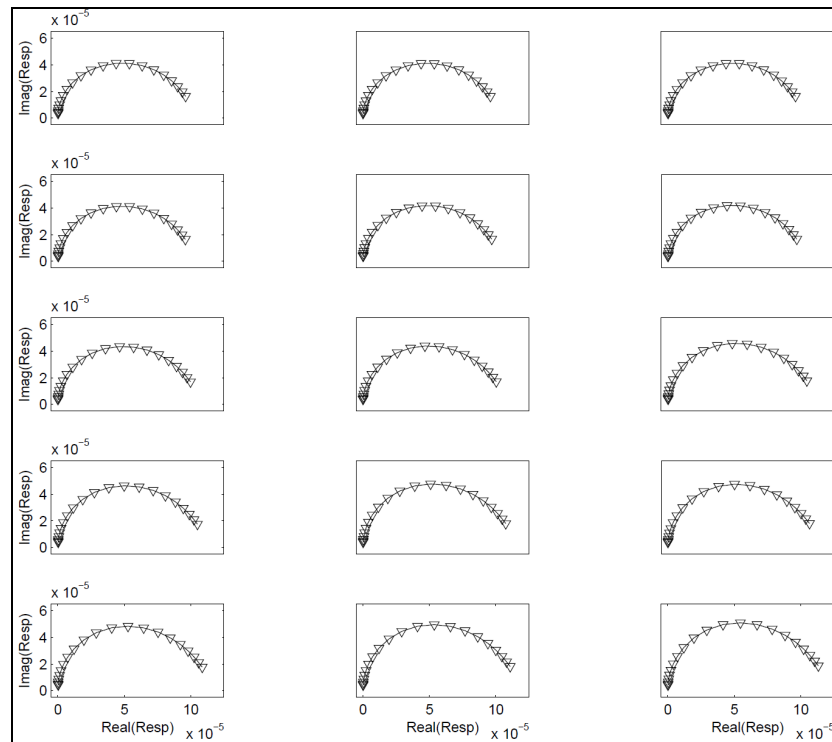


Fig. 12. Argand diagrams of the response from experimental measurements of a 9 mm shell casing at $x=0$, $y=0$, $z=3.2$ cm for three yaw and five pitch angles. Pitch angles range from 0° to 90° in 22.5° increments from top to bottom. Yaw angles range from 0° to 90° in 45° increments from left to right in the figure.

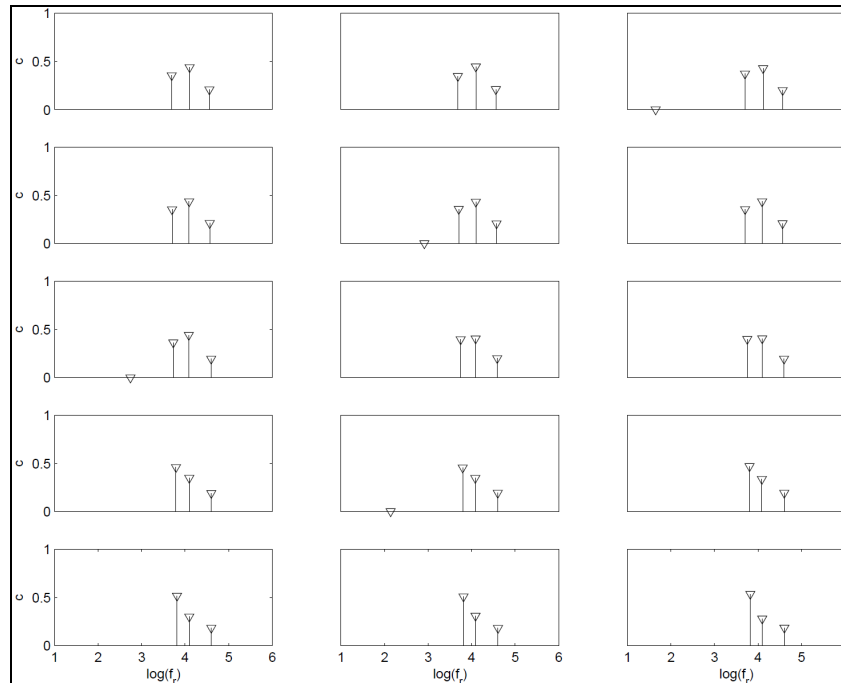


Fig. 13. Graphs of the discrete spectrum of relaxation frequencies of the response of a 9 mm shell casing at $x=0$, $y=0$, $z=3.2\text{cm}$ for three yaw and five pitch angles. Pitch angles range from 0° to 90° in 22.5° increments from top to bottom. Yaw angles range from 0° to 90° in 45° increments from left to right in the figure.

4. CONCLUSIONS

A new experimental facility has been established to measure the response of typical targets for EMI sensors as a function of location and orientation. This has been accomplished with a six-degree of freedom positioning system with five automated axes (the three translational axes and two rotational axes) and one manual axis. The EMI sensors are held fixed while targets are oriented using the rotational axes and then moved along a prescribed path through the measurement volume. Commercially available hardware has been used for the translational stages and one rotational stage while a custom-built rotational stage has been assembled to eliminate metal from the measurement region.

Measurements with this system provide a complete characterization of the targets for comparison to field measurements as well as with numerical modeling of EMI sensors for further hardware development. This type of data may also be used in the development of detection algorithms for EMI sensors. Future efforts with the experimental facility will include measurements of more targets and investigations of methods for summarizing the massive amounts of collected data into simple physical models. Further development of the processing algorithms will be done to help characterize more complicated targets and refine detection and discrimination methods for EMI sensors.

ACKNOWLEDGMENTS

This work is supported in part by the US Army Night Vision and Electronic Sensors Directorate, Science and Technology Division, Countermines Branch and in part by the U. S. Army Research Office under Contract Number W911NF-05-1-0257.

REFERENCES

1. Scott, W.R., Jr., "Broadband electromagnetic induction sensor for detecting buried landmines," *Proceedings of the 2007 IEEE Geoscience and Remote Sensing Symposium*, Barcelona, Spain, July 2007.
2. Scott, W. R., Jr., "Broadband Array of Electromagnetic Induction Sensors for Detecting Buried Landmines," *IGARSS 2008*, Vol. II, pp. 375-378.
3. P. Gao, L. Collins, P.M. Garber, N. Geng, and L. Carin, "Classification of Landmine-Like Metal Targets Using Wideband Electromagnetic Induction," *IEEE Transactions on Geoscience and Remote Sensing*, Vol. 38, No. 3, May 2000.

4. L. Collins, P. Gao, and L. Carin, "An Improved Bayesian Decision Theoretic Approach for Land Mine Detection," *IEEE Transactions on Geoscience and Remote Sensing*, Vol. 37, No. 2, March 1999.
5. G. D. Sower and S. P. Cave, "Detection and identification of mines from natural magnetic and electromagnetic resonances," in *Proc. SPIE*, Orlando, FL, 1995.
6. C. E. Baum, "Low Frequency Near-Field Magnetic Scattering from Highly, but Not Perfectly Conducting Bodies," Phillips Laboratory, *Interaction Note* 499, Nov. 1993.
7. E.B. Fails, P.A. Torriane, W. R. Scott, Jr, and L.M. Collins, "Performance of a four parameter model for modeling landmine signatures in frequency domain wideband electromagnetic induction detection systems," *Proceedings of the SPIE: 2007*, Vol. 6553, Orlando, FL, May 2007.
8. M. H. Wei, W. R. Scott, Jr., and J. H. McClellan, "Robust Estimation of The Discrete Spectrum of Relaxations for Electromagnetic Induction Responses," *submitted for publication in IEEE Transactions on Geoscience and Remote Sensing*.

APPLICATION OF ℓ_p -REGULARIZED LEAST SQUARES FOR $0 \leq p \leq 1$ IN ESTIMATING DISCRETE SPECTRUM MODELS FROM SPARSE FREQUENCY MEASUREMENTS

Mu-Hsin Wei, James H. McClellan, and Waymond R. Scott, Jr.

Georgia Institute of Technology
School of Electrical and Computer Engineering
777 Atlantic Drive NW, Atlanta, GA 30332-0250

ABSTRACT

It is difficult to robustly estimate the parameters of an additive exponential model from a small number of frequency-domain measurements, especially when the model order is unknown and the parameters must be constrained to be real. Recent work in sparse sampling and sparse reconstruction casts this problem as a linear dictionary selection problem by densely sampling the parameter space. We present a modified ℓ_p -regularized least squares algorithm, for $0 \leq p \leq 1$, and show that it is effective when the frequency sampling is sparse over a couple of decades and the parameters must be estimated over more than four decades. An empirical method for choosing the regularization parameter is also studied. Using tests on synthetic data and laboratory measurements for an EMI application, the proposed method is shown to provide robust estimates of the model parameters up to eighth order.

Index Terms— Parameter estimation, ℓ_1 minimization, sum of exponentials, basis pursuit.

1. INTRODUCTION

Additive exponential models are commonly used in science and engineering to model a wide range of physical phenomena such as the eddy currents for electromagnetic induction (EMI), dielectric material properties in polymer science, and many others in the fields of chemistry, biology, and speech, to name a few. It can be difficult to extract the model parameters from measurements when the number of parameters is more than a few, when the model order is unknown, or when the number of measurements is very small. Furthermore, when the measurements are made in the frequency domain and the exponential parameters must be real, very few techniques exist to solve the resulting constrained estimation problem. In [1] we developed a constrained linear least-squares method to estimate these models when the parameters are nonnegative, and demonstrated the utility and robustness of this algo-

rithm for wideband EMI systems. The method uses 21 measurements, equi-spaced in the *logarithmic* frequency domain, taken over a range of 2.5 decades, and estimates parameter values over 4.17 decades. We have tested this method on synthetic data and lab data, and have shown that it can reliably extract models. Recently, Austin *et al.* [2] studied parameter estimation for additive models through sparse sampling and reconstruction. They formulated a linear problem by enumerating an overcomplete dictionary of possible models. Then they proposed a sparse nonuniform sampling strategy based on the Fisher information, and demonstrated their method on a time-domain sum-of-exponentials model.

In this paper, we extend the frequency-domain technique [1] to remove the nonnegative constraint. We linearize the estimation problem with a dictionary as in [1, 2], and solve it with ℓ_p -regularized least squares for $0 \leq p \leq 1$. We exploit the fact that after linearizing the problem the solution vector is most likely sparse, and we show that a log-frequency sampling scheme performs nearly the same as one based on Fisher information. The proposed method requires no prior knowledge of the model order K and always returns real parameters. We demonstrate its robustness with results on synthetic and laboratory data, even when using high model orders and frequencies measured over several decades.

2. ESTIMATION METHOD

The EMI frequency response $H(\omega)$ of a metallic target, which is proportional to a projection of the magnetic polarizability tensor of the target, can be expressed as [3]:

$$H(\omega) = c_0 + \sum_{k=1}^K \frac{c_k}{1 + j\omega/\zeta_k} \quad (1)$$

where c_0 is the shift, K the model order, c_k the real spectral amplitudes, and ζ_k the relaxation frequencies. The parameter set $S = \{(\zeta_k, c_k) : k = 1 \dots K\}$ is called the Discrete Spectrum of Relaxation Frequencies (DSRF); each pair (ζ_k, c_k) is one relaxation. The term DSRF and spectrum will be used interchangeably.

This work is supported in part by the US Army REDCOM CERDEC Night Vision and Electronic Sensors Directorate, Science and Technology Division, Countermine Branch and in part by the U. S. Army Research Office under Contract Number W911NF-05-1-0257.

It is advantageous to model the EMI signal with (1) because the relaxation frequencies are invariant to target orientation, which is valuable in target detection. However, it is difficult in practice to obtain the model parameters in (1) from a small number of measurements. For most existing estimation methods, a good guess of the model order K is required for the fitting process to converge. Prior knowledge of K , however, is usually unavailable. The highly correlated summands in (1) and the nonlinear relation between $H(\omega)$ and ζ_k also make estimation difficult. Most existing methods often give sub-optimal solutions that are far from the truth, or return complex parameters that do not have physical meaning [4].

When the target response is measured at N distinct frequencies, (1) can be written in matrix form:

$$\begin{bmatrix} H(\omega_1) \\ H(\omega_2) \\ \vdots \\ H(\omega_N) \end{bmatrix} = \underbrace{\begin{bmatrix} 1 & \frac{1}{1+j\omega_1/\zeta_1} & \frac{1}{1+j\omega_1/\zeta_2} & \cdots & \frac{1}{1+j\omega_1/\zeta_K} \\ 1 & \frac{1}{1+j\omega_2/\zeta_1} & \frac{1}{1+j\omega_2/\zeta_2} & \cdots & \frac{1}{1+j\omega_2/\zeta_K} \\ \vdots & \vdots & \vdots & \ddots & \vdots \\ 1 & \frac{1}{1+j\omega_N/\zeta_1} & \frac{1}{1+j\omega_N/\zeta_2} & \cdots & \frac{1}{1+j\omega_N/\zeta_K} \end{bmatrix}}_{\mathbf{Z}} \begin{bmatrix} c_0 \\ c_1 \\ c_2 \\ \vdots \\ c_K \end{bmatrix} \quad (2)$$

$$\mathbf{h} = \mathbf{Z}\mathbf{c}$$

where $\omega_{\min} = \omega_1 < \omega_2 < \cdots < \omega_N = \omega_{\max}$, \mathbf{h} is the observation vector, \mathbf{c} the spectral amplitude vector augmented by the shift c_0 , and \mathbf{Z} a matrix containing information about the relaxation frequencies ζ .

To estimate the DSRF (i.e., ζ_k and c_k) from a given observation \mathbf{h} , the usual approach is to minimize the norm of the error, but this leads to a *nonlinear* optimization problem. Instead, we follow the strategy of basis pursuit to linearize the problem with an overcomplete dictionary. The overcomplete dictionary is a matrix $\tilde{\mathbf{Z}}$ that has the same form as \mathbf{Z} in (2), but with many more columns. To generate the columns, we enumerate a large set of M possible relaxation frequencies uniformly distributed in the log- ζ space ($M \gg K$), and create one column for each enumerated ζ [1]. Compared to the non-uniform sampling [2] based on the Fisher information where the step size is given by

$$\Delta(\tilde{\zeta}_m) = \alpha \left[\sum_{n=1}^N \left(\frac{\omega_n}{\omega_n^2 + \tilde{\zeta}_m^2} \right)^2 \right]^{-\frac{1}{2}}$$

the uniform log- ζ sparse sampling gives similar sample points (Fig. 1).

Since the dictionary matrix $\tilde{\mathbf{Z}}$ has $(M+1)$ columns, we redefine the unknown as an $(M+1)$ -element *weighted selector vector* $\tilde{\mathbf{c}}$ and rewrite the problem as:

$$\mathbf{h} = \tilde{\mathbf{Z}}\tilde{\mathbf{c}} + \text{error} \quad (3)$$

The vector $\tilde{\mathbf{c}}$ contains the shift estimator \tilde{c}_0 followed by the spectral amplitude estimators \tilde{c}_m . We expect the solution for $\tilde{\mathbf{c}}$ to have many zero elements because $M \gg K$, i.e., $\tilde{\mathbf{c}}$ will be

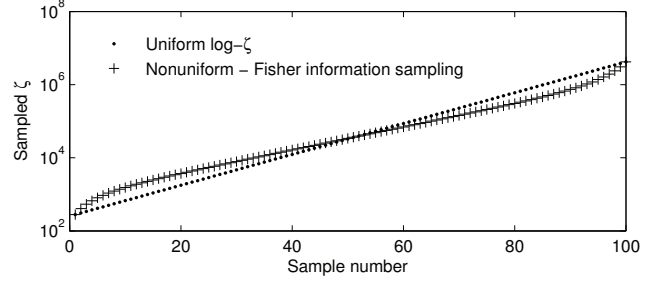


Fig. 1. Samples generated from uniform log- ζ sampling and non-uniform sampling based on the Fisher information.

sparse. We utilize the ℓ_p -regularized least squares technique, for $0 \leq p \leq 1$, because it promotes sparse solutions.

$$\arg \min_{\tilde{\mathbf{c}}} \|\tilde{\mathbf{Z}}'\tilde{\mathbf{c}} - \mathbf{h}'\|_2^2 + \lambda \|\tilde{\mathbf{c}}\|_p^p, \quad 0 \leq p \leq 1 \quad (4)$$

$$\text{where } \tilde{\mathbf{Z}}' = \begin{bmatrix} \Re(\tilde{\mathbf{Z}}) \\ \Im(\tilde{\mathbf{Z}}) \end{bmatrix} \text{ and } \mathbf{h}' = \begin{bmatrix} \Re(\mathbf{h}) \\ \Im(\mathbf{h}) \end{bmatrix}$$

where λ is the regularization parameter. Separating the real and imaginary parts in $\tilde{\mathbf{Z}}$ makes the whole system real. Ideally, in the best selected $\tilde{\mathbf{c}}$, only those \tilde{c}_m with corresponding $\tilde{\zeta}_m$ that are near a true ζ_k will be nonzero, and they will take on the correct spectral amplitudes c_k . It follows that a DSRF can then be deduced from the nonzero estimated \tilde{c}_m and their corresponding $\tilde{\zeta}_m$.

The ℓ_p -regularized least squares for $p < 1$ can be approximated by the iteratively reweighted ℓ_1 algorithm proposed by Candès *et al.* [5]. The weights are updated as suggested in [6]. We also adopt the ϵ -regularization technique used in the same paper. In summary, (4) is approximated by (see also [7]):

Algorithm 1: Approximated ℓ_p -regularized least square

Input: $\tilde{\mathbf{Z}}', \mathbf{h}', p, \lambda, \tilde{\mathbf{c}}^0$

- 1 $\tilde{\mathbf{c}}^n \leftarrow \tilde{\mathbf{c}}^0$
- 2 **for** $k \leftarrow 0$ **to** -8 **step** -1 **do**
- 3 $\epsilon \leftarrow 10^k$
- 4 **repeat**
- 5 $\tilde{\mathbf{c}}^{n-1} \leftarrow \tilde{\mathbf{c}}^n$
- 6 $w_i^n \leftarrow (|\tilde{c}_i^{n-1}| + \epsilon)^{p-1}$
- 7 $\tilde{\mathbf{c}}^n \leftarrow \arg \min \|\tilde{\mathbf{Z}}'\tilde{\mathbf{c}} - \mathbf{h}'\|_2^2 + \lambda \sum_{i=1}^{M+1} w_i^n |\tilde{c}_i|$
- 8 **until** $\|\tilde{\mathbf{c}}^n - \tilde{\mathbf{c}}^{n-1}\|_2 < \sqrt{\epsilon}/100$
- 9 **return** $\tilde{\mathbf{c}}^n$

The ℓ_1 minimization problem is solved by **11.15s**, a MATLAB optimizer proposed by Kim *et al.* [8]. We have also found that normalizing the input data \mathbf{h} , as well as the columns of $\tilde{\mathbf{Z}}'$ to have unit ℓ_2 norm increases the accuracy of estimation. Setting entries of $\tilde{\mathbf{c}}^0$ to all ones also seems to be effective. The nonzero entries of $\tilde{\mathbf{c}}$ selected by (4) are the relaxations need in the estimated DSRF, $\hat{S} = \{(\hat{\zeta}_l, \hat{c}_l) : l = 1 \dots L\}$.

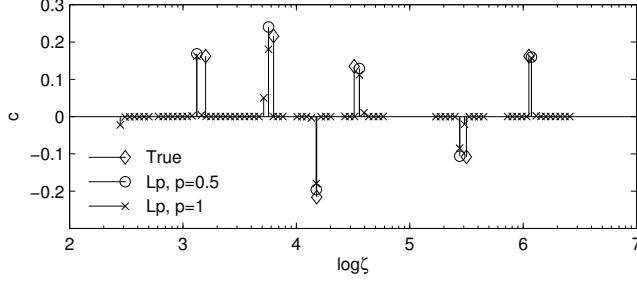


Fig. 2. Estimation of a synthetic six-relaxation DSRF. $p = 0.5$.

3. ESTIMATION RESULTS

The proposed estimation method is tested against synthetic and laboratory data to show its functionality, accuracy, and stability. The hardware system used is a wideband EMI sensor operating at 21 frequencies approximately logarithmically distributed over the range 300 Hz–90 kHz (2.5 decades) [9]. The synthetic data is generated in accordance with the hardware specification. The range of ζ for estimation is chosen such that $\log(\zeta_{\min})$ and $\log(\zeta_{\max})$ are 2.45 and 6.62, respectively, i.e., 4.17 decades. All estimations are performed with $M = 100$, and all presented spectra are normalized such that $\sum_{i=1} |c_i| = 1$. Spectral amplitudes less than 10^{-5} are not displayed. Unless specified, $p = 0.5$ is chosen as a representative case. The choice of λ is discussed in Section 4.

Notation: ζ and c are the true/theoretical relaxation frequencies and spectral amplitudes; $\hat{\zeta}$ and \hat{c} are the estimates.

3.1. Dissimilarity Measure Between Two DSRFs

In order to evaluate the goodness of the estimate, we need to define a measure of dissimilarity that is appropriate for sparse spectra with multiple peaks. We use the Earth Mover's Distance (EMD) [10] which quantifies the “amount of work” to morph one spectrum into the other. Strictly speaking the EMD is only defined for positive spectra, but we can account for negative spectral amplitudes by defining the distance function between two relaxations (ζ_i, c_i) and $(\hat{\zeta}_j, \hat{c}_j)$ to be:

$$d_{ij} = \begin{cases} |\log \zeta_i - \log \hat{\zeta}_j| & , c_i \hat{c}_j \geq 0 \\ 1 + |\log \zeta_i - \log \hat{\zeta}_j| & , c_i \hat{c}_j < 0 \end{cases}$$

which penalizes relaxations with different signs. Spectra are made nonnegative and normalized prior to the EMD computation. Notice that the EMD has units of decades.

3.2. Synthetic Six-relaxation DSRF

We test our method on a six-relaxation DSRF synthesized at 65 dB SNR with AWGN (Fig. 2). This is a case that cannot be handled by traditional nonlinear parameter optimization which tends to return complex-valued estimates [4]. Using $p = 0.5$, all six relaxation frequencies are recovered by

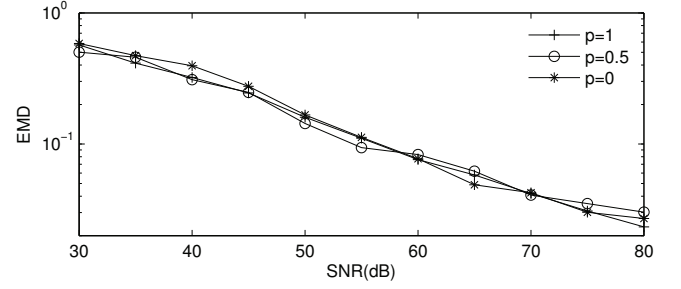


Fig. 3. Monte Carlo simulation on goodness of estimation vs. SNR performed on a four-relaxation DSRF. Sample size is 100 per SNR.

solving (4). Though the estimation is not perfect, it is nevertheless satisfactory. The estimated model parameters are real, and the deviation from truth is small. The EMD between the estimated and the true DSRF is 0.09 decades. The estimate using $p = 1$ is also shown in Fig. 2. It is less sparse, but its EMD is still small, 0.10 decades. Satisfactory estimates are also observed for model orders up to eight.

3.3. Signal to Noise Ratio

To see how the proposed method performs in noise, a Monte Carlo simulation versus SNR is run for several p 's. The true spectrum is a target with a four-relaxation DSRF including negative relaxations. The simulation result, shown in Fig. 3, shows the robustness of the estimation method at different signal-to-noise ratios. For all p 's, the EMD between the estimate and the truth increases as the SNR decreases. This suggests that the proposed method is functional in a range of SNR where the EMD is below some threshold. This threshold, however, depends on the application of the estimated spectrum. For example, if the DSRF produces features for classification, a more robust classifier may tolerate worse estimations and, therefore, allow lower SNR. It seems $p < 1$ offers performance similar to that of $p = 1$, but $p < 1$ does give sparser estimates as demonstrated above. The sparsity, however, is not reflected in the EMD measure.

3.4. Two Coplanar Coaxial Circular Loops

For laboratory data, a target with two coplanar coaxial circular loops of copper wire was constructed. The circumferences of the two loops were chosen to be 200 mm and 150 mm. The larger loop has a wire radius of 0.06 mm, and the smaller one of 0.32 mm. The EMI response of this target was measured in the laboratory and is shown in Fig. 4(a), and the estimated and theoretical DSRF are displayed in Fig. 4(b).

The estimated DSRF deviates from the theory with an EMD of 0.04 decades. We believe the extra estimated relaxation and the deviation is mostly due to the thin-wire approximation used in the theory [1]. The measured frequency response itself deviates from the theory slightly, but the devia-

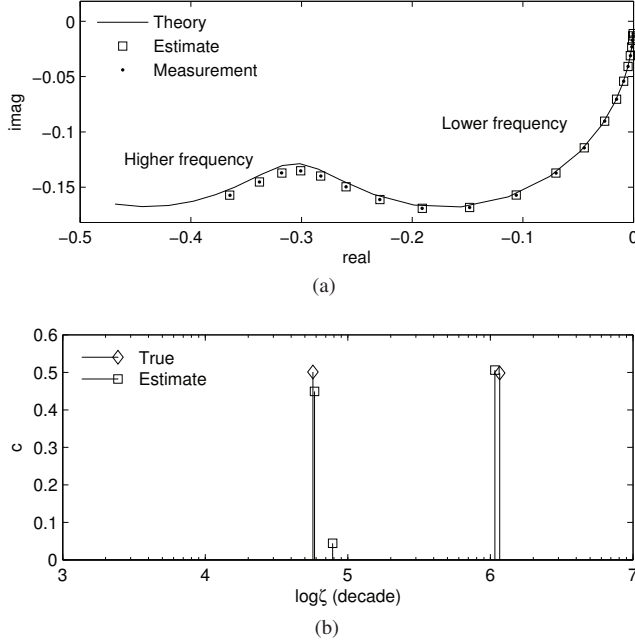


Fig. 4. (a) Laboratory measured frequency response of two coplanar coaxial circular loops. Responses are normalized such that $\|\mathbf{h}\|_2 = 1$. (b) Theoretical and estimated DSRF. $\log \zeta_k$ and c_k are (4.76 6.07) and (0.50 0.50), respectively. $\log \hat{\zeta}_l$ and \hat{c}_l are (4.77 4.89 6.03) and (0.45 0.04 0.51), respectively.

tion is small. We conclude that this estimated DSRF correctly represents the physical DSRF of the target.

4. CHOOSING λ

We propose an empirical method to find the best λ in (4) as a function of SNR. First, we build a collection of synthetic spectra with different model orders and a wide variety of distributions of relaxations. For each spectrum at a fixed SNR, the spectrum is estimated with different λ 's, and then the λ that gives the smallest error (EMD) is recorded. This is done for a range of SNR and is repeated 100 times to obtain an average. The result shown in Fig. 5 is for the case $p = 0.5$. The EMD plays an important role in finding the best λ when there are many peaks in the spectrum because it combines all the spectrum deviations into one number. Some authors only count the number of perfect reconstructions when evaluating the goodness of fit, but imperfect estimates are often acceptable and some level of error always occurs, especially for ill-conditioned dictionaries.

Surprisingly, for each spectrum, the best λ has a simple relationship with the SNR: $\log \lambda$ is linear vs. SNR. We can, therefore, choose the best λ based on the SNR through a simple linear equation such as (5). Although targets of different model orders have different lines of best λ , we have observed that the minimum EMD is not highly sensitive to the exact choice of λ ; changing by one or two decades gives an error

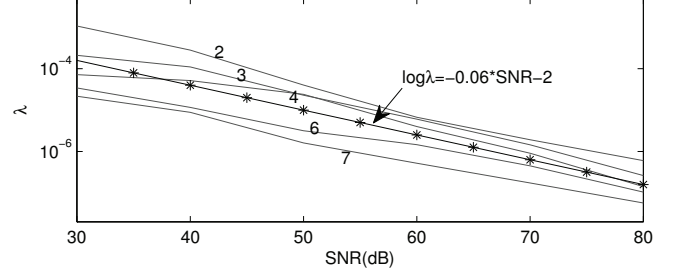


Fig. 5. Best λ vs. SNR for spectra of various model order. The line with markers is chosen to represent the best λ for all model orders.

very close to the minimum. As a result, there is some freedom in choosing the best λ in a practical application. For our problem setup, the λ is chosen by

$$\log \lambda = -0.06 \cdot \text{SNR} - 2 \quad (5)$$

The same empirical method can be repeated for other p 's, and the result is also a linear relationship between $\log \lambda$ and SNR. With field data we use (5) along with an estimate of the SNR to determine λ for use in **Algorithm 1**.

5. REFERENCES

- [1] M. Wei, W. R. Scott, Jr., and J. H. McClellan, "Robust estimation of the discrete spectrum of relaxations for electromagnetic induction responses," *IEEE Trans. Geosci. Remote Sens.*, to be published, Feb. 2010.
- [2] C. D. Austin, E. Ertin, J. N. Ash, and R. L. Moses, "On the relation between sparse sampling and parametric estimation," in *Proc. DSP Workshop*, 2009.
- [3] C. E. Baum, "On the singularity expansion method for the solution of electromagnetic interaction problems," Interaction Notes 88, Air Force Weapons Laboratory, 1971.
- [4] Y. Das and J. E. McFee, "Limitations in identifying objects from their time-domain electromagnetic induction response," in *Proc. SPIE*, 2002.
- [5] E. J. Candès, M. B. Wakin, and S. P. Boyd, "Enhancing sparsity by reweighted ℓ_1 minimization," *J. Fourier Anal. Appl.*, vol. 14, no. 5, pp. 877–905, 2008.
- [6] R. Chartrand and W. Yin, "Iteratively reweighted algorithms for compressive sensing," in *ICASSP*, Las Vegas, NV, Mar. 2008, pp. 3869–3872.
- [7] M. A. T. Figueiredo and R. D. Nowak, "A bound optimization approach to wavelet-based image deconvolution," in *ICIP*, Genoa, Italy, 2005, vol. 2, pp. 782–785.
- [8] S. J. Kim, K. Koh, M. Lustig, and S. Boyd, "An efficient method for compressed sensing," in *ICIP*, San Antonio, TX, 2007, vol. 3, pp. 117–120.
- [9] W. R. Scott, Jr., "Broadband array of electromagnetic induction sensors for detecting buried landmines," in *Proc. IGARSS*, Boston, MA, July 2008.
- [10] Y. Rubner, C. Tomasi, and L. J. Guibas, "A metric for distributions with applications to image databases," in *Proc. ICCV*, Bombay, India, Jan. 1998, pp. 59–66.

MODELING THE MEASURED EM INDUCTION RESPONSE OF TARGETS AS A SUM OF DIPOLE TERMS EACH WITH A DISCRETE RELAXATION FREQUENCY

Waymond R. Scott, Jr.^{*} and Gregg D. Larson[†]

^{*}School of Elec. and Comp. Eng., Georgia Institute of Technology, Atlanta, GA, USA 30332-0250

[†]Woodruff School of Mech. Eng., Georgia Institute of Technology, Atlanta, GA, USA 30332-0405

ABSTRACT

Broadband electromagnetic induction (EMI) sensors have been shown to be able to reduce false alarm rates and increase the probability of detecting landmines. To aid in the development of these sensors and associated detection algorithms, a testing facility and inversion technique have been developed to characterize the response of typical targets and clutter objects as a function of orientation and frequency.

Index Terms— *Electromagnetic induction, EMI, landmine detection, sensor*

1. INTRODUCTION

Simple electromagnetic induction (EMI) sensors are capable of detecting most landmines; however, they will also detect every buried metal object such as bottle tops, nails, shrapnel, bullets, etc. This results in an unacceptable false alarm rate. This is even more problematic for the detection of low-metal anti-personnel landmines as they are extremely difficult to distinguish from clutter using a simple EMI sensor. However, advanced EMI sensors that use a broad range of frequencies or a broad range of measurement times along with advanced signal processing have been shown to be capable of discriminating between buried landmines and many types of buried metal clutter [1-6]. The broadband responses of many targets are relatively invariant to burial depth; however, the responses of some objects vary when they are tilted at arbitrary angles, which could cause missed detections.

To aid in the development of EMI sensors and associated detection algorithms, a testing facility and inversion technique have been developed to characterize the response of typical targets and clutter objects with respect to location, orientation, and frequency. The data from these measurements are used to develop models that are valid for any orientation of the object. Similar measurements in the field would be very difficult to perform due to the difficulty of accurately placing and rotating the target. It is difficult to analytically or numerically predict the response of many of these objects with accuracy due to uncertainties in the material parameters and geometry of the metal components in the objects. The objects are modeled as simple sets of

magnetic dipoles with discrete relaxation frequencies. It is envisioned that the models derived in this work will be utilized to reduce false alarm rates and increase the probability of detection for EMI sensors through improvements in both the hardware and the processing algorithms used to detect and discriminate buried targets.

2. MEASUREMENT SYSTEM

A laboratory positioner was developed with three automated translational stages (x, y, and z), two automated rotational stages (yaw and pitch), and one manually-adjusted rotational stage (roll, not labeled) as indicated in Fig. 1 [7]. An EMI sensor array [8] is shown in Fig. 1b with the three-loop target. This system is used to measure the response of targets in a three-dimensional region as a function of angular orientation.

3. MODEL

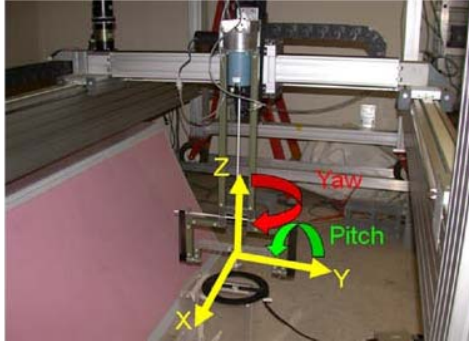
A simple dipole model is developed to predict the target response of an EMI system as a function of its position and orientation.

3.1. Magnetic Polarizability of a Target

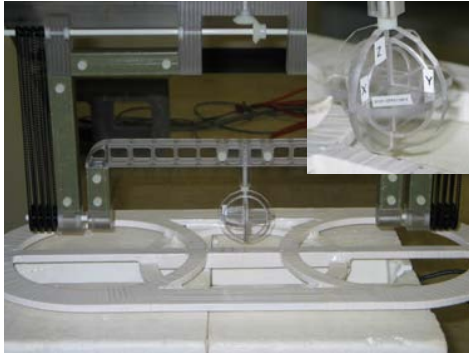
When a target is placed in a time-varying magnetic field, magnetic moments are induced due to two effects: the magnetic permeability of the target and the electrical conductivity that allows the induction of current. If the target is electrically small, the magnetic moments can be expressed in terms of the equivalent magnetic dipole moment, \mathbf{m} . The dipole moment can be calculated from the magnetic polarizability tensor, \mathbf{M} , when the exciting field \mathbf{H}_T is relatively constant over the extent of the object: $\mathbf{m} = \mathbf{M}\mathbf{H}_T$. A target will often have multiple relaxations and will have a corresponding tensor for each relaxation that contains the orientation/symmetry information for the relaxation. The magnetization for such a target can be written as the sum [2]:

$$\mathbf{M}(\omega) = T_0 \mathbf{T}_0 - \sum_k T_k \left(\frac{j\omega / \zeta_k}{1 + j\omega / \zeta_k} \right) \mathbf{T}_k \quad (1)$$

where T_k is a real constant, ζ_k is the relaxation frequency, and \mathbf{T}_k is a real, symmetric, second rank tensor. The first term is due to the bulk magnetic permeability of the target, which is assumed to be frequency independent, and the second term is due to the currents induced in the target. The tensor \mathbf{T}_k results from the path of the current for the k^{th} relaxation.



a)



b)

Fig. 1. Experimental measurement facility for EMI target characterization: a) Single EMI sensor head with automated translational (x , y , and z) and rotational (yaw about z and pitch about y) axes labeled, manual rotational axis (roll about x) unlabeled; b) EMI sensor head array with three-loop target.

3.2. EMI System

Consider the example EMI system that consists of transmit and receive coils which interact with a target. Here \mathbf{H}_T is the field at the target generated by the transmit coil when the coil is driven with the current I_T , and \mathbf{m} is the dipole moment induced on the target. It can be shown by using reciprocity that the received voltage due to the target is [9, 10]:

$$V_R = \frac{j\omega\mu}{I_R} \mathbf{H}_R^T \mathbf{m} = \frac{j\omega\mu}{I_R} \mathbf{H}_R^T \mathbf{M} \mathbf{H}_T \quad (2)$$

where \mathbf{H}_R is the magnetic field generated when the receiving loop driven with the current I_R . Note that \mathbf{H}_T , \mathbf{H}_R , and \mathbf{m} can be, and are likely to be, in different directions. The received

voltage is compared to a reference voltage to obtain the response \mathcal{R} of the system:

$$\mathcal{R} = \frac{V_R}{V_X} = \frac{\mu}{L_X I_T I_R} \mathbf{H}_R^T \mathbf{M} \mathbf{H}_T \quad (3)$$

where $V_X = j\omega L_X I_T$ is the reference voltage from a reference transformer with mutual inductance L_X which is also driven by transmit current I_T . The response of the system when the target is rotated by the Euler angles α , β , and γ can be written as

$$\mathcal{R} = \frac{\mu}{L_X I_T I_R} \mathbf{H}_R^T \mathbf{R}^T(\alpha, \beta, \gamma) \mathbf{M} \mathbf{R}(\alpha, \beta, \gamma) \mathbf{H}_T \quad (4)$$

where \mathbf{R} is a rotation matrix[11]. The angle α is the yaw angle, β is the pitch angle, and γ is the roll angle; the yaw and pitch angles are indicated in figure 1. The magnetic fields $\mathbf{H}_T(x, y, z)$ and $\mathbf{H}_R(x, y, z)$ are calculated as a function of position by direct application of the Biot-Savart law from the geometry of the wires in the coils.

4. ESTIMATION OF TARGET PARAMETERS

In a typical measurement, the response \mathcal{R} is measured as a function of position and orientation, and in this section, a method for inverting the measurement to obtain the model parameters is presented. Direct fitting of the parameters in equations 1 and 4 is difficult because of the non-linear relationship between the relaxation frequencies ζ_k and the orientation of the tensors with the response. The non-linear relation for ζ_k is dealt with using the procedure described in [12]. The non-linear relation with the orientation of the tensors is dealt with by using the symmetry of the target. The tensor \mathbf{T}_k is expanded in a set of basis tensors \mathcal{T}_k which span the allowable range of \mathbf{T}_k . This expansion allows for solution using a linear least-squares approximation procedure. For this paper, two types of expansions will be considered. First, all targets can be oriented so that \mathbf{T}_k is diagonal [11]. It can also be shown that \mathbf{T}_k is diagonal for certain targets with symmetries about the coordinate axes[13]. The three loop target shown in figure 1b is an example of a target with this symmetry. For these targets, \mathbf{T}_k is expanded as

$$\begin{aligned} T_k \mathbf{T}_k &= M_{k,xx} \mathcal{T}_{xx} + M_{k,yy} \mathcal{T}_{yy} + M_{k,zz} \mathcal{T}_{zz} \\ &= M_{k,xx} \begin{bmatrix} 1 & 0 & 0 \\ 0 & 0 & 0 \\ 0 & 0 & 0 \end{bmatrix} + M_{k,yy} \begin{bmatrix} 0 & 0 & 0 \\ 0 & 1 & 0 \\ 0 & 0 & 0 \end{bmatrix} + M_{k,zz} \begin{bmatrix} 0 & 0 & 0 \\ 0 & 0 & 0 \\ 0 & 0 & 1 \end{bmatrix}. \end{aligned} \quad (5)$$

Second, some targets have additional symmetry about the z -axis which can be used to further simplify the expansion:

$$T_k \mathbf{T}_k = M_{k,cy} \mathcal{T}_{cy} + M_{k,zz} \mathcal{T}_{zz}$$

$$= M_{k,cy} \begin{bmatrix} 1 & 0 & 0 \\ 0 & 1 & 0 \\ 0 & 0 & 0 \end{bmatrix} + M_{k,zz} \begin{bmatrix} 0 & 0 & 0 \\ 0 & 0 & 0 \\ 0 & 0 & 1 \end{bmatrix}. \quad (6)$$

A penny, a nail, and a rifle cartridge are examples of objects with this type of symmetry. In all of these expansions, the coefficients are positive since they are aligned with the physical dipoles.

A zero-mean down-track filter is applied to the measured response to lessen the effects of positional errors in the x direction, to increase the signal to noise ratio, to help mitigate the response to the positioning system, and to mostly remove the direct coupling between the transmit and receive coils[8]. The filtered response is obtained at the discrete observations O_p :

$$\mathcal{R}_F(O_p) = \frac{\mu}{L_X I_T I_R} \left\{ \sum_n M_{0n} \mathbf{P}_{pn} - \sum_k \left[\left(\frac{j\omega_p / \zeta_k}{1 + j\omega_p / \zeta_k} \right) \sum_n M_{kn} \mathbf{P}_{pn} \right] \right\}$$

where ω_p is the frequency at the p^{th} observation. \mathbf{P}_{pn} contains the filtering, the projections of the tensors on the fields and the rotation matrices:

$$\mathbf{P}_{pn} = \sum_g F(x_g + x_p) \mathbf{H}_R^T(x_g, y_p, z_p) \mathbf{R}^T \mathcal{T}_n \mathbf{R} \mathbf{H}_T(x_g, y_p, z_p) \quad (8)$$

where $x_p, y_p, z_p, \alpha_p, \beta_p$, and γ_p are the locations/orientations at the p^{th} observation and where F is the down-track filter described in [8]. The values of ζ_k are determined in this paper by computing the discrete spectrum of relaxation frequencies (DSRF) as described in [12] on a response that is averaged over all the discrete observations O_p . The parameters M_{kn} are obtained by writing (7) as a matrix equation as shown in [14]. Multiple locations and/or orientations are included to get enough measurements to make it possible to solve for the parameters M_{kn} . The non-zero values of M_{kn} will be positive, and many of the parameters M_{kn} can be zero since not every relaxation will have all the tensor components..

5. RESULTS

Two targets were measured that are made with loops of wire so that their theoretical parameters are easily estimated to demonstrate the accuracy of the modeling technique. The first loop target is made with 22 AWG copper wire formed into a circular loop with a circumference of 10 cm, which has a theoretical relaxation frequency of 10.0 kHz. The theoretical and estimated model parameters are graphed as a function of the relaxation frequency, $f_r = \zeta/2\pi$, in Fig. 2a for the single-loop target. The agreement between the theory

and experiment is very good. Since the loop is z-directed, the theory predicts a single z component for the dipole expansion at 10.0 kHz; however, the expansion in equation (8) is used for this inversion which allows for three components. Ideally, the inversion would return exactly zero amplitudes for the additional components, but because of measurement errors, the additional components will not always have an amplitude of exactly zero. The additional components near 10.0 kHz are seen to be very small in figure 2a. These components could be due to a small misalignment of the target in the measurement system. Note that in the measured results, there is a weak relaxation at 250 kHz that is not predicted theoretically. We believe that this is due to the finite thickness of the wire that is not taken into account in the theoretical model.

The second loop target is a three-loop target that consists of three orthogonal loops of copper wire as shown in Fig. 1b. The theoretical and estimated model parameters are graphed as a function of the relaxation frequency in Fig. 2b. Each relaxation frequency for this target has a different component due to the arrangement of the loops. The agreement between the theory and experiment is very good, even for this more complex target.

Results are shown in Figures 2c through 2e for an anti-personnel low-metal landmine, a nail, and a 9 mm cartridge. The parameters M_{0n} are due to the frequency independent magnetic permeability of the targets and are labeled as DC on the figures. These parameters are essentially zero for three of the targets since they are non-magnetic, but are non-zero for the landmine and the steel nail since they are magnetic. The magnetic targets have relaxation terms, M_{kn} , in addition to the magnetic terms, M_{0n} . The experimental results for this broad range of targets demonstrate the capability of the model to represent the targets.

6. CONCLUSIONS

An experimental facility has been established to measure the response of typical targets for EMI sensors as a function of location and orientation. A method of modeling the targets as an expansion of simple dipoles with discrete relaxations is presented along with a method to invert the measured responses to obtain the model parameters. The models are valid for any position and orientation of the target. Targets with known models were measured to establish the accuracy of the technique. Numerous other targets have been measured and their models catalogued.

ACKNOWLEDGMENTS

This work is supported in part by the US Army Night Vision and Electronic Sensors Directorate, Science and Technology Division, Countermining Branch and in part by the U. S. Army Research Office under Contract Number W911NF-05-1-0257.

REFERENCES

- [1] G. D. Sower and S. P. Cave, "Detection and identification of mines from natural magnetic and electromagnetic resonances," in *Proc. of SPIE 2496*, Orlando, FL, USA, 1995, pp. 1015-1024.
- [2] C. E. Baum, "Detection and identification of mines from natural magnetic and electromagnetic resonances," in *Detection and identification of visually obscured targets*, C. E. Baum, Ed., ed Philadelphia: Talor and Francis, 1999, pp. 163-218.
- [3] L. Collins, *et al.*, "An improved Bayesian decision theoretic approach for land mine detection," *Geoscience and Remote Sensing, IEEE Transactions on*, vol. 37, pp. 811-819, 1999.
- [4] G. Ping, *et al.*, "Classification of landmine-like metal targets using wideband electromagnetic induction," *Geoscience and Remote Sensing, IEEE Transactions on*, vol. 38, pp. 1352-1361, 2000.
- [5] E. B. Fails, *et al.*, "Performance of a four parameter model for modeling landmine signatures in frequency domain wideband electromagnetic induction detection systems," in *Proc. of the SPIE 6553*, 2007.
- [6] S. E. Yuksel, *et al.*, "Hierarchical Methods for Landmine Detection with Wideband Electromagnetic Induction and Ground Penetrating Radar Multi-Sensor Systems," in *Geoscience and Remote Sensing Symposium, 2008. IGARSS 2008. IEEE International*, 2008, pp. II-177-II-180.
- [7] G. D. Larson and W. R. Scott, Jr., "Automated, non-metallic measurement facility for testing and development of electromagnetic induction sensors for landmine detection," in *Proc. of the SPIE 7303*, 2009.
- [8] W. R. Scott, Jr., "Broadband Array of Electromagnetic Induction Sensors for Detecting Buried Landmines," in *Geoscience and Remote Sensing Symposium, 2008. IGARSS 2008. IEEE International*, 2008, pp. II-375-II-378.
- [9] H. Vesselle and R. E. Collin, "The signal-to-noise ratio of nuclear magnetic resonance surface coils and application to a lossy dielectric cylinder model. I. Theory," *Biomedical Engineering, IEEE Transactions on*, vol. 42, pp. 497-506, 1995.
- [10] K. F. Casey and B. A. Baertlein, "An overview of Electromagnetic methods in subsurface detection," in *Detection and identification of visually obscured targets*, C. E. Baum, Ed., ed Philadelphia: Talor and Francis, 1999, pp. 9-46.
- [11] G. Arfken, *Mathematical Methods for Physicists*, Second ed. San Diego, CA: Academic Press, 1985.
- [12] M. H. Wei, *et al.*, "Robust Estimation of the Discrete Spectrum of Relaxations for Electromagnetic Induction Responses," *Geoscience and Remote Sensing, IEEE Transactions on*, vol. 48, pp. 1169-1179, 2010.
- [13] C. E. Baum, "The magnetic polarizability dyadic and point symmetry," in *Detection and identification of visually obscured targets*, C. E. Baum, Ed., ed Philadelphia: Talor and Francis, 1999, pp. 219-242.
- [14] W. R. Scott, Jr. and G. D. Larson, "Measured dipole expansion of discrete relaxations to represent the electromagnetic induction response of buried metal targets," in *Proc. of the SPIE 7664*, 2010.

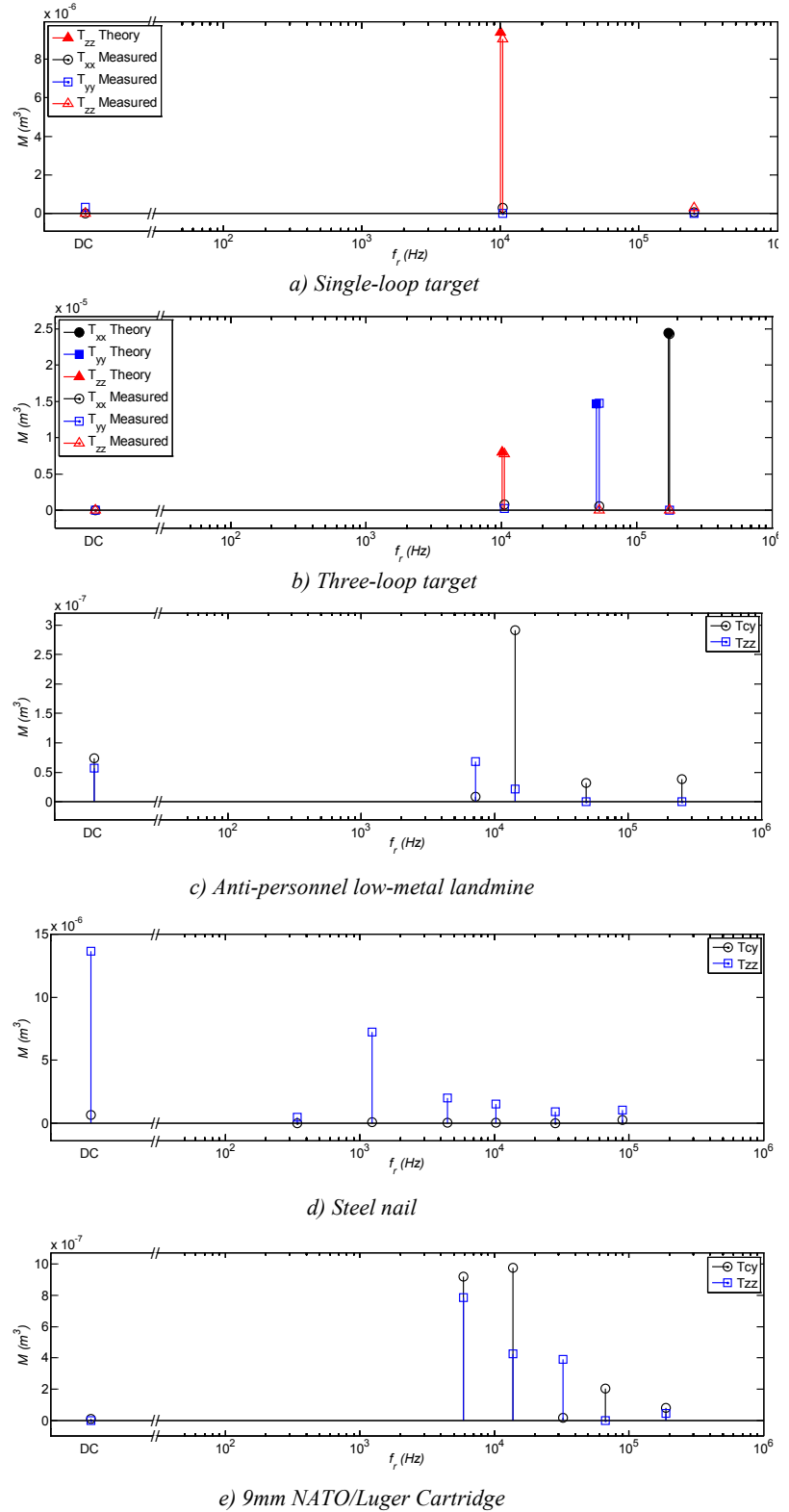


Fig. 2. Estimated model parameters as a function of relaxation frequency.

Measured dipole expansion of discrete relaxations to represent the electromagnetic induction response of buried metal targets

Waymond R. Scott, Jr.^{*} and Gregg D. Larson[†]

^{*}School of Elec. and Comp. Eng., Georgia Institute of Technology, Atlanta, GA, USA 30332-0250

[†]Woodruff School of Mech. Eng., Georgia Institute of Technology, Atlanta, GA, USA 30332-0405

ABSTRACT

Broadband electromagnetic induction (EMI) sensors have been shown to be able to reduce false alarm rates and increase the probability of detecting landmines. To aid in the development of these sensors and associated detection algorithms, a testing facility and inversion technique have been developed to characterize the response of typical targets and clutter objects as a function of orientation and frequency. The models are simple sets of magnetic dipoles with discrete relaxation frequencies. Results will be presented for a range of targets such as shell casings, wire loops, and landmines. It is envisioned that the models derived in this work will be utilized to reduce false alarm rates and increase the probability of detection for EMI sensors through improvements in both the hardware and the processing algorithms used to detect and discriminate buried targets.

Keywords: Electromagnetic induction, EMI, landmine detection, sensor, testing

1. INTRODUCTION

Simple electromagnetic induction (EMI) sensors are capable of detecting most landmines; however, they will also detect every buried metal object such as bottle tops, nails, shrapnel, bullets, etc. This results in an unacceptable false alarm rate. This is even more problematic for the detection of low-metal anti-personnel landmines as they are extremely difficult to distinguish from clutter using a simple EMI sensor. However, advanced EMI sensors that use a broad range of frequencies or a broad range of measurement times along with advanced signal processing have been shown to be capable of discriminating between buried landmines and many types of buried metal clutter [1-6]. The broadband responses of many targets are relatively invariant to burial depth; however, the responses of some objects vary when they are tilted at odd angles, which could cause missed detections. To aid in the development of the EMI sensors and associated detection algorithms, a testing facility and inversion technique have been developed to characterize the response of typical targets and clutter objects with respect to location, orientation, and frequency. The data from these measurements will be used to study the response of the targets and develop models that are valid for any orientation of the object. Similar measurements in the field would be very difficult to perform due to the difficulty of accurately placing and rotating the target. It is difficult to analytically or numerically predict the response of many of these objects with accuracy due to uncertainties in the material parameters and geometry of the metal components in the objects. Most of these objects can be modeled as simple sets of magnetic dipoles with discrete relaxation frequencies. It is envisioned that the models derived in this work will be utilized to reduce false alarm rates and increase the probability of detection for EMI sensors through improvements in both the hardware and the processing algorithms used to detect and discriminate buried targets.

In this paper, the measurement system is presented in section 2, the model used to represent the targets is presented in section 3, the method for inverting the measured data to get the parameters for the model is presented in section 4, and representative results are presented in section 5.

^{*} E-mail: waymond.scott@ece.gatech.edu, Tel: 404-894-3048

[†] E-mail: gregg.larson@me.gatech.edu, Tel: 404-894-6026

2. MEASUREMENT SYSTEM

A laboratory positioner was developed with three automated translational stages (x , y , and z), two automated rotational stages (yaw and pitch), and one manually-adjusted rotational stage (roll, not labeled) as indicated in Fig. 1 [7]. An EMI sensor array [8] is shown in Fig. 1b with the three-loop target. This system is used to measure the response of targets in a three-dimensional region as a function of angular orientation. Other typical targets include shell casings, ball bearings, coplanar wire coils, and landmines.

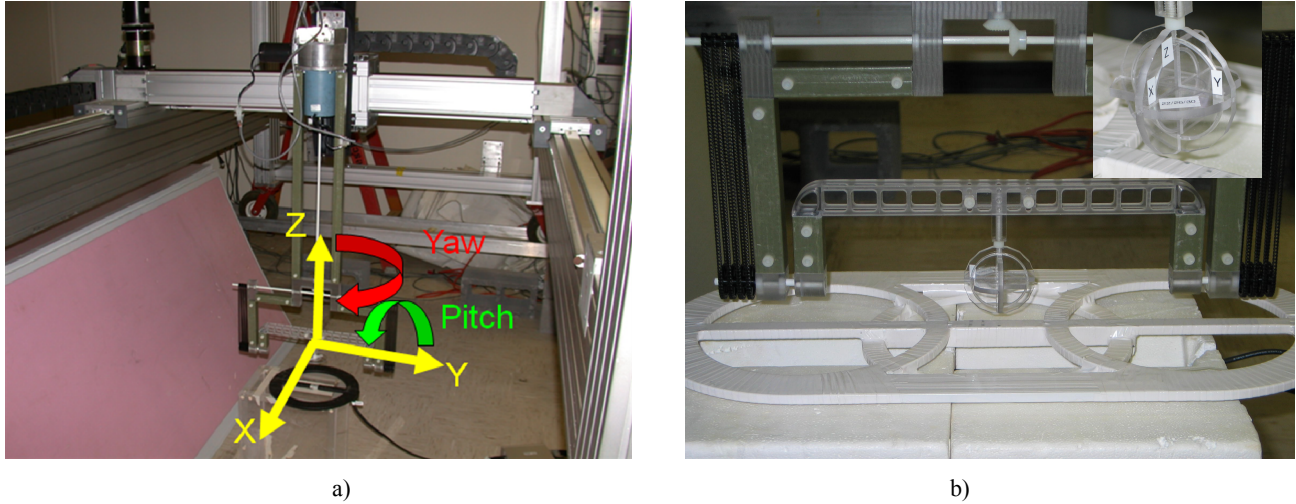


Fig. 1. Experimental measurement facility for EMI target characterization: a) Single EMI sensor head with automated translational (x , y , and z) and rotational (yaw about z and pitch about y) axes labeled, manual rotational axis (roll about x) unlabeled; b) EMI sensor head array with three-loop target (inset).

3. MODEL

A simple dipole model is developed to predict the response of the EMI systems shown in figure 1 to a target that is being tested in the system as a function of its position and orientation.

3.1. Magnetic Polarizability of a Target

When a target is placed in a time-varying magnetic field, magnetic moments are induced due to two effects: the magnetic permeability of the target and the electrical conductivity that allows the induction of current. If the target is electrically small, the magnetic moments can be expressed in terms of the equivalent magnetic dipole moment, \mathbf{m} . The dipole moment can be calculated from the magnetic polarizability, \mathbf{M} , when the exciting field \mathbf{H}_T is relatively constant over the extent of the object: $\mathbf{m} = \mathbf{M}\mathbf{H}_T$. A target will often have multiple relaxations and will have a corresponding tensor for each relaxation that contains the orientation/symmetry information for the relaxation. The magnetization for such a target can be written as the sum [2]:

$$\mathbf{M}(\omega) = T_0 \mathbf{T}_0 - \sum_k T_k \left(\frac{j\omega/\zeta_k}{1 + j\omega/\zeta_k} \right) \mathbf{T}_k \quad (1)$$

where T_k is a real constant, ζ_k is the relaxation frequency, and \mathbf{T}_k is a real, symmetric, second rank tensor. The first term is due to the bulk magnetic permeability of the target, which is assumed to be frequency independent, and the second term is due to the currents induced in the target. The tensor \mathbf{T}_k results from the symmetry of the current path for the k^{th} relaxation and can be expressed as sum of (projection matrices) simple dipoles:

$$\mathbf{T}_k \mathbf{T}_k = \sum_n M_{kn} \mathbf{n}_{kn} \mathbf{n}_{kn}^T = \sum_n M_{kn} \begin{bmatrix} \mathbf{n}_{x,kn} \\ \mathbf{n}_{y,kn} \\ \mathbf{n}_{z,kn} \end{bmatrix} \begin{bmatrix} \mathbf{n}_{x,kn} & \mathbf{n}_{y,kn} & \mathbf{n}_{z,kn} \end{bmatrix} \quad (2)$$

where M_{kn} is a positive real constant and \mathbf{n}_{kn} are orthogonal unit vectors representing the axis of the n^{th} dipole for the k^{th} relaxation frequency. As an example, a target that consists of three orthogonal loops of copper wire, as in Fig. 1b, was constructed with the parameters shown in Table I. The magnetization of this target is

$$\mathbf{M}(\omega) = -M_x \left(\frac{j\omega/\zeta_x}{1+j\omega/\zeta_x} \right) \begin{bmatrix} 1 & 0 & 0 \\ 0 & 0 & 0 \\ 0 & 0 & 0 \end{bmatrix} - M_y \left(\frac{j\omega/\zeta_y}{1+j\omega/\zeta_y} \right) \begin{bmatrix} 0 & 0 & 0 \\ 0 & 1 & 0 \\ 0 & 0 & 0 \end{bmatrix} - M_z \left(\frac{j\omega/\zeta_z}{1+j\omega/\zeta_z} \right) \begin{bmatrix} 0 & 0 & 0 \\ 0 & 0 & 0 \\ 0 & 0 & 1 \end{bmatrix} \quad (3)$$

where $M_k = \mu_o A_k^2 / L_k$, $\zeta_k = 2\pi f_{rk}$, A_k are the areas of the loops and, L_k are the self inductances of the loops with $k = x, y, z$.

Table I. Parameters for the three-loop target.

Loop Parameters			Theoretical Model Parameters		Measured Model Parameters	
Orientation	Diameter (cm)	Wire Gauge (AWG)	Magnetization $M_k * 10^6$ (m ³)	Relaxation Freq. (kHz)	Magnetization $M_k * 10^6$ (m ³)	Relaxation Freq. (kHz)
X	5	36	24.5	172	24.4	175
Y	4	30	14.7	50.2	14.7	52.6
Z	3	22	8.0	10.1	7.6	10.5

3.2. EMI System

Consider the example EMI system shown in figure 2 that consists of transmit and receive coils which interact with a target. Here \mathbf{H}_T is the field at the target generated by the transmit coil when the coil is driven with the current I_T , and \mathbf{m} is the dipole moment induced on the target. It can be shown by using reciprocity that the received voltage due to the target is [9, 10]:

$$V_R = \frac{j\omega\mu}{I_R} \mathbf{H}_R^T \mathbf{m} = \frac{j\omega\mu}{I_R} \mathbf{H}_R^T \mathbf{M} \mathbf{H}_T \quad (4)$$

where \mathbf{H}_R is the magnetic field generated with the receiving loop driven with the current I_R . Note that \mathbf{H}_T , \mathbf{H}_R , and \mathbf{m} can be, and are likely to be, in different directions. The received voltage is compared to a reference voltage to obtain the response \mathcal{R} of the system:

$$\mathcal{R} = \frac{V_R}{V_X} = \frac{\mu}{L_X I_T I_R} \mathbf{H}_R^T \mathbf{M} \mathbf{H}_T \quad (5)$$

where $V_X = j\omega L_X I_T$ is the reference voltage from a reference transformer with mutual inductance L_X which is also driven by transmit current I_T . The response of the system when the target is rotated by the Euler angles α , β , and γ can be written as

$$\begin{aligned}
\mathcal{R} &= \frac{\mu}{L_X I_T I_R} \mathbf{H}_R^T \mathbf{M}_R \mathbf{H}_T = \frac{\mu}{L_X I_T I_R} \mathbf{H}_R^T \mathbf{R}^T(\alpha, \beta, \gamma) \mathbf{M}_R \mathbf{R}(\alpha, \beta, \gamma) \mathbf{H}_T \\
&= \frac{\mu}{L_X I_T I_R} \mathbf{H}_R^T \mathbf{R}^T(\alpha, \beta, \gamma) \left\{ T_0 \mathbf{T}_0 - \sum_k T_k \left(\frac{j\omega / \zeta_k}{1 + j\omega / \zeta_k} \right) \mathbf{T}_k \right\} \mathbf{R}(\alpha, \beta, \gamma) \mathbf{H}_T
\end{aligned} \tag{6}$$

where \mathbf{R} is a rotation matrix[11]. The angle α is the yaw angle, β is the pitch angle, and γ is the roll angle; the yaw and pitch angles are indicated in figure 1. The magnetic fields $\mathbf{H}_T(x, y, z)$ and $\mathbf{H}_R(x, y, z)$ are calculated as a function of position by direct application of the Bio-Savart law from the geometry of the wires in the coils.

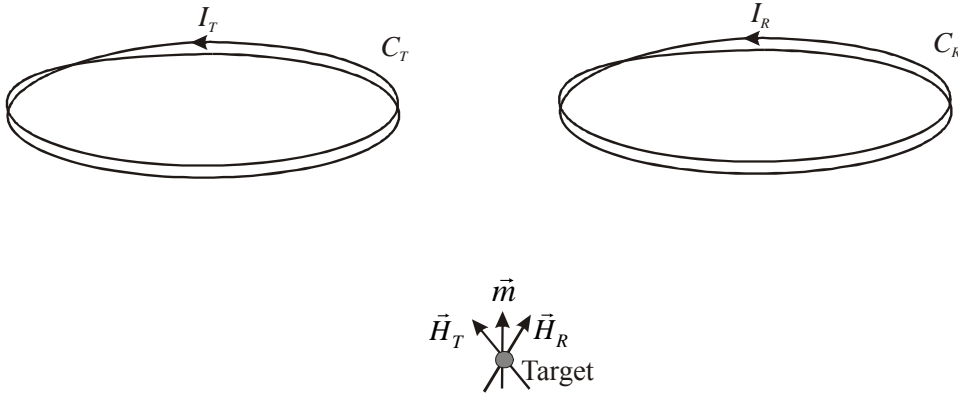


Figure 2a. Diagram of EMI system used with the reciprocity relation with both the transmit and the receive coils driven.

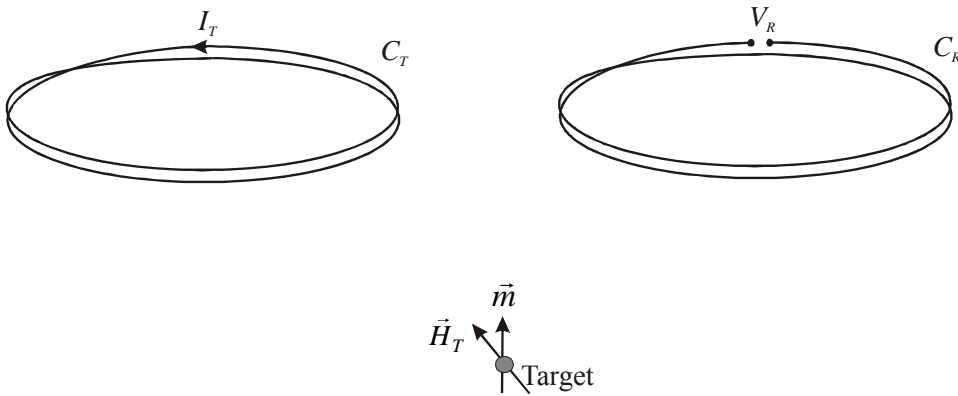


Figure 2b. Diagram of EMI system as it is physically configured with the transmit coil driven and receive coil used a receiver.

4. ESTIMATION OF TARGET PARAMETERS

In a typical measurement, the response \mathcal{R} is measured as a function of position and orientation, and in this section, a method for inverting the measurement to obtain the model parameters is presented. Direct fitting of the parameters in equations 2 and 6 is difficult because of the non-linear relationship between the relaxation frequencies ζ_k and the vectors

\mathbf{n}_{kn} with the response. The non-linear relation for ζ_k is dealt with using the procedure described in [12]. The non-linear relation for \mathbf{n}_{kn} is dealt with by using an alternate expansion of \mathbf{T}_k . Here, the tensor \mathbf{T}_k is expanded in a set of basis tensors \mathcal{T}_k which span the allowable range of \mathbf{T}_k :

$$T_k \mathbf{T}_k = \sum_n M_{kn} \mathcal{T}_n = \sum_n M_{kn} \begin{bmatrix} \mathcal{T}_{n,11} & \mathcal{T}_{n,12} & \mathcal{T}_{n,13} \\ \mathcal{T}_{n,21} & \mathcal{T}_{n,22} & \mathcal{T}_{n,23} \\ \mathcal{T}_{n,31} & \mathcal{T}_{n,32} & \mathcal{T}_{n,33} \end{bmatrix} \quad (7)$$

This expansion allows for solution of the parameters M_{kn} using a linear least-squares approximation procedure. However, there are two disadvantages of this expansion for an arbitrary target: first, the coefficients M_{kn} are no longer guaranteed to be positive, and second, more terms will be required. Up to six basis tensors can be required for a general target with an arbitrary initial orientation. Fortunately, most targets of interest have symmetry that negates these disadvantages. For this paper, three types of expansions will be considered. First, all targets can be oriented so that is \mathbf{T}_k diagonal [11]. It can also be shown that \mathbf{T}_k is diagonal for certain targets with symmetries about the coordinate axes[13]. The three loop target shown in figure 2b is an example of a target with this symmetry. For these targets, \mathbf{T}_k is expanded as

$$T_k \mathbf{T}_k = M_{k,xx} \mathcal{T}_{xx} + M_{k,yy} \mathcal{T}_{yy} + M_{k,zz} \mathcal{T}_{zz} = M_{k,xx} \begin{bmatrix} 1 & 0 & 0 \\ 0 & 0 & 0 \\ 0 & 0 & 0 \end{bmatrix} + M_{k,yy} \begin{bmatrix} 0 & 0 & 0 \\ 0 & 1 & 0 \\ 0 & 0 & 0 \end{bmatrix} + M_{k,zz} \begin{bmatrix} 0 & 0 & 0 \\ 0 & 0 & 0 \\ 0 & 0 & 1 \end{bmatrix} \quad (8)$$

Second, some targets have additional symmetry about the z-axis which can be used to further simplify the expansion:

$$T_k \mathbf{T}_k = M_{k,cy} \mathcal{T}_{cy} + M_{k,zz} \mathcal{T}_{zz} = M_{k,cy} \begin{bmatrix} 1 & 0 & 0 \\ 0 & 1 & 0 \\ 0 & 0 & 0 \end{bmatrix} + M_{k,zz} \begin{bmatrix} 0 & 0 & 0 \\ 0 & 0 & 0 \\ 0 & 0 & 1 \end{bmatrix} \quad (9)$$

A right regular polyhedral cylinder about the z-axis, a penny, and a rifle cartridge are examples of objects with this type of symmetry. Third, objects with even more symmetry like a sphere, a cube, a regular tetrahedron, etc. will only require one term in the expansion:

$$T_k \mathbf{T}_k = M_k \mathcal{T}_{sp} = M_k \begin{bmatrix} 1 & 0 & 0 \\ 0 & 1 & 0 \\ 0 & 0 & 1 \end{bmatrix} \quad (10)$$

In all of these expansions (8), (9), and (10), the coefficients are positive since they are aligned with the physical dipoles.

A zero-mean down-track filter is applied to the measured response to lessen the effects of positional errors in the x direction, to increase the signal to noise ratio, to help mitigate the response to the positioning system, and to mostly remove the direct coupling between the transmit and receive coils[8]:

$$\mathcal{R}_F(\omega, x, y, z, \alpha, \beta, \gamma) = \sum_g F(x_g) \mathcal{R}(\omega, x_g + x, y, z, \alpha, \beta, \gamma) \quad (11)$$

where F is the down-track filter described in [8]. The filtered response is obtained at the discrete observations O_p by combining equations (6) and (7):

$$\mathcal{R}_F(O_p) = \frac{\mu}{L_X I_T I_R} \left\{ \sum_n M_{0n} \mathbf{P}_{pn} - \sum_k \left[\left(\frac{j\omega_p / \zeta_k}{1 + j\omega_p / \zeta_k} \right) \sum_n M_{kn} \mathbf{P}_{pn} \right] \right\} \quad (12)$$

where ω_p is the frequency at the p^{th} observation. \mathbf{P}_{pn} contains the filtering, the projections of the tensors on the fields and the rotation matrices:

$$\mathbf{P}_{pn} = \sum_g F(x_g) \mathbf{H}_R^T(x_g + x_p, y_p, z_p) \mathbf{R}^T(\alpha_p, \beta_p, \gamma_p) \mathcal{T}_n \mathbf{R}(\alpha_p, \beta_p, \gamma_p) \mathbf{H}_T(x_g + x_p, y_p, z_p) \quad (13)$$

where $x_p, y_p, z_p, \alpha_p, \beta_p$, and γ_p are the locations/orientations at the p^{th} observation. The values of ζ_k are determined in this paper by computing the discrete spectrum of relaxation frequencies (DSRF) as described in [12] on a response that is averaged over all the discrete observations O_p . The sign of the responses are adjusted before averaging to ensure that the averaged response has a non-negative spectrum. The response is rewritten in a matrix equation for each location/orientation:

$$\begin{bmatrix} \mathcal{R}_F(O_p) \\ \mathcal{R}_F(O_p) \\ \mathcal{R}_F(O_p) \\ \vdots \\ \mathcal{R}_F(O_p) \end{bmatrix} = \begin{bmatrix} \mathbf{P}_{11} & \mathbf{P}_{12} & \cdots & \mathbf{P}_{1N} & \mathbf{P}_{11} \left(\frac{j\omega_1/\zeta_1}{1+j\omega_1/\zeta_1} \right) & \mathbf{P}_{12} \left(\frac{j\omega_1/\zeta_1}{1+j\omega_1/\zeta_1} \right) & \cdots & \mathbf{P}_{1N} \left(\frac{j\omega_1/\zeta_1}{1+j\omega_1/\zeta_1} \right) & \cdots & \mathbf{P}_{11} \left(\frac{j\omega_1/\zeta_K}{1+j\omega_1/\zeta_K} \right) & \cdots & \mathbf{P}_{1N} \left(\frac{j\omega_1/\zeta_K}{1+j\omega_1/\zeta_K} \right) \\ \mathbf{P}_{21} & \mathbf{P}_{22} & \cdots & \mathbf{P}_{2N} & \mathbf{P}_{21} \left(\frac{j\omega_2/\zeta_1}{1+j\omega_2/\zeta_1} \right) & \mathbf{P}_{22} \left(\frac{j\omega_2/\zeta_1}{1+j\omega_2/\zeta_1} \right) & \cdots & \mathbf{P}_{2N} \left(\frac{j\omega_2/\zeta_1}{1+j\omega_2/\zeta_1} \right) & \cdots & \mathbf{P}_{21} \left(\frac{j\omega_2/\zeta_K}{1+j\omega_2/\zeta_K} \right) & \cdots & \mathbf{P}_{2N} \left(\frac{j\omega_2/\zeta_K}{1+j\omega_2/\zeta_K} \right) \\ \mathbf{P}_{31} & \mathbf{P}_{32} & \cdots & \mathbf{P}_{3N} & \mathbf{P}_{31} \left(\frac{j\omega_3/\zeta_1}{1+j\omega_3/\zeta_1} \right) & \mathbf{P}_{32} \left(\frac{j\omega_3/\zeta_1}{1+j\omega_3/\zeta_1} \right) & \cdots & \mathbf{P}_{3N} \left(\frac{j\omega_3/\zeta_1}{1+j\omega_3/\zeta_1} \right) & \cdots & \mathbf{P}_{31} \left(\frac{j\omega_3/\zeta_K}{1+j\omega_3/\zeta_K} \right) & \cdots & \mathbf{P}_{3N} \left(\frac{j\omega_3/\zeta_K}{1+j\omega_3/\zeta_K} \right) \\ \vdots & \vdots & \vdots & \vdots & \vdots & \vdots & \vdots & \vdots & \vdots & \vdots & \vdots & \vdots \\ \mathbf{P}_{p1} & \mathbf{P}_{p2} & \cdots & \mathbf{P}_{pN} & \mathbf{P}_{p1} \left(\frac{j\omega_p/\zeta_1}{1+j\omega_p/\zeta_1} \right) & \mathbf{P}_{p2} \left(\frac{j\omega_p/\zeta_1}{1+j\omega_p/\zeta_1} \right) & \cdots & \mathbf{P}_{pN} \left(\frac{j\omega_p/\zeta_1}{1+j\omega_p/\zeta_1} \right) & \cdots & \mathbf{P}_{p1} \left(\frac{j\omega_p/\zeta_K}{1+j\omega_p/\zeta_K} \right) & \cdots & \mathbf{P}_{pN} \left(\frac{j\omega_p/\zeta_K}{1+j\omega_p/\zeta_K} \right) \end{bmatrix} \begin{bmatrix} M_{01} \\ M_{02} \\ \vdots \\ M_{0N} \\ M_{11} \\ M_{12} \\ \vdots \\ M_{1N} \\ \vdots \\ M_{K1} \\ \vdots \\ M_{KN} \end{bmatrix} \quad (14)$$

$$\mathcal{R}_p = \mathbf{A}_p \mathbf{M}$$

The real and imaginary parts are separated, making the entire system real and ensuring a real answer. Multiple locations and/or orientations are included to get enough measurements to make it possible to solve for the parameters M_{kn} :

$$\begin{bmatrix} \text{Re}(\mathcal{R}_p) \\ \text{Im}(\mathcal{R}_p) \end{bmatrix} = \begin{bmatrix} \text{Re}(\mathbf{A}_p) \\ \text{Im}(\mathbf{A}_p) \end{bmatrix} \begin{bmatrix} M_{01} \\ M_{02} \\ \vdots \\ M_{0N} \\ M_{11} \\ M_{12} \\ \vdots \\ M_{1N} \\ \vdots \\ M_{K1} \\ \vdots \\ M_{KN} \end{bmatrix} \quad (15)$$

Many of the parameters M_{kn} can be zero since not every relaxation will have all the tensor components and the non-zero values of M_{kn} will be positive. Since the parameters M_{kn} are non-negative, the function `lsqnonneg` in MATLAB which uses the algorithm found in [12] is used to solve (15).

5. RESULTS

Two targets were measured that are made with loops of wire so that their theoretical parameters are easily estimated to demonstrate the accuracy of the modeling technique. The first loop target is a simple loop of 22 AWG copper wire formed into a loop with a circumference of 10 cm, which has a theoretical relaxation frequency of 10.0 kHz. The theoretical and estimated model parameters are graphed as a function of the relaxation frequency, $f_r = \zeta/2\pi$, in Fig. 3 for

the single-loop target. The agreement between the theory and experiment is very good. Since the loop is z-directed, the theory predicts a single z component for the dipole expansion at 10.0 kHz; however, the expansion in equation (8) is used for this inversion which allows for three components. Ideally, the inversion would return exactly zero amplitudes for the additional components, but because of measurement errors, the additional components will not always have an amplitude of exactly zero. The additional components near 10.0 kHz are seen to very small in figure 3. These components could be easily due to a small misalignment of the target in the measurement system. Note that in the measured results, there is weak relaxation at 250 kHz that is not predicted theoretically, which we believe is due to the finite thickness of the wire that is not taken into account in the theoretical model.

The second loop target is the three-loop target shown in Fig. 1b with the theoretical model (3). The theoretical and estimated model parameters are shown in Table I and are graphed as a function of the relaxation frequency in Fig. 4 Each relaxation frequency for this target has a different component due to the arrangement of the loops. The agreement between the theory and experiment is very good even for this more complex target.

Results are shown in Figures 5 through 11 for a 1983 Lincoln penny, a nail, a 9 mm cartridge, a 0.45 caliber cartridge, a ferrite core, and two anti-personnel landmines. Some of these targets have been chosen for obvious familiarity while others were selected as representative examples of common landmines of interest. The parameters M_{0n} are due to the frequency independent magnetic permeability of the targets and are labeled as DC on the figures. These parameters are essentially zero for most of the targets since they are non-magnetic, but are non-zero for the steel nail, the ferrite core, and the two landmines since they are magnetic. All of the magnetic targets except for the ferrite core have relaxation terms, M_{kn} , in addition to the magnetic terms, M_{0n} . The experimental results for this broad range of targets demonstrate the capability of the model to represent the targets.

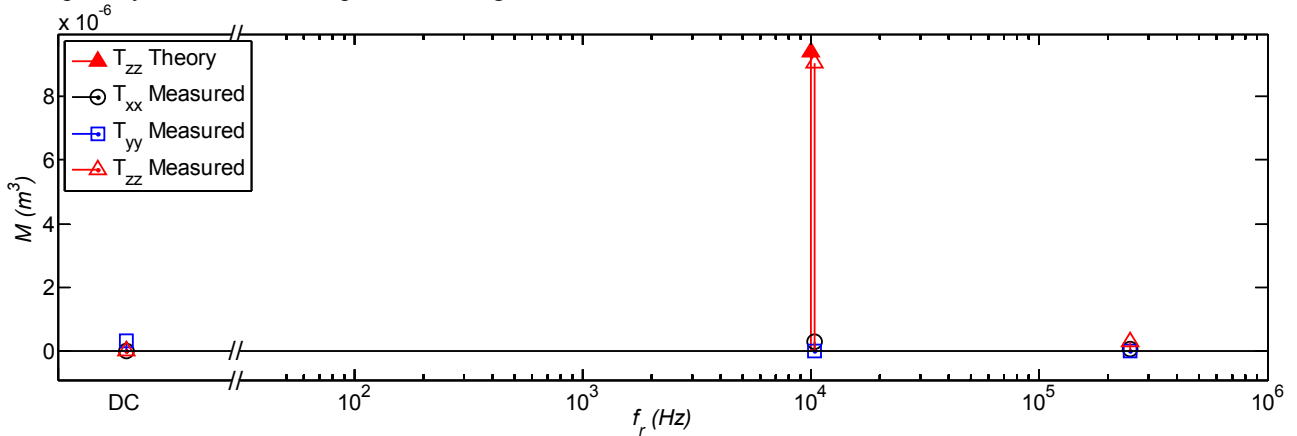
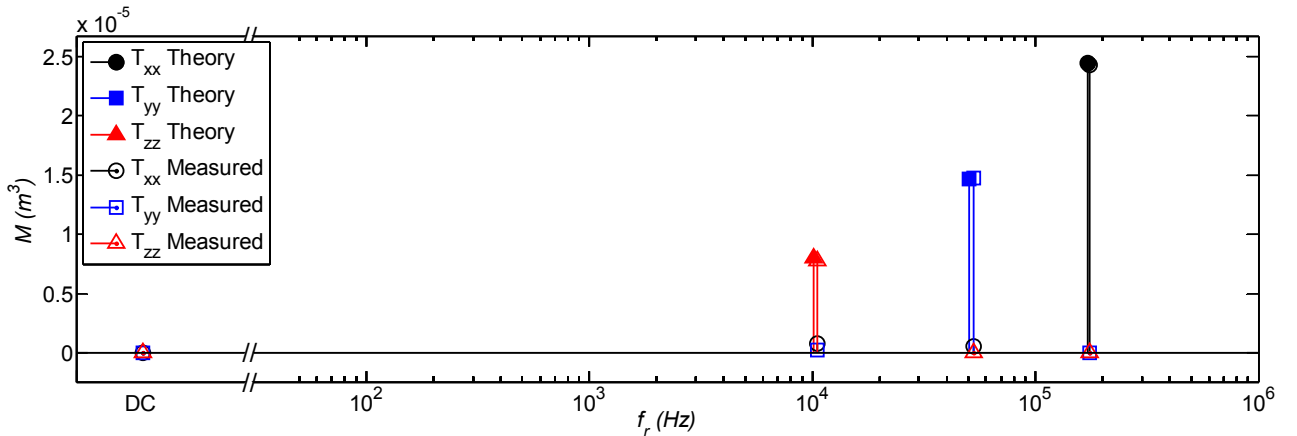


Fig. 3. Estimated and theoretical model parameters for the single-loop target as a function of relaxation frequency.



Hki 060Gunko cvyf "cpf "vj gqt gvkect'lo qf ghl'ctco gvgtu'ltq "vj g"vj t gg/rqqr "vcti gv'cu'c "hpevkqp"qlht grvzc'vkqp"t gs wgpe{0

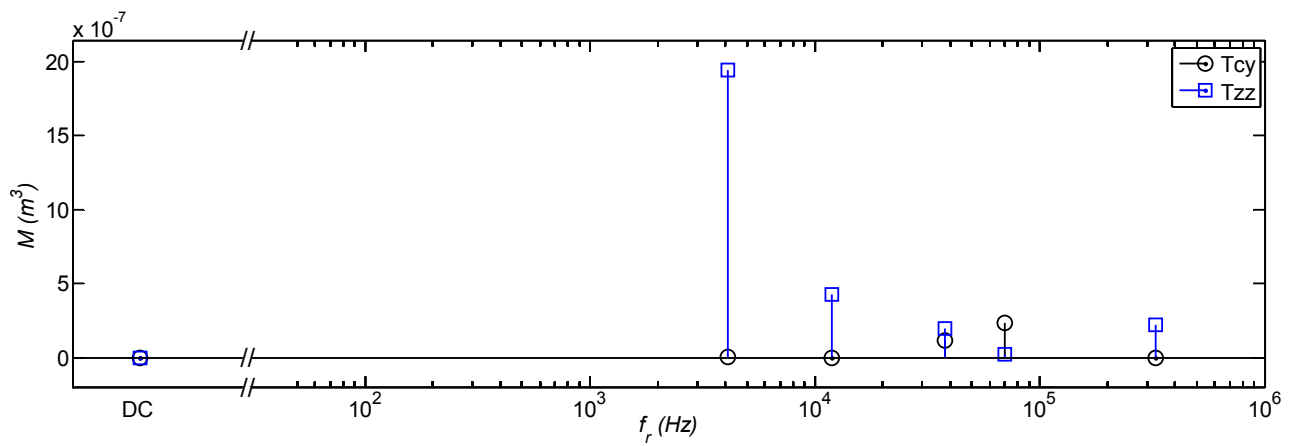


Fig. 5. Estimated model parameters for 1983 U.S Lincoln Penny as a function of relaxation frequency.

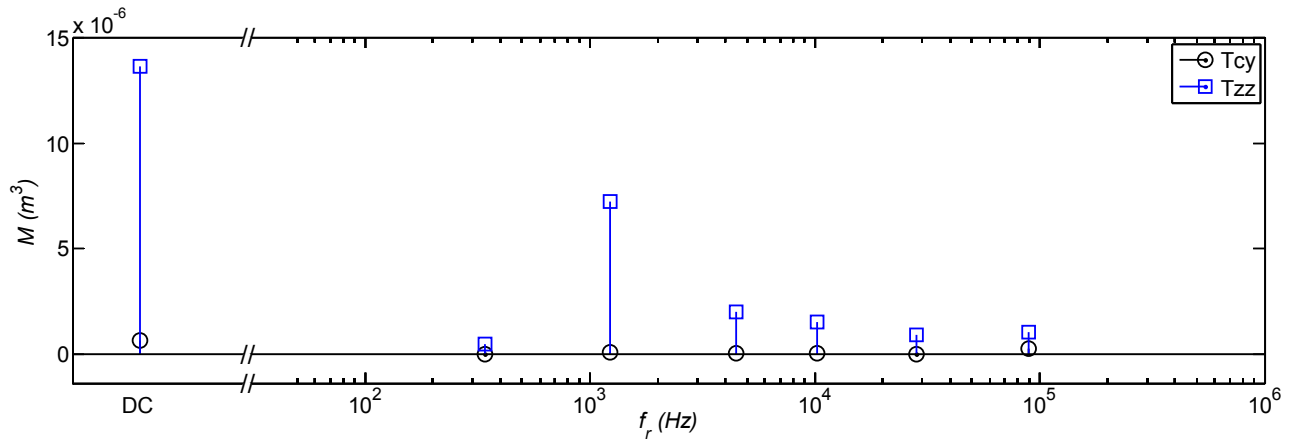


Fig. 6. Estimated model parameters for steel nail as a function of relaxation frequency.

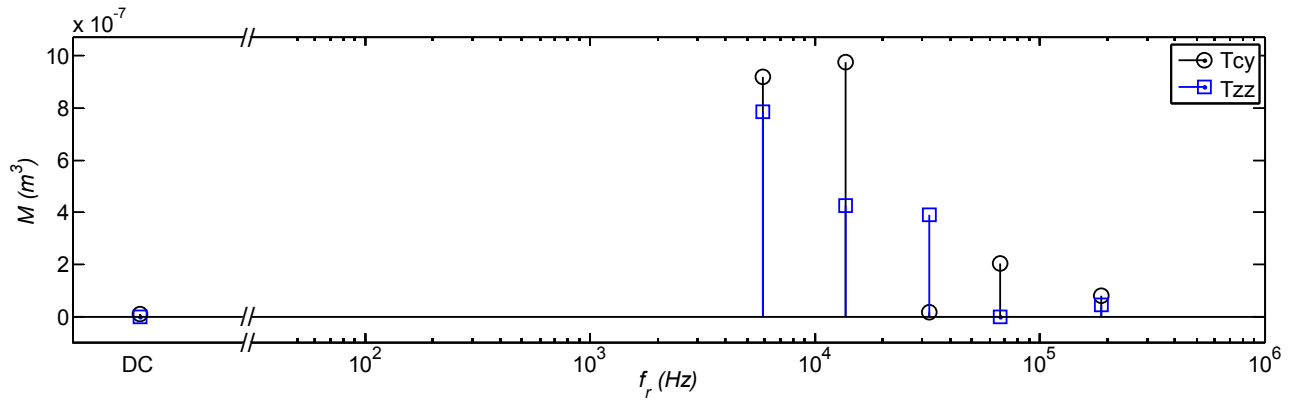


Fig. 7. Estimated model parameters for a 9mm NATO/Luger Cartridge as a function of relaxation frequency.

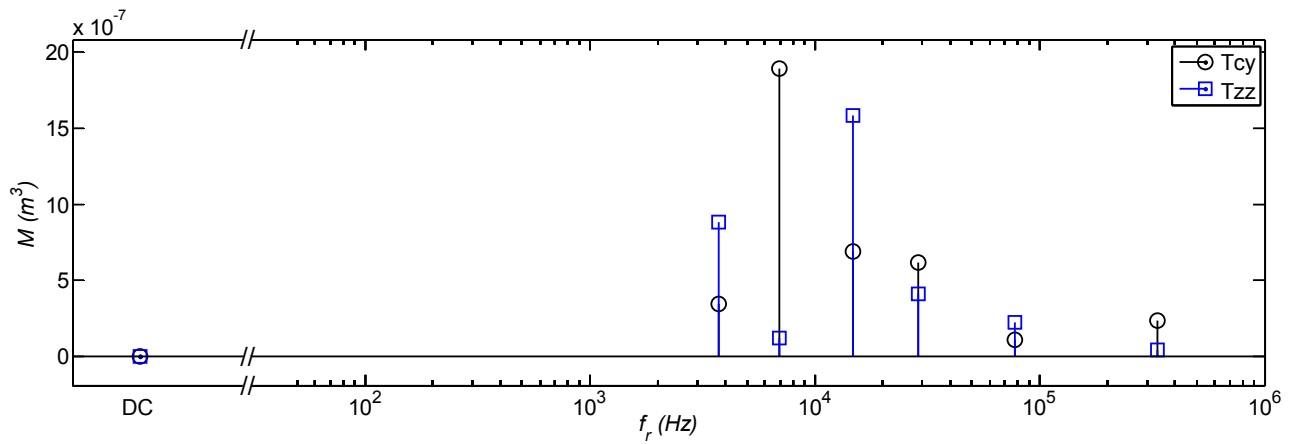


Fig. 8. Estimated model parameters for a 0.45caliber S&B Cartridge as a function of relaxation frequency.

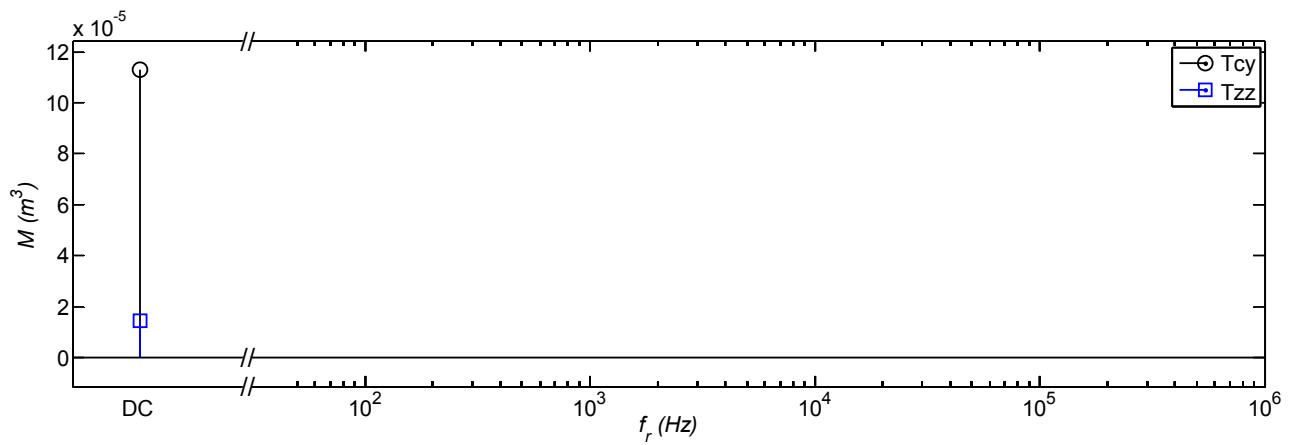


Fig. 9. Estimated model parameters for a Ferrite Core as a function of relaxation frequency.

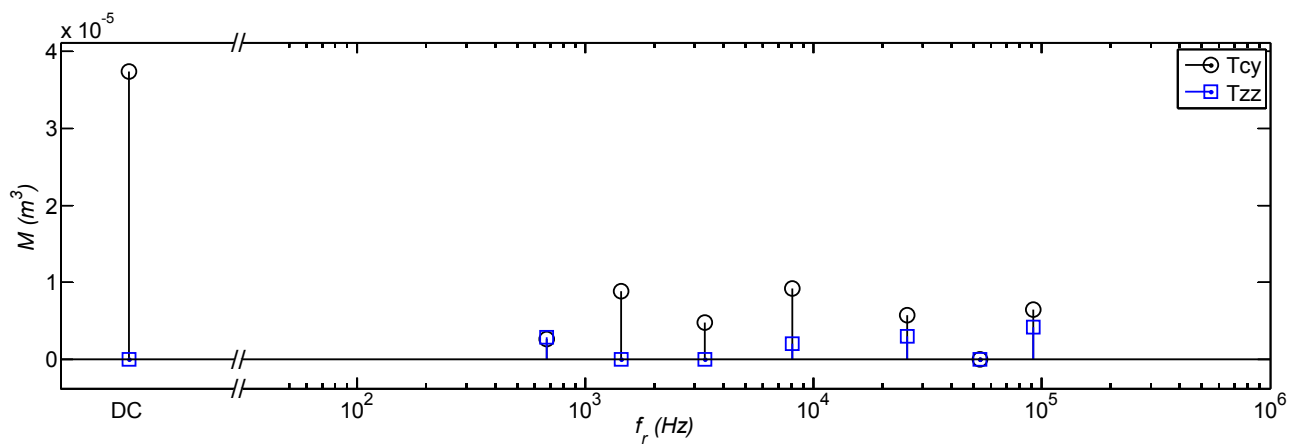


Fig. 10. Estimated model parameters for an anti-personnel medium-metal landmine as a function of relaxation frequency.

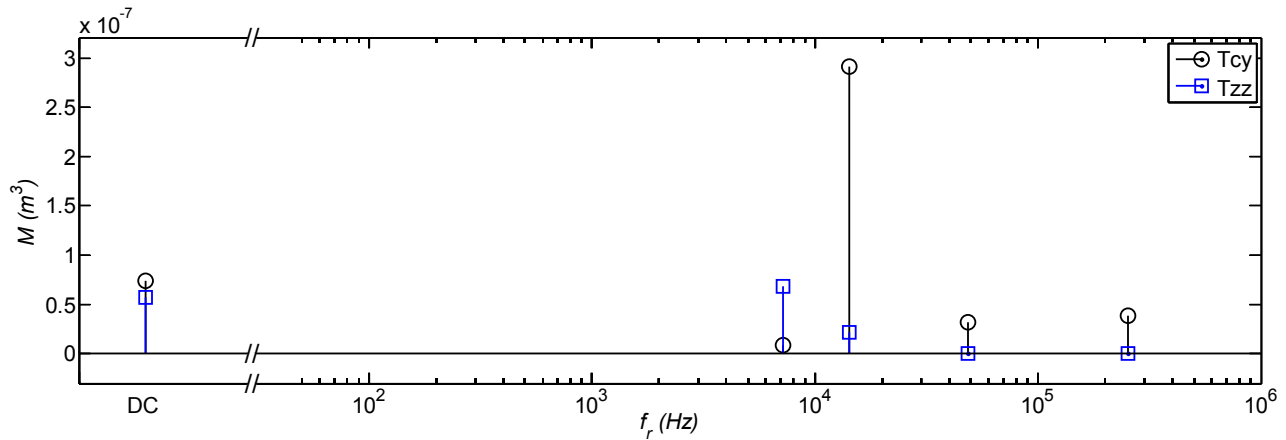


Fig. 11. Estimated model parameters for an anti-personnel low-metal landmine as a function of relaxation frequency.

6. CONCLUSIONS

An experimental facility has been established to measure the response of typical targets for EMI sensors as a function of location and orientation. A method of modeling the targets as an expansion of simple dipoles with discrete relaxations is presented along with a method to invert the measured responses to obtain the model parameters. The models are valid for any position and orientation of the target. Targets with known models were measured to establish the accuracy of the technique. Numerous other targets have been measured and their models catalogued. It is envisioned that the models derived in this work will be utilized in detection algorithms to reduce false alarm rates and increase the probability of detection for EMI sensors.

ACKNOWLEDGMENTS

This work is supported in part by the US Army Night Vision and Electronic Sensors Directorate, Science and Technology Division, Countermine Branch and in part by the U. S. Army Research Office under Contract Number W911NF-05-1-0257.

REFERENCES

- [1] G. D. Sower and S. P. Cave, "Detection and identification of mines from natural magnetic and electromagnetic resonances," in *Proc. of SPIE 2496*, Orlando, FL, USA, 1995, pp. 1015-1024.
- [2] C. E. Baum, "Detection and identification of mines from natural magnetic and electromagnetic resonances," in *Detection and identification of visually obscured targets*, C. E. Baum, Ed., ed Philadelphia: Talor and Francis, 1999, pp. 163-218.
- [3] L. Collins, *et al.*, "An improved Bayesian decision theoretic approach for land mine detection," *Geoscience and Remote Sensing, IEEE Transactions on*, vol. 37, pp. 811-819, 1999.
- [4] G. Ping, *et al.*, "Classification of landmine-like metal targets using wideband electromagnetic induction," *Geoscience and Remote Sensing, IEEE Transactions on*, vol. 38, pp. 1352-1361, 2000.
- [5] E. B. Fails, *et al.*, "Performance of a four parameter model for modeling landmine signatures in frequency domain wideband electromagnetic induction detection systems," in *Proc. of the SPIE 6553*, 2007.
- [6] S. E. Yuksel, *et al.*, "Hierarchical Methods for Landmine Detection with Wideband Electro-Magnetic Induction and Ground Penetrating Radar Multi-Sensor Systems," in *Geoscience and Remote Sensing Symposium, 2008. IGARSS 2008. IEEE International*, 2008, pp. II-177-II-180.
- [7] G. D. Larson and J. Waymond R. Scott, "Automated, non-metallic measurement facility for testing and development of electromagnetic induction sensors for landmine detection," in *Proc. of the SPIE 7303*, 2009.

- [8] W. R. Scott, "Broadband Array of Electromagnetic Induction Sensors for Detecting Buried Landmines," in *Geoscience and Remote Sensing Symposium, 2008. IGARSS 2008. IEEE International*, 2008, pp. II-375-II-378.
- [9] H. Vesselle and R. E. Collin, "The signal-to-noise ratio of nuclear magnetic resonance surface coils and application to a lossy dielectric cylinder model. I. Theory," *Biomedical Engineering, IEEE Transactions on*, vol. 42, pp. 497-506, 1995.
- [10] K. F. Casey and B. A. Baertlein, "An overview of Electromagnetic methods in subsurface detection," in *Detection and identification of visually obscured targets*, C. E. Baum, Ed., ed Philadelphia: Talor and Francis, 1999, pp. 9-46.
- [11] G. Arfken, *Mathematical Methods for Physicists*, Second ed. San Diego, CA: Academic Press, 1985.
- [12] M. H. Wei, *et al.*, "Robust Estimation of the Discrete Spectrum of Relaxations for Electromagnetic Induction Responses," *Geoscience and Remote Sensing, IEEE Transactions on*, vol. 48, pp. 1169-1179, 2010.
- [13] C. E. Baum, "The magnetic polarizability dyadic and point symmetry," in *Detection and identification of visually obscured targets*, C. E. Baum, Ed., ed Philadelphia: Talor and Francis, 1999, pp. 219-242.

Application of ℓ_p -regularized Least Squares For $0 \leq p \leq 1$ in Estimating Discrete Spectrum of Relaxations For Electromagnetic Induction Responses

Mu-Hsin Wei^a, Waymond R. Scott^a, Jr., James. H. McClellan^a, and Gregg D. Larson^b

^a School of Electrical and Computer Engineering;

^b School of Mechanical Engineering

Georgia Institute of Technology, Atlanta, Georgia 30332

ABSTRACT

Broadband EMI sensors have been shown to be capable of detecting and discriminating mines and subsurface explosive objects. It is advantageous to model the EMI frequency response of a target in terms of a discrete spectrum model (or equivalently a sum of real exponentials in the time domain) that is valuable in discrimination. However, in practice it is difficult to obtain the model parameters from measurements. We previously proposed a constrained linear method that can robustly estimate the model parameters when they are nonnegative. In this paper, we present a modified ℓ_p -regularized least squares algorithm, for $0 \leq p \leq 1$, that eliminates the nonnegative constraint. Using synthesized data and lab measurements, the proposed spectrum estimation method is shown to be effective. The results suggest that the proposed method can be used to obtain spectrum of targets for discrimination. We also propose a regularization parameter selection rule for the ℓ_p minimization.

Keywords: Electromagnetic induction (EMI), discrete spectrum of relaxation frequencies (DSRF), sum of exponentials, ℓ_1 minimization, target discrimination, detection

1. INTRODUCTION

Recent research has shown the use of broadband electromagnetic induction (EMI) sensors together with advanced signal processing are capable of discriminating between certain types of buried targets.^{1,2} In discrimination, it is advantageous to model the EMI response as a sum of real exponentials in the time domain or, equivalently, a discrete spectrum model in the frequency domain. Since the relaxation frequencies in the model are invariant to the target's relative orientation and position to the sensor, they can be used as a stable feature of a target.

The EMI frequency response $H(\omega)$ of a metallic target can be expressed as:³

$$H(\omega_n) = c_0 + \sum_{k=1}^K \frac{c_k}{1 + j\omega_n/\zeta_k}, \quad n = 1, 2, \dots, N \quad (1)$$

where c_0 is the shift, K the model order, c_k the real spectral amplitudes, ζ_k the relaxation frequencies, and ω_n the frequencies at which $H(\omega)$ is sampled. The parameter set $S = \{(\zeta_k, c_k) : k = 1 \dots K\}$ is called the Discrete Spectrum of Relaxation Frequencies (DSRF) or simply the spectrum; each pair (ζ_k, c_k) is one relaxation.

It is difficult in practice, however, to obtain the spectral parameters ζ_k and c_k from a given $H(\omega)$. The primary difficulty comes from when the model order K is unknown, the number of measurements N is small, or the model parameters must be real. Most existing methods require a good guess of K for the estimation process to converge. But prior knowledge of K is usually unavailable. Even when the estimation process does converge, the estimates could be far from the true values.⁴ In addition, existing methods may return complex estimates that lack of physical meaning. We previously proposed a constraint linear method that can robustly estimate DSRFs that are free from the difficulties described above.⁵ The method however presumes nonnegative spectra for the targets.

Further author information: (Send correspondence to Mu-Hsin Wei)

Mu-Hsin Wei: E-mail: m.wei@gatech.edu

Detection and Sensing of Mines, Explosive Objects, and Obscured Targets XV,
edited by Russell S. Harmon, John H. Holloway Jr., J. Thomas Broach, Proc. of SPIE
Vol. 7664, 76640F · © 2010 SPIE · CCC code: 0277-786X/10/\$18 · doi: 10.1117/12.852397

In this paper, we propose a more general estimation method using ℓ_p -regularized least squares ($0 \leq p \leq 1$) that can estimate spectra consisting of relaxations of mixed signs (bipolar). This proposed method first samples a range of relaxation frequencies, then linearize the estimation problem, and finally solve the problem using an approximated ℓ_p -regularized least squares. As argued by Chartrand, more accurate estimates may be obtained using $p < 1$ than $p = 1$.⁶ The ℓ_p minimization involves selecting a regularization parameter, which is also discussed in this paper. As with the previously proposed constrained optimization method, the ℓ_p method proposed here always returns real model parameters and is stable under noise.

The proposed method is found to be effective from tests on synthetic and laboratory data under various noise levels. Estimating the DSRF from field data also demonstrates that the proposed method can be used in practice. In the future, more work can be done on developing target discrimination algorithms based on the estimated DSRF. In addition, more work can be put into creating a better selection rule for the regularization parameter.

2. ESTIMATION METHOD

The usual approach to estimating the DSRF (i.e., the ζ_k and c_k) is to perform a nonlinear iterative search. However, we follow the strategy of basis pursuit that linearizes the estimation problem by sampling the relaxation frequencies.⁷ The estimation problem then becomes

$$\begin{bmatrix} H(\omega_1) \\ H(\omega_2) \\ \vdots \\ H(\omega_N) \end{bmatrix} = \underbrace{\begin{bmatrix} 1 & \frac{1}{1+j\omega_1/\tilde{\zeta}_1} & \frac{1}{1+j\omega_1/\tilde{\zeta}_2} & \cdots & \frac{1}{1+j\omega_1/\tilde{\zeta}_M} \\ 1 & \frac{1}{1+j\omega_2/\tilde{\zeta}_1} & \frac{1}{1+j\omega_2/\tilde{\zeta}_2} & \cdots & \frac{1}{1+j\omega_2/\tilde{\zeta}_M} \\ \vdots & \vdots & \vdots & \ddots & \vdots \\ 1 & \frac{1}{1+j\omega_N/\tilde{\zeta}_1} & \frac{1}{1+j\omega_N/\tilde{\zeta}_2} & \cdots & \frac{1}{1+j\omega_N/\tilde{\zeta}_M} \end{bmatrix}}_{\tilde{\mathbf{Z}}} \begin{bmatrix} \tilde{c}_0 \\ \tilde{c}_1 \\ \tilde{c}_2 \\ \vdots \\ \tilde{c}_K \end{bmatrix} + error$$

$$\mathbf{h} = \tilde{\mathbf{Z}}\tilde{\mathbf{c}} + error \quad (2)$$

where $\tilde{\zeta}_m$ are the *sampled* relaxation frequencies, \tilde{c}_m the corresponding spectral amplitude estimators, \mathbf{h} the observation vector, and $\tilde{\mathbf{Z}}$ the overcomplete dictionary. $\tilde{\mathbf{c}}$ is the weighted selector vector containing the shift estimator \tilde{c}_0 followed by the spectral amplitude estimators. We expect the solution for $\tilde{\mathbf{c}}$ to have many zero elements because $M \gg K$, i.e., $\tilde{\mathbf{c}}$ will be sparse.

The sampled ζ are generated by enumerating a large set of M *possible* relaxation frequencies uniformly distributed in the log- ζ space ($M \gg K$). While Austin *et al.* suggests sampling based on the Fisher information of the model,⁸ we found that uniform sampling produces a very similar set of sampled ζ . The uniform sampling, however, is simpler.

Since $\tilde{\mathbf{c}}$ is sparse, we estimate it using the ℓ_p -regularized least squares technique, for $0 \leq p \leq 1$, because it promotes sparse solutions.⁹ The objective function is

$$\arg \min_{\tilde{\mathbf{c}}} \|\tilde{\mathbf{Z}}'\tilde{\mathbf{c}} - \mathbf{h}'\|_2^2 + \lambda \|\tilde{\mathbf{c}}\|_p^p, \quad 0 \leq p \leq 1 \quad (3)$$

$$\text{where } \tilde{\mathbf{Z}}' = \begin{bmatrix} \Re(\tilde{\mathbf{Z}}) \\ \Im(\tilde{\mathbf{Z}}) \end{bmatrix}, \quad \mathbf{h}' = \begin{bmatrix} \Re(\mathbf{h}) \\ \Im(\mathbf{h}) \end{bmatrix},$$

and λ is the regularization parameter. Separating the real and imaginary parts in $\tilde{\mathbf{Z}}$ makes the whole system real and produces only real estimates. Ideally, in the optimal $\tilde{\mathbf{c}}$, only those \tilde{c}_m with corresponding $\tilde{\zeta}_m$ that are near a true ζ_k will be nonzero, and they will take on the correct spectral amplitudes c_k . It follows that a DSRF can then be deduced from the nonzero estimated \tilde{c}_m and their corresponding $\tilde{\zeta}_m$.

The ℓ_p -regularized least squares solution for $p < 1$ can be approximated by an iteratively reweighted ℓ_1 algorithm proposed by Candès *et al.*⁹ The weights are updated as suggested in Ref. 10. We also adopt the ϵ -regularization technique used in the same paper. In summary, (3) is approximated by (see also Ref. 11):

Algorithm 1: Approximated ℓ_p -regularized least squares

Input: $\tilde{\mathbf{Z}}', \mathbf{h}', p, \lambda, \tilde{\mathbf{c}}^0$

```
1  $\tilde{\mathbf{c}}^n \leftarrow \tilde{\mathbf{c}}^0$ 
2 for  $k \leftarrow 0$  to  $-8$  step  $-1$  do
3    $\epsilon \leftarrow 10^k$ 
4   repeat
5      $\tilde{\mathbf{c}}^{n-1} \leftarrow \tilde{\mathbf{c}}^n$ 
6      $w_i^n \leftarrow (|\tilde{c}_i^{n-1}| + \epsilon)^{p-1}$ 
7      $\tilde{\mathbf{c}}^n \leftarrow \arg \min \|\tilde{\mathbf{Z}}' \tilde{\mathbf{c}} - \mathbf{h}'\|_2^2 + \lambda \sum_{i=1}^{M+1} w_i^n |\tilde{c}_i|$ 
8   until  $\|\tilde{\mathbf{c}}^n - \tilde{\mathbf{c}}^{n-1}\|_2 < \sqrt{\epsilon}/100$ 
9 return  $\tilde{\mathbf{c}}^n$ 
```

The ℓ_1 minimization problem in step 7 is solved by `l1_ls`, a MATLAB optimizer proposed by Kim *et al.*¹² We have also found that normalizing the input data \mathbf{h} , as well as the columns of $\tilde{\mathbf{Z}}'$, to have unit ℓ_2 norm increases the accuracy of estimation. Setting entries of $\tilde{\mathbf{c}}^0$ to all ones also seems to be effective. However, the solution is insensitive to the initial value of $\tilde{\mathbf{c}}^0$. It can also be set to other values such as the solution to $\min \|\tilde{\mathbf{Z}}' \tilde{\mathbf{c}} - \mathbf{h}'\|_2$.¹⁰ The nonzero entries of $\tilde{\mathbf{c}}$ selected by (3) along with the corresponding $\tilde{\zeta}_m$ are the relaxations needed in the estimated DSRF, $\hat{S} = \{(\hat{\zeta}_l, \hat{c}_l) : l = 1 \dots L\}$.

3. ESTIMATION RESULTS

The proposed estimation method is tested on synthetic, laboratory, and field data to show its functionality, accuracy, and stability. The hardware system used is a wideband EMI sensor operating at 21 frequencies approximately logarithmically distributed over the range 300 Hz–90 kHz (2.5 decades).¹³ The synthetic data is generated in accordance with the hardware specification. The range of ζ for estimation is chosen such that $\log(\tilde{\zeta}_{\min})$ and $\log(\tilde{\zeta}_{\max})$ are 2.45 and 6.62, respectively, i.e., 4.17 decades.

All estimations are performed with $M = 100$,⁵ and all presented spectra are normalized such that $\sum |c_i| = 1$. Spectral amplitudes less than 10^{-5} are not displayed. Unless specified, $p = 0.5$ is chosen as a representative case. The regularization parameter λ is chosen based on the method described in Section 4. Results presented in this section may achieve higher accuracy with a more sophisticated λ selection rule. Here we demonstrate the usability of the proposed algorithm with a simple λ selection rule. See Section 4 for more discussion on the choice of λ .

3.1 Dissimilarity Measure Between Two DSRFs

In order to evaluate the goodness of the estimated DSRF, we need to define a measure of dissimilarity that is appropriate for sparse spectra with multiple peaks. We use the Earth Mover's Distance (EMD)¹⁴ which quantifies the “amount of work” to morph one spectrum into the other. Strictly speaking the EMD is only defined for positive spectra, but we can account for negative spectral amplitudes by defining the distance function between two relaxations (ζ_i, c_i) and $(\hat{\zeta}_j, \hat{c}_j)$ to be:

$$d_{ij} = \begin{cases} |\log \zeta_i - \log \hat{\zeta}_j| & , c_i \hat{c}_j \geq 0 \\ 1 + |\log \zeta_i - \log \hat{\zeta}_j| & , c_i \hat{c}_j < 0 \end{cases}$$

which penalizes relaxations with different signs. The penalization can be defined differently as suitable. Spectra are made nonnegative and normalized ($\sum |c_i| = 1$) prior to the EMD computation. Finally, notice that the EMD is measured in decades because it is examined in \log - ζ space.

3.2 Synthetic Six-relaxation DSRF

We test the proposed ℓ_p method (using $p = 0.5$) on a six-relaxation DSRF synthesized at 70 dB SNR with additive white Gaussian noise (Fig. 1). This is a case that cannot be handled by traditional nonlinear parameter optimization,⁴ or the nonnegative linear method.⁵ Though shifted slightly, all six relaxation frequencies are recovered by using **Algorithm 1**. The estimation result is satisfactory because the model parameters are real and the deviation from the truth is small. The EMD between the estimated and the true DSRF is 0.15 decades. There is one extra relaxation near $\log\zeta=2$ in the estimated spectrum, but it has a small amplitude and can be neglected.

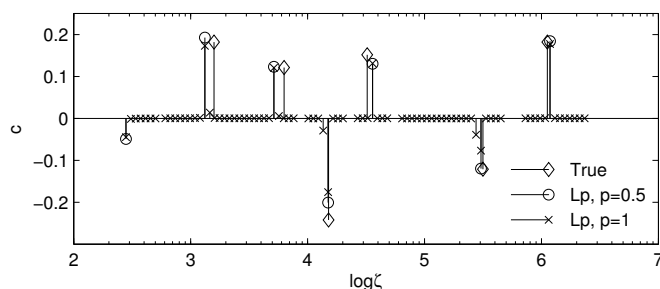


Figure 1: Theoretical and estimated DSRF of a six relaxation target.

The same spectrum is also estimated with $p = 1$ using `l1_ls`. In this case, many extra relaxations are introduced by the fitting process (Fig. 1). However, because the extra relaxations are very small in amplitude, the EMD is still small – 0.16 decades. Real targets are not likely to have a spectrum with many small relaxations around a strong relaxation. In fact, Baum argues that physical relaxation frequencies are discrete.³ However, the small relaxations introduced by $p = 1$ seem to give a continuous spectrum of relaxation frequencies. In this sense, $p < 1$ gives a sparser solution that more accurately resembles the expected physical spectrum even though this may not always be reflected in the EMD measure.

3.3 Signal to Noise Ratio

To see how the proposed method performs in noise, a Monte Carlo simulation versus SNR is performed. The true spectrum is from a target with a four-relaxation DSRF including negative relaxations. The simulation result shows the robustness of the estimation method at different SNRs (Fig. 2). The EMD between the estimate and the truth increases as the SNR decreases. This suggests that the proposed method is usable in a range of SNR where the EMD is below some threshold. This threshold, however, depends on the application of the estimated spectrum. For example, if the DSRFs are used as features for classification, a more robust classifier may tolerate worse estimations and, therefore, allow lower SNR. For our purpose, spectra with an EMD below 0.1 are considered visually similar, those with an EMD above 0.2 exhibit visual differences, but may still resemble each other. Thus, we consider 50 dB as the threshold SNR. In our laboratory measurements, a typical SNR for loop targets is 70 dB.

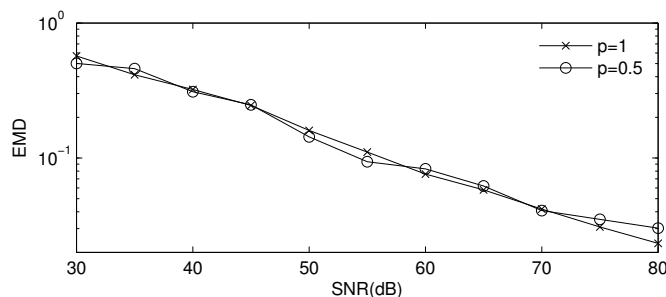


Figure 2: Monte Carlo simulation on goodness of estimation vs. SNR. Sample size is 100 per SNR.

3.4 Laboratory Data

We verify the functionality of the estimation method on laboratory data where we know the theoretical DSRF. An automated, non-metallic measurement facility is used to measure EMI responses of a target at various positions and orientations relative to the sensor.¹⁵ We observe that the proposed method is effective with laboratory data.

A target that consists of three mutually orthogonal copper loops is examined. The loop diameters and thickness are 3/20, 4/30, and 5/36, respectively in cm/AWG(American Wire Gauge). We pick a specific orientation and position relative to the EMI sensor that best shows the existence of bipolar relaxation amplitudes in a spectrum. The target frequency response of this configuration is shown in Fig. 3a, the SNR was estimated to be 38 dB, and its estimated DSRF in Fig. 3b. Theoretical data are also displayed. We see that the estimate and theory agree well, and the EMD between the theoretical and estimated DSRF is 0.10 decades.

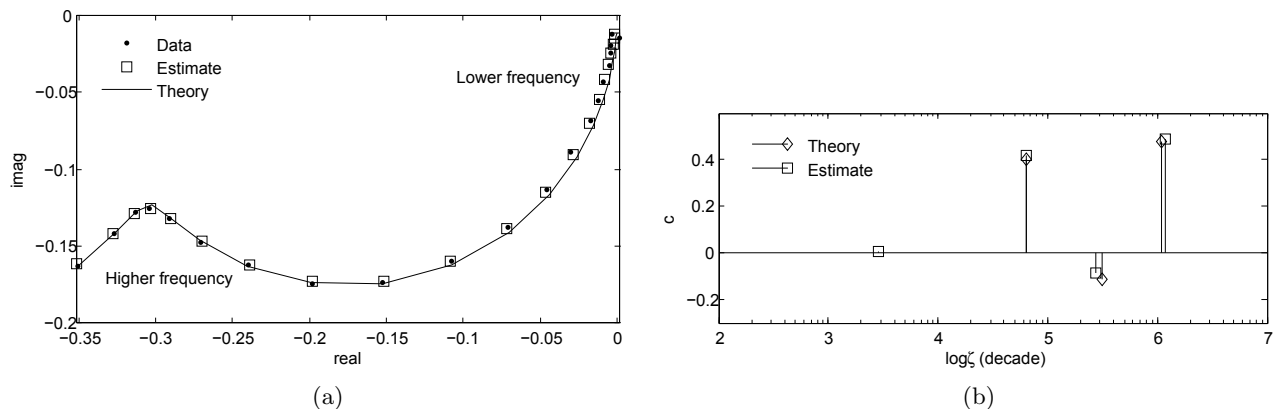


Figure 3: (a) Frequency response of three mutually orthogonal copper loops. The frequency response is normalized such that $\|\mathbf{h}\|_2 = 1$. (b) Theoretical and estimated DSRF of the response in (a).

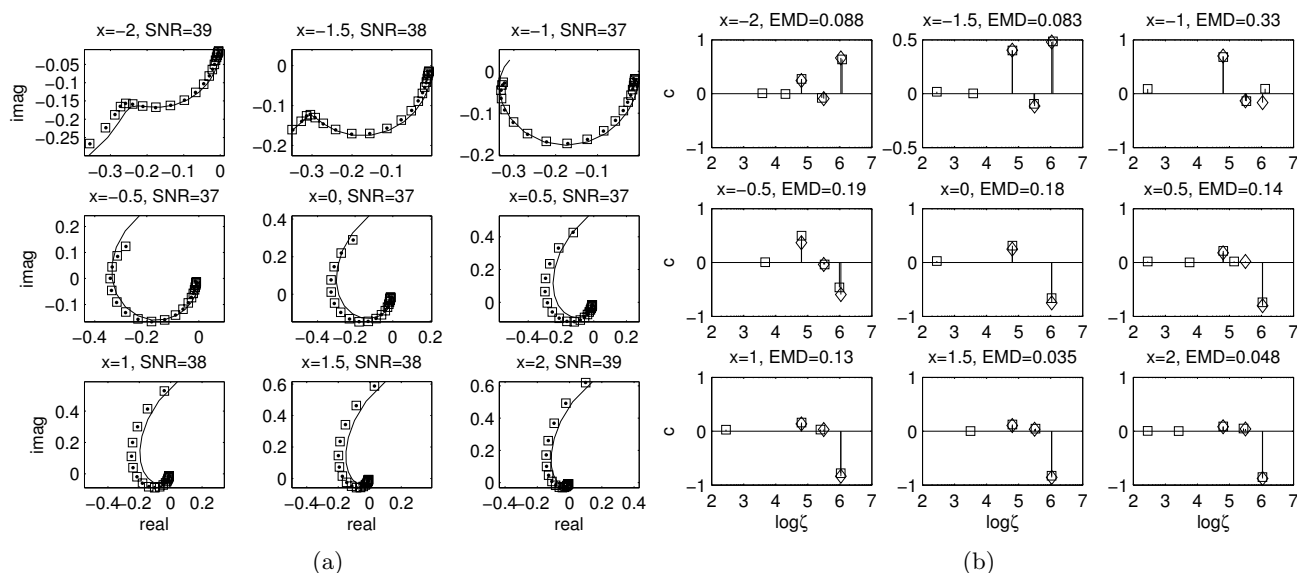


Figure 4: The plots share the same annotation as Fig. 3. (a) Frequency responses of the three mutually orthogonal copper loops at nine different x locations. (b) Theoretical and estimated DSRF of the corresponding responses in (a). The SNR is measured in dB, x positions in cm, and EMD in decades.

Next we examine the changes in the DSRF as the target moves relative to the EMI sensor. The same target configured at a fixed orientation is displaced at different positions along a horizontal axis (x). The vertical distance between the target and sensor is 6 cm. The EMI sensor is located at $x = 0$. Overall, the theory and measurement agree (Fig. 4).

As expected from the theory, while the frequency response changes dramatically as the target moves along the x axis, the corresponding change in the spectral domain only occurs in the spectral amplitudes. The three dominant relaxation frequencies remain unchanged. The proposed method successfully estimates the spectra that agree with this phenomenon. All three relaxation frequencies are consistently estimated. The extra relaxations all have small amplitudes that can be safely ignored. This invariant property of the relaxation frequencies makes the DSRF valuable especially for target discrimination.

3.5 Field Data

Here we demonstrate the functionality of the proposed method when applied to field data. From the consistency of the estimated DSRF, we suggest that these spectra can indeed be used as features for target discrimination. The proposed method is applied to three types of landmines. For each type of mine, measurements were collected from several mines buried at different depths and locations.

When estimating the DSRF from field data, we observe that the estimation method sometimes returns a single relaxation at ζ_1 or ζ_M (the endpoints of the sampled ζ domain), as we saw in the estimate in Fig. 1. This artifact could be easily removed manually or by a weighted least squares term. For this section, we adopt the latter approach to eliminate estimated relaxations at endpoints. This is simply done by replacing $\tilde{\mathbf{Z}}$ and \mathbf{h} in Eq. (3) with $\tilde{\mathbf{Z}}_w$ and \mathbf{h}_w , respectively, where

$$\begin{aligned}\tilde{\mathbf{Z}}_w &= W\tilde{\mathbf{Z}}, \\ \mathbf{h}_w &= W\mathbf{h},\end{aligned}$$

and W is a diagonal matrix with weights $[w_1, w_2, \dots, w_N]$ on the diagonal. To discourage over fitting at endpoints, we put less weight on the highest and lowest frequencies.

Using the weighted method, the DSRF of each sample was estimated and then plotted together with others of the same type (Figs. 5–7). For all three types of mine, the estimated DSRFs have consistent shapes. The relaxations that appear to be inconsistent are small in amplitude. For each type of mine the stronger relaxations share the same relaxation frequencies. While the true spectra of these field targets are unknown, from the consistency of the estimated spectrum, we have good faith that what is obtained is accurate. Various simulations and laboratory results from previous sections also support this view.

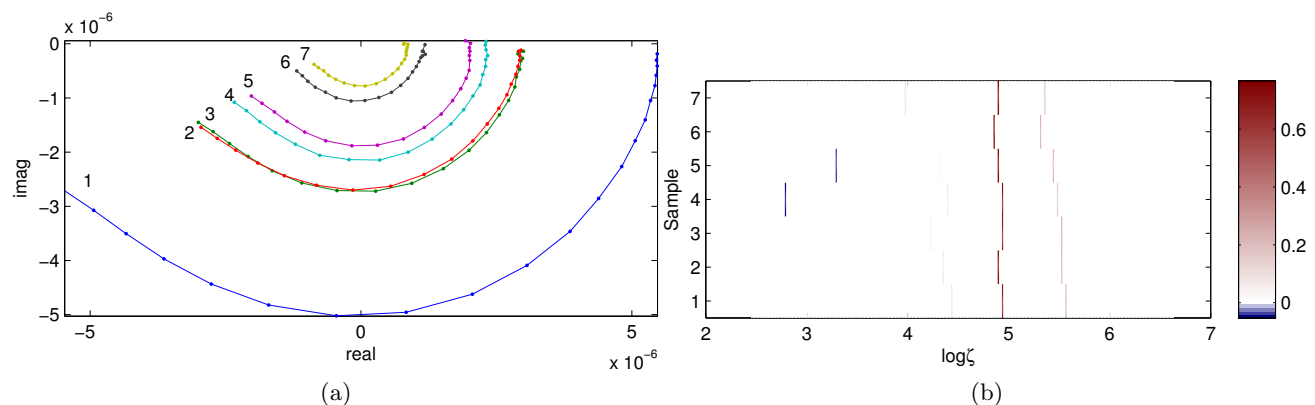


Figure 5: Frequency responses and estimated DSRFs of seven Type-I mines: a low-metal content, magnetic, weak EMI response antipersonnel mines. The SNR ranges from about 20 dB to 35 dB. (a) Raw frequency responses. (b) Estimated DSRFs. The spectral amplitude is represented by the color intensity.

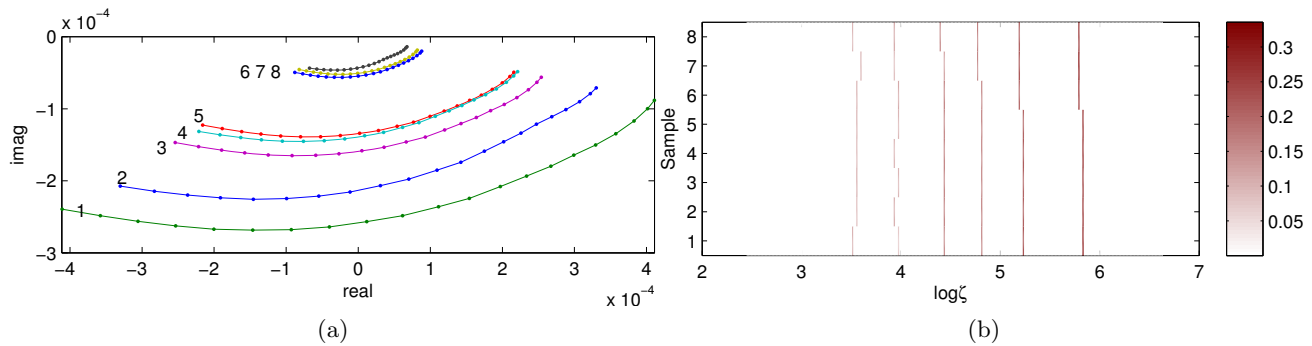


Figure 6: Frequency responses and estimated DSRFs of eight Type-II mines: a medium-metal content, magnetic, strong EMI response antipersonnel mine. The SNR ranges from about 55 dB to 70 dB. (a) Raw frequency responses. (b) Estimated DSRFs. The spectral amplitude is represented by the color intensity.

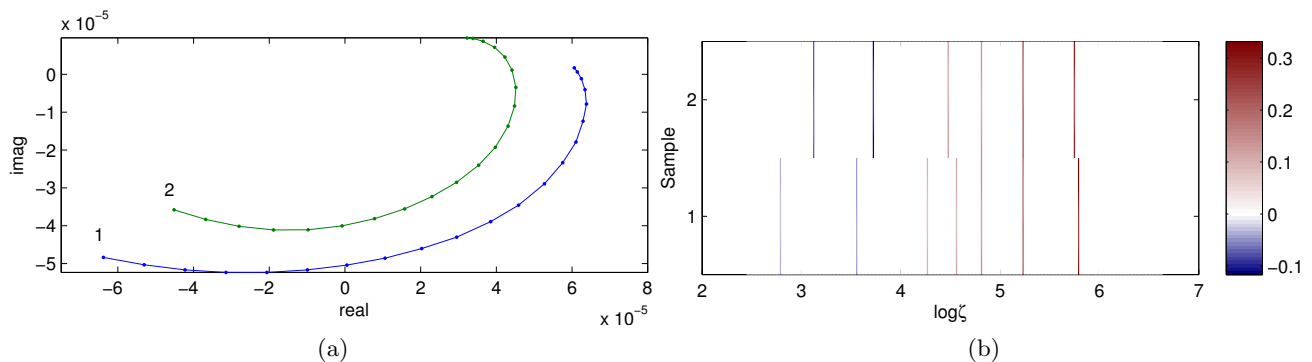


Figure 7: Frequency responses and estimated DSRFs of two Type-III mines: a medium-metal content, strong EMI response antipersonnel mine. The SNR is around 50 dB. (a) Raw frequency responses. (b) Estimated DSRFs. The spectral amplitude is represented by the color intensity.

4. CHOOSING λ

In this section, we examine the behavior of the proposed method in relation to the regularization parameter λ . We observe that the optimal λ that gives the minimum estimation error is quasi independent of the model order and has a simple relation to the SNR. We propose a simple λ selection formula that exploits this observation. All discussions and figures presented here assume $p = 0.5$ unless otherwise specified.

To understand how the goodness of estimation changes with λ and SNR, we conduct a cross-validation-like simulation. First, we build a collection of synthetic spectra with different model orders and a variety of distributions of relaxations. For each spectrum at a fixed SNR, the spectrum is estimated 100 times for each λ within a range, and the average goodness of fit, measured by the EMD between the available truth and the estimate, is recorded. This is done for a range of SNRs.

The simulation result (Fig. 8a) shows that for each model order the EMD (error) surface is well-behaved (i.e., smooth) with respect to the SNR and λ . Moreover, the surfaces are convex-shaped, implying that the minimum EMD is achievable by a unique λ for a specific model order and SNR. The wide valley of the surface also shows that the goodness of estimation is not very sensitive near the optimal λ .

On the other hand, we observe that for all model orders, the near-minimum EMD (the valley of the surfaces) occur in about the same SNR- λ region. This means that a single optimal selection rule may be applicable for all model orders. We confirm that this is possible when we average the EMD surfaces of different model orders (Fig. 8b). The averaged surface still exhibits all properties of a single model order surface - smooth, convex, and wide valley. From the averaged surface, we observe that using only the SNR value, we can pick a λ that is near optimal for all model orders. Tracing out the optimal λ at each SNR, we find that the optimal λ curve is almost linear (Fig. 8b). Then, intuitively, we approximate the optimal λ with a semilog function of SNR. This is done

by fitting the optimal $\log\lambda$ curve with a linear function. Weights may be added to promote certain SNR's that are more important.

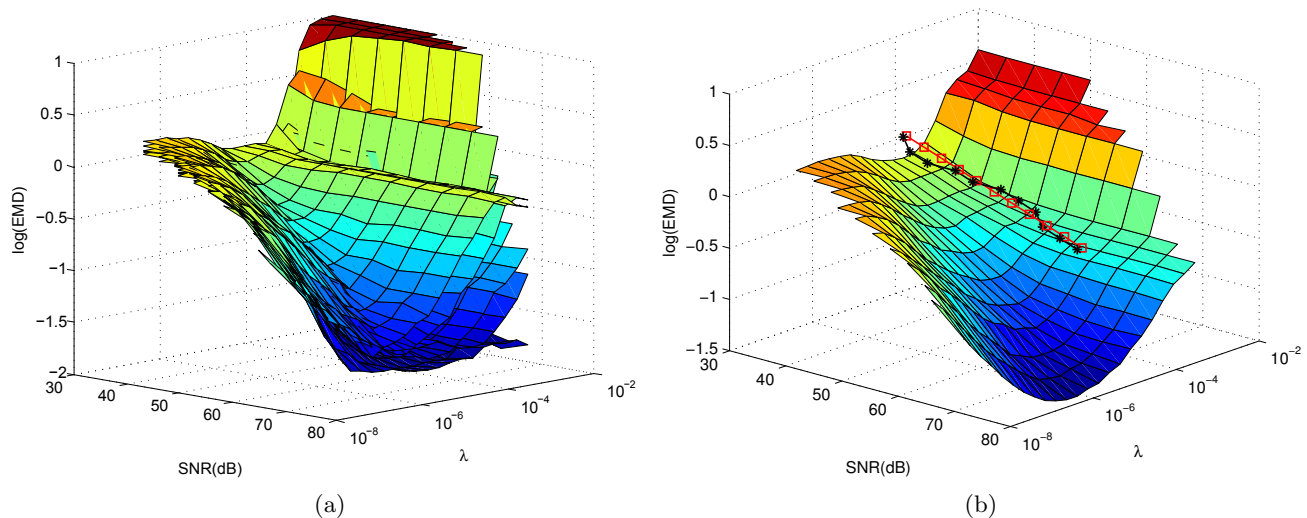


Figure 8: (a) Monte Carlo simulation of the goodness of estimation (EMD) of spectra of different model orders (one to six). Each spectrum constitutes one surface in the figure. (b) Average of EMD surfaces in (a). The curve with asterisk markers traces out the optimal λ 's. The line with square markers approximates the optimal λ 's.

For our problem setup, the λ is chosen by (also shown in Fig. 8b)

$$\log \lambda = -0.05 \cdot \text{SNR} - 2.2 \quad (4)$$

Since the surface has a wide-valley, the resulting λ selection rule is near-optimal as long as it lies in the valley, which is true in this case. In practice, this $\log\lambda$ selection rule that is linear in SNR allows the regularization parameter to be determined with negligible computation time. When processing the laboratory data, we use (4) along with an estimate of the SNR to determine λ for use in **Algorithm 1**. The same empirical method can be repeated for other p 's, and the result is also a linear relationship between $\log \lambda$ and SNR.

ACKNOWLEDGMENTS

This work is supported in part by the US Army REDCOM CERDEC Night Vision and Electronic Sensors Directorate, Science and Technology Division, Countermine Branch and in part by the U. S. Army Research Office under Contract Number W911NF-05-1-0257.

REFERENCES

- [1] Gao, P., Collins, L., Garber, P. M., Geng, N., and Carin, L., "Classification of landmine-like metal targets using wideband electromagnetic induction," *IEEE Trans. Geosci. Remote Sens.* **38**, 1352–1361 (May 2000).
- [2] Fails, E. B., Torriane, P. A., Scott, Jr., W. R., and Collins, L. M., "Performance of a four parameter model for modeling landmine signatures in frequency domain wideband electromagnetic induction detection systems," *Proc. SPIE* **6553**, 65530D (Apr. 2007).
- [3] Baum, C. E., "On the singularity expansion method for the solution of electromagnetic interaction problems," Interaction Notes 88, Air Force Weapons Laboratory (1971).
- [4] Das, Y. and McFee, J. E., "Limitations in identifying objects from their time-domain electromagnetic induction response," *Proc. SPIE* **4742**, 776–788 (Apr. 2002).
- [5] Wei, M., Scott, Jr., W. R., and McClellan, J. H., "Robust estimation of the discrete spectrum of relaxations for electromagnetic induction responses," *IEEE Trans. Geosci. Remote Sens.* **48**, 1169–1179 (Mar. 2010).

- [6] Chartrand, R., "Exact reconstruction of sparse signals via nonconvex minimization," *IEEE Signal Process. Lett.* **14**(10), 707–710 (2007).
- [7] Chen, S. S., Donoho, D. L., and Saunders, M. A., "Atomic decomposition by basis pursuit," *SIAM Review* **43**(1), 129–159 (2001).
- [8] Austin, C. D., Ertin, E., Ash, J. N., and Moses, R. L., "On the relation between sparse sampling and parametric estimation," *Proc. DSP Workshop*, 387–392 (Jan. 2009).
- [9] Candès, E. J., Wakin, M. B., and Boyd, S. P., "Enhancing sparsity by reweighted ℓ_1 minimization," *J. Fourier Anal. Appl.* **14**(5), 877–905 (2008).
- [10] Chartrand, R. and Yin, W., "Iteratively reweighted algorithms for compressive sensing," *Proc. ICASSP*, 3869–3872 (Mar. 2008).
- [11] Figueiredo, M. A. T. and Nowak, R. D., "A bound optimization approach to wavelet-based image deconvolution," *Proc. ICIP* **2**, 782–785 (2005).
- [12] Kim, S. J., Koh, K., Lustig, M., and Boyd, S., "An efficient method for compressed sensing," *Proc. ICIP* **3**, 117–120 (2007).
- [13] Scott, Jr., W. R., "Broadband array of electromagnetic induction sensors for detecting buried landmines," *Proc. IGARSS* (July 2008).
- [14] Rubner, Y., Tomasi, C., and Guibas, L. J., "A metric for distributions with applications to image databases," *Proc. ICCV*, 59–66 (Jan. 1998).
- [15] Larson, G. D. and Scott, Jr., W. R., "Automated, non-metallic measurement facility for testing and development of electromagnetic induction sensors for landmine detection," *Proc. SPIE*, 73030X (Apr. 2009).

CALIBRATION TECHNIQUE FOR BROADBAND ELECTROMAGNETIC INDUCTION SENSORS

Waymond R. Scott, Jr.

School of Electrical and Computer Engineering
Georgia Institute of Technology
Atlanta, GA, USA 30332-0250

ABSTRACT

A technique for calibrating broadband electromagnetic induction (EMI) sensors is presented. The technique is very simple and uses a powdered ferrite core as a calibration standard. The purpose of the calibration is to improve the accuracy of the sensor which enhances its ability to discriminate between different types of targets.

Approved for public release; distribution is unlimited.

Index Terms— *Electromagnetic induction, EMI, landmine detection, sensor*

1. INTRODUCTION

Broadband electromagnetic induction (EMI) sensors have been shown to be able to reduce false alarm rates and increase the probability of detecting landmines [1-4]. This requires that the EMI sensor measure the response of both the target and the soil very accurately. Although it is possible to carefully design the sensor to achieve highly accurate measurements without any calibration, the resulting restrictions place limits on some of the possible hardware configurations that can help the performance of the system. Even if the system is designed to be highly accurate without calibration, a calibration can still improve the accuracy or at least validate it.

Several types of calibration targets were investigated. Loops of wire have a response that is easily calculated and are often used as EMI targets [5], but the calculation is only accurate for very thin wires, and the loops are also difficult to make with precision. For example, the solder joint used to connect the wire can significantly affect its response [6]. Metallic spheres have a response that can be precisely calculated if their electromagnetic properties are precisely known [5], but multiple sizes of spheres will likely be needed to calibrate the sensor over the entire frequency range.

A simple method that uses a magnetic material to calibrate the sensor is presented in this paper. The method assumes that the magnetic material is purely magnetic and does not have any eddy-current losses. Several magnetic materials were considered such as paramagnetic and

ferrimagnetic materials. The paramagnetic materials were not used because of signal to noise issues due to their weak magnetic response. Soft ferrites are engineered ferrimagnetic materials which are designed to have constant permeability and low eddy-current losses in the frequency range of the EMI sensor. Several solid ferrite cores were tried for the calibration, but the effects of the eddy currents were discernable. Finally, we settled on powdered ferrite cores which have even lower eddy-current losses. We used Magnetics Molypermalloy Powder [7] (MPP) cores with a relative permittivity of 26. The effects of eddy currents were not observed with these cores.

2. PROCEDURE

Consider an idealized EMI system, Fig.1, that consists of a sensor head that has a transmit and a receive coil which interact with a target. Here \mathbf{H}_T is the field at the target generated by the transmit coil when the coil is driven with the current I_T , and \mathbf{M} is the magnetic polarizability of the target. It can be shown by using reciprocity that the received voltage due to the target is [8]:

$$V_R = \frac{j\omega\mu}{I_R} \mathbf{H}_R^T \mathbf{M} \mathbf{H}_T \quad (1)$$

where \mathbf{H}_R is the magnetic field generated with the receiving loop driven by the current I_R . The received voltage is compared to a reference voltage to obtain the ideal response R of the system:

$$R = \frac{V_R}{V_X} = \frac{\mu}{L_X I_T I_R} \mathbf{H}_R^T \mathbf{M} \mathbf{H}_T \quad (2)$$

where $V_X = j\omega L_X I_T$ is the reference voltage from an ideal reference transformer with mutual inductance L_X which is also driven by transmit current I_T .

The response can be viewed as a projection of the magnetic polarizability which is a complex, frequency dependent, symmetric, second-rank tensor. The response forms a shape when drawn on an Argand diagram with frequency as a parameter. These shapes can be used to discriminate between different types of metal targets. It is

important that the shape of the response be measured as accurately as possible to aid in discrimination. To calibrate the system, consider a purely magnetic target, for which the magnetic polarizability is purely real and frequency independent so the ideal response will also be purely real and frequency independent.

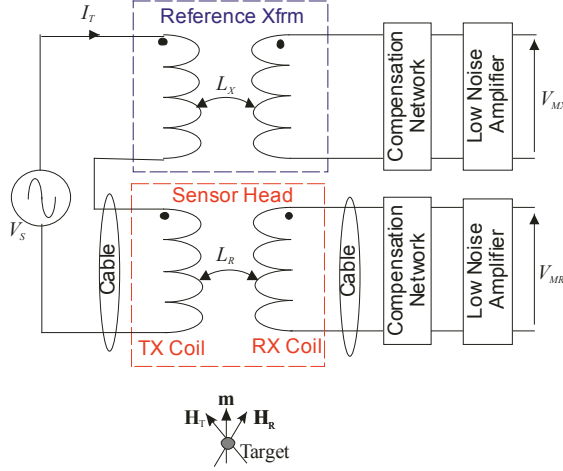


Fig. 1. Diagram of EMI system

The response R_M actually measured by the system will not be purely real and frequency independent due to imperfections in the hardware:

$$R_M(\omega_n) = \frac{V_{MR}}{V_{MX}} = S(\omega_n) \frac{G_R(\omega_n)}{G_X(\omega_n)} [R + R_C(\omega_n)] \quad (3)$$

where ω_n are the discrete measurement frequencies, G_R and G_X are the gains of data acquisition system, S accounts for the effects of the shielding, R_C accounts for the response due to the mutual coupling between the coils. Ideally, G_R , G_X , and S will be frequency independent and real; however, in a practical system they will be frequency dependent and complex. Ideally, R_C is zero, but it is finite in a practical system. G_R and G_X include the effects of the non-ideal nature of the coils, amplifiers, and digitizers. S is due to the shielding of the EMI head which partially shields the magnetic fields in addition to the electric fields at the higher frequencies [9]. This results in an error that is frequency dependent and worsens with increasing frequency.

The difference between a measurement with a target present and not present is made to eliminate the effect of R_C :

$$\begin{aligned} R'_M(\omega_n) &= R_M^{\text{Target}}(\omega_n) - R_M^{\text{No Target}}(\omega_n) \\ &= S(\omega_n) \frac{G_R(\omega_n)}{G_X(\omega_n)} R = GC(\omega_n) R \end{aligned} \quad (4)$$

Although we know that \mathbf{M} and R are real and frequency independent, we do not know their exact values so the calibration is separated into two parts: G and C . G is a real and frequency-independent gain, and C is the frequency

dependent calibration. The frequency-dependent part of the calibration is estimated as

$$C(\omega_n) = \frac{R'_M(\omega_n)}{\text{Real} \left[\frac{1}{N_i} \sum_{i=1}^{N_i} R'_M(\omega_i) \right]} \quad (5)$$

where we are assuming that the hardware imperfections have minimal effects at the lowest frequencies which is true for all of our systems: $C(\text{low frequencies}) \approx 1$. N_i is the number of frequencies used in the normalization and is typically 1 to 7 where $i=1$ corresponds to the lowest frequency. Using the same assumption, G is

$$G = S(\omega_1) \frac{G_R(\omega_1)}{G_X(\omega_1)} = \frac{G_R(\omega_1)}{G_X(\omega_1)} \quad (6)$$

since S is essentially one at the lowest frequency. Then, the calibrated measurement is

$$R_M^C(\omega_n) = \frac{R'_M(\omega_n)}{GC(\omega_n)} \quad (7)$$

3. RESULTS

The calibration technique has been used to calibrate two systems with good results. The first system (System A) which is presented in [9] and [10] is quite accurate without calibration, and the second system (System B) which has much larger coils and more turns on the coils is very inaccurate without calibration because of the interaction of the impedance of the coils and the preamplifiers.

Table I
Variation in the response to the MPP core shown in Figs. 2 and 3.

System	Uncalibrated	Calibrated
A	3%	0.06%
B	88%	1.5%

In Figs. 2 and 3 the response of the systems to a MPP ferrite core is graphed as a function of frequency which is expected to have a constant real part and a null imaginary part. This is clearly not true for the uncalibrated response of both systems, but the calibrated responses are seen to be much better. The variation in the responses before and after calibration is summarized in Table I. To obtain the calibrations C and G , numerous measurements of the MPP core response were measured with it in different positions and orientations and averaged together. For the response graphed on Figs. 2 and 3, the response was measured for a single orientation of the core using the down-track filter as is in [9, 10].

The response of these systems to a wire loop is presented in Figs. 4 and 5 both as an Argand diagram and as

a function of frequency. The theoretical response of these targets is easy to compute and is included on the graphs [5]. The calibrated response is closer to the expected result for both systems. The improvement is small but noticeable for System A, but with this small correction, the spectrums computed using the methods presented in [8, 11] were noticeably better. The improvement with System B is large and makes the results much more valuable to use in discrimination. The calibrated results also make it much easier to account for the magnetic properties of the soil within a detection algorithm.

4. ACKNOWLEDGMENT

This work is supported in part by the US Army REDCOM CERDEC Night Vision and Electronic Sensors Directorate, Science and Technology Division, Countermine Branch and in part by the U. S. Army Research Office.

4. REFERENCES

- [1] C. E. Baum, "Detection and identification of mines from natural magnetic and electromagnetic resonances," in *Detection and identification of visually obscured targets*, C. E. Baum, Ed., ed Philadelphia: Talor and Francis, 1999, pp. 163-218.
- [2] P. Gao, L. Collins, P. M. Garber, N. Geng, and L. Carin, "Classification of landmine-like metal targets using wideband electromagnetic induction," *IEEE Trans. Geosci. Remote Sens.*, vol. 38, no. 3, pp. 1352-1361, May 2000.
- [3] E. B. Fails, P. A. Torriane, W. R. Scott, Jr., and L. M. Collins, "Performance of a four parameter model for modeling landmine signatures in frequency domain wideband electromagnetic induction detection systems," in *Proc. SPIE*, 2007.
- [4] G. Ramachandran, P. D. Gader, and J. N. Wilson, "Granma: Gradient angle model algorithm on wideband EMI data for land-mine detection," *IEEE Geosci. Remote Sens. Lett.*, vol. 7, no. 3, pp. 535-539, 2010.
- [5] G. D. Sower, "Eddy current responses of canonical metallic targets theory and measurements," in *Detection and identification of visually obscured targets*, C. E. Baum, Ed., ed Philadelphia: Talor and Francis, 1999..
- [6] Lloyd S. Riggs, Larry T. Lowe, Jon E. Mooney, Thomas Barnett, Richard Ess and Frank Paca, "Simulants (decoys) for low-metallic-content mines: theory and experimental results", *Proc. SPIE 3710*, 64 (1999); doi:10.1117/12.357085
- [7] <http://www.mag-inc.com/>
- [8] W. R. Scott, Jr. and G. D. Larson, "Modeling the measured EM induction response of targets as a sum of dipole terms each with a discrete relaxation frequency," 2010 *IEEE International Geoscience and Remote Sensing Symposium*, Honolulu, HI, July 25-30, 2010.
- [9] Scott, W.R., Jr., "Broadband Electromagnetic Induction Sensor for Detecting Buried Landmines," 2007 *IEEE International Geoscience and Remote Sensing Symposium*, Barcelona, Spain, July 23 - 27, 2007.
- [10] Scott, W.R., Jr., "Broadband Array of Electromagnetic Induction Sensors for Detecting Buried Landmines," 2008 *IEEE International Geoscience and Remote Sensing Symposium*, Boston, Massachusetts, July 6 - 11, 2008.

- [11] Wei, M.-H., W. R. Scott, Jr., and J. H. McClellan, "Robust Estimation of The Discrete Spectrum of Relaxations For Electromagnetic Induction Responses," *IEEE Trans. Geoscience and Remote Sensing*, vol. 48, pp. 1169-1179, 2010.

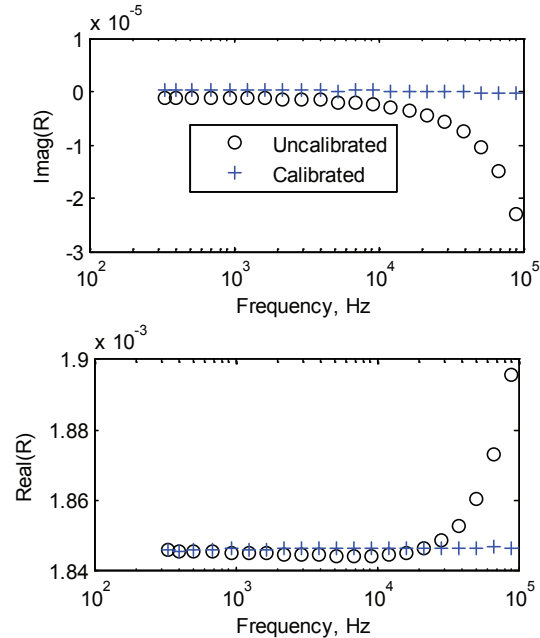


Fig. 2 Graph of the response of System A to a MPP core.

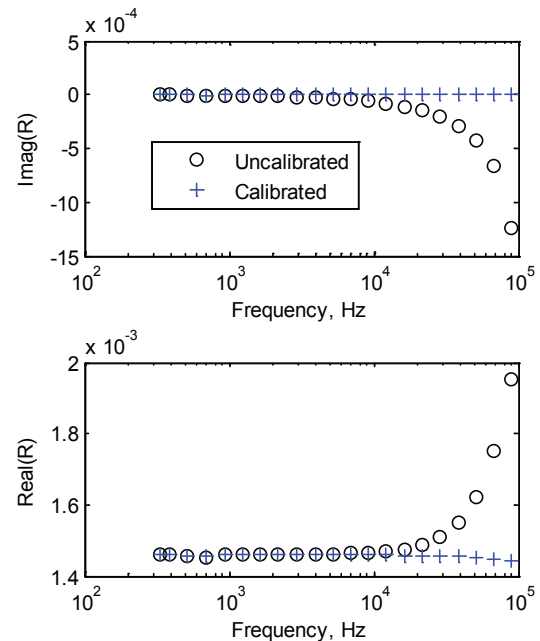


Fig. 3 Graph of the response of System B to a MPP core.

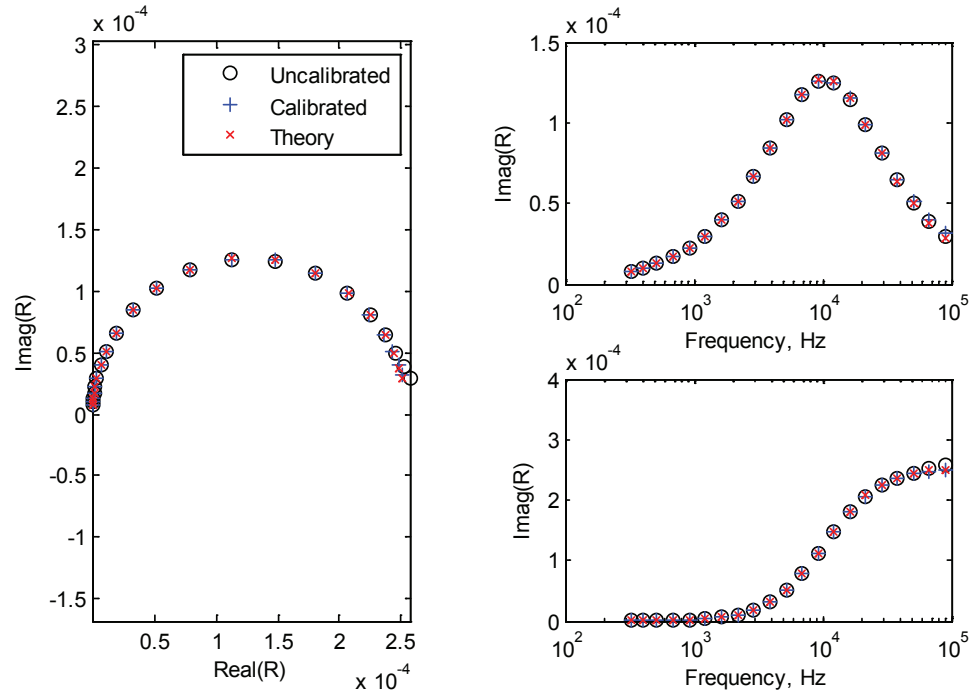


Fig. 4 Graph of the response of System A to a loop of 22 AWG wire with a circumference of 100mm. The diameter of the wire used for the theoretical computation was reduced by 2% to improve the comparison.

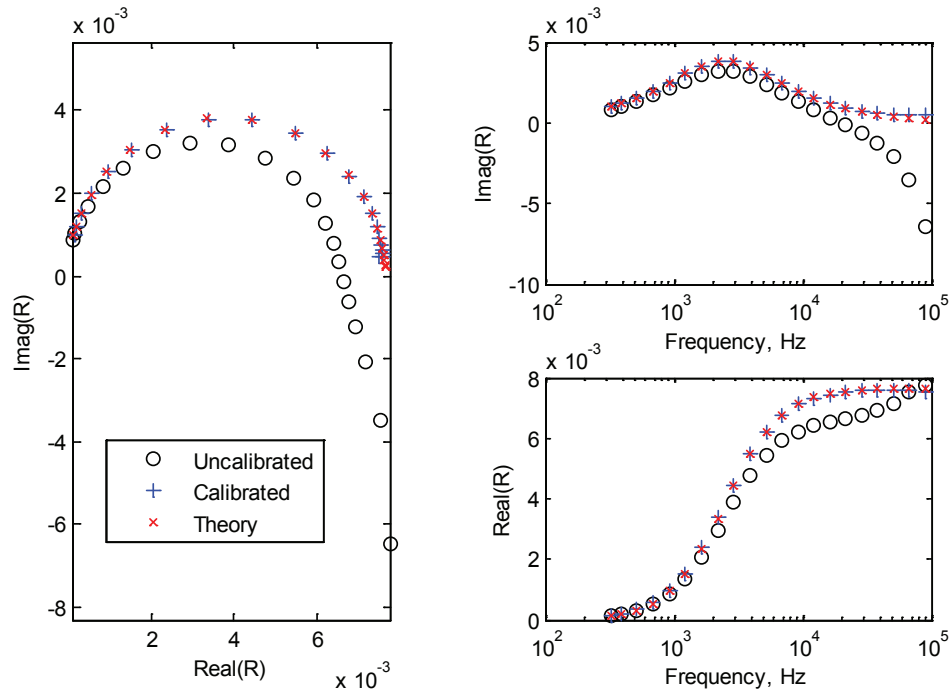


Fig. 5 Graph of the response of System B to a loop of 16 AWG wire with a circumference of 200mm.

LANDMINE DETECTION USING THE DISCRETE SPECTRUM OF RELAXATION FREQUENCIES

Mu-Hsin Wei, Waymond R. Scott, Jr., and James H. McClellan

Georgia Institute of Technology
School of Electrical and Computer Engineering
777 Atlantic Drive NW, Atlanta, GA 30332-0250

ABSTRACT

Several landmine detection techniques using electromagnetic induction (EMI) sensors have been proposed in the past decade. In this paper, we propose a class of detection techniques based on the discrete spectrum of relaxation frequencies (DSRF). Two DSRF detection methods are demonstrated: one using the support vector machine and one using the k-nearest neighbor method. A soil model is also proposed to identify EMI response from the magnetic properties of the soil. A detection framework is suggested to incorporate the soil model and the classifier. The robustness of landmine detection using the DSRF is demonstrated.

Approved for public release; distribution is unlimited.

Index Terms— Electromagnetic induction (EMI), discrete spectrum of relaxation frequencies (DSRF), detection, support vector machine.

1. INTRODUCTION

Landmine detection techniques based on EMI sensors have been actively developed in the past decade. Gao *et al.* suggested a Bayesian classification algorithm which uses the frequency response of targets as a feature [1]. Fails *et al.* [2] and Ramachandran *et al.* [3] both demonstrated success in detecting mines using nearest-neighbor classifiers based on an EMI model developed by Miller *et al.* [4].

We propose to detect landmines using an EMI model based on the discrete relaxations of the target [5]. This model has several attractive features, including a sound theoretical treatment, physical significance of model parameters, and orientation invariance. The EMI frequency response of a metallic object can be expressed as a sum:

$$H(\omega) = c_0 + \sum_{k=1}^L \frac{c_k}{1 + j\omega/\zeta_k}, \quad (1)$$

where c_0 is the shift, L the model order, c_k the real spectral amplitudes, and ζ_k the relaxation frequencies. The parameter set $S = \{(\zeta_k, c_k) : k = 1 \dots L\}$ is the DSRF. The DSRF of a target can be estimated using methods proposed in [6, 7].

The relaxation frequencies are invariant to the orientation and position of the target; only the spectral amplitudes change when the target is rotated or moved [5]. Therefore, the ζ_k can be used as a feature that is intrinsic to a target. Furthermore, since most landmines are buried in consistent orientations, the c_k are also often similar among different mines of the same type. Figure 1 demonstrates the consistency of the DSRF across instances of two different types of landmine [6]. While consistent within its own type, the two mines clearly have distinct DSRFs.

We propose to detect landmines using the DSRF as a feature. We propose two landmine classification methods: one based on the support vector machine (SVM) and one based on the k-nearest neighbor (kNN). A soil prescreener is also proposed. We suggest a detection framework that incorporates the proposed DSRF classifier and the soil prescreener. The resulting performance is robust and comparable to existing methods. The detection process is also very fast when using the SVM.

2. DETECTION METHODS

2.1. Target Classifier

We propose to classify a target based on its DSRF using the kNN or the SVM. With only two classes, landmine and not-landmine, the classification problem reduces to a detection problem.

In the case of kNN, the distance measure used to quantify the distance between two DSRFs is the Earth Mover's Distance (EMD) [8, 6]. The Euclidean distance is a poor measure of the similarity between the two DSRF because the relaxations of two DSRFs are usually sparse and not aligned. However, the EMD can account for the difference in the number of relaxations as well as when the relaxations are not aligned.

In the case of SVM, given a target's DSRF parameter set S , the target is classified/labeled using the decision function:

$$f(S) = \text{sign} \left(\sum_{i=1} \alpha_i y_i K(S_T^i, S) + b \right), \quad (2)$$

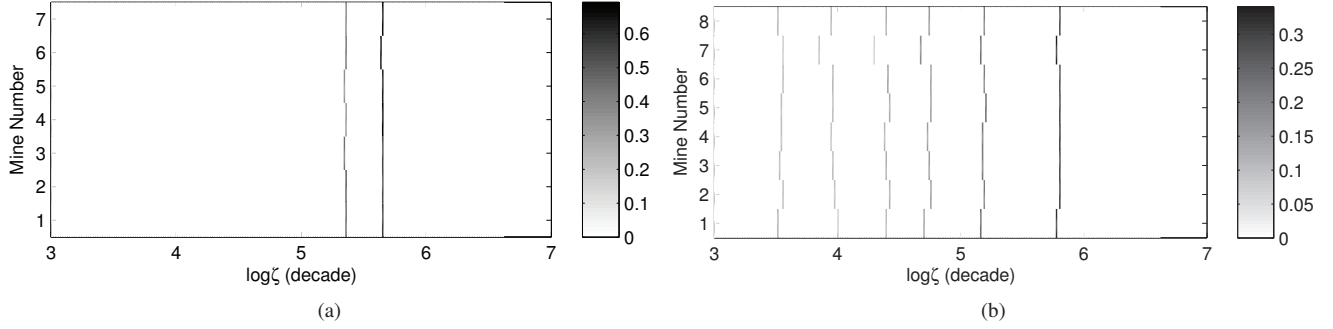


Fig. 1. Estimated DSRF of landmines. The spectral amplitude c_k is represented by the intensity: the darker the color, the larger the amplitude. (a) Seven low-metal content, nonmagnetic, moderate EMI response antipersonnel mines. (b) Eight medium-metal content, magnetic, strong EMI response antipersonnel mines.

where K is the kernel (explained shortly), S_T^i the training data, $y_i \in \{-1, +1\}$ the training class labels, α_i the trained weights, and b the trained threshold. (Only a few α s are nonzero, i.e., the α s are sparse. The S_T^i that correspond to the nonzero α_i are called the *support vectors*.)

For the kernel, we use a generalized radial basis function [9]:

$$K_{\text{EMD}}(S_1, S_2) = \exp(-\rho \text{EMD}(S_1, S_2)), \quad (3)$$

where ρ is a scaling parameter. For brevity, (3) is called the EMD kernel [10]. While it is not proven that the EMD kernel satisfies Mercer's condition (i.e., K_{EMD} is positive semi-definite), it is observed that the EMD kernel is positive semi-definite [10] in practice. At the least, it should be noted that kernels that do not satisfy Mercer's condition can still perform well [9].

2.2. Soil Prescreener

A soil model and a prescreener based on this model is presented here. The prescreener filters out responses that are like those due to the magnetic properties of the soil. The prescreening process is very efficient.

The frequency dependence of the soil responses share a similar trend. The real part has a linear trend with respect to the log-frequency, and the imaginary tends to be a constant [11, 12]. From these observations, we propose a model:

$$H_G(\omega) = p_1 + p_2 \left(\ln \omega + j \frac{\pi}{2} \right), \quad (4)$$

where p_1 and p_2 are model parameters. Given a response measured at N frequencies $\omega_1, \dots, \omega_N$, the response can be fitted to the model (4) via a least-squares minimization, which can be performed very efficiently.

The responses for 6000 samples collected at locations that reported to have no metal content are shown in Fig. 2. Some magnitudes are strong (> -125 dB) because metal targets

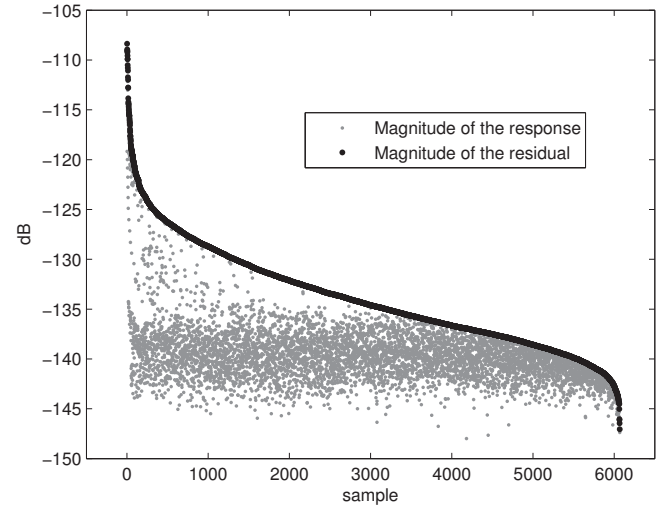


Fig. 2. Samples of blank responses fitted to the soil model (4). The samples are ordered so that response decreases with increasing sample number.

were actually present nearby. For most samples, the magnitude of the residual is noticeably smaller than the response indicating that the sample fits the soil model well.

Because the model describes a behavior very specific to the soil and is not usually observed in metallic objects, the model can be used as a prescreener to determine whether a target is present based on the fitting residual. Given a frequency response $H(\omega)$, the response is fitted to (4), and then the residual of the fit ϵ is used to determine whether a metallic object is present. A threshold θ is chosen to decide whether a metallic object is present:

$$\text{target present} = \begin{cases} \text{true} & \text{if } \epsilon > \theta \\ \text{false} & \text{otherwise.} \end{cases} \quad (5)$$

A reasonable choice of θ for our measurement is -135 dB, as suggested by Fig. 2.

2.3. Detection Framework

A detection framework that incorporates the soil prescreener and the target classifier is presented here. The framework is designed to be suitable for practical application where measurements are obtained sequentially in real-time. It is designed according to the scenario where a detection vehicle carrying the EMI sensors is driven forward and EMI responses h_n are collected sequentially.

The prescreener first screens out the responses that are absent of metallic objects. Responses that pass the prescreener (indicating a target is present) are then processed to estimate their DSRFs. Based on the estimated DSRF, the classifier then labels the responses as landmine or not-landmine.

The use of the prescreener significantly reduces the amount of data processed by the DSRF estimator and the target classifier. Because the prescreener takes very little computation time compared to the estimator and the classifier, the average computation time is also greatly reduced by using the prescreener.

A simple voting mechanism is employed to discourage temporary mislabeling of landmines by taking advantage of the sequential measurements. As the detection vehicle passes over the target, often multiple measurement are collected consecutively for that target. In this case, multiple labels x_i are produced, and a more confident decision can be made based on the recent labels. We determine that a landmine is present only when p out of the past q labels are marked as landmine. The voting rule reduces false-alarm rate and increases the confidence level.

The proposed framework is summarized as follows:

Detection Framework
Input: $h_n, \theta, p, x_{n-q+1} \dots x_{n-1}$
Output: decision_n
1 Fit h_n to soil model (4) and obtain residual ϵ .
2 if $\epsilon < \theta$ then
3 $x_n = 0$
4 else
5 \hat{S} = estimated DSRF of h_n
6 $x_n = \text{classify}(\hat{S})$ (0 or 1)
7 if $\sum_{i=n-q+1}^n x_i > p$ then
8 $\text{decision}_n = 1$
9 else
10 $\text{decision}_n = 0$
11 return decision_n

3. PERFORMANCE

The proposed method is applied on a data set acquired from a testing field that contains 62 types of targets, including 26 types of landmines as well as various types of metallic and

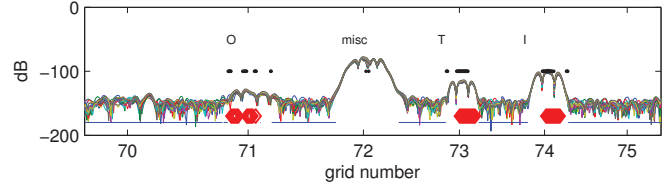


Fig. 3. A snapshot of the output of the detection framework. The curved lines are the strength of the responses measured at 21 frequencies. The target types are noted above the grid number. The blue lines (near -200 dB) indicate points that are marked as soil; black dots (at -100 dB) indicate points that are labeled as landmines; red diamonds indicate a declaration of landmine.

nonmetallic clutter. The testing field is divided into 11 lanes each lane containing 20 grid cells; there are 220 grid cells total. About 145 EMI responses are collected per grid cell. In total, 32,148 responses are collected for the whole field. The acquisition hardware used is described in [11].

The EMI responses are collected sequentially as the detection vehicle is driven down the lane, and the responses are fed into the detection framework described earlier. The parameters are chosen such that $p = 5$, $q = 20$, and $\theta = -135$ dB. A snapshot of the output of the framework is shown in Fig. 3. Because the way the responses are filtered [11], a target response has multiple lobes (e.g., grid 71 to 74), and only the main (center) lobe is used for processing. The center lobe is determined by the sign of the strongest imaginary part of the response.

In Fig. 3, we see that the soil prescreener is quite effective and the voting rule reduces false alarms. In grid 72, a miscellaneous clutter is labeled as a landmine for a few times, but because the number of mislabeling is small ($< p$), a landmine is not declared and a false alarm is avoided.

The performance of the detection framework using the SVM is summarized in Fig. 4. The receiver operating characteristic (ROC) curve achieves a high detection rate of 0.96 at a low false-alarm rate of 0.10. Other operating points also provide satisfactory performances.

The detection process takes little computer time. With a single pre-trained SVM, the whole test field (32,148 responses) can be classified using the above process (including estimating the DSRF) in 30 seconds on a 2.66 GHz CPU with 960 MB RAM.

The performance of the detection framework using the kNN is also shown in Fig. 4. The performance is comparable to that of the SVM. However, the processing time is much longer (10+ minutes) due to the many distance computations required to find the nearest neighbor per measurement. While the kNN may not be suitable for real-time application, it is quite robust when sufficient training data are available, as is the case here. When the training data is scarce, the SVM is likely to have smaller generalization error.

The classifiers are trained per grid using a leave-one-out

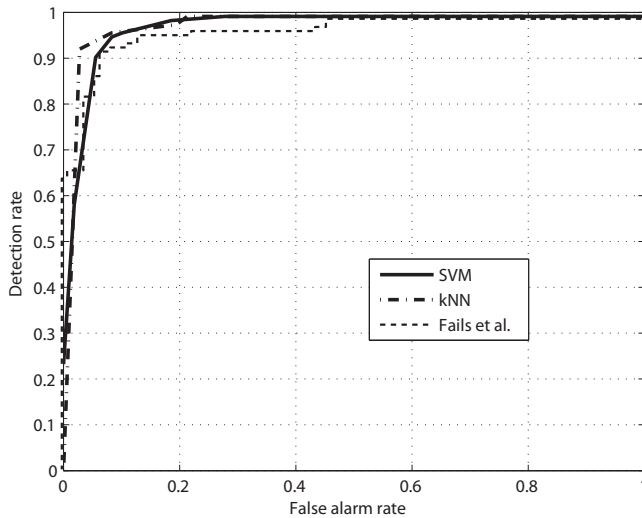


Fig. 4. ROC curves of the proposed method and that of Fails *et al.* [2]. For the kNN ROC curve, $k = 7$.

cross-validation (LOOCV), i.e., the classifiers are trained at each grid with responses from the other 119 grids. Only the strongest responses in a grid are used for training.

For comparison, Fig. 4 includes the ROC curve for the method of Fails *et al.* [2] where the performance is evaluated on the same data set using LOOCV. While the proposed method is slightly better, we note that the simulation done by Fails *et al.* is different from ours. Their method does not utilize sequential measurements.

We note that all the ROC curves in Fig. 4 saturate at 0.99 detection rate. This is due to the misclassification of one particular landmine. Upon close examination, we found that the response of this landmine is very weak and is indistinguishable from the soil response. In our framework, this target is filtered out by the prescanner.

More research can be done to further improve the performance. Other features, such as the soil response and the magnetic property of targets, may be included to provide even more robust performance. Here we only demonstrate the strong potential of using the DSRF for landmine detection.

4. ACKNOWLEDGMENT

This work is supported in part by the US Army REDCOM CERDEC Night Vision and Electronic Sensors Directorate, Science and Technology Division, Countermine Branch and in part by the U. S. Army Research Office.

5. REFERENCES

[1] P. Gao, L. Collins, P. M. Garber, N. Geng, and L. Carin, "Classification of landmine-like metal targets using wideband electromagnetic induction," *IEEE Trans.*

Geosci. Remote Sens., vol. 38, no. 3, pp. 1352–1361, May 2000.

- [2] E. B. Fails, P. A. Torriane, W. R. Scott, Jr., and L. M. Collins, "Performance of a four parameter model for modeling landmine signatures in frequency domain wideband electromagnetic induction detection systems," in *Proc. SPIE*, 2007.
- [3] G. Ramachandran, P. D. Gader, and J. N. Wilson, "Granma: Gradient angle model algorithm on wideband EMI data for land-mine detection," *IEEE Geosci. Remote Sens. Lett.*, vol. 7, no. 3, pp. 535–539, 2010.
- [4] J. T. Miller, T. H. Bell, J. Soukup, and D. Keiswetter, "Simple phenomenological models for wideband frequency-domain electromagnetic induction," *IEEE Trans. Geosci. Remote Sens.*, vol. 39, no. 6, pp. 1294–1298, June 2001.
- [5] C. E. Baum, "On the singularity expansion method for the solution of electromagnetic interaction problems," Interaction Notes 88, Air Force Weapons Laboratory, 1971.
- [6] M. H. Wei, W. R. Scott, Jr., and J. H. McClellan, "Robust estimation of the discrete spectrum of relaxations for electromagnetic induction responses," *IEEE Trans. Geosci. Remote Sens.*, vol. 48, no. 3, pp. 1169–1179, Mar. 2010.
- [7] M. Wei, W. R. Scott, Jr., and J. H. McClellan, "Estimation of the discrete spectrum of relaxations for electromagnetic induction responses using ℓ_p -regularized least squares for $0 \leq p \leq 1$," *IEEE Geosci. Remote Sens. Lett.*, vol. 8, no. 2, pp. 233–237, Mar. 2011.
- [8] Y. Rubner, C. Tomasi, and L. J. Guibas, "A metric for distributions with applications to image databases," in *Proc. ICCV*, Bombay, India, Jan. 1998, pp. 59–66.
- [9] O. Chapelle, P. Haffner, and V. N. Vapnik, "Support vector machines for histogram-based image classification," *IEEE Trans. Neural Netw.*, vol. 10, no. 5, pp. 1055–1064, 2002.
- [10] J. Zhang, M. Marszalek, S. Lazebnik, and C. Schmid, "Local features and kernels for classification of texture and object categories: A comprehensive study," in *CVPRW*, New York, 2006.
- [11] W. R. Scott, Jr., "Broadband array of electromagnetic induction sensors for detecting buried landmines," in *Proc. IGARSS*, Boston, MA, July 2008.
- [12] Y. Das, "Effects of magnetic soil on metal detectors: preliminary experimental results," in *Proc. SPIE*, New York, 2007, vol. 6553, p. 655306.

**ESTIMATION OF THE
DISCRETE SPECTRUM OF RELAXATIONS
FOR ELECTROMAGNETIC INDUCTION RESPONSES**

A Thesis
Presented to
The Academic Faculty

by

Mu-Hsin Wei

In Partial Fulfillment
of the Requirements for the Degree
Master of Science in the
School of Electrical and Computer Engineering

Georgia Institute of Technology
May 2011

To my loving parents.

ACKNOWLEDGEMENTS

I thank God. His love never fails. Through Him, new things are born and new lives begin. The creativity that shaped this work belongs to Him.

I am thankful for my advisers Dr. McClellan and Dr. Scott, for their patient guidance and valuable input. I would like to thank Dr. McClellan, who provided direction and encouragement. Most especially, I appreciate his care for the learning and development of students. I would like to thank Dr. Scott, who meticulously guided me since the beginning of the project. Many significant results from this thesis originated from his ideas. I consider it a great privilege to work under the supervision of Dr. McClellan and Dr. Scott, to whom I am deeply grateful.

I would like to thank my parents, who always support me and welcome me. I thank my sister Lily for her frequent encouragement and phone calls. I also acknowledge Tim and Sean, who although are far away but are close to heart.

I would also like to thank my friends and colleagues, for their friendship and support. Much of the credit of this work goes to these fantastic people. I especially like to thank my housemates, Jacob, Justin, and David, who kept me sane and positive.

This work is supported in part by the US Army REDCOM CERDEC Night Vision and Electronic Sensors Directorate, Science and Technology Division, Countermining Branch and in part by the U. S. Army Research Office under Contract Number W911NF-05-1-0257.

TABLE OF CONTENTS

DEDICATION	ii
ACKNOWLEDGEMENTS	iii
LIST OF TABLES	vi
LIST OF FIGURES	vii
SUMMARY	ix
I INTRODUCTION	1
1.1 Continuous Distribution of Relaxations	2
1.2 Discrete Spectrum of Relaxation Frequencies	3
1.3 DSRF Modeling Difficulties	4
1.4 Proposed Method	5
II ESTIMATION METHOD	6
2.1 Method Formulation	6
2.2 Implementation	8
2.3 Interpolation	9
2.4 Summary	10
III ESTIMATION PERFORMANCE	11
3.1 Dissimilarity Measure Between Two DSRFs	11
3.2 Synthetic Data	12
3.2.1 Two Coplanar Coaxial Loops	12
3.2.2 Six-relaxation DSRF	13
3.2.3 Signal to Noise Ratio	16
3.3 Laboratory Data	18
3.3.1 Single Loop	18
3.3.2 Two Coplanar Coaxial Circular Loops	19
3.3.3 Non-magnetic Sphere	20
3.4 Field Data	21
3.4.1 Dissimilarity Between Various Mine Types	24

IV CONCLUSIONS	26
APPENDIX A — THE EMI MODEL	27
APPENDIX B — NONNEGATIVE SPECTRUM	29
APPENDIX C — DENSITY OF DISCRETIZATION OF THE RELAX- ATION FREQUENCY SPACE	32
APPENDIX D — A CIRCUIT MODEL FOR TWO COPLANAR COAX- IAL CIRCULAR LOOPS	34
APPENDIX E — EARTH MOVER'S DISTANCE	36
REFERENCES	37

LIST OF TABLES

1	Estimation of a six-relaxation DSRF	15
---	---	----

LIST OF FIGURES

1	Splitting of an expected relaxation followed by interpolation. The sample points $\tilde{\zeta}$ do not coincide with ζ_{true} , so ζ_{true} is split into the two nearest sample points: $\tilde{\zeta}_a$ and $\tilde{\zeta}_b$. The estimation accuracy is increased by interpolating in $\tilde{\zeta}$ using \tilde{c}_a and \tilde{c}_b	9
2	Estimation of a simulated two coplanar coaxial circular loop target, for which $\log \zeta_k$ and c_k are (4.7552 6.0651) and (0.5013 0.4987), respectively. The estimates for $\log \hat{\zeta}_l$ and \hat{c}_l are (4.7557 6.0672) and (0.5010 0.4990), respectively.	13
3	Estimation of a six-relaxation DSRF. See Table 1 for numerical data. (a) Estimates by the proposed method. (b) Estimates by <code>invfreqs</code> with non-physical parameters removed.	14
4	Monte Carlo simulation on goodness of estimation vs. SNR performed on a four-relaxation DSRF. Sample size is 10,000 at each SNR. Error bars indicate the range of EMD between the 10th and 90th percentiles.	16
5	Monte Carlo simulation on goodness of estimation vs. SNR for different DSRFs with model order ranging from 1 to 10. Sample size is 10,000.	17
6	An instance of a frequency response added with a 25 dB AWGN.	18
7	(a) Frequency response of three independently measured single loops on an Argand diagram. Responses are normalized such that $\ \mathbf{h}\ _2 = 1$. Measurements are labeled in the form of AWG/circumference(mm). (b) Theoretical and estimated DSRF. Theoretical $\log \zeta_k$, from left to right, are 4.9364, 5.6416, and 6.0167. Estimated $\log \hat{\zeta}_l$, from left to right, are 4.9411, 5.6534, and 6.0195. All relaxations have an amplitude of unity.	19
8	(a) Laboratory measured frequency response of two coplanar coaxial circular loops on an Argand diagram. Theory deviates from the measurement at higher frequencies. Responses are normalized such that $\ \mathbf{h}\ _2 = 1$. (b) Theoretical and estimated DSRF. $\log \zeta_k$ and c_k are (4.7552 6.0651) and (0.5013 0.4987), respectively. The estimate $\log \hat{\zeta}_l$ and \hat{c}_l are (4.7768 6.0514) and (0.4941 0.5059), respectively.	19
9	DSRF estimation of a laboratory-measured sphere. The theoretical DSRF has an infinite sequence of relaxation frequencies.	20
10	Estimated DSRF of real landmines. The spectral amplitude is represented by the intensity: darker the color, larger the amplitude. (a) Seven Type-A landmines. (b) Eight Type-B landmines. (c) Seven Type-C landmines.	22
11	Normalized estimated $H(0)$ for landmines in Fig. 10. $H(0)$ is normalized by $\sum_{l=1}^L \hat{c}_l$	23
12	The EMD between samples from eleven types of landmines (A to K) and metal clutter. Darker colors denote smaller distances which indicate that two samples are more similar.	25

13	Monte Carlo simulation on density of discretization of ζ space. Each point on the curve is the average EMD over 10,000 samples.	33
14	Circuit model for two coplanar coaxial circular loops.	34

SUMMARY

This thesis presents a robust method for estimating the relaxations of a metallic object from its electromagnetic induction (EMI) response. The EMI response of a metallic object can be accurately modeled by a sum of real decaying exponentials. However, it is difficult to obtain the model parameters from measurements when the number of exponentials in the sum is unknown or the terms are strongly correlated. Traditionally, the time constants and residues are estimated by nonlinear iterative search that often leads to unsatisfactory results.

In this thesis, a constrained linear method of estimating the parameters is formulated by enumerating the relaxation parameter space and imposing a nonnegative constraint on the parameters. The resulting algorithm does not depend on a good initial guess to converge to a solution. Using tests on synthetic data and laboratory measurement of known targets the proposed method is shown to provide accurate and stable estimates of the model parameters.

CHAPTER I

INTRODUCTION

The landmine crisis remains today as landmines continue to maim or kill civilians everyday worldwide. The International Campaign to Ban Landmines reported that in the year of 2009, landmines and explosive remnants of war caused about 4000 casualties worldwide, of which over 60% are civilians [19] and more than 30% are children. Much effort and research has been invested in remediating landmines with one of the primary tasks being the detection of the landmine itself. However, landmine detection can suffer from a high false-alarm rate as the detectors also detect other metallic non-mine objects like gun shells, metal cans, and shrapnel. Therefore, it is of strong interest to discriminate between landmines and metallic non-mine objects.

Recent research has shown that discrimination between certain types of metallic objects (targets) is possible by using broadband electromagnetic induction (EMI) sensors together with advanced signal processing [6, 21, 11, 27, 9, 26]. Target discrimination using broadband EMI sensors is possible because the EMI response of a target is strongly related to the target's physical size, shape, orientation, and composition. EMI sensors work by illuminating a target of interest with a time-varying magnetic field, and then detecting the scattered magnetic field which is generated by the eddy currents induced on the target. The broadband EMI sensors measure the scattered field at a broad range of frequencies or measurement times. In a broadband EMI system, a target can be represented by its response at a small number of frequencies. The measured response can be fitted to a model, and discrimination of the target is performed based on the fitted model parameters.

The goal of this work is to model an EMI response in terms of its relaxations to assist target discrimination. Several different EMI models have been developed to analyze the EMI response of a target. These models can be categorized into two: continuous and discrete. While this thesis is concerned with the discrete model, the continuous model is

used by many [9, 26], and a discussion on this model is also provided.

1.1 Continuous Distribution of Relaxations

Several existing EMI models can be identified with parametric models employed in polymer science, which have an underlying continuous distribution of relaxations. For example, the parametric models proposed by Miller *et al.* [24] (which is widely used) can be rewritten in the form of the Cole-Cole dielectric relaxation model [5]. Other theoretical model for canonical targets can also be identified similarly [13, 35].

The fact that the dielectric response of materials has similar characteristics to the EMI frequency response allows the models and methods developed for dielectric materials be applied to the EMI response. Here, the analysis used in polymer science is employed to study some of the existing EMI models. It is advantageous to do so since many of the dielectric models and methods have been well-studied over the past fifty years, and much is known about the behavior and properties of the models. Other well-known dielectric models, such as the Havriliak-Negami and Cole-Davidson models could also be used in modeling the EMI response of targets with more complex shapes [8, 16].

A more general model to describe the models mentioned above is the distribution of relaxation times (DRT), which is an analysis tool used in polymer science to characterize materials [18]. The normalized DRT $G(\tau)$ is defined as:

$$H(\omega) = g_0 + g_\Delta \int_0^\infty \frac{G(\tau)}{1 + j\omega\tau} d\tau, \quad (1)$$

where $H(\omega)$ is the frequency response, τ the relaxation time, and g_0 and g_Δ are constants; $G(\tau)$ is normalized to have unity area.

The models mentioned above can all be expressed in terms of the DRT. For example, the Cole-Cole model (hence, Miller's model) and its DRT are [1]

$$H_{CC}(\omega) = g_0 + \frac{g_\Delta}{1 + (j\omega\tau_0)^\alpha}, \quad (2)$$

and

$$G_{CC}(\tau) = \frac{1}{2\pi\tau} \frac{\sin(\alpha\pi)}{\cosh(\alpha \log(\tau/\tau_0)) + \cos(\alpha\pi)}, \quad (3)$$

where τ_0 and α are model parameters.

It should be noted that the parametric models can be restrictive in the sense that the models have assumed underlying distribution and may not be appropriate for objects of more general shape. For example, $G_{CC}(\tau)$ is restricted to be symmetric with respect to τ_0 in $\log\text{-}\tau$ space because of the assumed structure of $H_{CC}(\omega)$. However, not all targets have symmetric DRTs. Using Cole-Cole to model such targets would result in a loss of information. Describing a target in terms of DRT makes less assumptions about the structure of the response, and therefore can model different targets more accurately.

1.2 Discrete Spectrum of Relaxation Frequencies

In the study of EMI, several researchers have provided a theoretical basis for representing the EMI response of a metallic object as a discrete sum of damped real exponentials [20, 2]. In terms of the DRT, an EMI response can be modeled as a special case of the DRT where the $G(\tau)$ is *discrete*. In addition, in the context of broadband EMI application, it is more intuitive and convenient to write (1) in terms of *relaxation frequencies* rather than relaxation times. Using the notation of relaxation frequency, (1) can be rewritten in discrete form as

$$H(\omega) = c_0 + \sum_{k=1}^K \frac{c_k}{1 + j\omega/\zeta_k}, \quad (4)$$

where c_0 is the shift, K the model order, c_k the real spectral amplitudes, and $\zeta_k = 1/\tau_k$ the relaxation frequencies. The underlying physical process of the model is discussed in Appendix A. The response at zero frequency $H(0) = \sum_{k=0}^K c_k$ is due to the DC magnetization of the target.

Aside from the shift, the EMI frequency response of a target can be precisely represented by the set $S = \{(\zeta_k, c_k) : k = 1 \dots K\}$ which is the discrete spectrum of relaxation frequencies (DSRF). Each pair (ζ_k, c_k) is one relaxation. The parameter c_0 is not considered part of the DSRF because it is just a shift of the frequency response. The term DSRF and spectrum are used interchangeably in this work.

The DSRF is related to a target's physical properties. The frequency response $H(\omega)$ is proportional to the projection of the magnetic polarizability tensor of the target being measured by the EMI sensor. The magnetic polarizability, hence the DSRF, of several canonical targets can be calculated analytically, and these formulas show how the DSRF

is related to the target’s physical properties such as conductivity, permeability, shape, size, and orientation [34, 3, 12].

The DSRF representation has other useful properties. The relaxation frequencies of a target are invariant to its relative orientation and position to the sensor. Only the spectral amplitudes change with orientation and position. The fact that the relaxation frequencies are intrinsic to a target makes the DSRF a valuable feature for target discrimination. Baum has coined the term “magnetic singularity identification” when using the relaxations (singularities) for identifying targets [3].

1.3 DSRF Modeling Difficulties

While modeling the EMI response in terms of the DSRF has several benefits, estimating the DSRF from the frequency response is not straightforward. Estimating the DSRF is equivalent to finding the parameters of a sum of exponentials, and techniques such as iterative nonlinear least squares fitting, the matrix pencil method, and modified Prony’s methods have been used in the past [29, 25]. Often these methods do not perform well when three or more relaxations are present. The goodness of fit strongly depends on a good guess of the model order, and is also very sensitive to the initial guess for the model parameters. More discussion on the performance of these methods can be found in [27, 7].

In practice, a good initial guess is hard to determine, and it is difficult, if not impossible, to have prior knowledge on the model order. For these reasons, most existing estimation methods are prone to not converging in the fitting process. Even if the fitting method converges well with a small residual, there is the concern that the estimated relaxations could be very different from the actual ones. It is possible that the estimate is merely a good numerical fit, but has no physical significance [7].

One robust spectrum estimation method is the MATLAB function `invfreqs` which implements the algorithm proposed by Levy [23]. `invfreqs` is robust in the sense that it can accurately estimate the spectrum of three or more relaxations, and its convergence is not sensitive to the initial guess. The major downside of this method is that it can return complex spectral amplitudes or negative relaxation frequencies that have no physical

meaning.

1.4 Proposed Method

In this thesis, it is proposed a method of estimating the DSRF that requires no prior knowledge of the model order and always returns real model parameters. The proposed method linearize the estimation problem by enumerating the relaxation parameter space and imposing a nonnegative constraint on the parameters [37]. While some targets may have negative DSRF, the proposed method works very well in practice. Even with the constraint, the proposed method can represent a much larger class of responses than the parametric models such as the Cole-Cole and Havriliak-Negami models. For well-known canonical targets, as presented in this work, the estimated DSRF is an approximate, if not an exact, representation of the actual physical DSRF.

CHAPTER II

ESTIMATION METHOD

The proposed DSRF estimation method is formulated in this chapter. To begin the formulation, it is first examined the frequency response when probed at multiple frequencies. When the target response is measured at N distinct frequencies, the DSRF model (4) can be written in matrix form

$$\begin{bmatrix} H(\omega_1) \\ H(\omega_2) \\ \vdots \\ H(\omega_N) \end{bmatrix} = \underbrace{\begin{bmatrix} 1 & \frac{1}{1+j\omega_1/\zeta_1} & \frac{1}{1+j\omega_1/\zeta_2} & \cdots & \frac{1}{1+j\omega_1/\zeta_K} \\ 1 & \frac{1}{1+j\omega_2/\zeta_1} & \frac{1}{1+j\omega_2/\zeta_2} & \cdots & \frac{1}{1+j\omega_2/\zeta_K} \\ \vdots & \vdots & \vdots & \ddots & \vdots \\ 1 & \frac{1}{1+j\omega_N/\zeta_1} & \frac{1}{1+j\omega_N/\zeta_2} & \cdots & \frac{1}{1+j\omega_N/\zeta_K} \end{bmatrix}}_{\mathbf{Z}} \begin{bmatrix} c_0 \\ c_1 \\ c_2 \\ \vdots \\ c_K \end{bmatrix}$$

$$\mathbf{h} = \mathbf{Z}\mathbf{c}, \tag{5}$$

where $\omega_{min} = \omega_1 < \omega_2 < \cdots < \omega_N = \omega_{max}$, \mathbf{h} is the observation vector, \mathbf{c} the spectral amplitude vector augmented by the shift c_0 , and \mathbf{Z} a matrix containing information about the relaxation frequencies ζ . The dimension of the matrix \mathbf{Z} is dependent on the number of relaxations present in the spectrum (i.e., the model order). In the case of a simple thin wire circular loop, there is only one relaxation, so \mathbf{Z} has two columns; the first column is always one to account for c_0 .

2.1 Method Formulation

To estimate the DSRF (i.e., ζ_k and c_k) from a given observation \mathbf{h} , the usual approach is to minimize the norm of the error, $\|\mathbf{h} - \mathbf{Z}\mathbf{c}\|$, but this leads to a *nonlinear* optimization problem. Instead, the strategy of basis pursuit is adopted to reformulate (5) as a linear problem with an overcomplete dictionary [4], and then nonnegative least squares is used to select the best basis, i.e., the best ζ . The overcomplete dictionary is a matrix $\tilde{\mathbf{Z}}$ that has the same form as \mathbf{Z} in (5), but with many more column (shown below). To generate

the columns, it is enumerated a large set of possible relaxation frequencies in $\log\text{-}\zeta$ space, and one column is created for each enumerated ζ . The enumeration is done by discretizing a range of relaxation frequencies into M sample points $\tilde{\zeta}_m$ that are uniformly distributed in the $\log\text{-}\zeta$ space. The range of relaxation frequencies is chosen such that, $\tilde{\zeta}_{min} \approx \omega_{min}$ and $\tilde{\zeta}_{max} \approx \omega_{max}$. The number M should be chosen large enough to ensure some $\tilde{\zeta}_m$ are in close proximity to the actual relaxation frequencies ζ_k . From simulations performed, a good choice of M gives roughly 25 sample points per decade. More discussion on the choice of M can be found in Appendix C.

Using the dictionary $\tilde{\mathbf{Z}}$, the estimation problem is rewritten as

$$\begin{bmatrix} H(\omega_1) \\ H(\omega_2) \\ \vdots \\ H(\omega_N) \end{bmatrix} = \underbrace{\begin{bmatrix} 1 & \frac{1}{1+j\omega_1/\tilde{\zeta}_1} & \frac{1}{1+j\omega_1/\tilde{\zeta}_2} & \cdots & \frac{1}{1+j\omega_1/\tilde{\zeta}_M} \\ 1 & \frac{1}{1+j\omega_2/\tilde{\zeta}_1} & \frac{1}{1+j\omega_2/\tilde{\zeta}_2} & \cdots & \frac{1}{1+j\omega_2/\tilde{\zeta}_M} \\ \vdots & \vdots & \vdots & \ddots & \vdots \\ 1 & \frac{1}{1+j\omega_N/\tilde{\zeta}_1} & \frac{1}{1+j\omega_N/\tilde{\zeta}_2} & \cdots & \frac{1}{1+j\omega_N/\tilde{\zeta}_M} \end{bmatrix}}_{\tilde{\mathbf{Z}}} \begin{bmatrix} \tilde{c}_0 \\ \tilde{c}_1 \\ \tilde{c}_2 \\ \vdots \\ \tilde{c}_M \end{bmatrix} + error$$

$$\mathbf{h} = \tilde{\mathbf{Z}}\tilde{\mathbf{c}} + error \quad (6)$$

where $\tilde{\mathbf{c}}$ is the $(M+1)$ -element *weighted selector vector*. Ideally, when the error between \mathbf{h} and $\tilde{\mathbf{Z}}\tilde{\mathbf{c}}$ is minimized, only those \tilde{c}_m with corresponding $\tilde{\zeta}_m$ that are near a true ζ_k will be nonzero, and they will take on the correct spectral amplitudes c_k . It follows that a DSRF can then be deduced from the nonzero estimated \tilde{c}_m and their corresponding $\tilde{\zeta}_m$. It is expected that a good solution for $\tilde{\mathbf{c}}$ has many zero elements.

The challenge in obtaining the correct $\tilde{\mathbf{c}}$ is that M is much greater than N , so the system in (6) is underdetermined and there is not a unique $\tilde{\mathbf{c}}$ to minimize the error. Any vector in the null space of $\tilde{\mathbf{Z}}$ can be added to $\tilde{\mathbf{c}}$ without changing the error. There are many ways to select a least-squares (LSQ) solution. The Moore-Penrose pseudoinverse picks the LSQ solution that has the smallest ℓ_2 norm. One can also compute a LSQ solution with the fewest nonzero components. However, neither of these LSQ solutions produces the correct spectrum. Details about existing techniques and the difficulties of solving such a system can be found in [15, 7, 17].

In the EMI application, it is found in this research that imposing a nonnegative constraint on $\tilde{\mathbf{c}}$ effectively eliminates a large portion of the null space of $\tilde{\mathbf{Z}}$ and the remaining solution space contains reasonable answers. Under the EMI system used in this study, it is observed that the real part of the frequency response decreases as the frequency increases, and the imaginary part remains negative for the great majority of targets. Having all the spectral amplitudes nonnegative is a sufficient condition to satisfying this observation. While it is shown that nonnegative DSRF is not a necessary condition, it is also shown that whenever the real part decreases with respect to the frequency, the spectral amplitudes are practically nonnegative. A detailed discussion on the applicability of the nonnegative constraint is provided in Appendix B.

Using the nonnegative constraint, 6 can be solved by optimizing

$$\arg \min_{\tilde{\mathbf{c}}} \|\tilde{\mathbf{Z}}' \tilde{\mathbf{c}} - \mathbf{h}'\| \quad \text{subject to } \tilde{\mathbf{c}} \geq 0 \quad (7)$$

where $\tilde{\mathbf{Z}}' = \begin{bmatrix} \Re(\tilde{\mathbf{Z}}) \\ \Im(\tilde{\mathbf{Z}}) \end{bmatrix}$ and $\mathbf{h}' = \begin{bmatrix} \Re(\mathbf{h}) \\ \Im(\mathbf{h}) \end{bmatrix}$.

Separating the real and imaginary parts makes the whole system real. The first element in $\tilde{\mathbf{c}}$, \tilde{c}_0 , can be guaranteed nonnegative by adding a sufficiently large real number to \mathbf{h} .

2.2 Implementation

The proposed estimation method can be easily implemented through the function `lsqnonneg` in MATLAB which uses the algorithm found in [22]. An alternative to `lsqnonneg` is the `CVX` package which implements convex optimization under MATLAB [14]. Both optimizers provides satisfactory results. However, `CVX` is a larger and more sophisticated program, but is slightly slower than `lsqnonneg` which was written exactly to solve least-square problems with a nonnegative constraint. Nevertheless, `CVX` would be of great interest if more constraints are to be added.

When using either `lsqnonneg` or `CVX`, it is found that normalizing the input data \mathbf{h} to have an ℓ_2 norm of unity increases the accuracy of estimation. Therefore, all data are scaled to an ℓ_2 norm of unity before optimization, and scaled back to the original norm after optimization. The original norm may contain useful information for target discrimination.

2.3 Interpolation

It is observed that in the estimated DSRF, an expected relaxation (ζ_{true}, c_{true}) is often split into two peaks located at the two sample points adjacent to ζ_{true} , as shown in Fig. 1. It is also observed that the two estimated spectral amplitudes add up to the true spectral amplitude c_{true} , and ζ_{true} is closer to the $\tilde{\zeta}$ with larger \tilde{c} . This phenomenon can be understood: the splitting of relaxation happens when the sample points $\tilde{\zeta}_m$ do not coincide with ζ_{true} , and c_{true} gets distributed among the two sample points that are the closest to ζ_{true} .

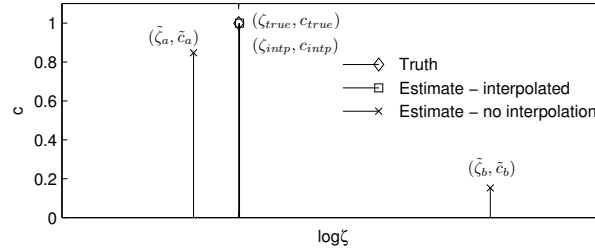


Figure 1: Splitting of an expected relaxation followed by interpolation. The sample points $\tilde{\zeta}$ do not coincide with ζ_{true} , so ζ_{true} is split into the two nearest sample points: $\tilde{\zeta}_a$ and $\tilde{\zeta}_b$. The estimation accuracy is increased by interpolating in $\tilde{\zeta}$ using \tilde{c}_a and \tilde{c}_b .

The accuracy of the estimation can be increased by taking advantage of this well-behaved and consistently recurring phenomenon. The splitting processes can be reversed. A true relaxation frequency could be restored by interpolating between two adjacent $\tilde{\zeta}_m$ with nonzero \tilde{c}_m according to their spectral amplitudes. The interpolated spectral amplitude is simply the sum of the two adjacent spectral amplitudes. Mathematically,

$$c_{intp} = \tilde{c}_a + \tilde{c}_b \quad (8)$$

$$\log(\zeta_{intp}) = \log(\tilde{\zeta}_a) + \frac{\tilde{c}_b}{\tilde{c}_a + \tilde{c}_b} \log(\tilde{\zeta}_b / \tilde{\zeta}_a). \quad (9)$$

The quantities are as depicted in Fig. 1. The sample points $\tilde{\zeta}_m$ are placed close enough that a simple linear interpolation in $\log\text{-}\zeta$ space gives satisfactory results. The interpolation is applied only on two adjacent nonzero relaxations.

After the interpolation is performed, any \tilde{c}_m with a value of zero is eliminated along with its corresponding $\tilde{\zeta}_m$. The resulting relaxation frequencies is denoted as $\hat{\zeta}_l$, with spectral amplitudes, \hat{c}_l , or in vector notation, $\hat{\zeta}$ and \hat{c} , both with length L . It is convenient and

desirable to interpret the estimation results by looking at $\hat{\boldsymbol{\zeta}}$ and $\hat{\mathbf{c}}$. Every entry in $\hat{\boldsymbol{\zeta}}$ is an estimate of one relaxation frequency of the target with its corresponding estimated spectral amplitude in $\hat{\mathbf{c}}$. The estimated DSRF $\hat{S} = \{(\hat{\zeta}_l, \hat{c}_l) : l = 1 \dots L\}$ is then compactly stored in $\hat{\boldsymbol{\zeta}}$ and $\hat{\mathbf{c}}$. In addition, the vector length L is an estimate of the model order K . Note that \tilde{c}_0 is not part of the DSRF and therefore not interpolated, and is not in the vector $\hat{\mathbf{c}}$.

2.4 Summary

To estimate the unknown DSRF $S = \{(\zeta_k, c_k)\}$ from a given set of observations \mathbf{h} over N frequencies, first decide on a relaxation frequency range $[\tilde{\zeta}_{min}, \tilde{\zeta}_{max}]$ and the number of points M to be sampled in this range. Then generate the sample points $\tilde{\zeta}_m$, construct a dictionary matrix $\tilde{\mathbf{Z}}$, perform the optimization described in (7), and finally obtain the estimated DSRF $\hat{S} = \{(\hat{\zeta}_l, \hat{c}_l)\}$ by interpolating the solution $\tilde{\mathbf{c}}$ returned by the optimizer.

The performance of the proposed method is discussed in detail in the following chapter.

CHAPTER III

ESTIMATION PERFORMANCE

To examine the performance of the proposed method, the method is tested against synthetic, laboratory, and field data. The method is shown to be accurate, stable, and fast. All estimations are performed with $M = 100$ and optimized with `lsqnonneg`. Prior to presenting the estimation results, an error measure is introduced.

In assessing the signal strength, the signal-to-noise ratio (SNR) is used. The signal power is computed by $\sum_{i=1}^N |H(\omega_i)|^2/N$. The noise power in synthesized data is equal to the variance of the noise. In laboratory and field data the background signal can be measured and is treated as noise when calculating the SNR.

The frequency response of targets are presented on Argand diagrams. Specifically, complex frequency response functions are plotted on a complex plane with the imaginary part as the vertical axis, the real part as the horizontal axis, and frequency as the parameter. All presented spectra are normalized such that $\sum_{i=1} c_i = 1$ (c_0 is separate). Normalization removes the influence of the signal amplitude which changes for many reasons.

Notation: ζ and c are the true/theoretical relaxation frequencies and spectral amplitudes; $\hat{\zeta}$ and \hat{c} are the estimates.

3.1 Dissimilarity Measure Between Two DSRFs

Before the goodness of estimation can be evaluated, some kind of measure is needed to assess the dissimilarity between the estimated DSRF and the truth. It is difficult, however, to compare two sparse spectra when the number of relaxations are different, which happens frequently. When the number of relaxations is the same ($K=L$), a possible measure of the dissimilarity between two spectra is

$$D(\hat{S}, S) = \frac{1}{I} \sum_{i=1}^I |\log \hat{\zeta}_i - \log \zeta_i| \quad (10)$$

$$\forall i \quad \hat{\zeta}_i \leq \hat{\zeta}_{i+1} \text{ and } \zeta_i \leq \zeta_{i+1},$$

where $I=K=L$. In (10) only the relaxation frequencies ζ_k are considered, and spectral amplitudes c_k are ignored. This approximation is reasonable and convenient when two spectra are visually similar. We refer to this dissimilarity measure as the deviation. It has the units of decades.

Another measure that is more comprehensive is the Earth Mover's Distance (EMD) [28, 10]. The EMD consistently quantifies the dissimilarity between two spectra, even when $K \neq L$. Intuitively, the EMD measures how much work it takes to morph one spectrum into the other. Specifically, one spectrum represents piles of earth with volume \hat{c}_l located at the associated $\hat{\zeta}_l$. The other spectrum represents holes in the ground with capacity c_k located at ζ_k . The distance between a pile of earth and a hole is naturally defined to be the difference between $\hat{\zeta}_l$ and ζ_k in log space, and the work to move some earth into a hole would be the amount of earth moved times the distance traveled. Then, the EMD is proportional to the least amount of work needed to move as much earth into the holes. For the DSRF, the EMD is measured in decades because it is almost always examined in log- ζ space. See Appendix E for details about the EMD.

3.2 *Synthetic Data*

In this section, the proposed estimation method is tested against synthetic data to show its functionality, robustness, and stability. The synthesized data is sampled at 21 frequencies approximately logarithmically distributed over the range 300 Hz–90 kHz. The range of ζ for estimation is chosen such that $\log(\tilde{\zeta}_{min})$ and $\log(\tilde{\zeta}_{max})$ are 2.4470 and 6.6223, respectively. This corresponds to a frequency range of 45 Hz–670 kHz, which is larger than the measured frequency range. With $M = 100$, the spacing between two sample points is 0.0422 decades. The number of samples and the frequencies are chosen to be the same as the laboratory hardware system, but the proposed method can also perform under different settings.

3.2.1 *Two Coplanar Coaxial Loops*

The performance of the proposed method is good when tested on a simulated two coplanar coaxial circular loops of copper wire. The two loops have circumferences 200 mm and

150 mm, respectively. The larger loop has a wire radius of 0.0635 mm (#36 AWG¹), and the smaller one a wire radius of 0.3215 mm (#22 AWG). A theoretical EMI response and the DSRF of this target is provided in Appendix D. The EMI response is simulated at a 70 dB signal-to-noise ratio (SNR) with additive white Gaussian noise (AWGN). The estimated spectrum is shown in Fig. 2 along with the true spectrum. The estimated spectrum is almost identical to the truth. The deviation from the true spectrum is 0.0013 decades, which is very small compared to the detectable ζ range, about 4 decades. The computation took 0.11 s on a 2.66 GHz CPU with 960 MB RAM.

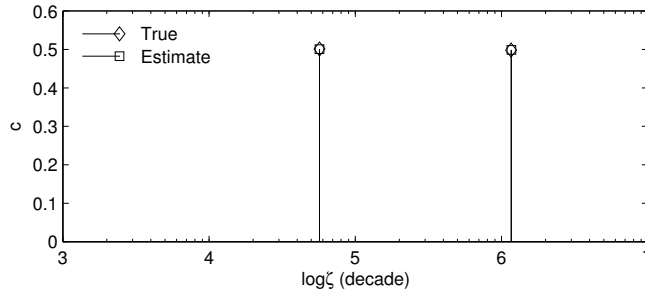


Figure 2: Estimation of a simulated two coplanar coaxial circular loop target, for which $\log \zeta_k$ and c_k are (4.7552 6.0651) and (0.5013 0.4987), respectively. The estimates for $\log \hat{\zeta}_l$ and \hat{c}_l are (4.7557 6.0672) and (0.5010 0.4990), respectively.

3.2.2 Six-relaxation DSRF

While existing sum-of-exponentials estimation methods can also successfully estimate a two-relaxation case, when the number of relaxations is three or more, these methods start to encounter problems such as returning complex model parameters or not converging [7]. Here, the proposed method is tested on a six-relaxation DSRF. The target response is synthesized at 70 dB SNR with AWGN:

$$H(\omega) = 1 + \sum_{k=1}^6 \frac{c_k}{1 + j\omega/\zeta_k} + noise. \quad (11)$$

The relaxation frequencies are chosen such that two ζ_k coincide with a sample point, one ζ_k is half way between two log- ζ sample points, and the rest are randomly in between sample points. The relaxation frequencies are chosen this way to demonstrate the functionality

¹American wire gauge

of the proposed method when the sample points do not coincide with the true relaxation frequencies.

The synthesized and estimated DSRFs are shown in Fig. 3(a) and Table 1. All six relaxation frequencies are correctly recovered. The estimated model parameters are real, and the deviation from truth is small. The EMD between the estimate and truth is 0.0365 decades. There is a seventh relaxation in the estimate introduced by the noise, but its spectral amplitude is small.

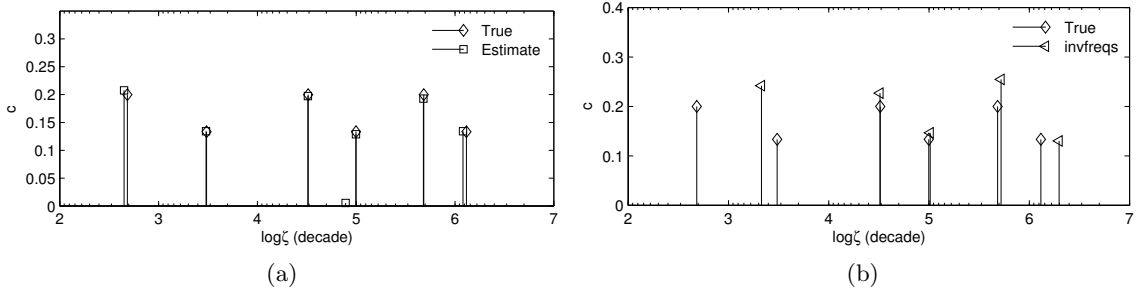


Figure 3: Estimation of a six-relaxation DSRF. See Table 1 for numerical data. (a) Estimates by the proposed method. (b) Estimates by `invfreqs` with nonphysical parameters removed.

The same DSRF is also estimated using `invfreqs`. The a priori model order is chosen to be 8 which is slightly higher than the actual but is reasonable because in practice it is difficult to know the actual model order. The estimated model parameters are recorded in Table 1. There are two estimated ζ that are complex and one negative. A physically possible DSRF can be obtained by throwing away these complex or negative relaxation frequencies. The resulting estimated DSRF is shown in Fig. 3(b). Three relaxations are correctly recovered, but the two left most expected relaxations are not. The EMD between the estimate and truth is 0.3323 decades, much higher than the EMD of the proposed method.

Table 1: Estimation of a six-relaxation DSRF

Truth	c_k	0.2000	0.1333	0.2000	0.1333	0.2000	0.1333			
	$\log \zeta_k$	2.6842	3.4855	4.5135	4.9985	5.6839	6.1162			
Proposed method	\hat{c}_l	0.2076	0.1343	0.1973	0.1286	0.1928	0.1341	0.0052		
	$\log \hat{\zeta}_l$	2.6515	3.4803	4.5109	4.9981	5.6801	6.0809	4.8931		
invfreqs	\hat{c}_l		0.2418	0.2269	0.1465	0.2546	0.1301	$-0.3902 \cdot 10^{-4}$	$-0.3902 \cdot 10^{-4}$	0.1334
	$\log \hat{\zeta}_l^\dagger$		3.3303	4.5111	5.0126	5.7188	6.2983	$-0.0012 + 0.0042i$	$-0.0012 - 0.0042i$	-0.0127

†Negative or complex values are not logged

Although a physically possible DSRF can be obtained by throwing away the nonphysical estimates, the resulting spectrum can be quite different from the truth. Using the actual model order or its neighboring numbers as the a priori model order does not preclude complex model parameters either. Nevertheless, when the true model order is low and the SNR is high, satisfactory estimates can be obtained from `invfreqs` by throwing out nonphysical parameters.

Returning complex or nonphysical estimates is a problem that plagues many methods, and there is not a proper way to deal with the complex estimates. The best way is perhaps to restrict the model parameters to be real and physical when setting up the problem, and this is the approach taken in the proposed method.

3.2.3 Signal to Noise Ratio

To see how the proposed method performs in noise, a Monte Carlo simulation versus SNR is run on a target with a four-relaxation DSRF. Goodness of estimation is measured by the EMD between the estimate and truth. The simulation result, shown in Fig. 4, shows the robustness of the estimation method at different signal-to-noise ratios.

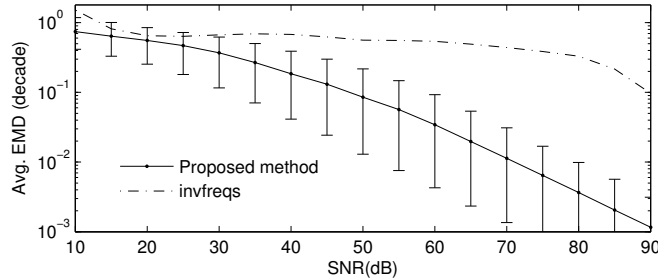


Figure 4: Monte Carlo simulation on goodness of estimation vs. SNR performed on a four-relaxation DSRF. Sample size is 10,000 at each SNR. Error bars indicate the range of EMD between the 10th and 90th percentiles.

As expected, the EMD between the estimate and the truth increases as the SNR decreases. This suggests that the proposed method is functional in a range of SNR where the EMD is below some threshold. This threshold, however, depends on the application of the estimated spectrum. For example, in the case of classification, a more robust classifier may tolerate worse estimations and, therefore, allow lower SNR.

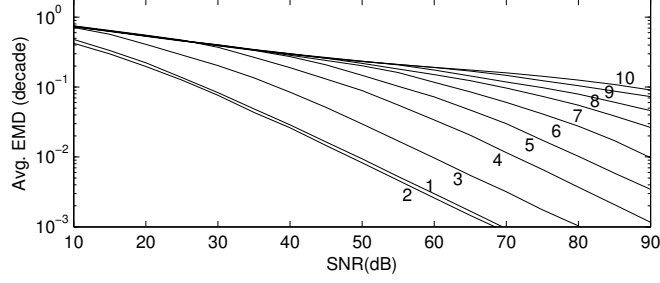


Figure 5: Monte Carlo simulation on goodness of estimation vs. SNR for different DSRFs with model order ranging from 1 to 10. Sample size is 10,000.

The same noise simulation was also performed on `invfreqs` using the actual model order as the a priori model order. Nonphysical parameters are removed from the estimate. As shown in Fig. 4, `invfreqs` barely functions except at around 90 dB SNR where its average EMD drops to 0.1 decades. In comparison, the proposed method has an average EMD one hundred times smaller than that of `invfreqs` at 90 dB SNR, and has low EMD for a wide range of SNR.

Figure 5 shows the same Monte Carlo simulation performed on DSRFs with different model orders using the proposed method. It is seen that a higher model order DSRF requires a higher SNR to achieve a given goodness of fit (EMD). Although the curves are different for each model order, all curves have the same behavior, i.e., the goodness of estimation is positively correlated to the SNR. The consistent trend of these curves suggests that the proposed method is stable and functional over a wide range of SNR.

While it seems rather high the SNR levels at which the simulations were conducted, it was observed that what would usually be a high SNR in other applications is noisy for the EMI application. For example (Fig. 6), a frequency response added with a 25 dB AWGN appears noisy even though a 25 dB AWGN would be considered as a very high SNR in other applications, like radar. In addition, the range of the SNR for the simulation was chosen to be close to what is observed in practice. In the laboratory measurements, a typical SNR for loop targets in this work is 70 dB when the target is placed 10 cm below the EMI sensor. In reality, the depth and size of the target are two dominant factors of SNR. The SNR increases with the size of the target, and decreases with the buried depth.

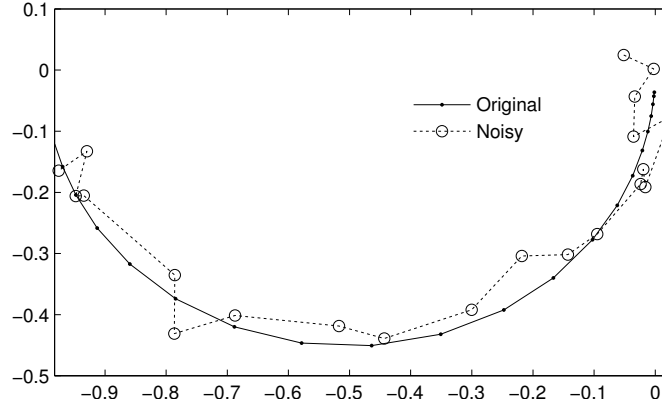


Figure 6: An instance of a frequency response added with a 25 dB AWGN.

3.3 Laboratory Data

The primary interest of this section is to examine the physical meaning of the estimated DSRF. It is shown here that the estimated spectrum agrees with the theoretical, physical DSRF derived from electromagnetic theory, and the estimate is not just another good fit to the data, which can be a problem for other estimation methods [7]. The data are measured with a wideband EMI sensor operating at 21 frequencies approximately logarithmically distributed over the range 300 Hz–90 kHz [30].

3.3.1 Single Loop

It is examined here the simplest case — a single thin wire circular loop. This target contains only one relaxation located at $\zeta = R/L$, where L is the inductance and R is the resistance of the loop. These quantities can be computed according to (26) and (27) in Appendix D. The theoretical EMI frequency response and DSRF can be found in [34].

Figure 7(a) shows three independently measured EMI responses for circular copper loops of circumferences 150, 200, 200 mm and AWG No. 24, 32, and 36, respectively. The theoretical and estimated DSRF are plotted together in Fig. 7(b). The estimates are seen to agree with the theory. The deviations from the theory are 0.0047, 0.0117, and 0.0028 decades for the loops with AWG No. 24, 32, and 36, respectively. All deviations are relatively small in the observable relaxation frequency range, and it can be concluded that the estimated DSRF is an accurate representation of the physical DSRF.

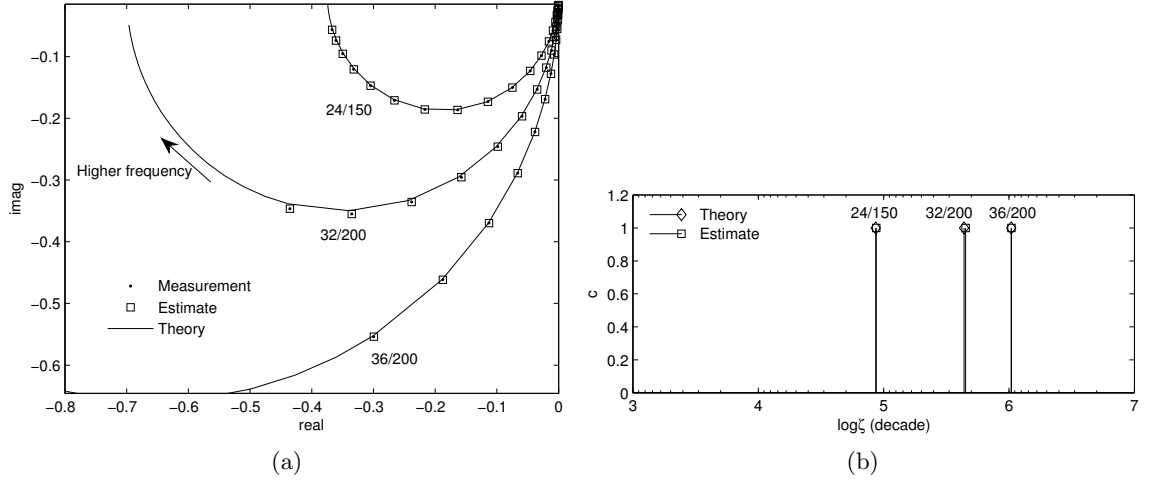


Figure 7: (a) Frequency response of three independently measured single loops on an Argand diagram. Responses are normalized such that $\|\mathbf{h}\|_2 = 1$. Measurements are labeled in the form of AWG/circumference(mm). (b) Theoretical and estimated DSRF. Theoretical $\log \zeta_k$, from left to right, are 4.9364, 5.6416, and 6.0167. Estimated $\log \hat{\zeta}_l$, from left to right, are 4.9411, 5.6534, and 6.0195. All relaxations have an amplitude of unity.

3.3.2 Two Coplanar Coaxial Circular Loops

To test the method on a more complicated spectrum, the two-coplanar-coaxial-circular-loops target is reconsidered. A physical target was built according to the same specifications described in Section 3.2.1. The EMI response of this target was measured in the laboratory and is shown in Fig. 8(a). The SNR is about 70 dB. The estimated and theoretical DSRF are displayed in Fig. 8(b).

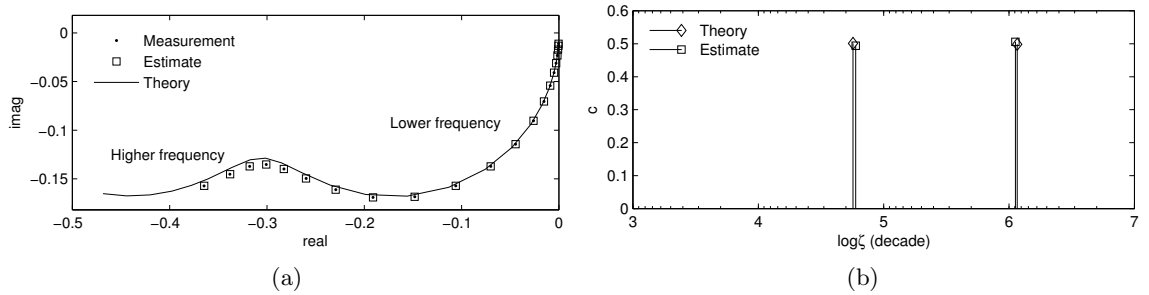


Figure 8: (a) Laboratory measured frequency response of two coplanar coaxial circular loops on an Argand diagram. Theory deviates from the measurement at higher frequencies. Responses are normalized such that $\|\mathbf{h}\|_2 = 1$. (b) Theoretical and estimated DSRF. $\log \zeta_k$ and c_k are (4.7552 6.0651) and (0.5013 0.4987), respectively. The estimate $\log \hat{\zeta}_l$ and \hat{c}_l are (4.7768 6.0514) and (0.4941 0.5059), respectively.

The estimated DSRF deviates from the theory slightly with a deviation of 0.0177 decades. This is most likely due to the thin-wire approximation used in the theory. In the theory, the wire radius is assumed to be much smaller than the loop radius. The inner loop (#22 AWG) has a loop radius to wire radius ratio of about of 47 which is not very high, meaning the wire cannot be modeled as infinitely thin. In addition, thicker wires have a secondary relaxation due to the off-wire-axial current flow which is not accounted for in the theory. At any rate, the deviation is small, and the estimated spectrum is very close to the theory. Thus, it can be concluded that this estimated DSRF is an accurate representation of the true DSRF of the physical target.

3.3.3 Non-magnetic Sphere

The spectrum of a metallic sphere is difficult to estimate because it contains an infinite sequence of relaxations, and the spacing between successive relaxation frequencies decreases as the relaxation frequency decreases [3]. The decrease in spacing makes the relaxations in the region of these closely spaced ζ indistinguishable from one another. It is therefore understood that it is impossible to perfectly recover the spectrum of a sphere. Here, the proposed method is tested against the EMI response of an aluminum sphere measured in the lab. The sphere has a radius of 0.9525 cm. The theoretical and estimated DSRF are plotted in Fig. 9. The EMD between the truth and estimate is 0.1088 decades.

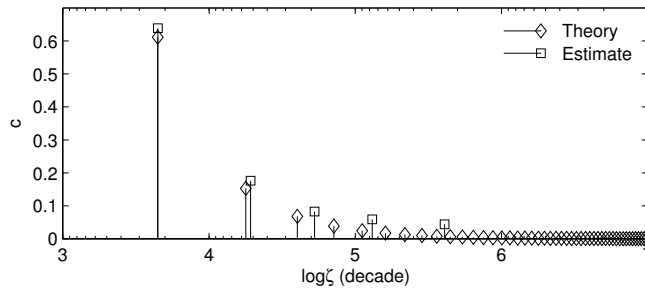


Figure 9: DSRF estimation of a laboratory-measured sphere. The theoretical DSRF has an infinite sequence of relaxation frequencies.

In the estimated DSRF, the first two relaxations are correctly recovered, but the remaining theoretical relaxations are accounted for by the other three estimated ones. It is observed that closely-spaced theoretical relaxations in one region are combined into one

estimated relaxation, and the theoretical spectral amplitudes in that region roughly add up to the estimated spectral amplitude. For example, the right-most estimated relaxation has an amplitude of 0.0438, and it accounts for the infinitely many theoretical relaxations to its right, which have an amplitude sum of 0.0521. The estimated DSRF, even though it cannot recover exactly the theoretical DSRF, is seen to approximate the theory. In this case of a sphere, the estimated DSRF is an approximation to the physical DSRF, and it is not just a good fit, but a fit that can be related to the physical properties of the target.

3.4 *Field Data*

As a final demonstration of the proposed method, it is estimated the DSRF of three types of landmines (Fig. 10). The EMI measurement system uses a dipole transmit coil and a quadrapole receive coil along with a down-track filter that is important to make the nonnegative constraint applicable for this system [30]. For each type of landmine, measurements were collected from several landmines buried at different depths and locations, and the DSRF of each sample was estimated and then plotted together with others of the same type. The spectral amplitudes are represented by the color intensity.

Figure 10(a) presents the DSRF of seven Type-A landmines: a low-metal content, non-magnetic, moderate EMI response antipersonnel landmine. The SNR ranges from about 45 dB to 60 dB. All seven Type-A landmines exhibit consistency in the relaxation frequencies and the spectral amplitudes. The average EMD between pairs of landmines is 0.0594 decades.

Figure 10(b) presents the DSRF of eight Type-B landmines: a medium-metal content, magnetic, strong EMI response antipersonnel landmine. The SNR ranges from about 55 dB to 70 dB. The spectra are consistent, both $\hat{\zeta}$ and \hat{c} exhibit the same behavior in all eight samples. Mine #7 differs from the others somewhat in $\hat{\zeta}$, but the number of relaxations and the trend of spectral amplitudes is the same as the other seven Type-B landmines. The average EMD between pairs of landmines is 0.1536 decades.

Figure 10(c) presents the DSRF of seven Type-C landmines: a low-metal content, magnetic, weak EMI response antipersonnel landmine. The SNR ranges from about 20 dB to

35 dB. The spectra are less consistent compared to Type-A and Type-B landmines, but notice that the prominent relaxations are all located around $\log\zeta=5$ decades. Since the response is weak, the noise could move the relaxations around as seen in Fig. 10(c). The average EMD between landmine pairs is 0.1490 decades, which is slightly lower than the average EMD in Fig. 10(b). This is because the two prominent relaxations in Fig. 10(b) are farther away from each other.

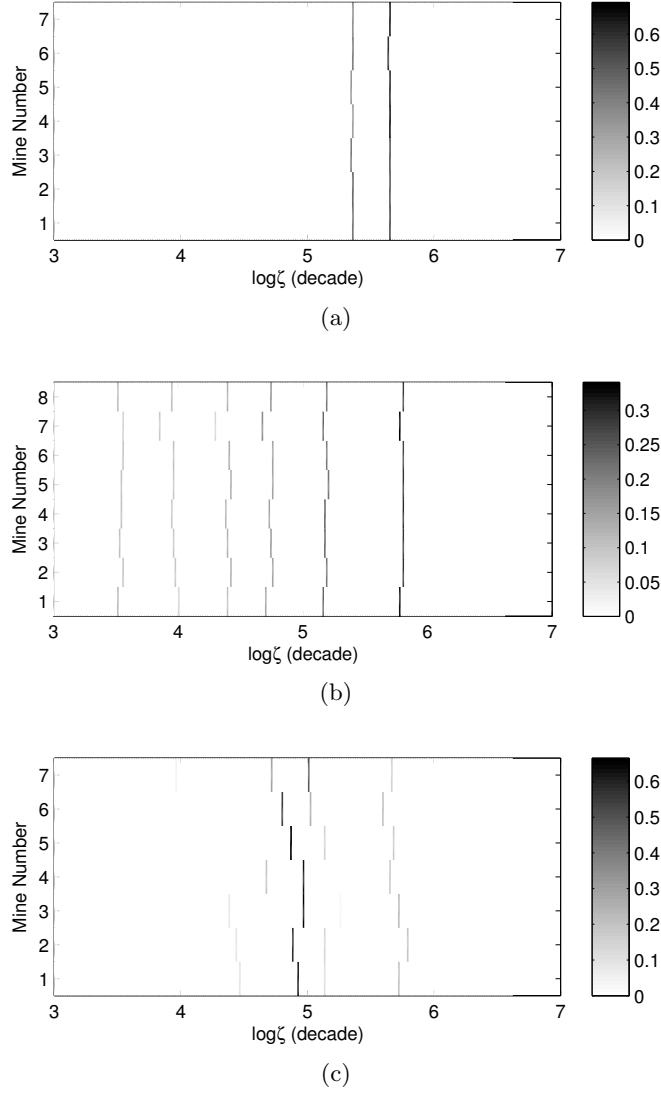


Figure 10: Estimated DSRF of real landmines. The spectral amplitude is represented by the intensity: darker the color, larger the amplitude. (a) Seven Type-A landmines. (b) Eight Type-B landmines. (c) Seven Type-C landmines.

The estimated $H(0)$ of the three types of landmines are normalized and plotted in

Fig. 11. The normalized $H(0)$ reflects the magnetic properties of the landmines. Type-A landmines are nonmagnetic and therefore have a normalized $H(0)$ close to zero. The other two types of landmines have a normalized $H(0)$ well above zero which reflects the magnetic content of the landmines. Variations in the estimated $H(0)$ are consistent with the variations in the DSRF.

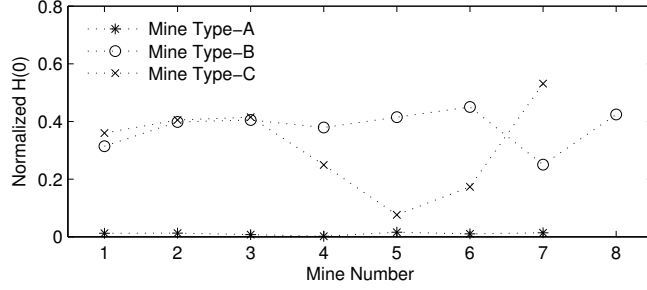


Figure 11: Normalized estimated $H(0)$ for landmines in Fig. 10. $H(0)$ is normalized by $\sum_{l=1}^L \hat{c}_l$.

The variation of the estimated DSRF and $H(0)$ could be caused by several factors such as manufacturing variations, corrosion, the magnetic properties of the soil, or measurement errors. Manufacturing variations in the shape of the metal parts and their electrical and magnetic properties can cause variations in the DSRF. Corrosion can change the properties of the metal parts which will change its response. It is possible that landmine #7 in Fig. 10(b) has a metal part slightly different from the other seven instances. The lower normalized $H(0)$ suggests a different magnetic property, and the slightly different DSRF reaffirms this small variation in the metal.

The response due to the magnetic properties of the soil can also influence the DSRF since the response of the soil is superimposed on the response of the target and it is not possible to completely separate the two. For the landmines presented in Fig. 10(c), the variation in the estimated $H(0)$ maybe primarily due to the magnetic properties of the soil. Since the magnetic shift observed in the response of the soil is on the same order of magnitude as the response of these landmines, the soil can have a strong influence on the landmine responses. On the other hand, landmines presented in Fig. 10(b) have much stronger EMI responses, and influence from the soil is therefore insignificant.

In general, landmine of one type have consistent estimated DSRFs. These stable and recurring DSRFs could be a valuable feature to be exploited in target discrimination. The estimated $H(0)$ can also be used as a feature when it is not overwhelmed by the noise or ground response.

3.4.1 Dissimilarity Between Various Mine Types

It is further demonstrated here the consistency of the estimated DSRF from targets of the same type and also the dissimilarity between different types of targets [36]. It is chosen one hundred independently measured field samples from eleven types of landmines and various metal clutter objects [30]. After estimating the DSRF of each sample, the EMD between all pairs of DSRFs is computed to generate the dissimilarity map shown in Fig. 12. The diagonal is zero because that is the EMD between a DSRF and itself which is zero.

It is seen that landmines of the same type are, in EMD units, close to each other, meaning landmines of the same type are similar. Mines of type **I** do not have small EMD among its sample pairs. The reason is unclear, but it is speculated that this target has negative relaxations as the real part of the responses do not always decrease with the frequency. Therefore, the estimated DSRF could be inaccurate. On the other hand, landmines and clutter, are far from each other, with few exceptions. Clutter that is similar to landmines may cause false alarms, but the EMD from clutter to any type of mine is mostly smaller than the EMD within that mine type. The plot simply shows the clustering of landmines and suggests the applicability of the DSRF for target discrimination.

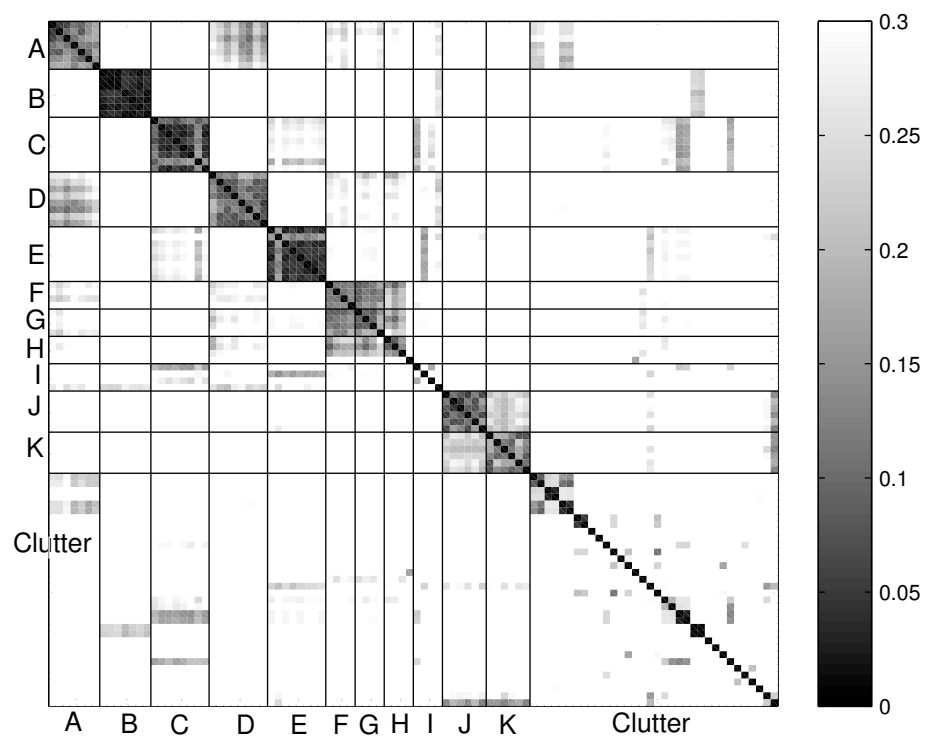


Figure 12: The EMD between samples from eleven types of landmines (A to K) and metal clutter. Darker colors denote smaller distances which indicate that two samples are more similar.

CHAPTER IV

CONCLUSIONS

In this thesis, a robust method is formulated to estimate the DSRF of a target. The proposed method does not require a priori knowledge of the model order and returns only real parameters. The proposed method is tested with a wide variety of data, targets, and noise levels, and is found to give stable, accurate, and quick estimates of the DSRF of a target. When the DSRF cannot be exactly recovered, the estimate is an approximation to the actual. In all cases, the estimated DSRF is directly related to the physical properties of the target.

The consistently estimated DSRF from targets of the same type suggests that the proposed method is a promising way to generate features for target discrimination. The rotational and positional invariability of the relaxation frequencies also suggests the potential of performing target discrimination using the DSRF. Designing a target discriminator based on the estimated DSRF would be a natural extension of this work.

APPENDIX A

THE EMI MODEL

The physical model of the EMI response and its relation to the DSRF model is presented here. The EMI response of a metallic object is the result of the interaction between the transmitting loops, the receiving loops, and the object's magnetic polarizability \mathbf{M} [31]:

$$H(\omega) = \alpha \mathbf{H}_R^T \mathbf{M}(\omega) \mathbf{H}_T, \quad (12)$$

where α is a real constant, \mathbf{H}_T is the magnetic field generated by the transmitting loop, \mathbf{H}_R is the magnetic field of the receiving loop if it is driven, and \mathbf{M} is a complex, frequency independent, second rank tensor.

Equation (12) can be expanded because the magnetic polarizability of a target can be written as a sum of relaxations [3]:

$$\mathbf{M}(\omega) = T_0 \mathbf{T}_0 - \sum_{k=1} T_k \left(\frac{j\omega/\zeta_k}{1 + j\omega/\zeta_k} \right) \mathbf{T}_k, \quad (13)$$

where T_k is a real constant and \mathbf{T}_k is a real, symmetric, second rank tensor. The first term is due to the bulk magnetic permeability of the target, which is assumed to be frequency independent, and the second term is due to the currents induced in the target [31].

Expanding \mathbf{M} in (12) using (13), the response becomes

$$\begin{aligned} H(\omega) &= \alpha \mathbf{H}_R^T \left[T_0 \mathbf{T}_0 - \sum_{k=1} T_k \left(\frac{j\omega/\zeta_k}{1 + j\omega/\zeta_k} \right) \mathbf{T}_k \right] \mathbf{H}_T \\ &= \alpha \left[T_0 \mathbf{H}_R^T \mathbf{T}_0 \mathbf{H}_T - \sum_{k=1} T_k \left(\frac{j\omega/\zeta_k}{1 + j\omega/\zeta_k} \right) \mathbf{H}_R^T \mathbf{T}_k \mathbf{H}_T \right] \\ &= d_0 - \sum_{k=1} d_k \frac{j\omega/\zeta_k}{1 + j\omega/\zeta_k}, \end{aligned} \quad (14)$$

where $d_k = \alpha T_k \mathbf{H}_R^T \mathbf{T}_k \mathbf{H}_T$, and it is noted that $\mathbf{H}_R^T \mathbf{T}_k \mathbf{H}_T$ is constant for a given position and orientation of the target relative to the sensors. This form provides more intuition of the physical process of the EMI, where, again, the first term is due to the bulk magnetic permeability of the target and the second term is due to the currents induced in the target.

The EMI model in (14) can be related to the model presented in Section 1.2 by

$$\begin{aligned}
H(\omega) &= d_0 - \sum_{k=1} d_k \frac{j\omega/\zeta_k}{1 + j\omega/\zeta_k} \\
&= d_0 - \sum_{k=1} d_k \frac{j\omega/\zeta_k}{1 + j\omega/\zeta_k} + d_k - d_k \\
&= \left(d_0 - \sum_{k=1} d_k \right) - \sum_{k=1} d_k \frac{j\omega/\zeta_k}{1 + j\omega/\zeta_k} - d_k \frac{1 + j\omega/\zeta_k}{1 + j\omega/\zeta_k} \\
&= \left(d_0 - \sum_{k=1} d_k \right) + \sum_{k=1} \frac{d_k}{1 + j\omega/\zeta_k} \\
&= c_0 + \sum_{k=1} \frac{c_k}{1 + j\omega/\zeta_k}.
\end{aligned}$$

It is identified that c_k and d_k are related by

$$d_k = c_k, \quad k = 1, 2, 3, \dots \quad (15)$$

$$d_0 = c_0 + \sum_{k=1} c_k. \quad (16)$$

APPENDIX B

NONNEGATIVE SPECTRUM

It is examined here the relation between the nonnegative spectral amplitudes and the observation that the real part of a frequency response decreases as the frequency increases. It is found that whenever the real part of a frequency response decreases with respect to the frequency, one can practically assume the spectral amplitudes are all nonnegative.

The EMI frequency response of a metallic target can be modeled as

$$H(\omega) = c_0 + \sum_{k=1}^K \frac{c_k}{1 + j\omega/\zeta_k}. \quad (17)$$

For a frequency response to have decreasing real part with respect to the frequency ω , it is sufficient but not necessary to have all nonnegative c_k , as shown in the derivation below. However, the derivation also suggests that whenever a c_k is negative it is either (a) very small in magnitude or (b) close to another positive c_k of larger magnitude, which makes this negative c_k practically nonnegative.

Suppose a response has two relaxations

$$H(\omega) = \frac{a}{1 + j\omega/\zeta_a} - \frac{b}{1 + j\omega/\zeta_b} \quad (18)$$

with $a, b > 0$. The real part of the response is

$$\text{Re}\{H(\omega)\} = \frac{a}{1 + \omega^2/\zeta_a^2} - \frac{b}{1 + \omega^2/\zeta_b^2}.$$

To have a decreasing real part with respect to the frequency, it must be satisfied that

$$\frac{d\text{Re}\{H(\omega)\}}{d\omega} = \frac{-2a\omega/\zeta_a^2}{(1 + \omega^2/\zeta_a^2)^2} + \frac{2b\omega/\zeta_b^2}{(1 + \omega^2/\zeta_b^2)^2} < 0. \quad (19)$$

Multiply by $(1 + \omega^2/\zeta_a^2)^2(1 + \omega^2/\zeta_b^2)^2/(2\omega)$:

$$-a\zeta_a^2(1 + \omega^2/\zeta_b^2)^2 + b\zeta_b^2(1 + \omega^2/\zeta_a^2)^2 < 0.$$

Express in the form $x^2 - y^2$:

$$[\sqrt{b}\zeta_b^{-1}(1 + \omega^2/\zeta_a^2)]^2 - [\sqrt{a}\zeta_a^{-1}(1 + \omega^2/\zeta_b^2)]^2 < 0.$$

Use the identity $x^2 - y^2 = (x + y)(x - y)$:

$$\begin{aligned} & [\sqrt{b}\zeta_b^{-1}(1 + \omega^2/\zeta_a^2) + \sqrt{a}\zeta_a^{-1}(1 + \omega^2/\zeta_b^2)] \cdot \\ & [\sqrt{b}\zeta_b^{-1}(1 + \omega^2/\zeta_a^2) - \sqrt{a}\zeta_a^{-1}(1 + \omega^2/\zeta_b^2)] < 0 \end{aligned}$$

The first term can be divided out because it is positive:

$$\sqrt{b}\zeta_b^{-1}(1 + \omega^2/\zeta_a^2) - \sqrt{a}\zeta_a^{-1}(1 + \omega^2/\zeta_b^2) < 0.$$

Rearrange in the powers of ω :

$$g(\omega) = \omega^2 \left(\frac{\sqrt{a}}{\zeta_a \zeta_b^2} - \frac{\sqrt{b}}{\zeta_a^2 \zeta_b} \right) + \frac{\sqrt{a}}{\zeta_a} - \frac{\sqrt{b}}{\zeta_b} > 0. \quad (20)$$

To satisfy (19) is to satisfy $g(\omega) > 0$. The following finds the minimum of $g(\omega)$ and ensures it is positive.

$$\frac{dg(\omega)}{d\omega} = 2\omega \left(\frac{\sqrt{a}}{\zeta_a \zeta_b^2} - \frac{\sqrt{b}}{\zeta_a^2 \zeta_b} \right) = 0$$

The extremum is at $\omega = 0$. To have this extremum be a minimum,

$$\begin{aligned} \left. \frac{d^2g(\omega)}{d\omega^2} \right|_{\omega=0} &= 2 \left(\frac{\sqrt{a}}{\zeta_a \zeta_b^2} - \frac{\sqrt{b}}{\zeta_a^2 \zeta_b} \right) > 0 \\ \frac{\sqrt{a}}{\zeta_a \zeta_b^2} &> \frac{\sqrt{b}}{\zeta_a^2 \zeta_b} \\ \frac{a}{b} &> \left(\frac{\zeta_b}{\zeta_a} \right)^2. \end{aligned} \quad (21)$$

Restrict the minimum be positive:

$$\begin{aligned} g(\omega = 0) &= \frac{\sqrt{a}}{\zeta_a} - \frac{\sqrt{b}}{\zeta_b} > 0 \\ \frac{\sqrt{a}}{\zeta_a} &> \frac{\sqrt{b}}{\zeta_b} \\ \frac{a}{b} &> \left(\frac{\zeta_a}{\zeta_b} \right)^2. \end{aligned} \quad (22)$$

Therefore, $H(\omega)$ has decreasing real part with respect to ω when (21) and (22) are satisfied. Or equivalently,

$$\frac{a}{b} > \max \left(\left(\frac{\zeta_a}{\zeta_b} \right)^2, \left(\frac{\zeta_b}{\zeta_a} \right)^2 \right). \quad (23)$$

This also requires $a > b$ since the right-hand side ≥ 1 .

To interpret this result, (23) is expressed in an alternative form. Take the log of (23) on both sides:

$$\frac{1}{2} \log \frac{a}{b} > |\log \zeta_a - \log \zeta_b|. \quad (24)$$

The right-hand side is the distance between the two relaxations in log space. When the negative component is relatively large (b large, $a/b \rightarrow 1$; recall that $a > b$) the left-hand side approaches zero and the distance approaches zero. When the negative component is far away from the positive one (right-hand side large), b is required to be relatively small to a . In either case, the negative relaxation would be overwhelmed by the positive relaxation, especially under the presence of noise.

A similar conclusion can be made about the imaginary part of a response is always negative. It is easy to prove that the nonnegative spectral amplitude is also a sufficient but not a necessary condition to having negative imaginary part. This proof is left as an exercise to the reader.

APPENDIX C

DENSITY OF DISCRETIZATION OF THE RELAXATION FREQUENCY SPACE

The number M in (5) decides the number of sample points placed in a relaxation frequency range. Equivalently, M controls the density of discretization of the ζ space. The denser the discretization, the more likely a sampled ζ is close to the true ζ . In the extreme case, if an infinite number of sample points fill up the relaxation frequency range, there must be one sampled ζ that coincides with the true ζ . Of course, computationally it would be impossible to estimate a DSRF with an infinite number of sample points. Even if the number of samples is kept finite, with a fixed number of observations N , the null space of $\tilde{\mathbf{Z}}$ gets larger and larger as M increases, and the number of possible bad estimates increases. It is therefore desirable to have M just large enough, so that the estimate is likely correct while the computational cost remains low.

To determine an good choice of M , a Monte Carlo simulation on the density of discretization of ζ space is performed over a range of M with different noise levels. The simulation result is shown in Fig. 13, where a higher EMD value means worse estimates. The figure suggests that M should be greater than 60 to avoid bad estimation due to insufficient sample points while M should be no greater than 200 because adding more sample points does not improve the goodness of fit. It is seen that within the range $60 < M < 200$, at lower signal-to-noise ratios (50–60 dB), better estimation is obtained with $M \approx 70$. While at higher SNRs (65–80 dB), better estimation is obtained with $M \approx 120$. In words, at lower SNR, lower discretization density gives more robust performance, which agrees with the intuition that larger dictionaries are more sensitive to perturbation of noise. On the other hand, when the SNR is high, higher discretization density delivers more accurate estimates. To accommodate a wide range of SNR, to chose $M \approx 100$ is a good compromise, and since the relaxation frequency range is about 4 decades, there are about 25 sample points per

decade.

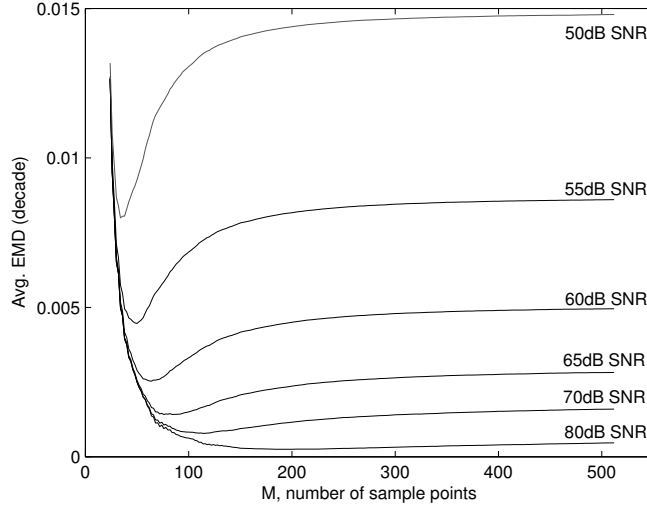


Figure 13: Monte Carlo simulation on density of discretization of ζ space. Each point on the curve is the average EMD over 10,000 samples.

Although the Monte Carlo simulation is performed on a two-relaxation target, the result should well represent the behavior of the estimation process in general. This is true as observed in simulations of different DSRF. Therefore, it can be inferred that, in general, a good choice of M is around 25 sample points per decade. As shown in the figure, the goodness of fit is not sensitive to the chosen M given it is large enough, so there is some freedom on choosing M .

APPENDIX D

A CIRCUIT MODEL FOR TWO COPLANAR COAXIAL CIRCULAR LOOPS

It is derived here a theoretical approximation to the magnetic polarizability of two coplanar coaxial circular loops in low-frequency realm. A larger loop of radius r_1 with wire radius a_1 is placed around a smaller loop of radius r_2 with wire radius a_2 . The wires have electric conductivity σ and relative permeability μ_r . Two loops are on the same plane and share the same center. The wire radius is assumed to be much smaller than the loop radius. i.e., $a \ll r$. This configuration of two coplanar coaxial circular loops can be modeled as a simple two coupled LR circuits shown in Fig. 14.

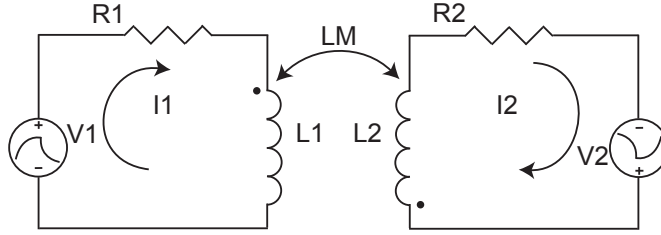


Figure 14: Circuit model for two coplanar coaxial circular loops.

The voltage $V(s)$ induced by the incident magnetic field on the loop is related to the incident magnetic excitation H^{inc} in Laplace domain through

$$V(s) = -s\mu_0 H^{inc} A, \quad (25)$$

where A is the loop area and μ_0 is the permeability of free space. Assume the incident magnetic field is normal to the plane containing the loops. In low frequency, the resistance R of the loop is

$$R = \frac{2r}{a^2\sigma}, \quad (26)$$

and the inductance L is [32]

$$L = r\mu_0 \left[\left(1 + \frac{a^2}{8r^2}\right) \ln\left(\frac{8r}{a}\right) + \frac{a^2}{24r^2} - 2 + \frac{\mu_r}{4} \right]. \quad (27)$$

The mutual inductance L_M between the two loops is [33]

$$L_M = \frac{2\mu\sqrt{r_1 r_2}}{k} \left[\left(1 - \frac{1}{2}k^2\right)K(k) - E(k) \right], \quad (28)$$

where

$$k^2 = \frac{4r_1 r_2}{(r_1 + r_2)^2}, \quad (29)$$

and K and E are the complete elliptic integrals.

In the Laplace domain, the system equation for the circuit is [34]

$$\begin{bmatrix} V_1 \\ V_2 \end{bmatrix} = \begin{bmatrix} R_1 + sL_1 & sL_M \\ sL_M & R_2 + sL_2 \end{bmatrix} \begin{bmatrix} I_1 \\ I_2 \end{bmatrix}. \quad (30)$$

Solve for the currents:

$$\begin{bmatrix} I_1 \\ I_2 \end{bmatrix} = \frac{-s\mu_0 H^{inc}}{(R_1 + sL_1)(R_2 + sL_2) - (sL_M)^2} \cdot \begin{bmatrix} R_2 + sL_2 & -sL_M \\ -sL_M & R_1 + sL_1 \end{bmatrix} \begin{bmatrix} A_1 \\ A_2 \end{bmatrix}. \quad (31)$$

The magnetic polarizability \mathbf{M} is then

$$\mathbf{M}(s) = \frac{A_1 I_1 + A_2 I_2}{H^{inc}} \quad (32)$$

$$= \frac{-s\mu_0 [A_1^2(R_2 + sL_2) + A_2^2(R_1 + sL_1) - 2sA_1 A_2 L_M]}{(R_1 + sL_1)(R_2 + sL_2) - (sL_M)^2}. \quad (33)$$

Perform partial fraction expansion:

$$\mathbf{M}(s) = -s \left(\frac{Q_1}{s - s_1} + \frac{Q_2}{s - s_2} \right) \quad (34)$$

$$= -(Q_1 + Q_2) + \frac{Q_1}{1 - s/s_1} + \frac{Q_2}{1 - s/s_2}, \quad (35)$$

where s_1 and s_2 are the roots of the denominator in (33) [12]:

$$s_{1,2} = \frac{-(R_1 L_2 + R_2 L_1) \pm \sqrt{(R_1 L_2 - R_2 L_1)^2 + 4R_1 R_2 L_M^2}}{2(L_1 L_2 - L_M^2)}. \quad (36)$$

Variable Q_1 and Q_2 are simply

$$Q_1 = \frac{\mu_0 [A_1^2(R_2 + s_1 L_2) + A_2^2(R_1 + s_1 L_1) - 2s_1 A_1 A_2 L_M]}{s_1 - s_2} \quad (37)$$

$$Q_2 = \frac{\mu_0 [A_1^2(R_2 + s_2 L_2) + A_2^2(R_1 + s_2 L_1) - 2s_2 A_1 A_2 L_M]}{s_2 - s_1}. \quad (38)$$

Using (36)–(38) the DSRF of two coplanar coaxial circular loops can be computed. The relaxation frequency $\zeta_k = -s_k$ with corresponding spectral amplitude Q_k .

APPENDIX E

EARTH MOVER'S DISTANCE

Given two distributions $\hat{S} = \{(\hat{\zeta}_i, \hat{c}_i) : i = 1 \dots L\}$ and $S = \{(\zeta_j, c_j) : j = 1 \dots K\}$, the Earth Mover's Distance (EMD) between the two distributions can be computed by solving the optimization problem [10]:

$$\text{Define } d_{ij} = |\log \hat{\zeta}_i - \log \zeta_j| \quad (39)$$

$$\text{EMD}(\hat{S}, S) = \min_{f_{ij}} \frac{\sum_{i=1}^L \sum_{j=1}^K f_{ij} d_{ij}}{\sum_{i=1}^L \sum_{j=1}^K f_{ij}} \quad (40)$$

$$\text{subject to } \sum_{j=1}^K f_{ij} \leq \hat{c}_i \quad i = 1 \dots L \quad (41)$$

$$\sum_{i=1}^L f_{ij} \leq c_j \quad j = 1 \dots K \quad (42)$$

$$\sum_{i=1}^L \sum_{j=1}^K f_{ij} = \min\left(\sum_{i=1}^L \hat{c}_i, \sum_{j=1}^K c_j\right) \quad (43)$$

$$f_{ij} \geq 0 \quad i = 1 \dots L, j = 1 \dots K \quad (44)$$

where f_{ij} is an intermediate variable used during the optimization. Adapting the illustration in Section 3.1, \hat{S} is the piles of earth and S the holes. Equation (41) guarantees no overdraw from each pile of earth, (42) guarantees no over fill at each hole, (43) sets the problem to fill up the holes with as much earth as possible, and (44) allows only moving earth into holes and not the reverse.

In this work, spectra should be normalized having sum of all spectral amplitudes be unity ($\sum c_i = 1$). In this case, the above optimization problem is simplified to having the denominator in (40) be one and the right-hand-side of (43) be unity. The EMD also becomes symmetric.

REFERENCES

- [1] BARSOUKOV, E. and MACDONALD, J. R., *Impedance spectroscopy*, ch. 2, p. 37. New Jersey: Wiley-Interscience, 2005.
- [2] BAUM, C. E., “On the singularity expansion method for the solution of electromagnetic interaction problems,” Interaction Notes 88, Air Force Weapons Laboratory, 1971.
- [3] BAUM, C. E., “Low-frequency near-field magnetic scattering from highly, bu not perfectly, conducting bodies,” in *Detection and Identification of Visually Obscured Targets* (BAUM, C. E., ed.), ch. 6, pp. 163–218, Philadelphia, PA: Taylor & Francis, 1999.
- [4] CHEN, S. S., DONOHO, D. L., and SAUNDERS, M. A., “Atomic decomposition by basis pursuit,” *SIAM Review*, vol. 43, no. 1, pp. 129–159, 2001.
- [5] COLE, K. S. and COLE, R. H., “Dispersion and absorption in dielectrics i. alternating current characteristics,” *J. Chem. Phys.*, vol. 9, pp. 341–351, Apr. 1941.
- [6] COLLINS, L., GAO, P., and CARIN, L., “An improved Bayesian decision theoretic approach for land minedetection,” *IEEE Trans. Geosci. Remote Sens.*, vol. 37, pp. 811–819, Mar. 1999.
- [7] DAS, Y. and MCFEE, J. E., “Limitations in identifying objects from their time-domain electromagnetic induction response,” in *Proc. SPIE*, vol. 4742, (Orlando, FL), pp. 776–788, Apr. 2002.
- [8] DAVIDSON, D. W. and COLE, R. H., “Dielectric relaxation in glycerol, propylene glycol, and n-propanol,” *J. Chem. Phys.*, vol. 19, pp. 1484–1490, Dec. 1951.
- [9] FAILS, E. B., TORRIONE, P. A., SCOTT, JR., W. R., and COLLINS, L. M., “Performance of a four parameter model for modeling landmine signatures in frequency domain wideband electromagnetic induction detection systems,” in *Proc. SPIE*, vol. 6553, (Orlando, FL), p. 65530D, Apr. 2007.
- [10] FISHER, B., “The earth mover’s distance,” Oct. 2008.
- [11] GAO, P., COLLINS, L., GARBER, P. M., GENG, N., and CARIN, L., “Classification of landmine-like metal targets using wideband electromagnetic induction,” *IEEE Trans. Geosci. Remote Sens.*, vol. 38, pp. 1352–1361, May 2000.
- [12] GENG, N., BAUM, C. E., and CARIN, L., “On the low-frequency natural response of conducting and permeable targets,” *IEEE Trans. Geosci. Remote Sens.*, vol. 37, pp. 347–359, Jan. 1999.
- [13] GRANT, F. S. and WEST, G. F., *Interpretation Theory in Applied Geophysics*, ch. 17. New York: McGraw-Hill, 1965.
- [14] GRANT, M., BOYD, S., and YE, Y., “CVX: Matlab software for disciplined convex programming,” July 2008.

- [15] HANSEN, P. C., *Rank-Deficient and Discrete Ill-Posed Problems: Numerical Aspects of Linear Inversion*. Philadelphia, PA: Society for Industrial Mathematics, 1998.
- [16] HAVRILIAK, S. and NEGAMI, S., "A complex plane representation of dielectric and mechanical relaxation processes in some polymers," *Polymer*, vol. 8, pp. 161–210, 1967.
- [17] HOLMSTRÖM, K. and PETERSSON, J., "A review of the parameter estimation problem of fitting positive exponential sums to empirical data," *App. Math. and Comp.*, vol. 126, pp. 31–61, Feb. 2002.
- [18] HONERKAMP, J. and WEESE, J., "A nonlinear regularization method for the calculation of relaxation spectra," *Rheol. Acta*, vol. 32, pp. 65–73, 1993.
- [19] INTERNATIONAL CAMPAIGN TO BAN LANDMINES, *Landmine Monitor 2010*. Ottawa: Mines Action Canada, 2010.
- [20] KAUFMAN, A. A. and EATON, P. A., *The theory of inductive prospecting*, ch. 3. Amsterdam: Elsevier, 2001.
- [21] KEISWETTER, D. A., WON, I. J., MILLER, J., BELL, T., CESPEDES, E., and O'NEILL, K., "Discriminating capabilities of multifrequency EMI data," in *Proc. IGARSS*, vol. 4, (Honolulu, HI), pp. 1415–1417, July 2000.
- [22] LAWSON, C. L. and HANSON, R. J., *Solving Least Squares Problems*, ch. 23. Englewood Cliffs, NJ: Prentice-Hall, Inc., 1974.
- [23] LEVY, E. C., "Complex-curve fitting," *IRE Trans. Automat. Contr.*, vol. 4, pp. 37–43, 1959.
- [24] MILLER, J. T., BELL, T. H., SOUKUP, J., and KEISWETTER, D., "Simple phenomenological models for wideband frequency-domain electromagnetic induction," *IEEE Trans. Geosci. Remote Sens.*, vol. 39, pp. 1294–1298, June 2001.
- [25] OSBORNE, M. R. and SMYTH, G. K., "A modified Prony algorithm for exponential function fitting," *SIAM J. Sci. Comp.*, vol. 16, no. 1, pp. 119–138, 1995.
- [26] RAMACHANDRAN, G., GADER, P. D., and WILSON, J. N., "Granma: Gradient angle model algorithm on wideband EMI data for land-mine detection," *IEEE Geosci. Remote Sens. Lett.*, vol. 7, no. 3, pp. 535–539, 2010.
- [27] RIGGS, L. S., MOONEY, J. E., and LAWRENCE, D. E., "Identification of metallic mine-like objects using low frequency magnetic fields," *IEEE Trans. Geosci. Remote Sens.*, vol. 39, pp. 56–66, Jan. 2001.
- [28] RUBNER, Y., TOMASI, C., and GUIBAS, L. J., "A metric for distributions with applications to image databases," in *Proc. ICCV*, (Bombay, India), pp. 59–66, Jan. 1998.
- [29] SARKAR, T. K. and PEREIRA, O., "Using the matrix pencil method to estimate the parameters of a sum of complex exponentials," *IEEE Antennas Propag. Mag.*, vol. 37, pp. 48–55, Feb. 1995.
- [30] SCOTT, JR., W. R., "Broadband array of electromagnetic induction sensors for detecting buried landmines," in *Proc. IGARSS*, (Boston, MA), July 2008.

- [31] SCOTT, JR., W. R. and LARSON, G. D., “Modeling the measured em induction response of targets as a sum of dipole terms each with a discrete relaxation frequency,” in *Proc. IGARSS*, (Honolulu, Hawaii), July 2010.
- [32] SMYTHE, W. R., SILVER, S., WHINNERY, J. R., and ANGELAKOS, D. J., “Electricity and magnetism,” in *American Institute of Physics Handbook* (GRAY, D. E., ed.), ch. 5, p. 29, NY: McGraw-Hill Book Company, Inc., 1963.
- [33] SMYTHE, W. R., *Static and Dynamic Electricity*, ch. 8, p. 335. NY: McGraw-Hill, 1968.
- [34] SOWER, G. D., “Eddy current responses of canonical metallic targets theory and measurements,” Interaction Notes 526, EG&G MSI, May 1997.
- [35] WARD, S. H., “Electromagnetic theory for geophysical applications,” in *Mining Geophysics* (HANSEN, D. A., HEINRICHS, JR., W. E., HOLMER, R. C., MACDOUGALL, R. E., ROGERS, G. R., SUMNER, J. S., and WARD, S. H., eds.), vol. 2, ch. 2, pp. 10–196, Tulsa, OK: The Society of Exploration Geophysicists, 1967.
- [36] WEI, M., SCOTT, JR., W. R., and MCCLELLAN, J. H., “Estimation and application of discrete spectrum of relaxations for electromagnetic induction responses,” in *Proc. IGARSS*, (Cape Town, South Africa), July 2009.
- [37] WEI, M., SCOTT, JR., W. R., and MCCLELLAN, J. H., “Robust estimation of the discrete spectrum of relaxations for electromagnetic induction responses,” *IEEE Trans. Geosci. Remote Sens.*, vol. 48, pp. 1169–1179, Mar. 2010.